TUDelft

Delft University of Technology

To new frontiers, Microbiology for nanotechnology and space exploration

Lehner, Benj

DOI
10.4233/uuid:acd7102b-339b-45b5-972e-fe3a2ad9c52e

Publication date
2019

Document Version
Final published version

Important note
To cite this publication, please use the final published version (if applicable).
Please check the document version above.

To new frontiers,

Microbiology for nanotechnology and space exploration

PROEFSCHRIFT

ter verkrijging van de graad van doctor

aan de Technische Universiteit Delft

op gezag van de Rector Magnificus prof. dr. ir. T.H.J.J. van der Hagen

voorzitter van het College voor Promoties

in het openbaar te verdedigen op

vrijdag 22 november 2019 om 10.00 uur

DOOR

Benjamin LEHNER

MASTER OF SCIENCE IN BIOLOGY
PARIS LODRON UNIVERSITÄT SALZBURG
GEBOREN TE VÖCKLABRUCK, OOSTENRIJK

Dit proefschrift is goedgekeurd door de promotors.

Samenstelling promotiecommissie

Rector magnificus	chairman
Prof. dr. ir. H.S.J. van der Zant	Technische Universiteit Delft, promotor
Dr. ir. S.J.J. Brouns	Technische Universiteit Delft, promotor

Onafhankelijke leden

Prof. dr. L.J. Rothschild	National Aeronautics Space Administration (NASA)
Dr. A. Cowley	European Space Agency (ESA)
Prof. dr. P. Ehrenfreund	Deutsches Zentrum für Luft und Raumfahrt (DLR)
Prof. dr. M. Dogterom	Technische Universiteit Delft
Prof. dr. C. Wyman	Technische Universiteit Delft, reservelid

Overig lid

Dr. A.S. Meyer	University of Rochester

Table of contents

1

Utilization of bacteria for nanotechnology and space applications

Benjamin A.E. Lehner, Rik Volger, Stan J.J. Brouns, Anne S. Meyer, Aidan Cowley, Lynn J. Rothschild and Herre S.J. van der Zant

Most of the time we associate microorganisms with illnesses, infections and polluted water, but this is only one part of the story. Microbes are the most diverse groups of organisms and we just start to understand them. Their adaptability allowed them to master different kinds of extreme environments and enabled them to produce as well as process a variety of molecules and materials. Throughout history, scientists, brewers, and farmers managed to utilize microbes for a variety of products, such as beer, wine, insulin and other medications, biofuels and many more. Therefore, bacteria can also be seen as nano-factories and they can be applied in many different ways. In this work, we explored the application of microorganisms in two unconventional sectors: nanotechnology and space applications, discussed in 1.1 and 1.2 of this chapter respectively.

1

1.1 The role of bacteria in nanotechnology

The research conducted throughout this thesis started with a concrete task: producing bulk graphene more sustainably and enable a technology to pattern its surface. Graphene is a novel material isolated in 2004 by Andre Geim and Konstantin Novoselov [1] and awarded with the Nobel prize in 2010. Graphene has excellent electronic, optical, and mechanical properties making it attractive for a variety of applications [2, 3]. However, the main problem is its production using current techniques, which are expensive, unsustainable and hard to up-scale. These issues could be resolved by a material known as microbially reduced graphene oxide [4-6]. We started with the abundant material graphite and oxidized it through a well-known chemical procedure originally developed in 1958 by the chemists Hummers and Offeman [7] (Fig. 1.1). Small modifications, additional treatment in an ultrasonic bath and filtering of big particles yielded in a well characterized distribution of single- and few layer graphene oxide (GO). This type of graphene has multiple oxygen groups (epoxy, hydroxyl, carboxyl) on its surface. In terms of conductivity and stability these group can be seen as defects (even though they are useful in other applications: chapter 4).

The organism *Shewanella oneidensis* MR1 is known for its capability to reduce, and therefore remove oxygen from metal oxides by using them as electron acceptor [8]. This mechanism evolved to remove free electrons produced during metabolic processes; human and most aerobic organism use oxygen for this process. It was previously shown that *Shewanella oneidensis* MR1 can also reduce GO to microbially reduce graphene oxide (mrGO) [4]. But the characterisation of the so produced nanomaterial was insufficient and no clear applicational were defined. In chapter 3 of this thesis we verify the conductive properties of mrGO and compare them to chemically reduced graphene oxide (crGO) produced via Hydrazine, the most spread chemical to reduce GO. The properties are not as good as the pristine graphene made by Geim and Novoselov, but we identified a variety of

applications (e.g. composite materials, biosensors & conductive inks) where sustainable microbial production could be beneficial.

Besides the production of graphene, its patterning via microbial processes was another goal. Two approaches, one microscopic (e-beam lithography) and one macroscopic (additive manufacturing) were tested. In the latter, we managed to reliable print *Shewanella oneidensis* in an alginate gel with a resolution of 1 mm (chapter 2) on a graphene oxide surface. However, we could not provide sufficient nutrients and penetrate deep enough into the stacked flakes of graphene oxide for the reduction process without tremendously decreasing the printing resolution. In the microscopic one, we spin coated PMMA on the top of graphene oxide and utilized an e-beam lithography approach to cut patterns out of the coating. The bacteria penetrated below the PMMA surface and reduced the entire side of the flake (chapter 3). This made it impossible to make conductive paths but allowed us to have only one single side of the graphene oxide reduced, which might be beneficial for additive manufacturing approaches. Conducting this research, we also discovered the utilization of these and other bacteria in the change of rocks to extract elemental iron and silicon. This led to collaborations with ESA and NASA, who are highly interested in possibilities to mine and colonize the Moon or Mars.
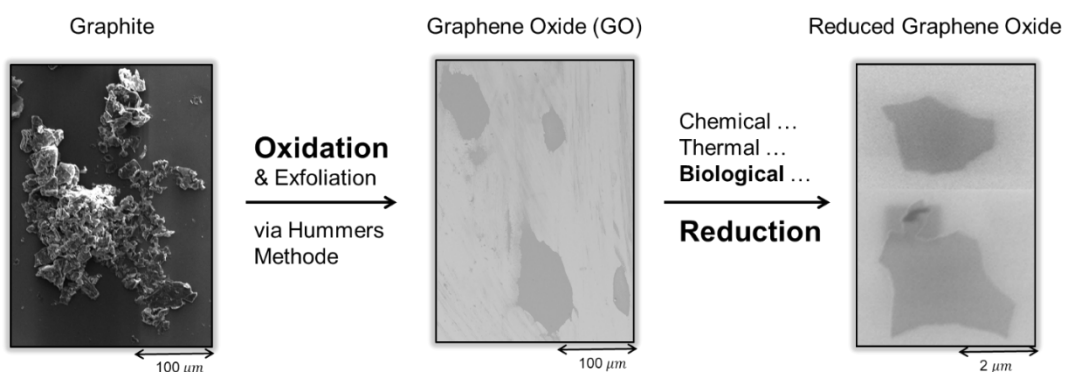

Fig. 1.1 SEM pictures to visualize the concept of the oxidation and exfoliation of graphite and the microbial reduction of graphene oxide to graphene.

1

1.2 The role of bacteria in space applications

All biological systems, including bioreactors, humans, plants, and algae, require a basic amount of nutrients primarily based on carbon and nitrogen in the form of sugars and amino acids. To establish a self-sufficient colony on another celestial body, a critical mass of these nutrients has to be supplied, and efficient recycling systems must be installed to reuse them. This section presents the reasoning why full-scale terraforming is not yet possible and why we have to rely on continual recycling and resupplying to achieve a first bio-based colony. It explains why a human presence in outer space will require an increased focus on biological systems to be sustainable and Earth-independent. We discuss the potential impact of current technologies such as life-support systems, *in situ* resource utilization, energy storage, and additive manufacturing. Finally, this section reveals how mechanochemical and biological solutions in conjunction might pave the way for future human exploration

1.2.1 Requirements for a human outpost

A human outpost on another celestial body needs to fulfill several requirements. For instance, transportation, shelter, supplies, waste removal, hazard protection, and power sources have to be provided to ensure its viability [9]. Every space exploration endeavor so far, however, used resources originating from Earth, which leads to high transportation costs and, ultimately, a high degree of dependence [10]. On Earth, a majority of resources acquired are produced by our biosphere. The establishment of an extraterrestrial biosphere might help to cut down dependence as well as the cost for nearly all the requirements for a human outpost.

Waste removal: One intrinsic attribute of our biosphere is its "circular economy" in which barely any resources are wasted. Different organisms evolved in all types of niches to use and process the waste products of other organisms. For a human outpost, we must copy this behavior. In particular, microorganisms can be a huge help in processing human fecal, wastewater,

and food leftovers (e.g. MELiSSA Loop [11]). This waste recycling is not limited to organic molecules. It has been shown that inorganic molecules (e.g. copper) can also be recycled this way [12].

Supplies: Food and oxygen supply might be the most traditional utilization of biological systems for space exploration [13]. A variety of crops and algae have been studied for applications in spacecrafts or human outposts. However, microorganisms also have been demonstrated to produce medicine on-demand, different types of plastics, and a variety of fuels and gases [14].

Power sources & transportation: The fuels and gases produced by microorganisms might be directly utilized for transportation [15]. Some organisms also play a critical role in alternative types of fuel cells [16].

Shelter & hazard protection: In shelter construction, biological systems probably have the least obvious potential for contribution. However, they are helpful in bio-leaching of ores [17], direct extraction of resources, and the formation of a barrier against cosmic radiation [9].

1.2.2 The benefit of microorganisms

During the last few decades, microorganisms have gained more attention in industrial applications [14]. This increased prominence is due to the improvement of synthetic biology and the realization of bacterial capability as **modifiable nano-factories**. Our genetic toolbox allows us to produce a variety of natural molecules in high quantities utilizing microorganisms. One of the prime examples is insulin [18] where a genetic modification led to a sustainable supply and, therefore, price-drop for the treatment of diabetics.

Beside their capability as nano-factories, microorganisms can be **stored** unchanging over decades in a -80 °C freezer. If one of the stored organisms is needed, a droplet is enough due to their **self-reproducing** properties. One freezer can, therefore, hold a library of different organisms that can be utilized on-demand. In addition to being stored, organisms can **evolve**

towards new environmental conditions to increase their potential in a hazardous environment.

On earth, a large group of bacteria - namely extremophiles - has evolved to **resist** for most organisms' deadly conditions. They can survive and even grow under strong radiation, extreme salinity or pH-values, high and low temperature, or without water. *Bacillus subtilis*, a sporulating organism, was even shown to survive the vacuum conditions of outer space [19].

All these properties (modifiable, nano-factories, storable, self-reproducing, capable of evolution, resistance) make microorganisms an excellent choice to support space exploration. Of course, planetary protection should always be considered. Thus, the use of microorganisms should be limited to closed environments on planets that have been confirmed not to host any native species. However, a biological toolbox might enable astronauts one day to survive at very remote places in the solar system.

1.2.3 Available nutrients

Biological systems have developed a variety of chemical processes to sustain themselves and proliferate. The only requirement is the abundance of sufficient quantities of carbon, nitrogen, hydrogen, oxygen, phosphorus, and sulfur mixed with the right culture of organisms. Each planet or natural satellite under consideration must have a sufficient amount of these elements available or a possibility to deliver them.

The limitations of our technology do not yet allow for true terraforming of entire planets [20]. One major reason for this failure is the deficit of necessary elements on nearly any planet in our solar system. For example, Mars and Neptune are missing nitrogen [21]. Saturn and Jupiter are gas planets mainly consisting of hydrogen and some helium [22].

Missing elements would have to be supplied from other parts of the solar system. The only planet which is likely to have all the necessary elements in a minimal concentration available is Venus, but its strong greenhouse effect leads to an unsuitable high surface temperature (720K) and pressure

(70atm) [23]. Those missing elements together with the insufficiency of available energy which is defined by the planet-sun distance makes terra-forming on a large scale with our current technology impossible.

Nevertheless, we can "terraform" a limited landscape with a self-defined atmosphere on almost every rocky planet, through the concentrating and supplying of certain elements. These processes require technical as well as biological solutions and some of them are described in this thesis.
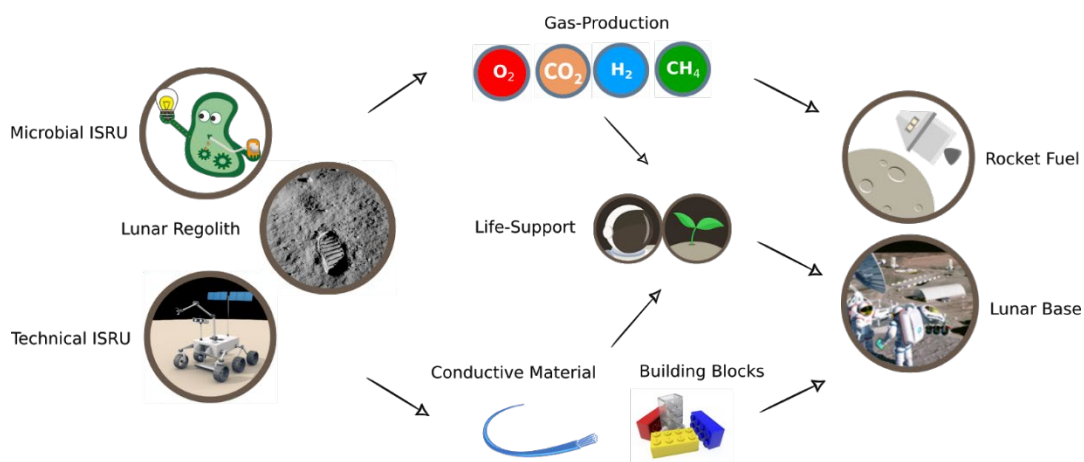
Fig. 1.2 Role of *in-situ* resource utilization (ISRU) and biological systems for the human presence (e.g. on the Moon). The key focus for exploration must be on the sustainable construction of a base, the continuous supply for astronauts (food, water, medicine) as well as the refuelling of rockets. © Pablo Soriano Lopez for some of the icons used.

1.2.4 Investigated biological systems

Biological approach to in-situ resource utilization (ISRU): On Earth, several organisms have evolved to utilize metals from solid mineral substrates as a key part of their metabolism (e.g. *Shewanella oneidensis [8]*, *Acidithiobacillus ferrooxidans* [17], and several members of the *Geobacter* genus [24, 25].) These organisms could be applied to refine specific metals from extraterrestrial regolith in mild or acidic conditions at ambient temperatures. In such a process, the wildtype organisms themselves could

be used, or their molecular machinery for metal interactions could be expressed in a model organism such as *Escherichia coli [26]* or *B. subtilis*. To sustain the previously described processes, the organisms require a supply of several nutrients to satisfy their need for carbon, nitrogen, and further micronutrients. A process relying on supplies from Earth can also be feasible if the process yields in a larger mass of purified product than input nutrients needed. Another option is to select an organism that can combine the extraction/leaching mechanism with the utilization of relatively energy-poor substrates from a life support waste stream, such as volatile fatty acids [27].

Life-Support, production of drugs, & radiation shielding: Biological systems have predominantly been investigated for the application of water cleaning, air recycling, food production and other in the life-support-systems integrated steps. The most efficient recycling and organic production mechanisms known have evolved in nature over billions of years, and the utilization of these will be key for human presence on any other planet or Moon [28]. Not only standard life support but also an on-demand supply of medication and other complex chemicals could theoretically be provided by microorganisms. A library of organisms ready to be cultivated when needed as well as processes to clean up the product (downstream) would be necessary to achieve biological life-support.

1.2.5 Conclusion

To colonize other planets, we will need to mimic working nutrient cycles on Earth, albeit in much smaller quantities and with fewer organisms. The smaller scale is necessary because it is not possible to terraform an entire planet, yet. Nearly all reachable planets are missing quantities of some critical elements that will have to be resupplied from somewhere else. A smart starting supply for the new colony, together with utilizing and concentrating of existing resources, is therefore key to a successful colony. This approach could be referred to as a "small-scale terraforming". The

available resources of the planet would thereby be concentrated to make a small closed environment suitable for human needs.

The needs can be described as (1) waste management, (2) supplies, (3) power-supply & transportation, and (4) shelter. For all these systems, a conjunction of biological and mechanochemical methodologies is necessary. Experience has showed us that there will always be a net loss of certain elements and molecules. In particular, the refueling of rockets will extract elements from the loop, and we have not yet achieved waste management with 100% efficiency. We will, therefore, be dependent on occasional resupply from Earth. Better biological processes result in more freedom and a less dependent colony.

In summary, a successful space colonialization will require a combination of the traditional mechanochemical approaches as well as novel microbial approaches. The reliability of current technological processes combined with the self-reproducing and more sustainable bacterial methods will lead to a mutual benefit. An identification of the exact necessities to achieve a semi-sufficient colony requires intensive tests [chapter 7] coupled with theoretical modeling [chapter 6,8]. However, these methodologies may lead humanity into a new era of space colonialization.

1

1.3 Thesis Outline

Chapter 2 on page 17: "A straightforward approach for 3D bacterial printing".

In chapter two we combine a standard additive manufacturing system with alginate chemistry to allow for 3D printing of bacteria in a reliable and reproducible way. This newly developed methodology uses an of the shelf 3D-printer with a regular syringe pump and allows to print bacteria in a variety of 2- and 3-dimensional structures. We combined this with synthetic biology to allow the production of specific chemicals after printing of the bacteria. The alginate gives a reversible scaffold which can be removed after the bacteria produced the wished material. Doing so this methodology can be applied to pattern surfaces with bacteria, produce certain molecules or allow a matrix for biofilm formation in a specific geometric form.

Chapter 3 on page 37: "Creation of conductive graphene materials by bacterial reduction".

Shewanella oneidensis MR-1 was used to remove oxygen from graphene oxide and restore the mechanical and electric properties. To define clear applications for microbially reduced graphene oxide (mrGO) we analysed the chemical and electrical properties of mrGO. The analysis compared the so-produced mrGO with chemically reduced graphene oxide (crGO). We showed a comparable but smaller conductive behaviour in single flakes as well as bulk of mrGO. This is mainly, due to incomplete reduction of oxygen groups on the surface of graphene oxide. Nevertheless, mrGO maintained the high surface to volume ratio better than crGO and is more sustainable in its production. We identified nanocomposites, biosensors and conductive inks as potential applications for mrGO. Further, we used a new cleanroom methodology for bacterial patterning to reduce single sides of graphene oxide, which might enable alignment for additive manufacturing approaches.

Chapter 4 on page 65: "Homogenous covalent biocompatible coating of graphene oxide for biomedical applications".

The for microbial reduction produced graphene oxide can also directly be modified for biomedical applications. In chapter 4 we present a novel way of a covalent binding with colamine (CA) and polyethylene glycol (PEG). This modification passivates the surface, which increases binding sensitivity and selectivity of target molecules. Our GO-CA-PEG construct can be used for a variety of biomedical applications (e.g. biosensors, drug delivery, tissue printing). The covalent passivation prevents unwanted interactions with other molecules, the high sensitivity decreases the needed concentration to detect potential targets and the high selectivity makes the process very specific.

Chapter 5 on page 85: "End-to-end mission design for microbial in-situ resource utilization activities as preparation for a moon village".

In chapter 5, a mission design to utilize bacteria for *in-situ* resource utilization (ISRU) on the Moon is presented. We propose a lander to hold a trial chamber for microbial and cell-culture experiments, a radionucleotide generator as power source and a rover to gather Lunar material. This architecture represents a precursor mission to understand microbial interaction and resource extraction from the Lunar regolith as well as toxicity tests for a variety of cell types. Two specific examples of extractions are namely discussed, the extraction of silicon and the extraction of iron from the Lunar regolith simulant JSC-1AF using synthetically modified bacteria.

Chapter 6 on page 117: "Mining Moon & Mars with microbes: Biological approaches to extract iron from Lunar and Martian regolith".

The feasibility of bacterial material extraction for space application on Moon and Mars was assessed in chapter 6. Bacterial kinetics and performance were modelled for a variety of proposed organisms (*Shewanella oneidensis, Acidithiobacillus ferrooxidans, Magnetospirilum magneticum* and *Escherichia*

coli) with a focus on iron extraction. *Shewanella oneidensis* was selected as the best organism to extract iron from a Martian surface through the reduction of iron(III) with an optimal mass payback time of 3.3 years. *Acidithiobacillus ferrooxidans* was selected as an optimal organism for iron extraction from the lunar surface through the oxidation of iron(II). However, *A. ferrooxidans* can only be feasibly used if the acids to keep it between a pH of 1-2 are produced *in-situ.*

Chapter 7 on page 145: "Extraction of iron from Lunar and Martian regolith simulants using a microbial approach in conjunction with 3D printing".

Chapter 7 investigates the experimental verification of *Shewanella oneidensis* induced magnetic extraction from the Martian regolith simulant JSC-Mars1. We successfully increased the amount of extracted material by up to 5.5 times after a 168h bacterial treatment and a handheld magnetic extraction methodology. Additional Lunar regolith simulants, which are having unlike real Lunar material also considerable amounts of iron(III), were successfully tested. The iron wt% in the samples increased between 17.1% (JSC-2A) and 43.6% (EAC-1) compared to untreated material. Those results make a successful application of our methodology in a real Mars colony very likely.

Chapter 8 on page 179: "Theoretical bioreactor design to perform microbial mining activities on Mars".

The implementation of the biomining reactor as a central building block is the core of chapter 8. Simulations of an upscaled 1400 litre *S. oneidensis* reactor combined with a 60 litre algae reactor for additional nutrients resolves in the production of 0.51 kg iron and 0.28 kg oxygen per day. The biomass, oxygen, carbon dioxide concentrations as well as the flow profiles and photosynthesis rates of one individual photobioreactor plate is modelled for the algae system. Regolith particle distribution, kinetics and flow velocity

is analysed for the biomining system. In the last part, planetary protection, an additional plant compartment and the impact of radiation are briefly discussed and incorporated into a full strategy for a Martian operation.

Chapter 9 on page 223: "Final remarks and future direction of this work". In the final chapter, an overview of further improvements in the reduction mechanism, the limits of the microbial reduction, experiments to further advance microbial nanomaterial treatment and the space applications as well as an outlook on biomining applications for space exploration is given.

1.4 References

[1] A.K. Geim, K.S. Novoselov, The rise of graphene, Nat Mater 6(3) (2007) 183-91.

[2] J. Peña-Bahamonde, H.N. Nguyen, S.K. Fanourakis, D.F. Rodrigues, Recent advances in graphene-based biosensor technology with applications in life sciences, Journal of Nanobiotechnology 16(1) (2018) 75.

[3] A.D. Franklin, DEVICE TECHNOLOGY. Nanomaterials in transistors: From high-performance to thin-film applications, Science 349(6249) (2015) aab2750.

[4] G. Wang, F. Qian, C.W. Saltikov, Y. Jiao, Y. Li, Microbial reduction of graphene oxide by Shewanella, Nano Research 4(6) (2011) 563-570.

[5] G. Liu, X. Zhang, J. Zhou, A. Wang, J. Wang, R. Jin, H. Lv, Quinone-mediated microbial synthesis of reduced graphene oxide with peroxidase-like activity, Bioresour Technol 149 (2013) 503-8.

[6] E.C. Salas, Z. Sun, A. Luttge, J.M. Tour, Reduction of graphene oxide via bacterial respiration, ACS Nano 4(8) (2010) 4852-6.

[7] J.H. William, S.; Offeman, R. E., Preparation of Graphitic Oxide, J. Am. Chem. Soc 80 (1958) 1339.

[8] O. Bretschger, A. Obraztsova, C.A. Sturm, I.S. Chang, Y.A. Gorby, S.B. Reed, D.E. Culley, C.L. Reardon, S. Barua, M.F. Romine, J. Zhou, A.S. Beliaev, R. Bouhenni, D. Saffarini, F. Mansfeld, B.-H. Kim, J.K. Fredrickson, K.H. Nealson, Current Production and Metal Oxide Reduction by Shewanella

oneidensis MR-1 Wild Type and Mutants, Applied and Environmental Microbiology 73(21) (2007) 7003.

[9] L.J. Rothschild, Synthetic biology meets bioprinting: enabling technologies for humans on Mars (and Earth), Biochem Soc Trans 44(4) (2016) 1158-64.

[10] C. Schwandt, J.A. Hamilton, J.D. Fray, I.A. Crawford, W. Marshall, The production of oxygen and metal from lunar regolith, Planetary and Space Science 74(1) (2012) 49-56.

[11] L. Hendrickx, H. De Wever, V. Hermans, F. Mastroleo, N. Morin, A. Wilmotte, P. Janssen, M. Mergeay, Microbial ecology of the closed artificial ecosystem MELiSSA (Micro-Ecological Life Support System Alternative): Reinventing and compartmentalizing the Earth's food and oxygen regeneration system for long-haul space exploration missions, Research in Microbiology 157(1) (2006) 77-86.

[12] J. Urbina, Biomining: A Biological Approach to Recycling Elemental Components from End-Of-Life Electronics, Microbiology and Environmental Toxicology, University of California Santa Cruz, 2018.

[13] M. Montague, G.H.t. McArthur, C.S. Cockell, J. Held, W. Marshall, L.A. Sherman, N. Wang, W.L. Nicholson, D.R. Tarjan, J. Cumbers, The role of synthetic biology for in situ resource utilization (ISRU), Astrobiology 12(12) (2012) 1135-42.

[14] S. Herrera, Industrial biotechnology—a chance at redemption, Nature Biotechnology 22 (2004) 671.

[15] B. Kartal, J.T. Keltjens, Anammox Biochemistry: a Tale of Heme c Proteins, Trends in Biochemical Sciences 41(12) (2016) 998-1011.

[16] S. Belz, M. Buchert, S. Fasoulas, Utilization of Microalgae and Regenerative Fuel Cells for Life Support and Energy Production, 43rd International Conference on Environmental Systems, American Institute of Aeronautics and Astronautics 2013.

[17] J.U. Navarrete, I.J. Cappelle, K. Schnittker, D.M. Borrok, Bioleaching of ilmenite and basalt in the presence of iron-oxidizing and iron-scavenging bacteria, International Journal of Astrobiology 12(2) (2013) 123-134.

[18] N.A. Baeshen, M.N. Baeshen, A. Sheikh, R.S. Bora, M.M.M. Ahmed, H.A.I. Ramadan, K.S. Saini, E.M. Redwan, Cell factories for insulin production, Microbial Cell Factories 13 (2014) 141.

[19] G. Horneck, R. Moeller, J. Cadet, T. Douki, R.L. Mancinelli, W.L. Nicholson, C. Panitz, E. Rabbow, P. Rettberg, A. Spry, E. Stackebrandt, P. Vaishampayan, K.J. Venkateswaran, Resistance of Bacterial Endospores to Outer Space for Planetary Protection Purposes—Experiment PROTECT of the EXPOSE-E Mission, Astrobiology 12(5) (2012) 445-456.

[20] B.M. Jakosky, C.S. Edwards, Inventory of CO2 available for terraforming Mars, Nature Astronomy 2(8) (2018) 634-639.

[21] NASA, Neptune, The Windiest Planet, (2013).

[22] S.K. Atreya, M.H. Wong, T.C. Owen, P.R. Mahaffy, H.B. Niemann, I. de Pater, P. Drossart, T. Encrenaz, A comparison of the atmospheres of Jupiter and Saturn: deep atmospheric composition, cloud structure, vertical mixing, and origin, Planetary and Space Science 47(10) (1999) 1243-1262.

[23] V.A. Krasnopolsky, V.A. Parshev, Chemical composition of the atmosphere of Venus, Nature 292 (1981) 610.

[24] L.A. Zacharoff, D.J. Morrone, D.R. Bond, Geobacter sulfurreducens Extracellular Multiheme Cytochrome PgcA Facilitates Respiration to Fe(III) Oxides But Not Electrodes, Frontiers in Microbiology 8(2481) (2017).

[25] A.L. Neal, L.K. Clough, T.D. Perkins, B.J. Little, T.S. Magnuson, In situ measurement of Fe(III) reduction activity of Geobacter pelophilus by simultaneous in situ RT-PCR and XPS analysis, FEMS Microbiology Ecology 49(1) (2004) 163-169.

[26] C.P. Goldbeck, H.M. Jensen, M.A. TerAvest, N. Beedle, Y. Appling, M. Hepler, G. Cambray, V. Mutalik, L.T. Angenent, C.M. Ajo-Franklin, Tuning Promoter Strengths for Improved Synthesis and Function of Electron Conduits in Escherichia coli, ACS Synthetic Biology 2(3) (2013) 150-159.

[27] ESA, Compartment I: The liquefying compartment, 2015.

[28] B.A.E Lehner, C.N Haenggi, J. Schleppi, S.J.J. Brouns, A. S. Meyer, A. Cowley, Bacterial modification of lunar and Martian regolith for plant growth in life support systems, 69th International Astronautical Congress, International Astronautical Federation, Bremen, 2018.

2

A straightforward approach for 3D bacterial printing

Benjamin A.E. Lehner, Dominik T. Schmieden and Anne S. Meyer*

Sustainable and personally tailored materials production is an emerging challenge to society. Living organisms can produce and pattern an extraordinarily wide range of different molecules in a sustainable way. These natural systems offer an abundant source of inspiration for the development of new environmentally-friendly materials production techniques. In this chapter, we describe the first steps towards the 3-dimensional printing of bacterial cultures for materials production and patterning. This methodology combines the capability of bacteria to form new materials with the reproducibility and tailored approach of 3D printing systems. For this purpose, a commercial 3D printer was modified for bacterial systems, and new alginate-based bio-ink chemistry was developed. Printing temperature, printhead speed, and bio-ink extrusion rate were all adapted and customized to maximize bacterial health and spatial resolution of printed structures. Our combination of 3D printing technology with biological systems enables a sustainable approach for the production of numerous new materials.

2.1 Introduction

The development of more sustainable materials production is an urgent need for our current society. Traditional materials production processes can utilize massive quantities of polluting chemicals, and too often the products are not naturally degradable [1]. One newly emerging approach to solve this problem is the production of materials by bacteria, either synthetically modified [2-4] or unmodified [5,6]. Many bacteria can carry out advanced chemical reactions to produce materials, including amyloid-based adhesives [7], bio-based electrical switches [8], microbially-produced nacre [9], and a variety of bioplastics [10], under ambient conditions without using or producing toxic compounds. However, current microbial materials production techniques do not allow the generation of bespoke material structures in a reliable or reproducible way. To allow for the production of complex patterned biomaterials, we have coupled bacterial materials production with 3D printing technology [11].

Additive manufacturing allows for the production of tailored products fulfilling individual needs and enables entrepreneurs and companies to produce small batches or only on-demand [12]. A wide variety of 3D printing approaches have been developed for additive manufacturing of non-biological materials, including stereolithography, selective laser sintering, electron beam melting (EBM), Laser Engineered Net Shaping, and PolyJet [13, 14]. The vast majority of current 3D printing techniques involve one or more steps that are deadly for cells. Therefore, new technologies have been developed for cellular printing with medical and biological applications including visualization, education, and transplantation [15-17]. To date, these techniques are quite expensive (between 5,000 and 200,000 USD [18]) and not yet well adapted for bacteria.

The area of biological printing is primarily dominated by three different technologies. Thermal inkjet bioprinting uses CT or MRI images as guides

to deploy fluid dots layer by layer, which solidify to a gel after a short heating phase in the extruder [19]. Direct write bioprinting utilizes printheads made of syringes or needles that transport liquid bioink via mechanical or pneumatic systems and uses a low-melting-point scaffold material [20, 21]. Spheroid organ printing employs tiny tissue spheroids to assist the self-organizational and self-assembling character of real tissues [22]. A few efforts have been made to apply these technologies to bacterial printing, but all current approaches suffer limitations of poor spatial resolution [23] or require laborious clean-room fabrication of microstructures that shape the printed bacteria [24]. To achieve a cost-efficient technology for bacterial printing that is compatible with incubation of printed bacteria at elevated temperatures, a new technology must be developed that allows high printing resolution without the requirement for cleanroom facilities.

Our newly developed microbial 3D printer can deposit bacteria cells in specific three-dimensional patterns for the ultimate goal of materials production. Our printing platform uses a modified commercially available 3D printer to extrude a mixture of bacteria and alginate that solidifies into a gel upon contact with a calcium chloride-treated printing surface. This combination of straightforward chemistry and easy, readily available technology enabled us to print reproducible 3-dimensional samples with high spatial resolution. The combination of our straightforward technique to print 3D microbial structures with the material-modifying properties of bacteria will result in high-resolution deposition of bacteria and the fabrication of spatially patterned materials.

2.2 Results and Discussion

2.2.1 3D printer and bio-ink

In order to create a straightforward bacterial 3D printer, multiple modifications were made to an inexpensive (300 USD) commercial 3D printer (Fig. 2.1A). The extruder of the printer was removed and replaced with a pipette tip (Fig. 2.1B, 3a) and a system of tubing (Fig 2.1B, 3c). This alteration allows the liquid biological ink ("bio-ink") to be transported under ambient temperatures that are amenable to microbes, rather than the elevated temperatures that are applied to melt plastic filament. A secondary pipette tip was affixed to the printhead (Fig. 2.1B, 3b) to allow for rapid alternation between the deposition of different types of bio-ink. A syringe pump (Fig 2.1A, 1) was added to the system to generate continuous but adjustable flows of bio-ink through the sets of tubing into the pipette tips. Printed shapes are created through the flow of bio-ink through the movable printhead while it is in motion, the trajectory of which is programmably controlled by an external computer. The shape of printed objects can be created *in silico* through computer-aided design (CAD) programs, then converted into printing instructions for the 3D printer using slicing and printer-specific software. These adaptations can be performed on all 3D printing systems that employ an accessible and removable extruder.

A custom bio-ink was developed that would allow bacteria and chemical substrates for materials production to flow through the printhead in liquid state, then rapidly solidify upon contact with the printing surface to form a stably patterned shape. The bio-ink consists of live bacteria mixed with dissolved alginate. When the bio-ink is extruded onto a surface containing calcium ions during the printing process, cross-linking of the alginate molecules is triggered, forming a stable, biocompatible aerogel scaffold within seconds [25, 26]. In order to optimize the bio-ink composition, the alginate and calcium ion concentration were systematically varied (from

0.5% w/v to 6% w/v alginate; and 0.0087 mol/cm^2 to 0.44 mol/cm^2 CaCl$_2$) and tested in the printing system. Insufficient concentrations of alginate and calcium ions resulted in poor gelation and low printing resolution, while excessive concentrations led to premature gelation of the bio-ink, blocking the pipette tip and preventing further printing. The optimal conditions were found to be 1 M CaCl$_2$ and 2.5% w/v alginate. With our printer system, each printed layer can only contain materials that are present in the active syringe; the mixture of materials from two different syringes within one layer is not possible due to the rate of scaffold formation. However, a wide range of different types of materials is compatible with alginate polymerization and may be admixed in the active syringe for inclusion in individual printed layers [21, 27].
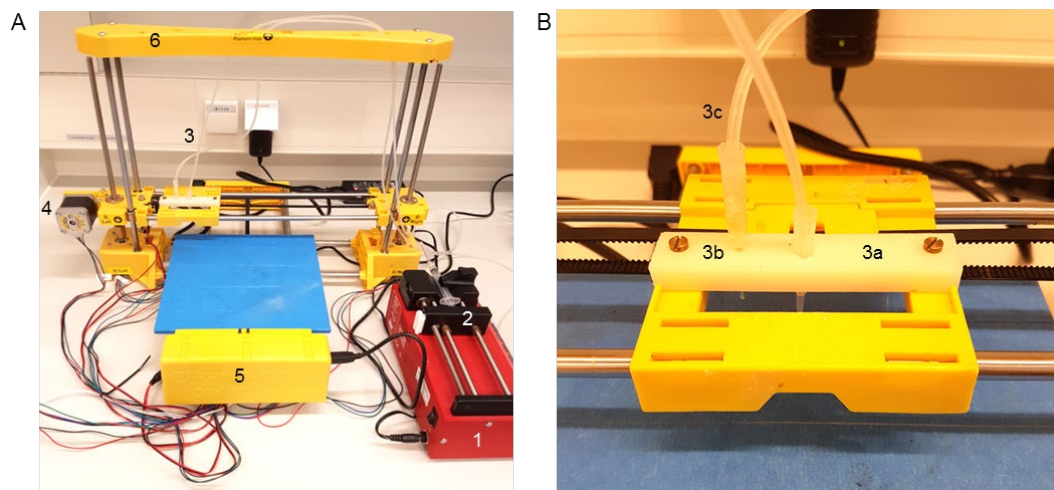
Fig. 2.1 Bacterial 3D printing system. (A) Overview of all bioprinter components. 1: syringe pump, 2: syringe filled with bio-ink, 3: extruder holder, 4: one of three step-motors for positioning, 5: breadboard and hardware of the printer, 6: frame of the printer. (B) Detailed view of the modified extruder. 3a: active pipette tip, 3b: secondary pipette tip for layering materials, 3c: tubing system.

2.2.2 Printing reproducibility and resolution

The reproducibility and consistency of the printing process was assessed by analysing patterned monolayers that were printed using the optimized bio-

ink. An elliptical form with two long straight lines on each side was chosen as the printing object in order to test the performance of the printer in fabricating both curved and straight-edged structures (Fig. 2.2A). Following printing, the width of each printed structure was measured at six different positions, sampling a variety of straight and curved portions. No statistically significant differences were seen among any of the widths measured at the same position in different prints (One-way ANOVA with Tukey PostHoc, p-value: 0.964, CV%: 11.16) (Fig. 2.2B). These data indicate that our printer and bio-ink can fabricate printed structures of varying shapes in a consistently uniform manner.
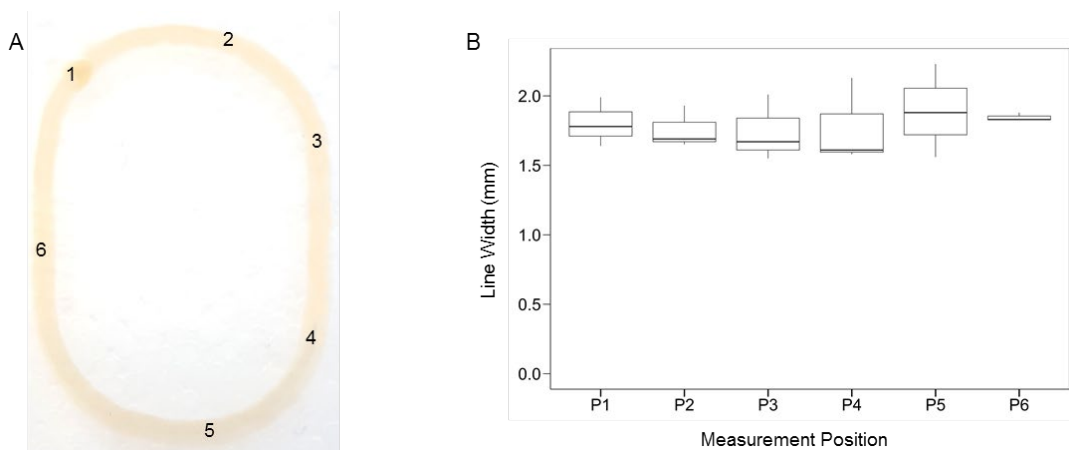
Fig. 2.2 Reproducible printing of alginate structures. (A) A representative printed elliptical structure. The numbers indicate the locations of the 6 measurement positions. (B) The distribution of measured line widths at 6 different positions within elliptical printed structures (n = 3). The tops and bottoms of the boxes represent the 75th and the 25th percentiles, respectively; the lines within the boxes are the median values; and the tops and bottoms of the vertical lines are the maximum and minimum values. No significant differences exist between the width distributions of any of the different positions (One-way ANOVA, Tukey PostHoc test, p-value: 0.964).

In order to maximize the printer resolution, a range of printing parameters was tested. The two most critical factors affecting the printed line width

2

were found to be the extrusion rate of the syringe pump and the movement speed of the printhead, in agreement with previous work [28]. A range of printhead movement speeds (100-500 mm/min) and syringe pump extrusion rates (17-50 µL/min) were applied to print straight lines of bio-ink. In general, increased printing resolution could only be achieved by adjusting both parameters in parallel: e.g. slower printhead movement speeds required slower syringe pump rates. Other less-critical factors contributing to printer resolution were the distance between the printhead and the printing surface, as well as the uniformity of the printing surface. The narrowest line width obtainable was 1.00 ± 0.15 mm, achieved with a printhead movement speed of 200 mm/min and a syringe pump extrusion rate of 33 µL/min (Fig. 2.3A).

The printer can be directed to deposit bio-ink directly on top of previously printed material to create multi-layered structures. A second aerogel layer can be printed on top of a base layer at a range of different syringe pump extrusion rates, with no modification of the printing commands (Fig. 2.3A). Fabrication of structures taller than two layers in height requires an increase of the z-position of the printhead by 0.15 mm/layer. Stacked layers of bio-ink are able to solidify due to interaction with calcium ions that have diffused from the printing surface up through the first printed layer(s). Each additional printed layer resulted in a fractional increase in the width of the final structure, due to the time required for the new layer to gelate (Fig. 2.2A, B). No significant change in the final width was observed when the time between printing of successive layers was varied between 40 and 240 seconds (Student's T-test, p-value: 0.963, CV_{40s}: 18.36, CV_{240s}: 20.82), indicating that multi-layered structures can be printed at different paces with no loss of resolution. The total time required to print a 14-layered ellipse with a pause of 40 seconds between printing successive layers was 15 minutes.

To characterize the spatial resolution of 3-dimensional printed structures, 14-layered elliptical structures were printed. The structures' widths were measured following deposition of each layer. The heights of the structures were measured for only a subset of layers, since each height measurement required removal of the gel from the printing surface, halting the printing process. The average line width increased significantly but incrementally for the first six layers, with an average increase of 0.14 ± 0.01 mm per layer between layers 1 and 6 (Fig. 2.3B). Following the sixth layer, the line widths approached a plateau; no significant differences were observed between the line widths of any of the layers between layers 6 and 14 (One-way ANOVA with Tukey Posthoc test, p-value: 0.995). The height of the printed material was observed to increase continually, by an average of 0.16 ± 0.02 mm per layer. The final 14-layered structures were 2.14 ± 0.11 mm in height, with a width of 2.32 ± 0.37 mm. These measurements indicate that our printing system is capable of fabricating 3-dimensional structures at sub-millimeter-scale precision in all dimensions. Further improvements in resolution may be possible by rebuilding our system using a commercial 3D printer employing more accurate printhead positioning [15].
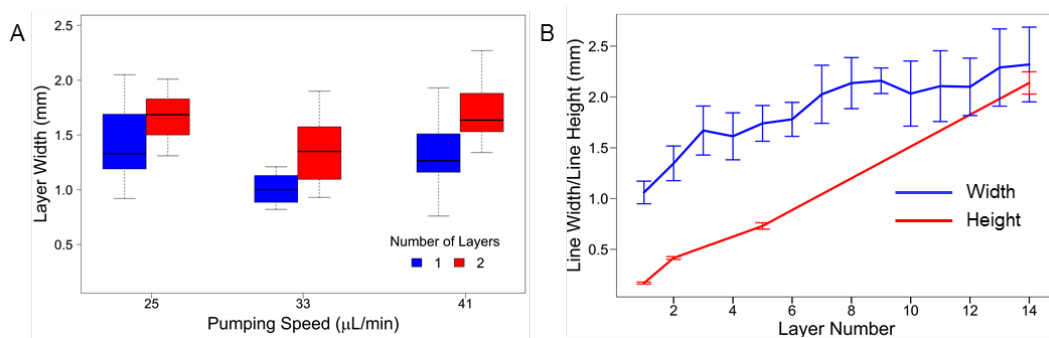

Fig. 2.3 Printing at millimeter-scale resolution in three dimensions. (A) The distribution of widths of single- and double-layered structures printed at different syringe pump speeds (n=4). The printhead movement speed was 200 mm/min in all cases. The tops and bottoms of the boxes represent the 75th and the 25th percentiles, respectively; the lines within the boxes are the median values; and

the tops and bottoms of the vertical lines are the maximum and minimum values. (B) The line width (blue) and line height (red) of printed structures containing up to 14 layers (n=3). Error bars indicate the standard error.

Since some applications may require the printing of multi-layered structures containing spatially separated bacterial strains, the internal structure of multi-layered printed bacteria was analyzed. Bi-layered structures were printed containing engineered *Escherichia coli*, in which the bacteria in bottom layer of bio-ink expressed the yellow fluorescent protein mVenus, and the bacteria in the top layer expressed the blue fluorescent protein mCerulean. Each layer was printed using separate tubing and pipette tips to prevent contamination of the top layer by bacteria printed in the previous layer. After 24 hours of incubation, the structure was imaged at different depths using confocal microscopy, and the extent of bacterial mixing between the layers was quantified through image analysis. The bottom layer was 81% ± 5% homogeneous, while the top layer was 93% ± 5% homogeneous (Fig. 2.4).

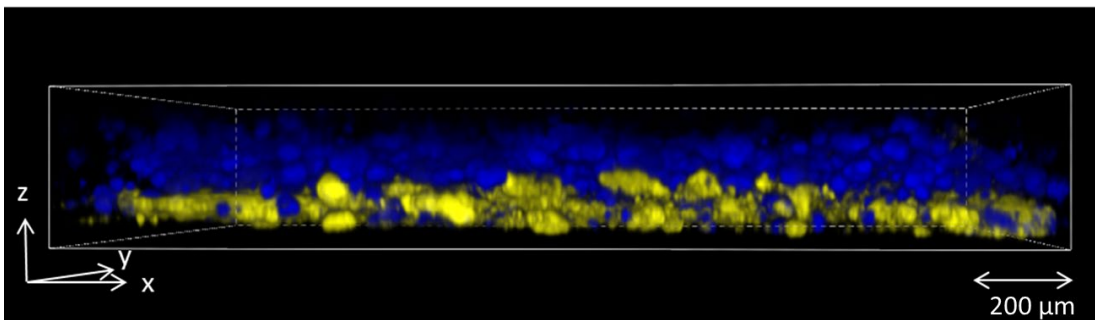Fig. 2.4 Internal structure of printed layers. Modified strains of *E. coli* expressing two different fluorescent proteins were printed one on top of the other in a 2-layered square. After 24 hours of incubation, the internal structure of the printed bacterial layers was inspected by confocal microscopy. The bottom layer contained 81% ± 5% blue fluorescent cells, while the top layer contained 93% ± 5% yellow cells.

This analysis indicates good separation of bacteria between adjacent printed layers, even after extensive periods of incubation. The lower layer may have been less pure due to incomplete solidification before printing of the top layer, which could be improved via an increased waiting time between printing of layers.

2.2.3 Survival and metabolic activity of printed bacteria

In order for our alignate-based printing system to be successfully applied to microbial materials production, bacteria must be able to survive well within the alginate gel. To test this property, *E. coli* was incorporated into alginate aerogels, and gels were incubated for varying amounts of time from 0 to 48 hours at 37°C. The gels were then added to a solution of sodium citrate to chelate the calcium ions and dissolve the gel. The samples were grown on Luria-Bertani (LB)-agar plates to determine the number of viable cells (colony forming units). An increase in colony forming units observed between the first two data points may indicate that bacterial growth occurs within the alginate gel during the first 24 hours after gel production (Fig. 2.5A). Thereafter, colony forming units remained fairly constant for up to 48 hours. Comparison with bacteria that were incubated in non-printed, liquid bio-ink indicated that the printing process initially reduces the viability of *E. coli* by approximately 50% (Fig. 2.5B). Thereafter, the levels of viable bacteria in the non-printed bio-ink remained nearly constant, likely due to nutrient limitation. The dramatic increase in the number of viable bacteria in the printed gel resulted in an overall increase in viability of approximately 200% in comparison to the non-printed bio-ink, which may be due to the additional nutrients in the agar printing substrate and the lower bacterial density after printing. Bacteria can thus remain viable within the alginate gel of our bio-ink for at least two days following gel formation, providing sufficient time for microbial-mediated materials production or patterning to occur.
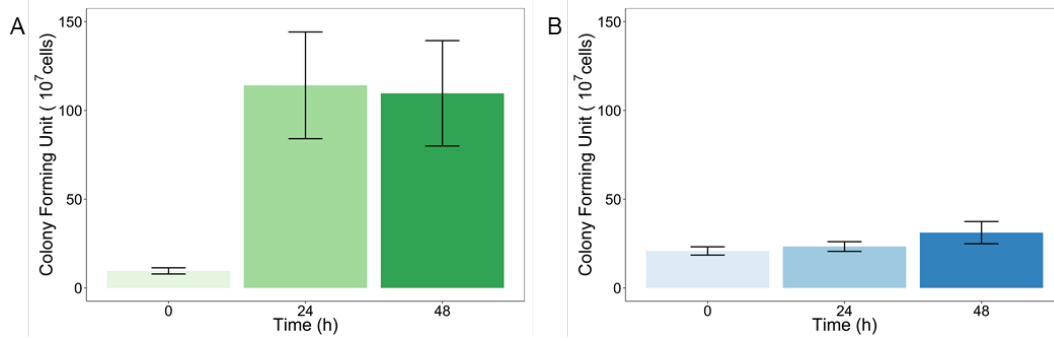
Fig. 2.5 Robust bacterial survival within printed alginate gels and planktonic bio-ink. The number of colony forming units is shown for *E. coli* printed within alginate gels (A) or as a planktonic sample (B), incubated for varying amounts of time (n=6). Error bars indicate the standard error.

Both survival and metabolic activity of the printed bacteria are key factors to demonstrate the applicability of our printing system. To assess the ability of our printed bacteria to create a product, *E. coli* containing the rhamnose-inducible red fluorescent protein RFP were printed onto an agar plate containing the rhamnose inducer. The gel was incubated, and the color of the gel was monitored over 48 hours. After 8 hours of incubation, the induced bio-ink showed a noticeable red colour, which became very intense after 48 hours (Fig. 2.6). This experiment demonstrates that our printed bio-ink is able to support the production of bacterially-made materials over short periods of time. Our printing system could be readily applied to the patterned production of bacterially-created materials in a variety of different formats. Bio-ink containing both active bacteria and material precursors could be printed onto a neutral surface, to create a three-dimensionally patterned aerogel within which the bacteria chemically convert the precursors to the desired final product. The thorough comingling of bacteria and chemical substrates within the gel in this configuration would lead to high efficiency of material production. Alternately, alginate gel containing only the chemical precursor could be printed and then immersed within a liquid bacterial culture to create a final 3D-patterned material that is largely bacteria-free. In a third scenario,

bacteria-containing bio-ink could be printed onto a surface that is coated with material precursors, which the bacteria could then convert into a two-dimensionally patterned final product. This approach has the appealing feature that the alginate gel could be dissolved away after the fact, leaving behind only the final material.
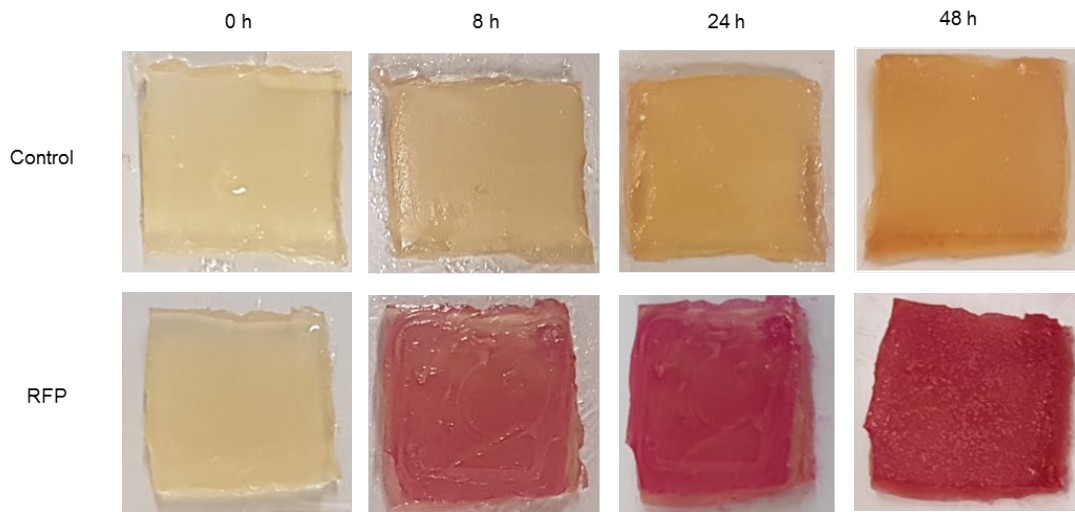
Fig. 2.6 Metabolic activity within printed alginate gels. *E. coli* with and without a rhamnose-inducible RFP plasmid were printed onto a substrate containing rhamnose. Printed gels were incubated at 37°C, and color changes were observed over time.

2.3 Conclusion

The work shown here demonstrates the development of macroscopic material printing with millimeter-scale resolution using removable aerogels and bacterial chemistry. This approach enables us also to print precursor or supportive material directly with the bacteria. The printing technique is inexpensive, straight-forward, and can produce bacterial structures of a wide variety of three-dimensional shapes without requiring printing scaffolds, excepting structures that contain internal bridges or enclosed hollow spaces. The technology is well-suited for the use of wild-type organisms or synthetically modified bacteria, which could be designed to

carry out new combinations of microbial reactions to create a great number of different types of materials. Connecting our novel and straightforward bacteria printing techniques with approaches of synthetic biology will further improve its value as a "green" material production process and patterning methodology. The ease and simplicity of our printing approach will allow any interested research group to adapt and improve this process at low cost for multiple possible applications.

2.4 Materials and Methods

2.4.1 Printing system

The extruder and heater of a standard 3D printer (CoLiDo DIY) were removed and replaced by a pipette tip, a tubing system, and a syringe pump (Fig. 2.1). Silicon tubing (VWR DENE 3100103/25) with an inner diameter of 1 mm and an outer diameter of 3 mm was used to connect a 200 µL pipette tip to a 10 mL syringe. The syringe was loaded with 10 mL of printer bio-ink and mounted in a syringe pump (ProSense B.V. NE-300). A secondary 200 µL pipette tip was affixed to the printhead (Fig. 2.1A, 3b) and connected to silicon tubing to allow for rapid exchange of the pipette tip to deposit a second type of material. Printed objects were drawn in the free online CAD program Tinkercad, sliced via the RepRap Slic3r software, and manually adapted and implemented for printing using CoLiDo software.

2.4.2 Bacterial strains, plasmids, and culturing

Escherichia coli K12 MG1655 was transformed with an SB101 plasmid containing RFP under the control of a rhamnose-inducible promoter. *Escherichia coli* Top10 cells were transformed with plasmids AM420 or AM421. Cells were cultured overnight in LB media supplemented with the appropriate antibiotic (25 µg/mL ampicillin or kanamycin) at 37°C with continuous shaking at 250 rpm.

Plasmid AM420 is a p15A-derived plasmid carrying an ampicillin resistance gene, a constitutively expressed *lacI* gene, and the gene for the blue fluorescent protein mCerulean (gene sequence originally from pZS2-123 [29], Addgene plasmid # 26598) behind an IPTG-inducible promoter. Plasmid AM421 is a pSC101-derived plasmid carrying a kanamycin resistance gene, a constitutively expressed *tetR* gene, and the gene for the yellow fluorescent protein mVenus (gene sequence originally from mVenus N1 [30], Addgene plasmid # 27793) behind an anhydrotetracycline-inducible promoter.

2.4.3 Printer bio-ink & substrate

To obtain 10 mL of bio-ink containing *E. coli*, 10 mL of overnight bacterial culture (O.D.$_{600}$ of approximately 2.5) was spun down at 4000 rpm for 3 minutes and the supernatant discarded. The cells were resuspended in 5 mL of sterile LB medium (Sigma Aldrich). A 5 mL mixture of sodium alginate (5% w/v, Sigma Aldrich) was added to the solution, followed by vortexing.

A Petri dish (150 mm x 15 mm) was filled with 20 mL of agar (1.5% w/v) dissolved in LB medium. The printing surface was prepared by the equally distributed application of 500 μL 1 M $CaCl_2$ onto the agar surface.

2.4.4 Resolution and height measurements

Printing resolution was determined by measuring the width and height of printed samples with a digital caliper (GEDORE No. 711) three times per position for each layer. Prior to the start of printing, the petri dish lid containing the agar printing surface was affixed to the printer platform using double-faced adhesive tape to prevent changes in the position of the substrate during measurements. Width measurements were recorded for successive layers printed onto the same base layer. Measurement positions within printed ellipses were selected prior to printing: two random points within curved end regions, two random points in straight-edged side

2

regions, and two random points in the transitional area between curved and straight regions. To determine the height of printed samples, the printed structure was removed from the agar printing surface, therefore additional printed layers could not be added post measurement.

2.4.5 Printing and imaging of layered alginate gels containing fluorescent bacteria

Printing substrate including inducers (1 mM IPTG to induce mCerulean expression, 50 ng/mL anhydrotetracycline to induce mVenus expression) was prepared in a Petri dish. A sheet of dialysis membrane (Spectra/Por 2 Dialysis Tubing, 12-14 kD MWCO, Spectrum Europe B.V., The Netherlands) was placed on the agar prior to printing, to ensure diffusion of nutrients and inducers from the agar substrate to the printed gel while facilitating eventual transfer of the gel onto a microscope slide. A single rectangular layer of bio-ink was printed containing *E. coli* with AM421, then a second rectangular layer of bio-ink containing *E. coli* with AM420 was printed on top of the first layer, using separate tubing and pipette tips to avoid bacterial cross-contamination.

After 24 hours of incubation at 37°C, the printed gels and underlying dialysis membranes were sliced with a scalpel. Samples were transferred onto a microscope slide and imaged with a Nikon A1+ fluorescence confocal microscope (magnification 200x, excitation wavelengths 457 or 514 nm, detected wavelengths 465-500 or 525-555 nm for mCerulean or mVenus, respectively).

2.4.6 Bacterial survival

To determine bacterial survival, 5 mL of an overnight culture of *E. coli* K12 MG1655 (O.D.$_{600}$ of approximately 2.5) was spun down at 4000 rpm for 3 minutes and the supernatant discarded. The bacterial pellet was resuspended in 5 mL of fresh LB medium containing 2% w/v sodium alginate by vortexing until all ingredients were entirely dissolved. A portion

of the bio-ink was used to print a 6-layered rectangular quadrangle. The gel was allowed to solidify for 30 minutes before the first sample was taken. The remainder of the bio-ink was incubated in unsolidified liquid form at 37°C as a positive control showing planktonic growth. After 0 h, 24 h, or 48 h of incubation at 37°C, 0.3 g of the gel was removed and dissolved in 1.75 mL of 1 M sodium citrate solution. For planktonic samples, 200 µL samples were removed, containing approximately the same volume of bio-ink as that sampled from the printed gel. Colony forming units (CFU) were determined following the protocol of Karas et al. [31]. In short, each sample was serially diluted three times (in ten-fold increments from 10^{-1} to 10^{-8}), and 5 µL of each dilution was pipetted in triplicate onto a LB-agar plate. The plates were incubated at 37°C for 24 hours, and visible colonies were counted.

2.4.7 Production of RFP by printed bacteria

Two 6-layered, square-shaped gels were printed on an LB-agar plate containing 0.2% rhamnose. One gel contained *E. coli* with a rhamnose-inducible RFP-producing plasmid, and the other one contained wild-type *E. coli* K12 MG1655. The agar around the printed gel was removed to increase its visibility. The printed gels were photographed under constant light conditions over a 48-hour period.

2.4.8 Statistical methods

R-Studio was used to perform the statistical analyses. All datasets were assumed to be normally distributed and were checked for outliers with a Dixon's Q-Test. Unless noted, no outliers were removed from the datasets. One-way ANOVA was used to compare multiple data sets, and two-sample Student's t-test was used for comparing two data sets. In cases where the ANOVA test showed a significant difference, a Tukey's post-hoc test was used to obtain an overview of all significant differences occuring within the dataset.

2.5 References

[1] T. Hiraishi, Poly(aspartic acid) (PAA) hydrolases and PAA biodegradation: current knowledge and impact on applications, Appl Microbiol Biotechnol 100(4) (2016) 1623-30.

[2] B.C. Stanton, A.A. Nielsen, A. Tamsir, K. Clancy, T. Peterson, C.A. Voigt, Genomic mining of prokaryotic repressors for orthogonal logic gates, Nat Chem Biol 10(2) (2014) 99-105.

[3] J. Bonnet, P. Yin, M.E. Ortiz, P. Subsoontorn, D. Endy, Amplifying genetic logic gates, Science 340(6132) (2013) 599-603.

[4] A. Prindle, J. Selimkhanov, H. Li, I. Razinkov, L.S. Tsimring, J. Hasty, Rapid and tunable post-translational coupling of genetic circuits, Nature 508(7496) (2014) 387-91.

[5] R.A. Verlinden, D.J. Hill, M.A. Kenward, C.D. Williams, I. Radecka, Bacterial synthesis of biodegradable polyhydroxyalkanoates, J Appl Microbiol 102(6) (2007) 1437-49.

[6] I. Sulaeva, U. Henniges, T. Rosenau, A. Potthast, Bacterial cellulose as a material for wound treatment: Properties and modifications. A review, Biotechnol Adv 33(8) (2015) 1547-71.

[7] C. Zhong, T. Gurry, A.A. Cheng, J. Downey, Z. Deng, C.M. Stultz, T.K. Lu, Strong underwater adhesives made by self-assembling multi-protein nanofibres, Nat Nanotechnol 9(10) (2014) 858-66.

[8] A.Y. Chen, Z. Deng, A.N. Billings, U.O. Seker, M.Y. Lu, R.J. Citorik, B. Zakeri, T.K. Lu, Synthesis and patterning of tunable multiscale materials with engineered cells, Nat Mater 13(5) (2014) 515-23.

[9] D.T. Schmieden, Meyer, A.S., Aubin-Tam, M.-E., Using bacteria to make improved, nacre-inspired materials., MRS Advances 1(8) (2016) 559-564.

[10] P. Hofer, P. Vermette, D. Groleau, Introducing a new bioengineered bug: Methylobacterium extorquens tuned as a microbial bioplastic factory, Bioeng Bugs 2(2) (2011) 71-9.

[11] G. Wang, Yao, L., Wang, W., Ou, J., Cheng, C.-Y. and Ishii, H., xPrint: A Modularized Liquid Printer for Smart Materials Deposition, ACM (Proceedings of the 2016 CHI Conference on Human Factors in Computing Systems) (2016) 5743-5752.

[12] E. Matias, B. Rao, 3D Printing: On Its Historical Evolution and the Implications for Buisness, Proceedings of PICMET'15 (Management of the Technology Age) (2015).

[13] K. Wong, V.;, A. Hernandez, A Review of Additive Manufactoring, Hindawi 2012 (2012).

[14] K. Cooper, G., Rapid Prototyping Technology, Marcel Dekker Inc2005.

[15] S.V. Murphy, A. Atala, 3D bioprinting of tissues and organs, Nat Biotechnol 32(8) (2014) 773-85.

[16] F. Pati, D.H. Ha, J. Jang, H.H. Han, J.W. Rhie, D.W. Cho, Biomimetic 3D tissue printing for soft tissue regeneration, Biomaterials 62 (2015) 164-75.

[17] F. Pati, J. Jang, D.H. Ha, S. Won Kim, J.W. Rhie, J.H. Shim, D.H. Kim, D.W. Cho, Printing three-dimensional tissue analogues with decellularized extracellular matrix bioink, Nat Commun 5 (2014) 3935.

[18] D. Sher, The Top 15 Bioprinters, 2015. (Accessed 30.01 2017).

[19] X. Cui, T. Boland, D.D. D'Lima, M.K. Lotz, Thermal inkjet printing in tissue engineering and regenerative medicine, Recent Pat Drug Deliv Formul 6(2) (2012) 149-55.

[20] C.M. Smith, A.L. Stone, R.L. Parkhill, R.L. Stewart, M.W. Simpkins, A.M. Kachurin, W.L. Warren, S.K. Williams, Three-dimensional bioassembly tool for generating viable tissue-engineered constructs, Tissue Eng 10(9-10) (2004) 1566-76.

[21] J.P. Armstrong, M. Burke, B.M. Carter, S.A. Davis, A.W. Perriman, 3D Bioprinting Using a Templated Porous Bioink, Adv Healthc Mater 5(14) (2016) 1724-30.

[22] V. Mironov, R.P. Visconti, V. Kasyanov, G. Forgacs, C.J. Drake, R.R. Markwald, Organ printing: tissue spheroids as building blocks, Biomaterials 30(12) (2009) 2164-74.

[23] G.K. Dosier, Methods for Making Construction Material Using Enzyme Producing Bacteria, Google Patents, 2011.

[24] J.L. Connell, E.T. Ritschdorff, M. Whiteley, J.B. Shear, 3D printing of microscopic bacterial communities, Proc Natl Acad Sci U S A 110(46) (2013) 18380-5.

2

[25] C.K. Kuo, P.X. Ma, Ionically crosslinked alginate hydrogels as scaffolds for tissue engineering: part 1. Structure, gelation rate and mechanical properties, Biomaterials 22(6) (2001) 511-21.

[26] K.F. Almqvist, L. Wang, J. Wang, D. Baeten, M. Cornelissen, R. Verdonk, E.M. Veys, G. Verbruggen, Culture of chondrocytes in alginate surrounded by fibrin gel: characteristics of the cells over a period of eight weeks, Ann Rheum Dis 60(8) (2001) 781-90.

[27] S. Kim, Y. Yoo, H. Kim, E. Lee, J.Y. Lee, Reduction of graphene oxide/alginate composite hydrogels for enhanced adsorption of hydrophobic compounds, Nanotechnology 26(40) (2015) 405602.

[28] D.D. Hernandez, Factors Affecting Dimensional Precision of Consumer 3D Printing, International Journal of Aviation, Aeronautics, and Aerospace 2(4) (2015).

[29] D.M. Cox RS, Elowitz MB. J A synthetic three-color scaffold for monitoring genetic regulation and noise. , Biol Eng. 4 (2010).

[30] C.H. Koushik SV, Thaler C, Puhl HL, Vogel SS, Cerulean, Venus, and VenusY67C FRET reference standards., SS. Biophys J. 91(12) (2006) L99-L101.

[31] V.O. Karas, I. Westerlaken, A.S. Meyer, The DNA-Binding Protein from Starved Cells (Dps) Utilizes Dual Functions To Defend Cells against Multiple Stresses, J Bacteriol 197(19) (2015) 3206-15.

3

Creation of conductive graphene materials by bacterial reduction

Benjamin A.E. Lehner, Vera A.E.C. Janssen, Ewa M. Spiesz, Dominik Benz,

Stan J.J. Brouns, Anne S. Meyer*, and Herre S.J. van der Zant*

This chapter describes a microbial reduction approach for producing graphene that utilizes the bacterium *Shewanella oneidensis* in combination with modern nanotechnology to enable a low-cost, large-scale production method. The bacterial reduction approach presented in this paper increases the conductance of single graphene oxide flakes as well as bulk graphene oxide sheets by 2.1 to 2.7 orders of magnitude respectively while simultaneously retaining a high surface-area-to-thickness ratio. *Shewanella*-mediated reduction was employed in conjunction with electron-beam lithography to reduce one surface of individual graphene oxide flakes. This methodology yielded conducting flakes with differing functionalization on the top and bottom faces. Therefore, microbial reduction of graphene oxide enables the development and up-scaling of new types of graphene-based materials and devices with a variety of applications including nano-composites, conductive inks, and biosensors, while avoiding usage of hazardous, environmentally-unfriendly chemicals.

3.1 Introduction

Pristine graphene was the first two-dimensional material to be identified [1]. The one-atom thickness of single-layer graphene gives it the highest possible surface-to-volume ratio and 97% optical transparency [2]. Its electrical conductivity of up to 108 S/m and thermal conductivity of 4800 to 5300 W/mK are superior to those of the most conductive elements (i.e., silver, gold and copper) [3, 4]. Additionally, the Young's modulus of 1 TPa and intrinsic strength of 130 GPa identify graphene as the strongest measured material to date [5]. These exceptional properties have led to various applications for graphene in bioanalytics, drug carriers, composite materials, improved transistors, batteries, hydrogen storage, and photocatalysis, among others [6-14]. However, the primary hurdle to the widespread usage of graphene-based materials is the lack of reliable, clean, cost-efficient, and scalable graphene production.

The two predominant production methods for graphene are chemical vapor deposition (CVD) and exfoliation of graphite. CVD set-ups utilize a substrate material (e.g. copper) onto which methane is deposited, forming single-layer graphene. Their major drawbacks are the limited surface area of the substrate, the need for a specialized atmosphere for graphene growth, and difficulties in removing the grown graphene from the substrate [15]. While the quality of CVD-produced graphene is typically high, industrial up-scaling is challenging and expensive [16, 17]. Methodologies for exfoliation of graphite are diverse, but one promising technique for scalable production is the oxidation and exfoliation of graphite to graphene oxide (GO), followed by its subsequent reduction to graphene (Fig. 3.1) [14, 18-20]. The production of graphite oxide and its exfoliation to GO can be performed using synthetic chemistry and have been demonstrated to be scalable as well as cost-efficient [18, 19, 21]. In contrast, the reduction of GO to graphene often involves the usage of harsh chemistry (e.g. hydrazine), which can add undesired nitrogen groups onto the surface, has

very high energy demands, and can cause п−п stacking of the freshly-produced layers of reduced graphene oxide, removing the advantageous properties that result from the two-dimensionality of graphene [14, 22, 23].

One intriguing possibility to reduce graphene oxide in a more sustainable, easily up-scalable, and cost-efficient way is via the metal-oxide-reducing bacterium *Shewanella oneidensis* [24-26]. *S. oneidensis* has evolved to use inorganic materials as an electron acceptor during anaerobic respiration [27]. *S. oneidensis* can deliver electrons to inorganic acceptor materials both by electron shuttles and via direct surface-to-surface contact mediated by its Mtr respiratory pathway, which consists of multiple different proteins which pass electrons from the bacterial cytoplasm, through the cell membranes, and up to the surface of the bacterium [25,26]. When graphene oxide is provided, the electrons from *S. oneidensis* react with the oxygen groups of the graphene oxide, leading to a restoration of the sp^2 orbitals forming the characteristic hexagonal lattice of graphene. Graphene oxide contains epoxyl, carboxyl, and hydroxyl groups both on the upper and lower surfaces of the flakes [14]. These groups have different binding energies, and it is not yet known which of those groups can be reduced by *Shewanella oneidensis*.

The bacterial mechanism of GO reduction avoids harsh chemicals and could potentially be upscaled using bioreactors [24-26]. However, the conductivity of single flakes, the average thickness after reduction, and the structural quality of microbially-reduced graphene oxide (mrGO) have not yet been determined, making it impossible to identify the feasibility of the microbial production approach and the range of potential applications for reduced graphene oxide produced through this method. A high conductance and surface-to-volume ratio would make mrGO applicable to field effect transistors (FET), biosensors, transparent conductors, batteries, graphene polymer nanocomposites, and conductive inks [28-33].

Thorough characterization of the conductive properties of mrGO requires a combination of single-flake measurements, to identify the intrinsic resistance within flakes, and bulk measurements, to evaluate the effectiveness of inter-flake charge movement. In this chapter, we combined for the first time conductance measurements of microbially-reduced flakes with determination of their surface-area-to-thickness ratio and compared them to GO and chemically-reduced graphene oxide (crGO). Our analyses indicate that microbial reduction of a GO suspension produces a 2.5 orders-of-magnitude increase in conductance, with no significant change in the flake thickness. X-ray photoelectron spectroscopy (XPS) analysis of the microbially-reduced graphene oxide revealed that C-O(H) hydroxyl bonds were strongly influenced by the bacterial reduction, while C=O groups were not affected, in dramatic contrast to the chemically-reduced GO. The flake thickness of mrGO was shown to be significantly lower than in crGO and remained constant over a two-week storage period, which is essential for bio-ink and biosensor applications. By combining the reduction capabilities of *Shewanella oneidensis* with electron-beam lithography a completely new methodology was developed to functionalize the surfaces of single graphene oxide flakes on only one side, which could improve the selectivity of biosensors or tune the structural properties of nanocomposites.

3.2 Results & discussion

3.2.1 Microbial reduction of graphene oxide

In order to produce microbially-reduced graphene oxide, graphite was first oxidized and exfoliated to graphite oxide via an optimized Hummers and Offeman method (Fig. 3.1) [19, 21]. Graphite oxide production was monitored via a color change from black to yellow (Fig 3.2A). The multi-layered graphite oxide stacks were sonicated and filtered to obtain one-layer to few-layer flakes of graphene oxide (Fig. 3.1). The resultant flakes

were then incubated with *S. oneidensis* in rich growth medium under either aerobic or anaerobic conditions (Fig. 3.2B), and reduction to mrGO was observed via the reverse color change from yellow to black (Fig. 3.2A) and continuous optical density measurement (O.D.$_{600}$) using a UV-VIS Spectrometer at 600 nm (Fig. 3.2C). To compare the degree of reduction, the average absorbance due to the growth of bacteria under the same conditions (n=9) and the baseline absorbance of graphene oxide were subtracted (Fig. 3.2D). Both the aerobic and anaerobic conditions for microbial reduction yielded a robust increase in the amount of rGO, which plateaued after 30 hours. The aerobic reduction initially displayed a lag phase, potentially because of the usage of oxygen as additional electron acceptor. There was no significant difference between the amount of rGO production under aerobic vs. anaerobic conditions after 48 hours (Students T-test two-tailed, two samples with equal variance, p=0.52, n=6).
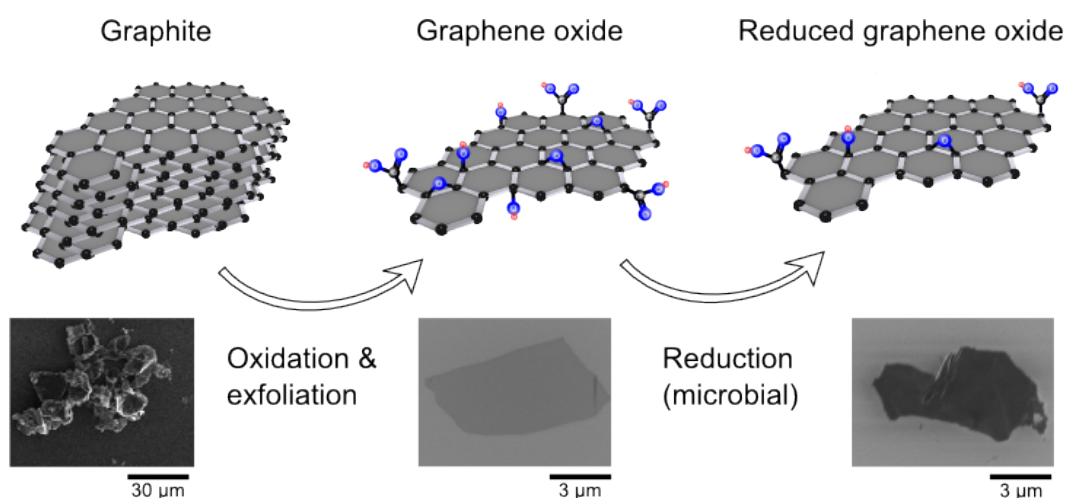
Fig. 3.1 Schematic overview of the generation of reduced graphene oxide by oxidizing and exfoliating graphite to form graphene oxide (GO), which is then reduced to produce reduced graphene oxide (rGO). Grey hexagons represent the carbon back-bone, the blue dots represent oxygen, and the red dots represent hydrogen. Scanning Electron Microscopy (SEM) images obtained of flakes extracted from the bulk solution are included to illustrate each step.

3
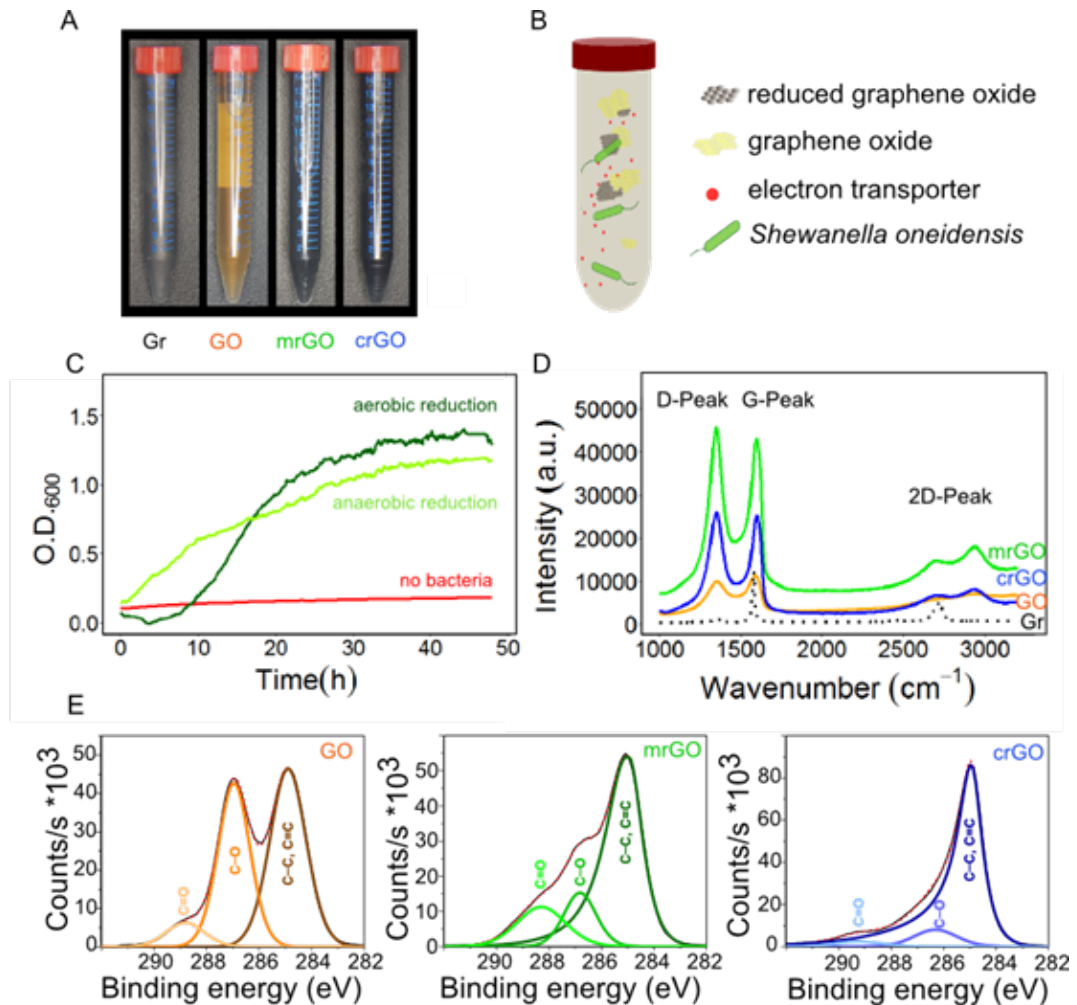
Fig. 3.2 Chemical analyses of microbially- and chemically-reduced graphene oxide. (A) Change of optical properties during generation of reduced graphene oxide. Samples are, from left to right, graphite (Gr), graphene oxide (GO), microbially-reduced graphene oxide (mrGO), and chemically-reduced graphene oxide (crGO). (B) Schematic of microbial GO reduction. *Shewanella* reduced GO flakes at room temperature in liquid medium via direct contact as well as through secreted electron transporter molecules. (C) Production of rGO over time for aerobic (dark green) and anaerobic (light green) microbial reduction in TSB growth medium, measured via optical density at 600 nm. The O.D.$_{600}$ values of a sample containing only *Shewanella* bacteria in TSB and the baseline O.D.$_{600}$ value of a sample containing only GO have been subtracted from each data set. A no-bacteria control, composed of only GO in TSB is shown in red. (D) Raman spectra of graphite (black), GO (orange), mrGO (green), and crGO (blue). (E) X-Ray Photoelectron Spectroscopy (XPS) of GO (left), mrGO (middle), and crGO (right).

3

Additional tests utilizing a minimal growth medium and added carbon sources (e.g. lactate) were conducted but did not result in a more efficient reduction of GO. For all further experiments, we performed microbial reduction using a rich growth medium in an aerobic environment (schematically shown in Fig. 3.2B), due to the ease and inexpensiveness of the procedure. To determine the quality of the reduced GO samples, the chemical properties of the graphene derivatives were analyzed following the reduction of graphene oxide utilizing *S. oneidensis* (for mrGO) or hydrazine (for crGO). The reduction efficiency (carbon/oxygen ratio) and the amount of defects were determined, since these properties contribute substantially to the emergent electrical and physical properties of graphene materials [22]. We used Raman spectroscopy to evaluate the status of the sp^2 and sp^3 orbitals in the GO, mrGO, and crGO samples. The amounts of defects in graphene can be estimated via the ratio of the intensities of the D peak and the G peak in the Raman spectrum, (I(D)/I(G)), as well as the width of these peaks [34]. The G peak results from in-plane vibrations primarily from sp^2 hybridization characteristic of highly-ordered materials such as graphene or graphite, while out-of-plane vibrations due to structural defects or sp^3 bonds resulting from oxygen binding are the main contributor to the D peak [35]. After oxidation, both peaks became wider due to the increased amount of disorder in comparison to graphite (Gr vs. GO, Fig 3.2D) [36]. Oxidation also resulted in an increase in the I(D)/I(G) ratio, apparently due to a decreased contribution of in-plane vibrations (G-peak), as well as oxygen binding to the carbon lattice, which caused increased out-of-plane vibrations (D-peak). The I(D)/I(G) ratio continued to increase upon chemical as well as microbial reduction. This change can be attributed to the formation of new sp^2 domains increasing the number of graphene-like domains [37].

For mrGO, we obtained an I(D)/(I(G) ratio of 1.00 ± 0.09 (n=4), which was not significantly different from the I(D)/(I(G) ratio measured for crGO

(1.00 ± 0.03, n=4, p=0.79). Both values were 15% larger and significantly different from the I(D)/(I(G) ratio obtained for GO (0.85 ± 0.03, n=4) (One-way ANOVA with Tukey PostHoc test, p-values: GO-mrGO = 0.049, GO-crGO = 0.012, n=4), indicating a decreased amount of defects in the microbially-reduced GO samples in comparison to GO.

As the number of layers, as well as wrinkles and multiple types of defects in the lattice, may contribute to the D peak in graphene materials [38], the I(D)/I(G) ratio is a less reliable indicator to quantify the grade of reduction. X-Ray photoelectron spectroscopy (XPS) allows for a better quantification of reduction as well as the identification of the elemental composition and the chemical states in the sample (i.e. C-C and C=C bonds vs. C-O bonds or C=O bonds) of mrGO in comparison to crGO and GO (Fig. 3.2E). The atomic percentage (atomic %), calculated via the peak area, of C-C and C=C bonds, was 32.7 ± 1.0% for GO and increased to 48.0 ± 1.0% in mrGO and 72.9 ± 1.0% in crGO. This percentage increase in carbon bonds was caused by the removal of oxygen during the reduction processes. Accordingly, the peak area of C-O and C=O bonds was 31.6 ± 0.2% for GO and decreased to 22.5 ± 2.0% for mrGO and 11.8 ± 1.2% for crGO. The data also showed that the peak area (in atomic %) of C=O bonds was not affected by microbial reduction (5.6 ± 0.3% GO and 6.4 ± 1.9% in mrGO) but decreased after chemical reduction (0.7 ± 0.7% in crGO [17, 25]. A colony forming unit (CFU) assay was performed to assess the toxicity of GO for *Shewanella oneidensis*. No harmful effects on the growth of the bacteria in presence of graphene oxide were found (Fig. 3.3).
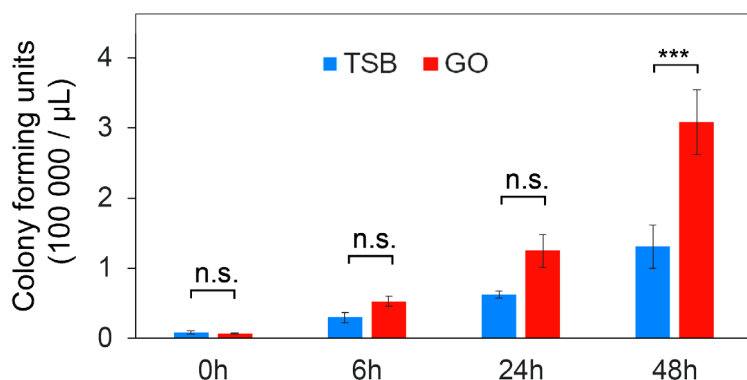
Fig. 3.3 Colony forming units (CFU) during the bacterial reduction of graphene oxide. During bacterial reduction of graphene oxide (GO) in solution, samples were removed after 0, 6, 24, and 48 hours, and the concentration of colony forming units was determined ("GO" condition). A control condition without GO was assessed ("TSB" condition), as well as a sample containing no bacteria, which consistently displayed no colony forming units (not shown). The sample containing GO displayed significantly higher colony forming units after 48 hours compared to the no-GO control (One-way ANOVA with Tukey PostHoc test 48h_GO to 48h_TSB: $p = 0.0016$, $n=6$). All significant differences are denoted with (***) for highly significant (p-value < 0.01). Error bars are the standard error of the mean.

3.3.2 Conductive characterization of graphene oxide

To quantify the electronic properties of our microbially-reduced GO, we measured the current as a function of a bias voltage (I-V curves) of bulk samples (Fig. 3.4A) as well as of single flakes (Fig. 3.4B, C, D). For the bulk conductance measurements, GO, mrGO, and crGO were deposited onto non-conductive filter paper. Microbial reduction caused an average increase in the current of 2.1 orders of magnitude, and chemical reduction caused an increase of 3.2 orders of magnitude at the same bias voltage. The conductance of these bulk samples are directly comparable because the samples share the same physical dimensions. The conductance of graphene materials in a bulk ensemble can arise from electrons travelling either within single flakes or due to flake-to-flake transport. To understand

3

the role of charge carrier movement between flakes versus charge movement within our GO flakes, single-flake conductance were measured. Single flakes of GO, mrGO, and crGO were deposited onto a Si/SiO2 chip (Fig. 3.4B). Atomic force microscopy (AFM) measurements were performed to obtain geometrical data for the individual flakes (thickness, width, and length), in order to compensate for differing flake geometries. The I-V curves of flakes with similar geometry (a length-to-width ratio between 2.1 and 2.4) showed a 2.7 order-of-magnitude increase of the current at the same bias voltage for mrGO (55.32 S/m) relative to GO (0.11 S/m), and a 3.3 order-of-magnitude increase for crGO (216.56 S/m) relative to GO (0.11 S/m) (Fig. 3.4C).

The data from the I-V curves and AFM analysis was used to calculate the sheet resistance (Rs) of GO, mrGO, and crGO (n= 11-18). These values are independent of the individual flake widths and lengths and are thus directly comparable. Rs was calculated using Rs = R * W / L with R the measured resistance, W width of the flake, and L its length or distance between the probes. The Rs value for GO (817 ± 423 MΩ) is 1.6 orders of magnitude higher than mrGO (13.2 ± 5.2 MΩ) and 2.3 orders of magnitude larger than crGO (2.5 ± 0.6 MΩ) flakes. To rule out the possibility that the resistance could be a function of the thickness, a population of flakes thinner than 10 nm (Fig. 3.4E) was analysed. No significant differences were identified between the sheet resistances of single flakes that were thinner than 10 nm (GO: 972 ± 591 MΩ; mrGO: 9.9 ± 3.2 MΩ; crGO: 2.1 ± 0.9 MΩ) in comparison with single flakes from the same species with thicknesses between 10 and 100 nm (One-way ANOVA with Tukey PostHoc test, $p > 0.05$).
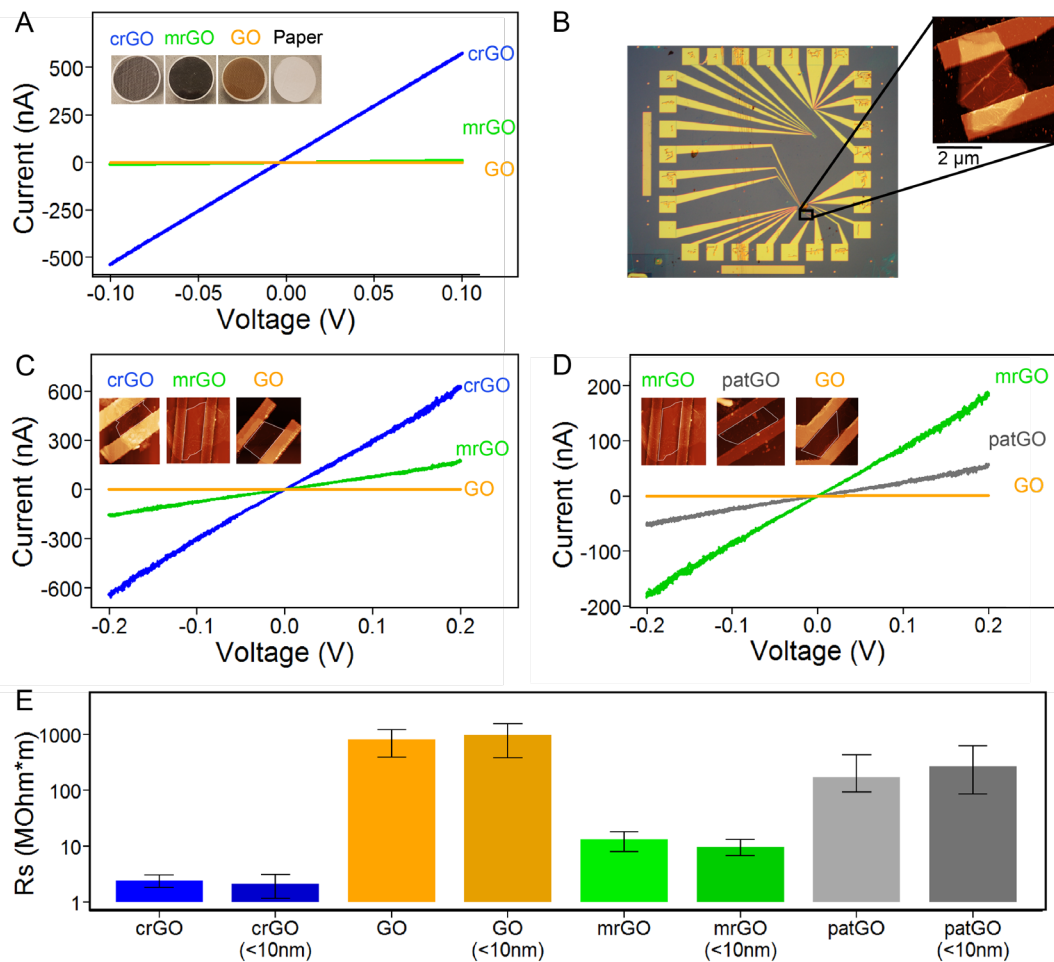
Fig. 3.4 Resistance and patterning of microbially-reduced graphene oxide. (A) Bulk measurements of conductance performed on graphene oxide (orange), chemically-reduced graphene oxide (blue), and microbially-reduced graphene oxide (green) with a voltage bias of +/- 0.1 V. The conductance increased by 3.2 orders of magnitude upon chemical reduction and by 2.1 orders of magnitude upon microbial reduction. Insets show bulk samples deposited onto filter paper. (B) Light microscopy and AFM image (inset) of a chip used to perform single-flake conductance measurements. (C) Conductance measurements of single flakes (shown in insets by AFM imaging) with comparable geometries at a voltage bias of +/- 0.2 V. The conductance increased by 3.3 orders of magnitude upon chemical reduction (blue) and by 2.7 orders of magnitude upon microbial reduction (green). (D) Conductance measurements of microbially-reduced and microbially-patterned single flakes with comparable shapes (shown in insets by AFM imaging) at a voltage bias of +/- 0.2 V. Patterned flakes (patGO, grey) were

selectively reduced on only one side of the flake, resulting in an increase of conductance by 1.1 orders of magnitude. (E) The average sheet resistance determined for single-flake samples. The Rs value for GO (817 ± 423 MΩ (SEM)) is 1.6 orders of magnitude higher than for mrGO flakes (13.2 ± 5.2 MΩ (SEM)) and 2.3 orders of magnitude larger than for crGO (2.5 ± 0.6 MΩ (SEM)) flakes. Measured flakes were divided into two groups based on the flake thicknesses: thickness between 10-100 nm, or thickness less than 10 nm (labelled "<10 nm").

To generate patterned graphene oxide (patGO) flakes with only one reduced surface, GO was drop-casted onto a Si/SiO2 chip. Afterwards, two layers of PMMA were spin-coated on top of the GO layer. E-beam lithography was used to create one to three windows per flake in the PMMA layer lying overtop of the GO flakes, with an average surface area of 25 μm^2. The exact dimensions and number of windows varied with the size of the flake. The windows were designed to allow bacteria to interact with the surface of the GO so that bacterial reduction could occur only on one side of the GO flake. These devices were microbially reduced with *S. oneidensis*, after which the conductance was determined in the same manner as for the single-flake conductance measurements. The conductance of patterned GO was 1.1 orders of magnitude larger than for GO (patGO: 171 ± 265 MΩ), which is intermediate between the conductance increase of mrGO with respect to GO (Fig. 3.4D, E). The microbially-reduced graphene oxide flakes were analysed by AFM to detect any remaining adherent bacteria. After the final washing steps, only one out of eleven mrGO flakes showed a bacterium on its surface (Fig. 3.5). In contrast, an average of ~2 bacteria per flake were identified in the AFM scans of the patterned GO flakes, likely due to the decreased amount of washing in this procedure (Fig. 3.6).
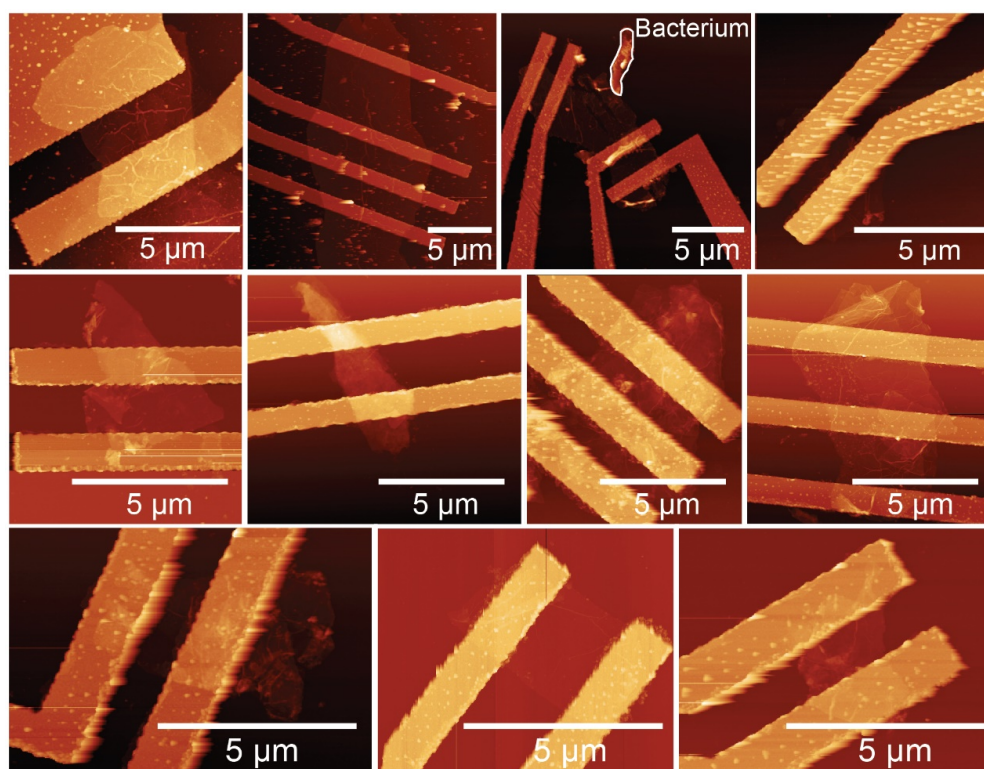
Fig. 3.5 AFM scans of microbially reduced graphene oxide (mrGO) flakes. In only one out of eight flakes (top row, 3rd from the left) was a bacterium visible. The size and shape of the bacterium was atypically large and unhealthy.
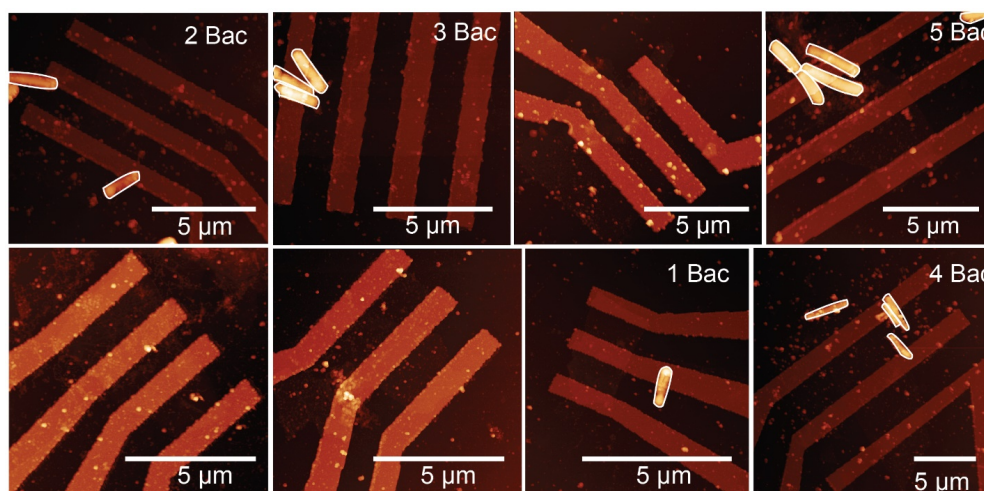
Fig. 3.6 AFM scans of the patterned graphene oxide (patGO) flakes. Multiple flakes had bacteria on their upper surface. These remaining bacteria are likely due to the reduced washing steps and the deposition of the entire device into a liquid filled with bacteria.

3

3.2.3 Thickness and surface-area of the so-obtained flakes

Aggregation of reduced graphene oxide materials over time can lead to a more graphite-like structure, negatively impacting their electrical and physical properties [39]. To quantify the thickness distributions and surface area of the microbially-produced graphene oxide flakes, we performed AFM and light microscopy measurements of the graphene oxide samples (GO, mrGO, crGO). Half of the samples of a particular batch were measured immediately ("fresh" samples), and the other half were measured after two weeks of storage in water at room temperature ("stored" samples). Single flakes of GO, mrGO, and crGO were deposited onto a Si/SiO2 chip using the same method as for the previous single-flake conductance measurements, and we compared their thicknesses via AFM measurements (Fig. 3.7A).

When comparing the thicknesses of the stored vs. fresh samples, no significant differences were observed for either mrGO or GO (One-way ANOVA with Tukey PostHoc test, $p > 0.05$). However, the chemically-reduced GO flakes showed a significant change after storage, with a doubling of the average thickness (One-way ANOVA with Tukey PostHoc test, $p = 0.032$). When different GO materials were compared, the average thickness values for the fresh samples showed higher average values for crGO than for GO and mrGO, but the differences were not significant (crGO: 31.3 ± 7.0 nm; GO: 10.2 ± 0.4 nm; mrGO: 10.4 ± 0.4 nm). Among stored samples, the average thickness values for stored crGO flakes (56.4 ± 14.1 nm) were significantly higher than those of stored GO (10.4 ± 1.5 nm, $p = 2e-6$) and stored mrGO (11.6 ± 0.2 nm, $p = 2e-6$) (One-way ANOVA with Tukey PostHoc test).

Most applications favour graphene with minimal thickness (1-3 layers) and maximal surface area. This combination allows a transfer of the material's nanomaterial properties (high tensile strength, conductance) into macroscopic technology. To compare the surface-area-to-thickness proportionality of our mrGO samples, the surface area of individual flakes

was determined via light microscopy imaging, and the thickness values obtained from AFM measurements. The calculated surface-area-to-thickness ratio for each flake was assigned to one of four groups (>1000:1, 1000:1-2000:1, 2000:1-3000:1, >3000:1) (Fig. 3.7B). Graphene oxide showed the best distribution of surface-area-to-thickness ratios; 27% of the flakes had a ratio of over 3000:1, 27% had a ratio between 3000:1 and 2000:1, 33% of the flakes had a ratio between 2000:1 and 1000:1, and only 13% had a ratio below 1000:1. For mrGO, 15% of the flakes had a ratio higher than 3000:1; 8% had a ratio between 3000:1 and 2000:1, 38% had a ratio between 2000:1 to 1000:1, and 39% had a ratio below 1000:1. The proportion of high surface-area-to-thickness was the lowest for crGO, where no flakes showed a ratio above 2000:1. The ratio between 2000:1 to 1000:1 was only 23%, and a large majority of 77% was below 1000:1. The mean values for the surface-area-to-thickness showed a significant difference between crGO (707.88 ± 495.79 µm) and GO (2647.38 ± 485.51 µm, $p = 0.0007$), but no significant differences were observed between GO and mrGO ($p = 0.0677$) or mrGO and crGO ($p = 0.1988$) (One-way ANOVA with Tukey PostHoc test, n=13). Thus, overall mrGO flakes maintained lower thickness and higher surface-area-to-thickness ratios in comparison to crGO flakes.
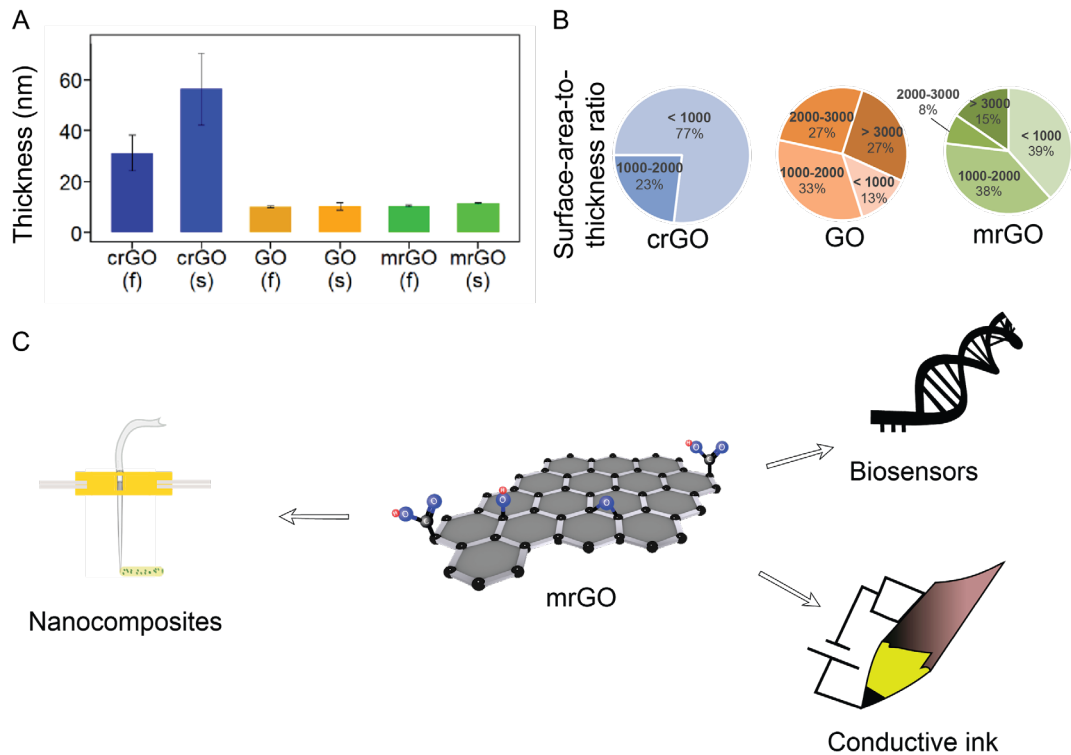
Fig 3.7 The thickness and surface-area-to-thickness ratio of mrGO flakes are key attributes for potential applications. (A) The average thickness of single flakes were determined via AFM. Graphene oxide (GO), microbially-reduced graphene oxide (mrGO), and chemically-reduced graphene oxide (crGO) were measured fresh ("f") and after a two-week storage ("s") in water. A significant difference was measured between the thicknesses of the crGO and the microbially-reduced and the GO flakes (mrGO: p = 2e-6, GO: p = 2e-6), but not between the stored and fresh crGO flakes (p = 0.32) (One-way ANOVA with Tukey PostHoc test). (B) The surface-area-to-thickness ratio was determined for single flakes of GO, mrGO, and crGO and assigned to one of four groups (> 3000:1, 3000:1-2000:1, 2000:1-1000:1, < 1000:1). (C) Proposed applications for mrGO based on its thickness and conductance properties. Biosensors are of interest because of the high surface-area-to-thickness ratio, the storability, and the remaining C=O double bonds which allow the possibility of chemical modifications. Nanocomposites could also benefit from the C=O double bonds as well as the feasibility of patterning, and the conductive ink industry could benefit from the conductivity combined with the improved storability in water as compared to chemically-reduced graphene oxide.

3.4 Conclusion

This work is the first study to show the properties and applicability of microbially reduced and patterned graphene oxide with a focus on its conductance and surface-area-to-thickness ratio. *Shewanella oneidensis* was used as a model organism for microbial reduction, and we compared the microbially-produced mrGO to graphene oxide that was chemically reduced using hydrazine, the most popular method to produce rGO. Raman spectrometry, O.D. measurements, and XPS were utilized to determine the chemical and optical changes during the microbial and chemical reduction. AFM, SEM, and light microscopy revealed the flake dimensions in different reduction states. Conductivity measurements of bulk and single flakes allowed for an electrical characterization of our samples.

Analyses of the microbial reduction process under aerobic and anaerobic conditions confirmed that both conditions can allow for robust mrGO production (Fig. 3.2C). The anaerobic process is more suitable for large-scale bioreactor applications since no oxygenation is needed, and it is more cost-efficient [40]. In contrast, the aerobic process is easier to handle on a smaller scale since no anaerobic equipment is required, and the samples may easily be transported.

The XPS and Raman measurements of differently-produced graphene oxide samples showed that chemical treatment with hydrazine removes almost all oxygen bonds from GO, while microbial reduction has little effect on the carbon-oxygen double bonds (Fig. 3.2D, E). This comparison with the starting material (graphene oxide) allows a better understanding of the fundamental reduction capability of *Shewanella oneidensis*. We hypothesize that the higher bond energy of C=O in comparison to C-OH and C-O-C makes it unable to be reduced via the *Shewanella* reduction mechanism. Similarly, *Shewanella* is only able to utilize a limited set of inorganic terminal electron acceptors [41] due to the moderate reduction capabilities of its electron-donating proteins and small molecules. Microbial reduction

of GO resulted in a 2.7 order-of-magnitude increase of conductance for single flakes of mrGO as well as an increase in conductance of 2.1 orders of magnitude in bulk mrGO samples (Fig. 3.4A, C). Even though the conductivity of mrGO is lower than that measured for crGO, the presence of the C=O double bonds in mrGO may prevent additional п-п stacking of the rGO flakes, leading to the observation that the flake thickness seems to be better conserved upon mrGO production than for crGO production (Fig. 3.7A). The production of smaller-thickness flakes for mrGO samples could be a significant advantage for applications that rely on a high surface-to-volume ratio.

Our experimental results showed that chemically-reduced flakes are more likely to form thicker aggregates than microbially-reduced flakes. In both fresh and stored samples, crGO flakes were thicker and had a worse surface-area-to-thickness ratio in comparison to GO and mrGO. Furthermore, the average flake thickness of crGO samples increased significantly after a two-week storage period, which was not observed for either GO or mrGO samples. The increased amount of layers in chemically-reduced samples may be due to п-п stacking of crGO flakes occurring during the reduction process and continuing during storage. Thus, the high surface-area-to-thickness ratio and the improved storability of mrGO in comparison to crGO identifies mrGO as an effective material for applications requiring prolonged storage, such as conductive inks, biosensors, and materials for additive manufacturing.

The distinct chemical and conductive properties of mrGO in relation to crGO and GO indicate several promising application areas for mrGO (Fig. 3.7C). The conservation of the carbon-oxygen double bonds in mrGO, shown through the XPS measurements, could be a valuable source for chemical modifications, which are necessary for most biosensors [42]. At the same time, the mrGO is up to 2.7 magnitudes more conductive than graphene oxide, which would enable applications requiring both chemical modification and electrical measurements (e.g. for field-effect transistor

biosensors) [42, 43]. The lower proportion of carbon-oxygen single bonds in mrGO compared to GO could decrease the amount of accidentally-bound biomolecules during biosensing in comparison to GO and, therefore, increase the selectivity of biosensors made from mrGO in comparison to GO [44]. The improved storability of mrGO in water coupled with the 2.7 orders-of-magnitude increase in conductance may be beneficial for conductive inks as well. Finally, the possibility to spatially pattern mrGO flakes and the associated single-sided reduction would help to improve 3D-structural alignment in nanocomposites [45] such as high-resolution bioprinting applications or composite (nano) materials, and could potentially be used for self-alignment of materials and sensors.

Microbially-reduced graphene is distinguished from crGO by its improved surface-to-volume ratio (displayed via the surface-area-to-thickness ratio), better storability, the conservation of its carbon-oxygen double bonds, and a more sustainable production methodology, while having a comparable conductivity. Further improvement in the degree of reduction of mrGO could be possible through the use of a different metal-reducing bacteria strain [46, 47], highlighting the importance of continuous efforts towards cultivating and characterizing environmental bacteria. A direct improvement of the reductive behavior of *S. oneidensis* and its kinetics has also been achieved by increasing the number of electron shuttles, both by adding additional synthetic electron shuttles to the medium as well as by introducing genetic modifications to the bacterium itself to increase endogenous production of electron shuttle molecules [26, 48]. All samples in this study were produced on a laboratory scale, and the next logical step towards economic feasibility would be upscaling in a bioreactor system. The upscaling of our methodology would allow a continuous process for the production of reduced GO to be initiated in bioreactors that would operate without the use of harsh chemistry or high energies. The results here obtained also indicate that the bacterial residues can be nearly completely washed away post-reduction. This approach would, therefore,

be more sustainable and eco-friendlier than the currently-used thermal or chemical methodologies, while maintaining the surface-to-volume ratio, which is critical for various applications of reduced graphene oxide.

3.4 Materials and Methods

3.4.1 Bacterial strains and culturing

Shewanella oneidensis MR-1 (ATCC® 700550™) was aerobically and anaerobically cultured in rich Tryptic Soy Broth (TSB) media (Sigma Aldrich) or minimal media (28 mM NH_4Cl, 1.34 mM KCl, 5 mM NaH_2PO_4, 0.7 mM Na_2SO_4, 1 mM $MgSO_4 \cdot 7H_2O$, 20 mM PIPES [piperazine-*N*,*N*-bis(2-ethanesulfonic acid)], 52 mM NaCl, 0.2 mM $CaCl_2$, and trace elements (1 liter of medium contains 10 mg $FeCl_2 \cdot 4H_2O$, 5 mg $MnCl_2 \cdot 4H_2O$, 3 mg $CoCl_2 \cdot 4H_2O$, 2 mg $ZnCl_2$, 0.5 mg $Na_2MoO_4 \cdot 4H_2O$, 0.2 mg H_3BO_3, 1 mg $NiSO_4 \cdot 6H_2O$, 0.02 mg $CuCl_2 \cdot 2H_2O$, 0.06 mg $Na_2SeO_3 \cdot 5H_2O$, and 0.08 mg $Na_2WO_4 \cdot 2H_2O$) [49] containing 20mM L-lactate (Sigma Aldrich) and/or 20mM Sodium fumarate dibasic (Sigma Aldrich) overnight at 30°C under continuous shaking (250 rpm).

3.4.2 Graphene oxide production

Graphite oxide was prepared using a modified Hummers and Offeman method [26, 46]. Briefly, 0.5 g graphite (pure graphite flakes with an average flake size of 45 μm (Ma -399.5 RG), NGS Trading & Consulting GmbH) was mixed with 20 mL H_2SO_4 (Sigma Aldrich) and 5 mL HNO_3 (Sigma Aldrich) under continuous stirring and on an ice bath. After 30 minutes of stirring, 3 g $KMnO_4$ (Sigma Aldrich) was added, after which the solution was stirred on an ice bath for 30 minutes, followed by incubation on the ice bath for one hour. The sample was heated to 35°C for 3 hours and diluted with 40 mL ultrapure water, followed by an incubation at 35°C for 2 hours. Then 100 mL ultrapure water was added and a second oxidation with 20 mL of H_2O_2 was initiated. The graphite oxide solution was ultra-sonicated at 40 kHz (Carl Roth D30 ultrasonicator) for 2 hours and

was allowed to settle overnight. The supernatant, now mainly consisting of graphene oxide, was decanted and washed with 5% HCl (Sigma Aldrich), acetone (Sigma Aldrich), and distilled water. Finally, the non-exfoliated flakes were removed via centrifugation (3000 rpm for 10 min), and the exfoliated flakes were lyophilized at -50°C for 1 day (Christ Alpha 1-2 LD Plus lyophilizer) [50].

3.4.3 Chemical reduction of graphene oxide

For the chemical conversion of graphene oxide to its reduced form, 30 mg of graphene oxide was dissolved in 100 mL distilled water and mixed vigorously. The sample was placed into a fume hood, and 120 μL hydrazine (35 wt% in H_2O, Sigma Aldrich) and 1 mL ammonia solution (28 wt% in H_2O, VWR International BV) were added. The solution was stirred at a temperature of 95°C for 3 hours. Since the weight ratio of hydrazine to graphene oxide was 7:10, all hydrazine was used up during the reaction [51].

3.4.4 Biological reduction of graphene oxide

TSB medium including a concentration of 0.5 mg/mL graphene oxide was prepared and vigorously mixed. An overnight culture of *Shewanella oneidensis* MR-1 was diluted with this solution to an O.D.$_{600}$ of 0.1 A.U.. The reduction was performed aerobically or anaerobically for 48 hours under continuous shaking (250 rpm) at room temperature in a 96-well plate (Sigma Aldrich). The anaerobic experiments were performed in anaerobic vessels (Sigma Aldrich) within a glove box (Plas Labs) and under nitrogen atmosphere. The growth of the bacteria was observed via measurement of optical density at 600 nm using a plate reader (Synergy HTX, Multimode reader).

3.4.5 Single-flake deposition and inspection

A volume of 0.25 mL graphene oxide flakes, microbially-reduced graphene oxide flakes, or chemically-reduced graphene oxide flakes with a

concentration of 0.1 mg/mL in water was drop-casted onto a Si/SiO$_2$ (285 nm SiO$_2$) device (Microchemicals) with premade gold markers. The residual solvent was washed away with acetone and isopropanol for all samples. The devices were inspected for sufficient sample deposition under an optical microscope (Olympus BX 5, with DP25 camera), and images were acquired of samples. After alignment of the images using QCAD® software, electrical leads were drawn onto selected flakes via the following procedure. Two layers of PMMA (PMMA A6 495K followed by PMMA A3 950K) were sequentially spin-coated onto the surface of the device at 4500 rpm and baked for 12 minutes at 175°C. The CAD file was uploaded to and patterned with an e-beam system (Raith EBPG 5000+), and layers of titanium (5 nm) and gold (75 nm) were evaporated onto the surface using an e-gun for metal evaporation of metals (Temescal FC2000). The PMMA was lifted off in hot acetone (80°C), and an isopropanol washing step was performed. The device was inspected again under the optical microscope to check for lost flakes or improperly drawn leads prior to conductance measurement. After conductance measurements, the graphene oxide flakes were inspected again via optical microscopy as well as via a scanning electron microscope (FEI NovaNanoSEM) using 5-15 kV voltage and 5 mm working distance.

3.4.6 Single flake conductance measurements

A probe station (TTP4 Desert, Lakeshore) was used to measure a varying voltage bias (+/- 0.2 V) applied to GO, mrGO, crGO, and patGO samples. The current as a function of the voltage bias was recorded and used to calculate the resistance of individual flakes over a set of distances (R (resistance) = V (voltage) / I (current)). AFM measurements (AFM Dimension FastScan, Brucker, tapping mode in air, fast-scan tip) were taken of the outer dimensions and the thickness of the single flakes to determine the size distribution of the flakes and calculate the intrinsic

resistivity (ρ (resistivity) = R (resistance) * A (area) / L (length)) and sheet resistance (R_S (sheet resistance) = R (resistance) * W (width) / L (length)).

3.4.7 Bulk conductance measurement

Graphite, graphene oxide, microbially-reduced graphene oxide, and chemically-reduced graphene oxide were prepared, and 15 mL of a 0.5 mg/mL solution of each sample was vacuum filtered (Vacuum Filtration Unit Buchner Medium 60 mL Frit Funnel 250 mL Erlenmeyer Flask) through a 0.2 µm PTFE filter (Whatman, PTFE membrane filters). The deposited material was rinsed once in a 10% solution of HCl and 5 times in MilliQ water. Thereafter, the filter paper was air-dried, and conductance was measured over its full diameter using a probe station (TTP4 Desert, Lakeshore).

3.4.8 Bacterial lithography

Graphene oxide was deposited via drop casting onto a Si/SiO_2 device (Microchemicals). Suitable flakes (high surface area low thickness) were inspected and selected under an optical microscope (Olympus BX 5, with DP25 camera). Two layers of PMMA were spin-coated onto the surface of the device. QCAD® software was used to design windows (dimensions 5x5 µm^2) in the PMMA layers, which were cut out via an e-beam system (Raith EBPG 5000+). After five washing steps in distilled water, the devices were placed into a *Shewanella* solution with a starting $O.D._{600}$ of 0.1. The devices were incubated in the solution for 48 hours at room temperature. The conductance was measured following the method for single-flake conductance measurements.

3.4.9 X-ray photoelectron spectroscopy (XPS)

X-ray photoelectron (XPS) spectra were recorded on a ThermoFisher K-Alpha system using Al Kα radiation with a photon energy of 1486.7 eV. The samples were immobilized onto a copper tape (Plano GmbH, G3397) and

3

loaded into the XPS chamber without further purification. High-resolution XPS spectra were acquired using a spot size of 400 µm, 50 eV pass energy, and 0.1 step size, with 40 scans (for carbon and nitrogen spectra) or 10 scans (for oxygen spectrum) with charge neutralizing. The peaks were calibrated for the C 1s peak at 285 eV. Quantitative analysis of the separate binding states was carried out by deconvoluting the high-resolution spectra using ThermoFisher Advantaged software. Gaussian-Lorentzian product functions were used to fit the peaks after Smart-type background subtraction. The chemical bond ratios were then calculated by correcting the peak areas with the TPP-2M sensitivity factor. All fits that occurred in both spectra were cross-checked to verify their fit-match.

3.5.10 Statistics

R-Studio was used for data analysis and visualization. All datasets were checked for outliers with a Dixon's Q-Test. Unless noted, no outliers were removed from the datasets. The variance was tested using an F-test, and Student's t-test with either equal or unequal variances was used for comparing two data sets, with a significance level of $\alpha = 0.05$. We used a one-way ANOVA with Tukey PostHoc Test to compare more than two datasets.

3.5.11 Surface-Area-to-Thickness ratio

For analysis of the surface-area-to-thickness ratios of individual flakes, flakes were separated into four distinct groups (< 1000:1, 1000:1 - 2000:1, 2000:1 – 3000:1, > 3000:1). The surface area was measured from SEM images using ImageJ and divided by the average thickness obtained from the AFM to calculate the ratio.

3.5.12 Colony Forming Units (CFU) to check the bacterial survival rate

Colony forming units (CFU) were determined following the protocol of Karas et al [52]. In short, each sample was serially diluted in ten-fold

increments from 10^{-0} to 10^{-7}. A volume of 5 µL from each dilution was pipetted in triplicates onto a LB agar plate. The plates were incubated at 22°C for 24 hours, and visible colonies were counted.

3.6 References

[1] Novoselov KS, *et al.* (2004) Electric field effect in atomically thin carbon films. *Science* 306(5696):666-669.

[2] Kumar R, *et al.* (2014) Graphene as a transparent conducting and surface field layer in planar Si solar cells. *Nanoscale Res Lett* 9(1):349.

[3] Marinho B, Ghislandi M, Tkalya E, Koning CE, & de With G (2012) Electrical conductivity of compacts of graphene, multi-wall carbon nanotubes, carbon black, and graphite powder. *Powder Technology* 221:351-358.

[4] Balandin AA, *et al.* (2008) Superior Thermal Conductivity of Single-Layer Graphene. *Nano Letters* 8(3):902-907.

[5] Lee C, Wei X, Kysar JW, & Hone J (2008) Measurement of the elastic properties and intrinsic strength of monolayer graphene. *Science* 321(5887):385-388.

[6] Zhu X, *et al.* (2015) Application of nanomaterials in the bioanalytical detection of disease-related genes. *Biosens Bioelectron* 74:113-133.

[7] Shi S, *et al.* (2015) The application of nanomaterials in controlled drug delivery for bone regeneration. *J Biomed Mater Res A* 103(12):3978-3992.

[8] Palermo V, Kinloch, I. A., Ligi S., Pugno N.M. (2016) Nanoscale Mechanics of Graphene and Graphene Oxide in Composites: A Scientific and Technological Perspective. *Advanced Materials* 28(29):6232-6238.

[9] Franklin AD (2015) DEVICE TECHNOLOGY. Nanomaterials in transistors: From high-performance to thin-film applications. *Science* 349(6249):aab2750.

[10] Chen JS & Lou XW (2013) SnO(2)-based nanomaterials: synthesis and application in lithium-ion batteries. *Small* 9(11):1877-1893.

[11] Dimitrakakis GK, Tylianakis E, & Froudakis GE (2008) Pillared Graphene: A New 3-D Network Nanostructure for Enhanced Hydrogen Storage. *Nano Letters* 8(10):3166-3170.

[12] Liu Y, *et al.* (2018) Graphene on {116} faceted monocrystalline anatase nanosheet array for ultraviolet detection. *Nanoscale*.

[13] Rodriguez-Perez L, Herranz MA, & Martin N (2013) The chemistry of pristine graphene. *Chem Commun (Camb)* 49(36):3721-3735.

[14] Dreyer DR, Park S, Bielawski CW, & Ruoff RS (2010) The chemistry of graphene oxide. *Chem Soc Rev* 39(1):228-240.

[15] Araujo PT, Terrones M, & Dresselhaus MS (2012) Defects and impurities in graphene-like materials. *Materials Today* 15(3):98-109.

[16] Zhang Y, Zhang L, & Zhou C (2013) Review of Chemical Vapor Deposition of Graphene and Related Applications. *Accounts of Chemical Research* 46(10):2329-2339.

[17] Chen B, *et al.* (2014) How good can CVD-grown monolayer graphene be? *Nanoscale* 6(24):15255-15261.

[18] Abdolhosseinzadeh S, Asgharzadeh H, & Seop Kim H (2015) Fast and fully-scalable synthesis of reduced graphene oxide. *Scientific Reports* 5:10160.

[19] William JH, S.; Offeman, R. E. (1958) Preparation of Graphitic Oxide. *J. Am. Chem. Soc* 80:1339.

[20] Moon IK, Lee J, Ruoff RS, & Lee H (2010) Reduced graphene oxide by chemical graphitization. *Nat Commun* 1:73.

[21] Marcano DC, *et al.* (2010) Improved synthesis of graphene oxide. *ACS Nano* 4(8):4806-4814.

[22] Chua CK & Pumera M (2014) Chemical reduction of graphene oxide: a synthetic chemistry viewpoint. *Chem Soc Rev* 43(1):291-312.

[23] Schniepp HC, *et al.* (2006) Functionalized single graphene sheets derived from splitting graphite oxide. *J Phys Chem B* 110(17):8535-8539.

[24] Salas EC, Sun Z, Luttge A, & Tour JM (2010) Reduction of graphene oxide via bacterial respiration. *ACS Nano* 4(8):4852-4856.

[25] Jiao Y, *et al.* (2011) Deciphering the electron transport pathway for graphene oxide reduction by Shewanella oneidensis MR-1. *J Bacteriol* 193(14):3662-3665.

[26] Liu G, *et al.* (2013) Quinone-mediated microbial synthesis of reduced graphene oxide with peroxidase-like activity. *Bioresour Technol* 149:503-508.

[27] Fan G, Dundas CM, Graham AJ, Lynd NA, & Keitz BK (2018) Shewanella oneidensis as a living electrode for controlled

radical polymerization. *Proceedings of the National Academy of Sciences* 115(18):4559.

[28] Bollella P*, et al.* (2017) Beyond graphene: Electrochemical sensors and biosensors for biomarkers detection. *Biosens Bioelectron* 89(Pt 1):152-166.

[29] Zhou M, Zhai Y, & Dong S (2009) Electrochemical Sensing and Biosensing Platform Based on Chemically Reduced Graphene Oxide. *Analytical Chemistry* 81(14):5603-5613.

[30] Pei S & Cheng H-M (2012) The reduction of graphene oxide. *Carbon* 50(9):3210-3228.

[31] Novoselov KS*, et al.* (2012) A roadmap for graphene. *Nature* 490:192.

[32] Huang L, Huang Y, Liang J, Wan X, & Chen Y (2011) Graphene-based conducting inks for direct inkjet printing of flexible conductive patterns and their applications in electric circuits and chemical sensors. *Nano Research* 4(7):675-684.

[33] Xu LY, Yang GY, Jing HY, Wei J, & Han YD (2014) Ag-graphene hybrid conductive ink for writing electronics. *Nanotechnology* 25(5):055201.

[34] Talukdar Y, Rashkow J, Lalwani G, Kanakia S, & Sitharaman B (2014) *The Effects of Graphene Nanostructures on Mesenchymal Stem Cells* pp 4863–4877.

[35] Lalwani G, Xing W, & Sitharaman B (2014) *Enzymatic Degradation of Oxidized and Reduced Graphene Nanoribbons by Lignin Peroxidase*.

[36] Kim HJ*, et al.* (2014) Unoxidized Graphene/Alumina Nanocomposite: Fracture- and Wear-Resistance Effects of Graphene on Alumina Matrix. *Scientific Reports* 4:5176.

[37] Yang D*, et al.* (2009) Chemical analysis of graphene oxide films after heat and chemical treatments by X-ray photoelectron and Micro-Raman spectroscopy. *Carbon* 47(1):145-152.

[38] Ferrari AC & Basko DM (2013) Raman spectroscopy as a versatile tool for studying the properties of graphene. *Nat Nanotechnol* 8(4):235-246.

[39] Chowdhury I, Mansukhani ND, Guiney LM, Hersam MC, & Bouchard D (2015) Aggregation and Stability of Reduced Graphene Oxide: Complex Roles of Divalent Cations, pH, and Natural Organic Matter. *Environmental Science & Technology* 49(18):10886-10893.

[40] Abdelgadir A, *et al.* (2014) Characteristics, process parameters, and inner components of anaerobic bioreactors. *Biomed Res Int* 2014:841573.

[41] Myers CR & Nealson KH (1988) Bacterial Manganese Reduction and Growth with Manganese Oxide as the Sole Electron Acceptor. *Science* 240(4857):1319.

[42] Zhang Q, *et al.* (2015) Graphene oxide-based optical biosensor functionalized with peptides for explosive detection. *Biosens Bioelectron* 68:494-499.

[43] Masoudipour E, Kashanian S, Maleki N, Karamyan A, & Omidfar K (2018) A novel intracellular pH-responsive formulation for FTY720 based on PEGylated graphene oxide nano-sheets. *Drug Dev Ind Pharm* 44(1):99-108.

[44] Liu J, Liu Z, Barrow CJ, & Yang W (2015) Molecularly engineered graphene surfaces for sensing applications: A review. *Anal Chim Acta* 859:1-19.

[45] Lehner BA, Schmieden DT, & Meyer AS (2017) A Straightforward Approach for 3D Bacterial Printing. *ACS Synth Biol*.

[46] Wang G, Qian F, Saltikov CW, Jiao Y, & Li Y (2011) Microbial reduction of graphene oxide by Shewanella. *Nano Research* 4(6):563-570.

[47] Kostka JE, Dalton DD, Skelton H, Dollhopf S, & Stucki JW (2002) Growth of Iron(III)-Reducing Bacteria on Clay Minerals as the Sole Electron Acceptor and Comparison of Growth Yields on a Variety of Oxidized Iron Forms. *Applied and Environmental Microbiology* 68(12):6256.

[48] Yang Y (2015) Enhancing Bidirectional Electron Transfer of Shewanella oneidensis by a Synthetic Flavin Pathway. *ACS Synthetic Biology* 4(7):815-823

[49] Tang YJ, Laidlaw D, Gani K, & Keasling JD (2006) Evaluation of the effects of various culture conditions on Cr(VI) reduction by Shewanella oneidensis MR-1 in a novel high-throughput mini-bioreactor. *Biotechnology and Bioengineering* 95(1):176-184.

[50] Lee G & Kim BS (2014) Biological reduction of graphene oxide using plant leaf extracts. *Biotechnol Prog* 30(2):463-469.

[51] Li D, Muller MB, Gilje S, Kaner RB, & Wallace GG (2008) Processable aqueous dispersions of graphene nanosheets. *Nat Nanotechnol* 3(2):101-105.

[52] Karas, V. O., Westerlaken, I., and Meyer, A. S. (2015) The DNA-Binding Protein from Starved Cells (Dps) Utilizes Dual Functions to Defend Cells against Multiple Stresses, *J Bacteriol* 197: 3206-3215.

4

Homogenous and Biocompatible Covalent coating of Graphene Oxide for Biomedical Applications

Benjamin A.E. Lehner, Dominik Benz, Stanlislav A. Moshkalev, Anne S. Meyer, Monica A. Cotta*, Richard Janissen*

Graphene oxide (GO) has immense potential for widespread usage in biomedical applications due to its stability, maximal surface-to-volume ratio and modifiability. However, development of GO-based therapies/tools has been hindered due to its poor chemical properties causing unspecific bonds. Here, we present a simple yet powerful method for covalently functionalizing graphene oxide with colamine and poly(ethylene glycol) that results in dramatic improvement in the chemical stability, biocompatibility and coating density while suppressing non-specific adhesion. This modified graphene oxide is now well-suited for a variety of new *in-situ* applications including biosensors, nanocomposites and drug carriers.

4.1 Introduction

Since its discovery in 2004, graphene in both its pristine and oxidized form has been proposed for a wide variety of applications, ranging from nanocomposite material developments to biomedical applications [1, 2]. The unique combination of characteristics of this 2D material, such as the high surface-to-volume ratio, coupled with excellent electrical properties, chemical resistance, thermal stability, and solubility in aqueous solutions, make graphene oxide (GO) of particular interest for biomedical applications including label-free biosensors and, more recently, drug delivery carriers [1, 3] For example, previous studies have shown the feasibility of using GO in applications for drug delivery (e.g. Paxitacel, FTY720, siRNA, PCA), early disease-detecting biosensors (e.g. Parkinson's disease, Alzheimer, prostate cancer, glucose immunosensing), tissue engineering, and cell imaging, among others [1, 3-8].

From a physicochemical point of view, these applications share the same critical requirements to enable their applicability and overall performance. Ideally, the organo-chemical coating of GO should provide a homogenous surface coverage with high (bio)molecule density, stable chemical attachment, and high biocompatibility, while suppressing non-specific biomolecule adhesion [9-11]. These characteristics have been shown to directly impact the target biomolecule selectivity and sensitivity (in the case of biosensors), and the immune response in organisms [9-14].

While the challenges of biocompatibility and suppression of nonspecific biomolecule adhesion can be addressed by using physically and chemically inert ethylene glycol polymer (PEG) material coating, achieving chemically stable, dense, and homogenous functionalization of GO remains difficult [13]. To date, the immobilization of biomolecules to GO is primarily realized using weak

non-covalent and reversible binding strategies for attachment of (bio)molecules based on electrostatic forces (e.g. π-stacking, van der Waals forces), and only a few approaches have been developed for covalent attachment of chemical moeities to residual oxygen-containing functional groups of GO [8, 15]. Candidates for possible covalent attachment points of GO include the randomly distributed epoxide and the relatively abundant hydroxyl groups within the GO hexagonal lattice, as well as the less-abundant carboxylic groups and the ketones located at the edges of GO flakes [1, 3]. One current strategy is the functionalization of carboxylic groups at GO flake edges to provide anchors for covalent biomolecule attachment. This modification can be achieved either via chemical reduction using hydrazine, which in turn also removes most of the other oxygen-containing functional groups, or via peptide binding through exposure to EDC (N-(3-dimethyl-aminopropyl-N'-ethyl carbodiimide)) together with NHS (N-hydroxy-succinimide) reactive groups [5, 16]. However, this strategy is imperfect, particularly for GO. In flakes with larger dimensions, the use of carboxylic groups does not provide the required coating density on the GO lattice and provides insufficient biocompatibility [12, 14].

To improve GO coating coverage, more recent developments have focused on the covalent attachment of an alkoxysilane crosslinker to surface hydroxyl groups scattered across the GO plane. APTES (3-aminopropyl-triethoxysilane) has been a common choice for this approach despite the fact that APTES modification can promote the formation of inhomogeneous and polymerized multilayers, thus proving to be inadequate for applications involving nanostructures [13,17–19]. As a promising alternative, colamine (β-hydroxy ethylamine) has recently shown a superior functionalization performance for nanoscale semiconductor structures, for which it can provide dense and homogeneous monolayer coatings bound to

hydroxyl groups [13, 20]. In the case of GO, the use of colamine as a crosslinker would modify both hydroxyl and epoxide groups across the material plane, potentially increasing the coating coverage.

4.2 Results & discussion

In this work, we demonstrate the applicability of colamine and subsequent PEG functionalization to GO mono-, bi-, and multilayers. In a stepwise and bottom-up fashion, we address on a quantitative level the surface coating quality and biomolecule recognition efficiency for DNA, as well as the nonspecific biomolecule adhesion-suppressing performance of different coatings.

4.2.1 Comparison between colamine and APTES coatings

We first coated SiO_2 supports with APTES, colamine (CA), or CA conjugated with PEG and evaluated the ability of each coating to suppress nonspecific ssDNA adhesion (Fig. 4.1A). Deposition of the coatings onto SiO_2-standards was carried out using wet chemistry approaches to avoid any possible impacts of different curing temperatures and low pressures on the chemical integrity of the GO [19]. Atto647N-labeled 40-base-pair ssDNA was allowed to non-specifically adhere onto the different coatings, and quantitative fluorescence microscopy was used to measure its density (Fig. 4.1B). In comparison to the standard APTES coating, CA coating exhibited a statistically significant 40% decrease in nonspecific ssDNA adhesion. The decrease in adhesion can be explained by the more homogeneous and denser surface coverage of the CA, while APTES coverage is incomplete and exposes bare areas of SiO_2 where electrostatic binding of ssDNA can occur. The addition of biocompatible PEG to CA strongly improved the suppression of nonspecific ssDNA-adhesion by ~95% compared to APTES. This profound improvement likely resulted from both the chemically and physically inert character of PEG and the increased distance between the surface and biomolecule that PEG provides (with a Flory radius of ~5 nm)

to overcome the effective Debye length range (~1 nm in physiological conditions) where strong electrostatic interactions occur [21]. Since the use of CA and PEG coatings fulfilled the physicochemical requirements for coating inertness and biocompatibility needed for *in situ* biomedical applications, we next focused on developing a functionalization procedure for CA+PEG-coated GO.
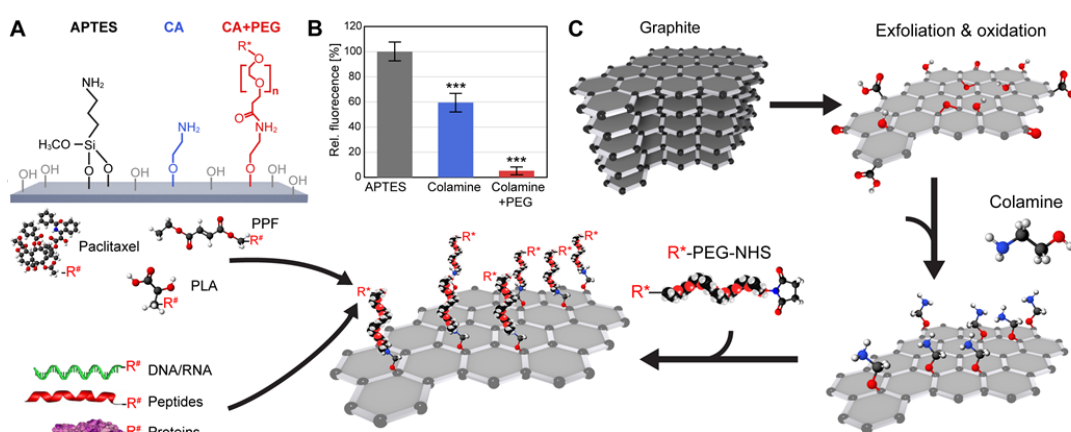
Fig. 4.1 (A) Suppression of nonspecific DNA adhesion by colamine coating and functionalization of graphene oxide. (B) For different coatings (APTES, colamine (CA), colamine and polyethylene glycol (PEG)) covalently bound to surface hydroxyl groups, nonspecific adhesion of Atto647N-labeled 40b ssDNA was quantitatively assessed via fluorescence intensity (n = 5; AVG±SD), normalized to the value for APTES (unpaired two-tailed t-test, p: *** ≤ 0.001). (C) After exfoliation and oxidation of graphite to GO, colamine was covalently bound to both epoxide and hydroxyl groups on the GO surface plane. A secondary biocompatible layer consisting of NHS-PEG-R was covalently attached to primary amino groups provided by the colamine coating. Potential covalent immobilization of biomolecules and drugs to PEGylated GO are displayed. Various binding strategies using different functional groups (R*) for PEG and target molecules are possible (e.g. peptide binding, sulfhydryl crosslinking).

4.2.2 Synthesis and inspection of graphene oxide

The bottom-up workflow of our strategy for functionalizing GO can be divided into three major steps (Fig. 4.1C). First, graphite is chemically exfoliated and oxidized using a modified Hummers and Offeman method to produce GO [22]. In a second step, the hydroxyl (and epoxide) groups of the GO are covalently functionalized with CA in an anhydrous solvent. The last step is the covalent coupling of heterobifunctional NHS-PEG-R to the surface amine groups. The functional group R can be adjusted to any chemical biomolecule-coupling strategy (Fig. 4.1C).

Prior to the covalent CA coating, the dimensions, layer-thickness, and degree of oxidation of GO were assessed via Scanning Electron Microscopy (SEM), Atomic Force Microscopy (AFM), and Raman spectroscopy. AFM topography measurements (Fig. 4.2A) revealed an average GO layer thickness (Fig. 4.2B) of 7±4 nm, equivalent to three to four layers of GO. With a measured average total GO surface area (Fig. 4.2C, H_2O) of 320 ± 60 μm^2, the GO flakes displayed a high surface-to-volume ratio (SVR) of ~290, which is an important quality factor to achieve a high molecule/drug density at small carrier sizes and increase stability in nanocomposites. Scanning Electron Microscopy showed a fundamentally changed surface topology between graphite (Fig 4.3A) and graphene oxide (Fig. 4.3B). Raman spectroscopy inspection (Fig. 4.3C) of the GO flakes revealed a slight shift of the G peak, caused by in-plane vibrations of sp^2-bonded carbon atoms, and the appearance of a second-order vibrational D peak. The latter was likely caused by out-of-plane vibrations attributable to defects in the hexagonal carbon lattice and existing oxidative functional groups. The global increase observed in peak widths could have reflected an increase of structural disorder [23]. The GO flakes with high surface-to-volume ratio and verified oxidation were tested for monodispersity in two commonly used organic solvents prior to covalent CA coating. As the functionalization with CA occurred over 12 h, we tested the monodispersity of the GO flakes over 24 h in the polar aprotic solvents DMSO (dimethyl

sulfoxide) and DMF (dimethyl formamide) (Fig. 4.2C). Compared to GO flakes in H2O, the GO flakes in both organic solvents showed no significant differences in flake dimensions, and as such, either is suitable for maintaining monodispersity during the CA-coating process.
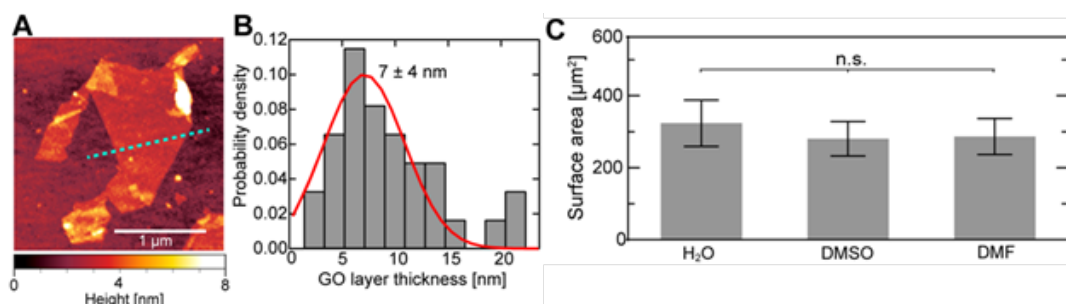
Fig. 4.2 Dimensions of GO flakes after graphite exfoliation and oxidation. (A) Example AFM topography image of a single-layer GO flake with a thickness of ~1.4±0.2 nm (cyan dotted line depicts measured example cross section). (B) GO flake thickness distribution measured via AFM. A majority of GO flakes exhibit few-layer graphene with an average thickness of 7 ± 4 nm (red Gaussian fit; n = 33). (F) Average total surface area (± SD; n = 100) of GO flakes stored in water (7 days), DMSO, and DMF (24 h each) exhibits no significant differences (one-way ANOVA with Tukey post-hoc test (n.s. = non-significant)).
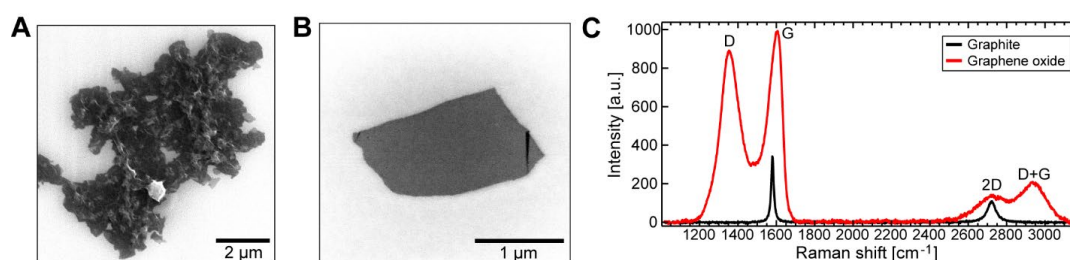
Fig. 4.3 Scanning electron microscopy (SEM) and Raman spectroscopy of primary graphite material and exfoliated graphene oxide (GO). (A) SEM micrograph of a graphite flake used as primary material before exfoliation and oxidation on a silicon dioxide surface. (B) SEM micrograph of an exfoliated and reduced GO flake on a silicon dioxide surface. (C) Raman spectrometry of primary graphite (black) material and GO sheets (red). The D peak appears after oxidation due to out-of-plane vibrations caused by oxygen atoms. All peaks in GO are broader than in graphite due to the increased amount of induced structural defects.

4.2.3 Functionalization of graphene oxide

We next performed the covalent functionalization of GO with CA in DMSO and DMF using the same protocol as for SiO_2. The presence of CA and the ether formation of oxygen-containing functional groups (Fig. 4.4A) upon CA addition was measured via X-ray photoelectron spectroscopy (XPS). Following GO functionalization with CA, the presence of CA on the GO surface was indicated by the emergence of a new peak for C-N bonds (286.17 eV) in the carbon spectrum (DMSO: Fig. 4.4B; DMF: Fig. 4.5A), together with a significant relative increase in N-C bonds (401.57 eV) content (Fig. 4.4E) in the nitrogen spectrum (DMSO: Fig. 4.4C; DMF: Fig. 4.5B). The N-N bond peak (399.55 eV) likely originated from the fixation tape, and N-C bonds from residual contamination in the untreated GO sample. Upon treatment with CA, the C-O-C peak (288.70 eV) notably increased in the oxygen spectrum (Fig. 4.4E; DMSO: Fig. 4.4D; DMF: Fig. 4.5C), indicating successful ether formation between CA and GO surface hydroxyl and epoxide functional groups. The changes in N-C and C-O-C bond content upon CA coating (Fig. 4.4E) were approximately the same in both solvents ($[\text{N-C}]_{CA}/[\text{N-C}]_{control}$ ~5; $[\text{C-O-C}]_{CA}/[\text{C-O-C}]_{control}$ ~2).
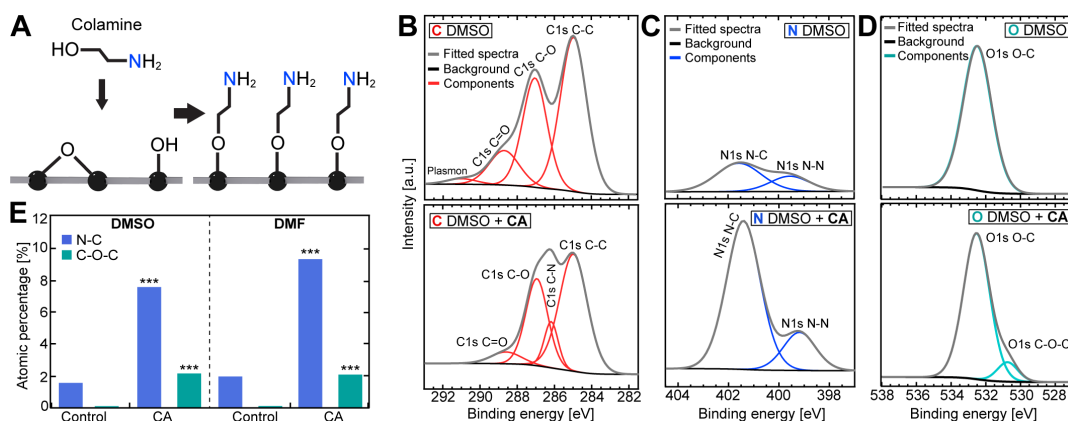
Fig. 4.4 X-ray photoelectron spectroscopy (XPS) analysis of CA-functionalized GO. (A) Schematic of covalent binding of CA to surface hydroxyl and epoxide groups. (B) Carbon, (C) nitrogen, and (D) oxygen XPS spectra before (top panels) and after (bottom panels) addition of CA in DMSO. (E) Relative atomic amounts of oxygen and nitrogen extracted from the peak fittings to the XPS spectra depicted in (C), (D) and Fig. 4.5. The oxygen content decreased significantly while nitrogen content showed a 2-fold increase using DMSO and DMF. Grey lines in (B) and (C) represent deconvoluted multi-peak fittings (unpaired two-tailed t-test, significance level P: *** ≤ 0.001).
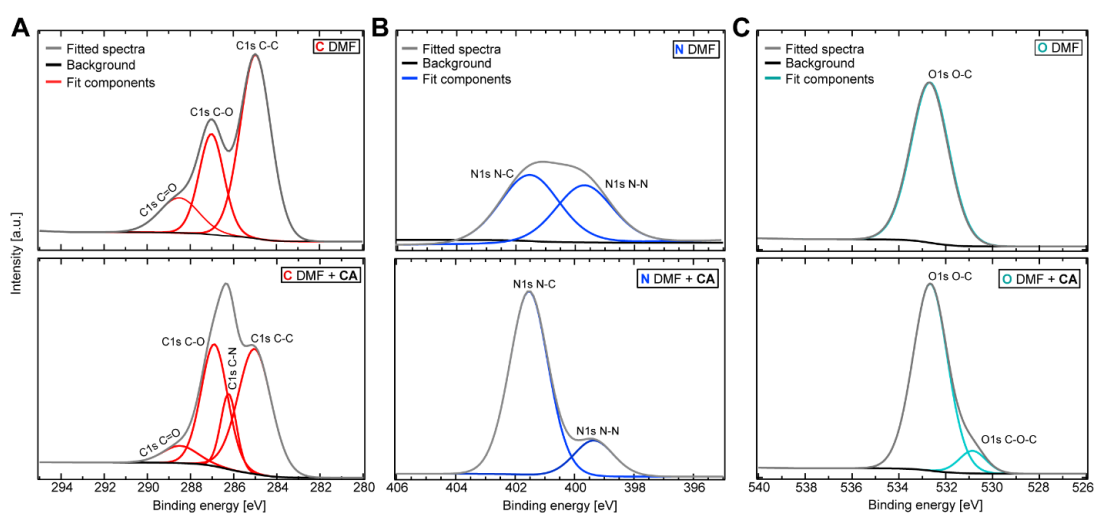
Fig. 4.5 X-ray photoelectron spectroscopy (XPS) analysis of CA-functionalized of GO in DMF. (A) Carbon, (B) nitrogen, and (C) oxygen XPS spectra before (top panels) and after (bottom panels) addition of CA. A carbon-nitrogen binding exhibited the best fit for the XPS spectrum with CA treatment (bottom panels), reflecting a 2-fold increase in peak intensity. Grey lines represent deconvoluted multi-peak fittings.

4.2.4 Passivation and labelling of the GO-CA complex

The CA-coated GO flakes were next functionalized with heterobifunctional NHS-PEG-COOH (MW 3,400) using the same process as for SiO_2. To evaluate the surface coverage and the ability of this coating to suppress nonspecific adhesion of DNA, we again used fluorescence microscopy. Since GO exhibits strong auto-fluorescence in the green over the red emission wavelength (Fig. 4.6), in agreement with previous reports, we chose the fluorophore Atto647N as a label [24] for 40 base-pair receptor ssDNA.
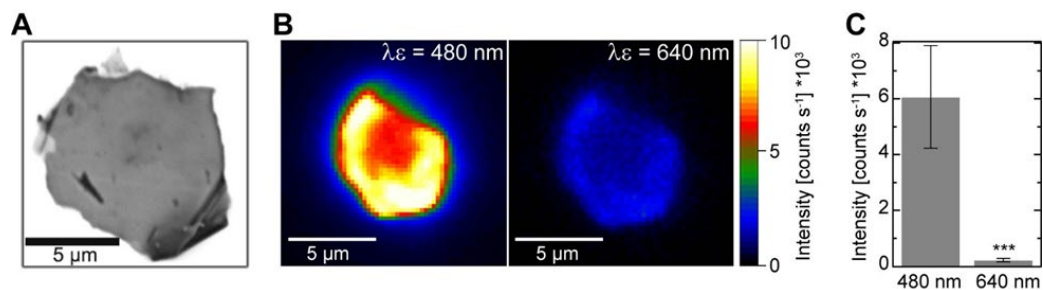
Fig. 4.6. Autofluorescence of exfoliated graphene oxide (GO). (A) SEM micrograph of exfoliated GO tested for autofluorescence. (B) Example false-colour fluorescence images of a GO flake show different autofluorescence intensity in the green and red emission wavelength regimes (lem = 550/50 and 690/20 nm, respectively). (C) Quantified fluorescence intensity of GO areas at different wavelengths exhibit significantly lower autofluorescence in the red wavelength regime (unpaired two-tailed t-test, significance level P: *** ≤ 0.001).

The amino-labelled ssDNA (Fig. 4.7A) was then covalently coupled to the PEG via standard peptide binding. Upon addition of Att647N-labeled ssDNA of the same sequence we observed a low fluorescence intensity (Fig. 4.7A, control), indicating that PEG coverage was sufficiently high so that it suppressed nonspecific DNA adhesion. In contrast, the addition of complementary target ssDNA exhibited, on average, a 10-fold higher fluorescence intensity (Fig. 4.7A, target), indicating successful coupling of the receptor ssDNA to the PEG molecules. To analyse the coverage of the PEG coating added to GO, CA-PEG-ssDNA functionalized GO flakes were allowed to hybridize to complementary target ssDNA labelled with Atto647N. False-colour fluorescence microscopy of these samples (Fig. 4.7B) exhibited dense and homogeneous coating. The slight irregularities can originate from defects in GO material integrity or from the edges of GO sheets of different dimensions stacking upon each another. Complementary photobleaching experiments (Fig. 4.7B) revealed spatially uniform bleaching of DNA-coupled fluorophores (Fig. 4.7B, t = 6 min) with a 2-fold decrease in intensity (Fig. 4.7C).

4
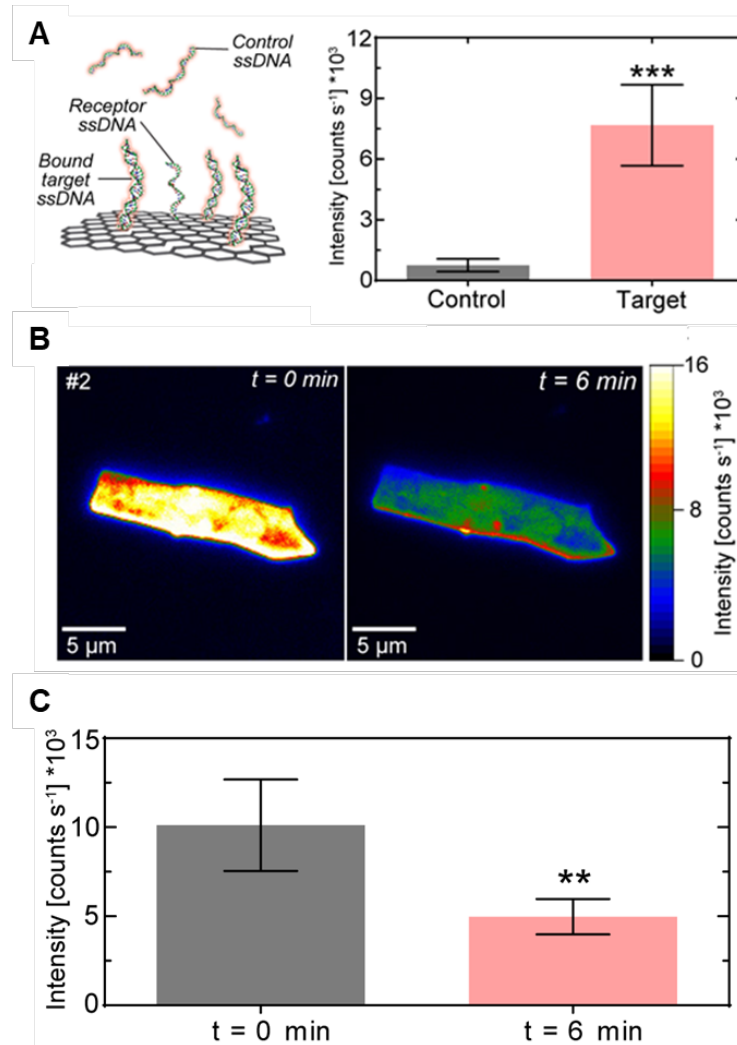
Fig. 4.7 Specific binding and nonspecific adhesion of ssDNA on functionalized GO. (A) Experiment schematics (left) and fluorescence intensity (right) of receptor ssDNA-functionalized (n = 8) GO flakes upon adding both Atto647N-labeled non-complementary (control) and complementary ssDNA (target). (B) Photobleaching experiment demonstrated uniform photobleaching of target ssDNA after t = 6 min continuous light irradiation. (C) Fluorescence intensity of n = 3 ssDNA-functionalized GO samples before and after t = 6 min of continuous light irradiation (unpaired two-tailed t-test: p: ** ≤ 0.01; *** ≤ 0.001).

4.3 Conclusion

Our study demonstrates the successful covalent functionalization of organic two-dimensional GO using a simple yet powerful methodology. We show a vast improvement in coating density and homogeneity by applying CA in comparison to alcoxysilanes (APTES) using wet chemistry. By adding PEG crosslinkers, the methodology can lead to efficient nonspecific adhesion-suppressing performance, which improves the biocompatibility required for drug carriers as well as the signal-to-noise ratio for early disease-detection biosensor platforms. Additionally, the freedom to select different functional groups at the PEG polymer terminal expands the technique to molecules which are restricted in the selection of functional groups with different covalent coupling strategies.

Furthermore, the significant enhancement of chemical robustness, biocompatibility, and reliability of functionalized GO produced via this methodology meets the requirements for GO-based biosensors and nanocomposites used for tissue printing and other organic reconstruction methodologies [25, 26]. This chemical modification can be readily extended to current applications using conductive nanoscale structures for electrochemical measurements within living tissues and cells [27].

4

4.4 Materials and Methods

4.4.1 Preparation of graphene oxide Sheets

Graphene oxide (GO) was prepared using a modified Hummers method from natural crystalline colloidal graphite (Pure graphite flakes NGS Trading & Consulting GmbH with an average flake size of 45 µm (Ma -399.5 RG)) [28]. A volume of 69 mL concentrated H_2SO_4 was added to a mixture containing 3 g of graphite flakes and 1.5 g of $NaNO_3$ and cooled to 0 °C. Afterwards, 9 g $KMnO_4$ was gently titrated while monitoring that the reaction temperature remains below 20 °C. The mixture was then heated up to 35 °C under stirring for further 30 min. A volume of 138 mL water was added slowly in small portions to produce a large exotherm, up to 98 °C, and the temperature was maintained for another 15 min. Afterwards, the sample mixture was cooled using an ice bath for 10 min. A volume of 420 mL water and 3 mL H_2O_2 were added producing another exotherm. After air cooling, the mixture was filtered with a polyester fibre filter (Millipore, 0.22 micron pore size, Merck Millipore, Germany). The filtrate was centrifuged at 4,000 rpm for 4 h and the supernatant was discarded. The remaining material was washed several times, each with 200 mL ddH_2O, 200 mL of 30 % (v/v) HCl and 200 mL of ethanol. After each washing step, the mixture was again filtered and centrifuged as described above. The resulting material was coagulated with 200 mL of ether and filtered using a PTFE membrane (Merck Millipore, Germany) with a pore size of 0.45 µm. The resulting solid was vacuum-dried (14 psi) for 12 h at room temperature.

4.4.2 Scanning electron microscopy of graphene oxide

Graphene oxide (GO) preparation was evaluated using scanning electron microscopy (SEM) imaging. GO material was imaged with a desktop SEM (FEI NovaNanoSEM) on prime Si + SiO_2 (dry) wafers (Microchemicals). Imaging was performed using 5-15 kV voltage and 5 mm working distance.

4.4.3 X-ray photoelectron spectroscopy of functionalized graphene oxide

X-ray photoelectron (XPS) spectra were acquired on a ThermoFisher K-Alpha system using Al Kα radiation with a photon energy of 1,486.7 eV. The samples were loaded into the spectrometer without further purification, immobilized onto a copper tape (Plano GmbH, G3397). High resolution XPS spectra were acquired using a spot size of 400 μm, 50 eV pass energy, and 0.1 step size, conducting 40 scans (for carbon and nitrogen spectra). Charge neutralization was applied to minimize the effect of surface charges. All peaks were calibrated referencing the carbon 1s peak to 285 eV. The additional high-resolution spectra were used to determine the binding states by deconvolution the peaks using Thermo Avantage (v 5.952). After smart-type background subtraction, the peaks were fitted using Gaussian-Lorentzian product functions. The atomic ratios were then quantitatively determined by correcting the peak areas with the TPP-2M sensitivity factor and were compared with their corresponding peaks to verify the fits.

4.4.4 Raman Spectrometry and Atomic Force Microscopy (AFM)

Graphite and graphene oxide samples were deposited by drop-casting on Si + SiO$_2$ wafers. Confocal Raman spectrometry (inVia Reflex, Renishaw, UK) was performed using a diode laser at 785 nm at 10% laser intensity with a signal integration time of 10 s, coupled to a low-noise CCD detector (Centrus, Renishaw, UK). Sample positioning was executed manually, and 5 to 10 flakes were measured for each experimental condition. Spectrum analysis was performed with R-Studio.

AFM topography images (AFM Dimension FastScan, Brucker) were acquired in air in tapping mode using silicon nitride cantilevers (FASTSCAN-A, Bruker) with a nominal spring constant of ~18 N/m and resonance frequency of ~800 kHz. The dimensions and height of the GO flakes (5 measurements/flake) were extracted and analysed with ImageJ.

4.4.5 Graphene oxide surface functionalization

The applied surface functionalization procedure within this study (Fig. 4.1C) is based on a modified method described previously [13, 28]. Here, GO flakes were incubated for 12 h in anhydrous DMSO (dimethyl sulfoxide, Sigma, USA) or DMF (dimethyl fumarate, Sigma Aldrich) containing 5 M 2-Aminoethanol hydrochloride (Sigma Aldrich, USA), after initial sonication for 30 min. Afterwards, 100 µL of the GO-solution was deposited onto a cleaned borosilicate cover glass support, washed with DMSO (or DMF, respectively), twice with ethanol, and finally rinsed with ddH$_2$O. After drying in a nitrogen flow, the physiosorbed GO-sheets were PEGylated by depositing 2 mM of heterobifunctional NHS-PEG-COOH (MW 3,400, LaysanBio, USA) in anhydrous chloroform containing 0.5 % (v/v) triethylamine for 1 h at room temperature. After the PEGylation process, the supports were washed five times with ddH$_2$O and dried in a nitrogen flow. For covalent ssDNA attachment, amino-labeled 40b ssDNA oligonucleotides (5´-NH2-CCACTCG TGACGCATTCACCTCAGC AGCACTCCTC CTCGG-3´, Purimex, Germany) were conjugated to the PEG-coated substrates via peptide binding using a concentration of 10 pmol/µL ssDNA in 100 mM MES (2-(N-morpholino)ethanesulfonic acid, Sigma, USA) buffer (pH 4.7) containing 50 mM EDC (1-Ethyl-3-(3-dimethylaminopropyl)-carbodiimide, Sigma, USA) for 1 h reaction time at room temperature. After ssDNA immobilization, the support was washed twice with water, 10 min in a 10 mM KCl (potassium chloride, Sigma, USA) solution to eliminate unspecific adhered oligonucleotides, and finally 5 min in ddH$_2$O followed by drying in a nitrogen flow. The hybridization of the Atto647N-labeled complementary 40b ssDNA strand (5´-Atto647N-CCGAGGAGGAGTGCTG CTGAGGTGAATGCGTCACGAGTGG-3´, Purimex, Germany) was carried out for 1 h at room temperature in TRIS-HCl buffer (20 mM TRIS, 100 mM NaCl, pH 8.4). Afterwards, the samples were washed in 2×SSC (saline-sodium citrate, pH 8.4) buffer for 5 min, and in 0.01×SSC buffer for another 5 min to remove non-specific adsorbed ssDNA.

4.4.6 Fluorescence microscopy

The successful immobilization of ssDNA was performed using an epifluorescence microscope (Nikon TE2000U, USA) with a Peltier-cooled back-illuminated EMCCD camera (IXON3, 1024×1024 pixels, Andor, Ireland) for sensitive fluorescence detection in combination with a 100× oil-immersion objective (CFI APO TIRF, NA. 1.45, Nikon, USA). Fluorophore excitation was achieved by a 150 W mercury-vapor lamp combined with specific filter set (F41-008 AHF, Tübingen, Germany) according to the excitation and emission wavelength of the Att647N fluorophore (640 nm, 690/20 nm, respectively) used in this study. For each sample, the fluorescence intensity (in photon counts/s) was measured by taking the average over five areas consisting of 10×10 pixels. Each experiment was repeated three times to test the reproducibility and for statistical analysis.

4.4.7 Quantitative evaluation of non-specific DNA adhesion-suppressing coatings performance

Wide field fluorescence microscopy was used to evaluate the degree of non-specific adhesion of DNA on the different chemical surface compositions. For these experiments, 24×24 mm borosilicate cover glasses (Menzel GmbH, Germany) were cleaned by incubating them in a 5% (v/v) aqueous Hellmanex II-solution (Hellma GmbH, Germany) and sonicated for 20 min at 40°C. Afterwards, the glasses were washed thoroughly with ddH$_2$O and sonicated again for 20 min in ddH$_2$O. The glass supports were then dried in a nitrogen flow and the generation of hydroxyl-groups was carried out applying oxygen plasma (SE80, Barrel Asher Plasma Technology, USA) for 15 min (50 sccm O$_2$, 200 W, 100 mTorr). For the different surface coating, APTES ((3-Aminoproply)triethoxysilane, Sigma Aldrich, USA) and colamine (β-hydroxyethylamine, Sigma Aldrich, USA) were attached covalently to the treated cover glasses. The silanization with APTES was performed by adding 10 µl APTES between two cleaned cover glasses followed by an incubation for 15 min at 75°C. The silanized glass

supports were then rinsed thoroughly with ethanol, ddH$_2$O, and dried in a nitrogen flow. The colamine coating and PEGylation were performed in the same way as described for GO functionalization.

The non-specific adhesion of ssDNA on these coated glass slides with APTES, colamine, and the additional PEG crosslinker used in this study was tested via fluorescently labelled DNA. To do so, 1 µM of Atto647N-labeled 40b ssDNA in TRIS/HCl buffer 20 mM TRIS, 100 mM NaCl, pH 8.4) was added to the differently coated surfaces and incubated for 1 h at room temperature in a humid atmosphere. Afterwards, the surfaces were washed three times with TRIS/HCl buffer for 5 min each, shortly with ddH$_2$O, and dried gently in a nitrogen flow before fluorescence microscopy.

4.5 References

[1] D. P. Singh, C. E. Herrera, B. Singh, S. Singh, R. K. Singh and R. Kumar, Mater. Sci. Eng. C, 2018, 86, 173–197.

[2] K. S. Novoselov, A. K. Geim, S. V Morozov, D. Jiang, Y. Zhang, S. V Dubonos, I. V Grigorieva and A. A. Firsov, Science, 2004, 306, 666–9.

[3] P. Bollella, G. Fusco, C. Tortolini, G. Sanzò, G. Favero, L. Gorton and R. Antiochia, Biosens. Bioelectron., 2017, 89, 152–166.

[4] C. Zhang, L. Wang, T. Zhai, X. Wang, Y. Dan and L.-S. Turng, J. Mech. Behav. Biomed. Mater., 2016, 53, 403–413.

[5] E. Masoudipour, S. Kashanian, N. Maleki, A. Karamyan and K. Omidfar, Drug Dev. Ind. Pharm., 2018, 44, 99–108.

[6] F. Yin, K. Hu, Y. Chen, M. Yu, D. Wang, Q. Wang, K.-T. Yong, F. Lu, Y. Liang and Z. Li, Theranostics, 2017, 7, 1133–1148.

[7] W. Raza and S. B. Krupanidhi, ACS Appl. Mater. Interfaces, 2018, 10, 25285–25294.

[8] A. M. Díez-Pascual and A. L. Díez-Vicente, ACS Appl. Mater. Interfaces, 2016, 8, 17902–17914.

[9] J. Peña-Bahamonde, H. N. Nguyen, S. K. Fanourakis and D. F. Rodrigues, J. Nanobiotechnology, 2018, 16, 75.

[10] L. Nicu and T. Leichle, J. Appl. Phys., 2008, 104, 111101 (16 pp.).

[11] J. H. Park, G. Von Maltzahn, L. Zhang, A. M. Derfus, D. Simberg, T. J. Harris, E. Ruoslahti, S. N. Bhatia and M. J. Sailor, Small, 2009, 5, 694–700.

[12] I. Dudek, M. Skoda, A. Jarosz and D. Szukiewicz, Arch. Immunol. Ther. Exp. (Warsz)., 2016, 64, 195–215.

[13] R. Janissen, P. K. Sahoo, C. A. Santos, A. M. da Silva, A. A. G. von Zuben, D. E. P. Souto, A. D. T. Costa, P. Celedon, N. I. T. Zanchin, D. B. Almeida, D. S. Oliveira, L. T. Kubota, C. L. Cesar, A. P. de Souza and M. A. Cotta, Nano Lett., 2017, 17, 5938–5949.

[14] N. Luo, J. K. Weber, S. Wang, B. Luan, H. Yue, X. Xi, J. Du, Z. Yang, W. Wei, R. Zhou and G. Ma, Nat. Commun., 2017, 8, 14537.

[15] J.-L. Han, X. Xia, Y. Tao, H. Yun, Y.-N. Hou, C.-W. Zhao, Q. Luo, H.-Y. Cheng and A.-J. Wang, Water Res., 2016, 102, 619–628.

[16] K. Xiong, Q. Fan, T. Wu, H. Shi, L. Chen and M. Yan, Mater. Sci. Eng. C, 2017, 81, 386–392.

[17] R. Konnerth, C. Cervetti, A. Narita, X. Feng, K. Müllen, A. Hoyer, M. Burghard, K. Kern, M. Dressel and L. Bogani, Nanoscale, 2015, 7, 12807–12811.

[18] E. Metwalli, D. Haines, O. Becker, S. Conzone and C. G. Pantano, J. Colloid Interface Sci., 2006, 298, 825–831.

[19] F. Zhang, K. Sautter, A. M. Larsen, D. A. Findley, R. C. Davis, H. Samha and M. R. Linford, Langmuir, 2010, 26, 14648–14654.

[20] T. Naz, A. Afzal, H. M. Siddiqi, J. Akhtar, A. Habib, M. Banski and A. Podhorodecki, Appl. Nanosci., 2015, 5, 425–433.

[21] E. Stern, R. Wagner, F. J. Sigworth, R. Breaker, T. M. Fahmy and M. A. Reed, Nano Lett., 2007, 7, 3405–3409.

[22] J. William S. Hummers and R. E. Offeman, J. Am. Chem. Soc, 1958, 80, 1339.

[23] H. J. Kim, S.-M. Lee, Y.-S. Oh, Y.-H. Yang, Y. S. Lim, D. H. Yoon, C. Lee, J.-Y. Kim and R. S. Ruoff, Sci. Rep., 2015, 4, 5176.

[24] J. Shang, L. Ma, J. Li, W. Ai, T. Yu and G. G. Gurzadyan, Sci. Rep., 2012, 2, 792.

[25] N. Gao, T. Gao, X. Yang, X. Dai, W. Zhou, A. Zhang and C. M. Lieber, Proc. Natl. Acad. Sci., 2016, 113, 14633–14638.

[26] J. C. Boga, S. P. Miguel, D. de Melo-Diogo, A. G. Mendonça, R. O. Louro and I. J. Correia, Colloids Surfaces B Biointerfaces, 2018, 165, 207–218.

[27] P. B. Kruskal, Z. Jiang, T. Gao and C. M. Lieber, Neuron, 2015, 86, 21–24.

[28] W. J. Hummers and R. E. Offeman, J. Am. Chem. Soc., 1958, 80(6), 1339.

[29] R. Janissen, L. Oberbarnscheidt and F. Oesterhelt, Colloids and surfaces. B: Biointerfaces, 2009, 71(2), 200-207.

4

5

End-to-end mission design for microbial in-situ resource utilization activities as preparation for a Moon village

Benjamin A.E. Lehner*, Jonathan Schlechten, Andrea Filosa, Alberto Canals Pou, Daniele G. Mazzotta, Francesco Spina, Leo Teeney, Jessica Snyder, Saffira Tjorn, Anne S. Meyer, Stan J.J. Brouns, Aidan Cowley, Lynn J. Rothschild

In-situ resource utilization (ISRU) is increasingly featured as an element of human long-term exploration and settlement missions to the Lunar surface. In this study, all requirements to test a biological approach for ISRU are validated, and an end-to-end mission architecture is proposed. The general mission consists of a lander with a fully autonomous bioreactor able to process Lunar regolith and extract elemental iron and silicon. The elemental iron or silicon could either be stored or directly utilized to generate construction material. To maximize the success rate of this mission, potential landing sites for future missions are studied, and technical details are analysed. This design might not only be one step further towards an international Moon village but may also enable similar missions to ultimately colonize Mars and further explore our solar system.

5.1 Introduction

Multiple efforts are now under way to enable sustainable exploration beyond the ISS and LEO. Space agencies are embracing exploration with commercial and international partners in order to return to the Lunar surface, and in doing so, bring back new knowledge and potentially resources, and open new opportunities for innovation. In this context, new technological concept demonstrations are increasingly sought for surface missions and payloads. In particular, activities that can potentially enable sustainable exploration for missions on the surface for lengths up to and surpassing 40 days, are being considered. In this chapter, we present a novel mission design which leverages modern advances and understanding in synthetic biology to realize an ISRU focused concept that could become an exploration enabling architecture, as well as enabling valuable scientific investigations pertaining to the Lunar environment.

5.1.1 Mission objectives & benefits

Developing the capability to use local planetary resources is critical for future sustainable long-duration missions on the Lunar and Martian surface. The mission here described proposes a novel ISRU biology-based method, which would permit the extraction of metals and gases from Lunar regolith, helping to reduce the cost of human missions [1]. While a primary role of ISRU for a Lunar Outpost would be the production of oxygen [2], accessing Lunar metals is needed for the development of a Lunar infrastructure, and supply from Earth would be mass and thus cost prohibitive [3]. The production of metals and gases from this mission will not enable full independence of Earth supplies, but it would prove the potential of biological ISRU and reduce the resources that are brought from Earth [4].

The objectives of this mission concept are:

a) Test a life-support system designed for the bacteria working in an encapsuled Lunar environment.

b) Demonstrate the ability to process Lunar regolith and extract elemental iron, silicon and more by landing a fully autonomous bioreactor on the Lunar surface. The extracted material could be used as raw material, e.g. for manufacturing using 3D printing technology.

c) Prove the capability of storing gases (H_2, O_2, CO_2, CH_4) generated by the bacteria during the metabolic process. Over time, this arrangement could store significant amounts of gas-by-products, useful for a permanent human outpost.

d) Test the toxicity of Lunar dust, low-gravity and the high-radiation environment on simple organisms.

c) Extend the International Space Station (ISS) cooperation model, allowing international partners to develop systems/subsystems of the rover and bioreactor.

d) Increasing the number of complex biomolecules on the Moon to enable future food supply (The availability for certain biomolecules (carbon, nitrogen-containing) is key to enable sustainable food supply *in situ*) [5].

5.2.2 Assumptions

Several major assumptions were made in the conceptual design of the mission architecture and are listed below:

(1) The mission is assumed to advance the objectives of, and take place within, the overall framework of the Global Exploration Roadmap [6]. Taken as part of a broader effort, the mission would have a higher chance of success, would build key resource utilization knowledge prior to human exploration, and leverage the presence of other capabilities being developed as part of the global exploration roadmap (GER).

(2) The mission will be a collaboration between several ISECG members with different contributions.

(3) The mission will be a technology development and demonstration mission to advance capabilities required for further incremental, sustainable robotic and human-robotic exploration.

(3) The bioreactor system will have the capacity of being fully autonomous.
(4) Public or private launch vehicles capable of carrying the proposed payload space agencies or private companies will be available by the timeframe of the mission.

5.1.3 Similar mission architectures

NASA, ESA, and other space agencies have for long exposed the importance of ISRU to reduce the cost of the missions. Upcoming missions include robotic capabilities to acquire and process local resources:

- ESA drills and science instruments on Roscosmos's Luna 27 (PROSPECT) will demonstrate the thermochemical extraction of water from Lunar regolith [6].

- Selected to fly on NASA's Mars 2020 mission, MOXIE (Mars Oxygen ISRU Experiment) is a payload that will produce oxygen from the Martian atmosphere using solid oxide electrolysis (SOXE) [7].

- Instruments aboard the lander and rover from the ISRO's Chandrayaan-2 mission will collect data on the Moon's thin envelope of plasma [8].

- As part of the recently canceled Prospector Mission, a rover would have excavated volatiles such as hydrogen, oxygen, and water from the Moon [9].

- Other missions include biological experiments to perform on the Lunar surface: the Chang'e 4 Chinese mission executed in 2018 delivered a lander to the far side of the Moon carrying, among other instruments and experiments, a container with potatoes, *Arabidopsis thaliana* seeds and silkworm eggs. Together, the plants and silkworms are expected to create a simple ecosystem [10, 11].
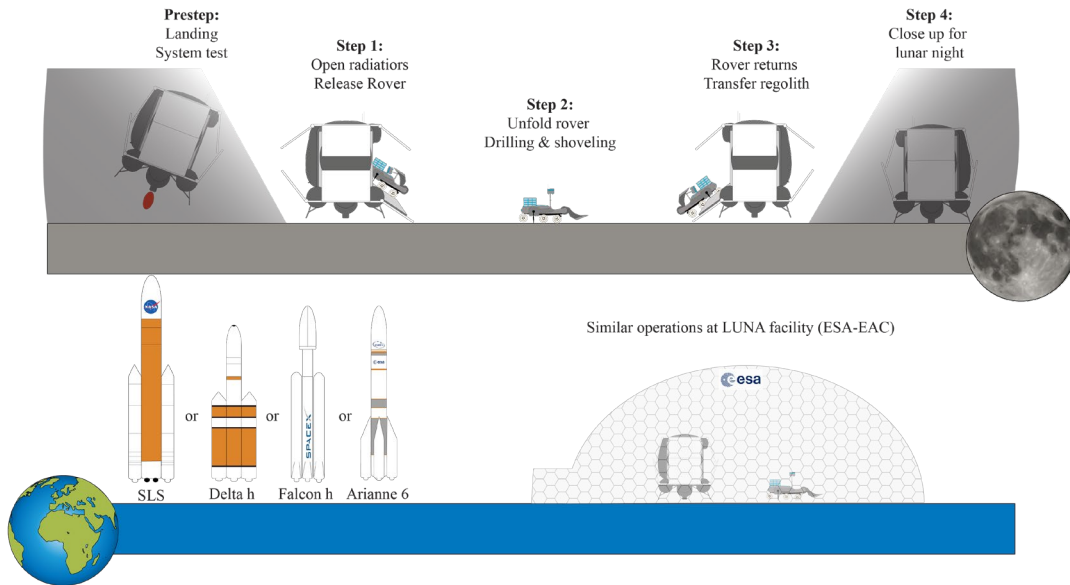
Fig. 5.1 Overview of the mission architecture. A heavy launcher (SLS, Arianne 6, Delta IV heavy or Falcon heavy) will be used to transport the lander to the Lunar surface. After the landing and an initial system test, during dawn its rover will be released, unfolded and start to collect Lunar regolith. The rover returns the samples to the lander/bioreactor and several biological tests can be performed. Throughout Lunar night the rover will stay in the lander and start after the night again with step 1. A similar experiment is performed at the LUNA facility at the European Astronaut Centre. This enables direct comparison of the cellular growth.

Also, other methods have been studied to evaluate their potential to produce oxygen and metal from Lunar resources to support human exploration of space.

For example, the electrolysis of molten Lunar regolith, also termed Magma process, requires an electrolytic cell where the regolith is molten, and in which a potential is applied such that oxygen evolves at the anode and metal deposits at the cathode [12].

The electrolysis of solid Lunar regolith approach, which derived from the FFC-Cambridge process for the electro-deoxidation of metals and metal oxides [13]. Additionally, there are numerous mission architectures proposed in scientific literature [14, 15].

5.2 The general mission architecture

5.2.1 Overview

The mission architecture, laid out in this section, is intended to fit within the sustainability principles of the global exploration roadmap (GER) including affordability and partnerships, exploration benefit, and capability evolution [6]. A partnership between different nations is proposed to increase affordability and provide opportunities for different partners to contribute in their areas of interest and expertise. ISRU technologies which will be of use in future space exploration missions are demonstrated, and advancements in the technology would be available for terrestrial uses such as on-demand pharmaceutical production.

The mission consists of two main systems to be landed on the Lunar surface together; a landing vehicle containing a bioreactor and all necessary support subsystems, and a robotic rover capable of autonomous and teleoperations. The rover will be capable of collecting and depositing regolith into the bioreactor to perform the main mission objectives and will perform operations throughout the Lunar day. During the Lunar night, the rover will be housed inside the landing vehicle for protection.

The major stages of the mission are as follows:

1) Landing of the reactor and gatherer-rover, initial system commissioning.

2) Regolith collection operations begin – the rover will gather Lunar regolith with a surface drill and with a shovel (collection of regolith with smaller particle sizes is targeted as it is more easily processed by the bacteria).

3) Biological experiments are performed in the bioreactor (e.g. material extraction).

4) Repetition of mission stages 2 and 3.

Throughout the mission, the repetition of regolith collection and material extraction will allow different cell systems to be tested with a variety of

microorganisms as well as cell-cultures, to maximize science output and test different approaches. Regolith from different areas of interest could be collected for analysis. Direct comparisons will also be made with terrestrial analog experimentation, for example, experiments performed at the LUNA facility of the European Space Agency [16].

5.3.2 Landing Site

In order to find a suitable site for a settlement, many parameters have to be taken into account. These parameters can generally be separated into three categories: (1) Operational conditions; (2) Availability of natural resources; (3) Features of scientific interest.

Historically, the operational conditions were always prioritized as the selection of the site was primarily constrained by technical factors. In 1959, the Project Horizon study [17] determined that, given the constraints related to the environment, the communication systems and the energy requirements for the rockets, the site should not be located further than 20° from the optical center of the Moon. During the Apollo program, Lunar topography was also taken into account for the selection of a landing site [18] as a smooth terrain is critical for landing operations.

In the near future, more powerful launchers such as the SLS and the Falcon Heavy as well as relay satellites[19] will make it possible for a Lunar base to be located virtually anywhere on the Moon's surface. The latest technologies in the domain of autonomous landing and hazard detection [20] will also make sites with rougher terrain accessible.

For this mission, the priority is set on operational factors. In this context, one of the biggest constraints is power production. Therefore, we consider sites located at the poles, where particular topographic features combined with orbital mechanics allow good illumination conditions for long periods of time. These areas are also characterized by relatively stable temperature conditions, which may be critical to the mission operations. The same region was chosen by NASA for its Lunar outpost reference design [21].

A particularly interesting possibility is the summit of the Malapert mountain, close to the south pole it has been estimated that this site receives sunlight for 93% of the Lunar year [22]. Due to its elevation of about 4700 meters above the Lunar reference radius [23], this location also allows for a line of sight communication with Earth, possibly a second base on the rim of the Shackleton crater and many regions of scientific interest around the South Pole. Features of scientific interest are also located in the direct vicinity of Malapert mountain. A crater located at the south of the peak is considered a possible "cold trap" [24]. A portion of the south pole Lunar map was evaluated regarding a suitable area for mission operations and landing. (Fig. 5.2A). An important factor was the average slopes and distances in this area to allow for a smooth movement of the rover.

The area chosen for mission operation is characterized by an average slope of about 12° (Fig. 5.2B). This approximated value is obtained by modeling the region as a geometrical plane passing through points A, B, L (Fig. 5.2A). The region close to the point C shows a flatter terrain and is more suitable for lander operation (Fig. 5.2B). Point C is also close to the summit of Malapert mountain, reaching better illumination condition, and avoiding shadows generated by surrounding reliefs. Nevertheless, the area around point C is characterized by a rough terrain and several impact craters that can be easily explored and avoided by rover operations but can be disastrous for the landing. As a result, even if point C remains a good candidate as a landing site, point L is preferred in this mission since it supposed that illumination conditions are not very different with respect to point C.

Point	Coordinates
A	85.8° S, 0.0°E
B	85.8° S, 3.4° E
C	86.0° S, 3.4° E
D	86.0° S, 0.0° E
L	85.9° S, 1.7° E

Path	Distance	Average Slope
AB	7250 m	5°
BC	5130 m	8°
CD	6970 m	-3°
DA	5130 m	-12°
AC	8570 m	9°
BD	8870 m	4°
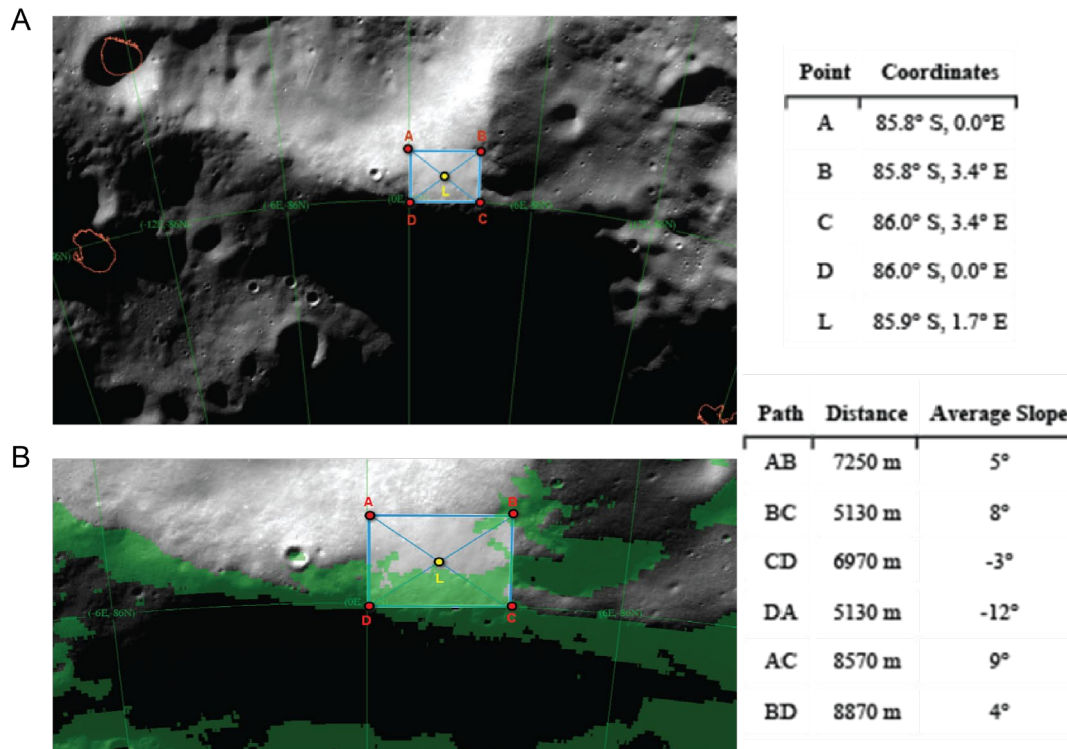
Fig. 5.2 Landing site analysis. (A) Position of the landing site (point L), and approximative area of operations (square ABCD). Coordinates, distances and average slopes in between the field of operation are displayed on the right. (B) The marked areas (green) indicate terrain slope values below 10 degrees. [http://bit.ly/2PE69Ru, quickmap.lroc.asu.edu]

5.3 Bioreactor/Lander

5.3.1 Lander design

The approximate lander dimensions are 5 metric tons (+ rocket fuel for landing), 4.5 m wide and 6 m high. Based on these dimensions, a heavy lifter would be needed to transport this reactor to the Moon [25-28]. A main part of the reactor is its resupply tanks and radioisotope thermal generator (RTG) power source to ensure continuous operations for years (Fig. 5.3A). All tanks would be equipped with an external valve allowing them for refilling if needed [29].

5
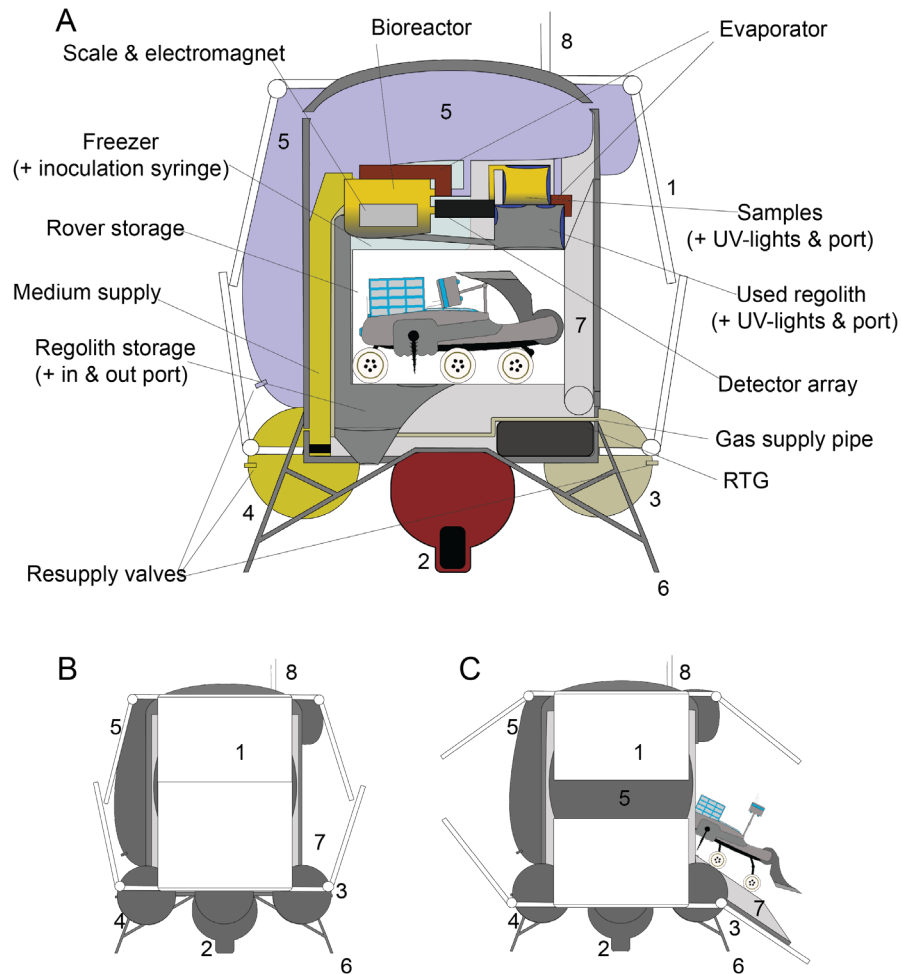
Fig. 5.3 Overview of the lander with its external structures: heat radiators (1), landing engine (2), gas tank (3), medium tank (4), water tank (5), landing legs (6), rover ramp (7), and communication antenna (8). (A) Central cut of the lander showing the main internal structures to resupply and run the bioreactor as well as store the rover throughout space-travel and Lunar nights. (B) External structures of the lander in its closed position (left) with the radiators (1) attached to the body and the ramp (7) still closed as well as in its open position (7) (right) with the radiators (1) spread out and the rover being released.

5.3.2 Tanks

The main tank (top and mid of the reactor) is filled with sterilized water (Fig. 5.3 (5)) which has several functions. Passively it will be used as a radiation shield against cosmic rays and a heat reservoir throughout the Lunar night. For the latter function, heat coils connected to the RTG are

used to keep the water above its freezing point and to store heat there before the night starts. Water used in the bioreactor will be transported back into the tank via evaporation after each growth experiment. The main loss of water per iteration will be caused by the liquid used during the microbial growth. An optional design would store the water in separate hydrogen and oxygen tanks and use a fuel cell to produce water and energy on demand (not shown here).

The tanks at the lower part of the reactor are filled with growth medium (Fig. 5.3 (4)), a gas mixture (Fig. 5.3 (3)) and rocket fuel (Fig. 5.3 (2)). The growth medium is in the form of a compressed, sterilized powder and it will be premixed with water while being pushed into the bioreactor. The gas (mainly O_2, N_2) is used to mix the reactor liquid (bubble reactor) continuously [29].

Assuming a delta-v of 1870 m/s and a mass of 5 tons, approximately 4300 kg of fuel will be needed for the initial landing. Five spherical tanks with a volume of one m^3 each are providing the necessary space for this fuel. The emptied fuel tanks will be reused after the landing to store excess gas produced throughout the experiments.

5.3.3 Bioreactor

The central piece of equipment is the 5 L bioreactor coupled to the scientific instruments. All supply valves and ports are installed in redundancy to ensure proper function of the system. This reactor is filled up in several steps (Fig. 5.4):

I. Lunar regolith gathered by the rover is transported into the reactor with an Archimedean screw mounted in a 45° angle;

II. Water and medium are premixed and used to fill up the reactor;

III. The gas flow is initiated to achieve improved mixing;

IV. A syringe is used to inoculate the bioreactor with the organism of interest (stored in a freezer);

V.   Start of the actual experiment: Every hour the optical density at 650 nm ($O.D._{650}$) and total cell counts are observed (see chapter 3.3). The tested material is stored in an extra area and regularly sterilized with UV radiation. The experiment runs between 12 and 48 hours at a constant temperature depending on the scientific or operational question. A scale, centrifuge, ChemCam [30] and electromagnet can be used for further analysis or extraction. The gas is reused for the entire experiment duration;

VI.   UV lamps will be used to sterilize the bioreactor and terminate the processes. Two additional optical density and cell count measurements should verify this termination;

VII. The temperature in the reactor is increased, and the gases are evacuated and measured;

VIII. Water will be evaporated and fed back into the water tanks. The solid material (cells, rest of the medium and regolith) will be transported in a storage compartment and further sterilization processes are initiated. The compartment has an airlock to remove material from the storage and transport it outside;

IX.   The whole system will be sterilized again and is ready for a new experiment. If a different type of regolith is used (other area or different drilling depth), all regolith storage chambers must be emptied;
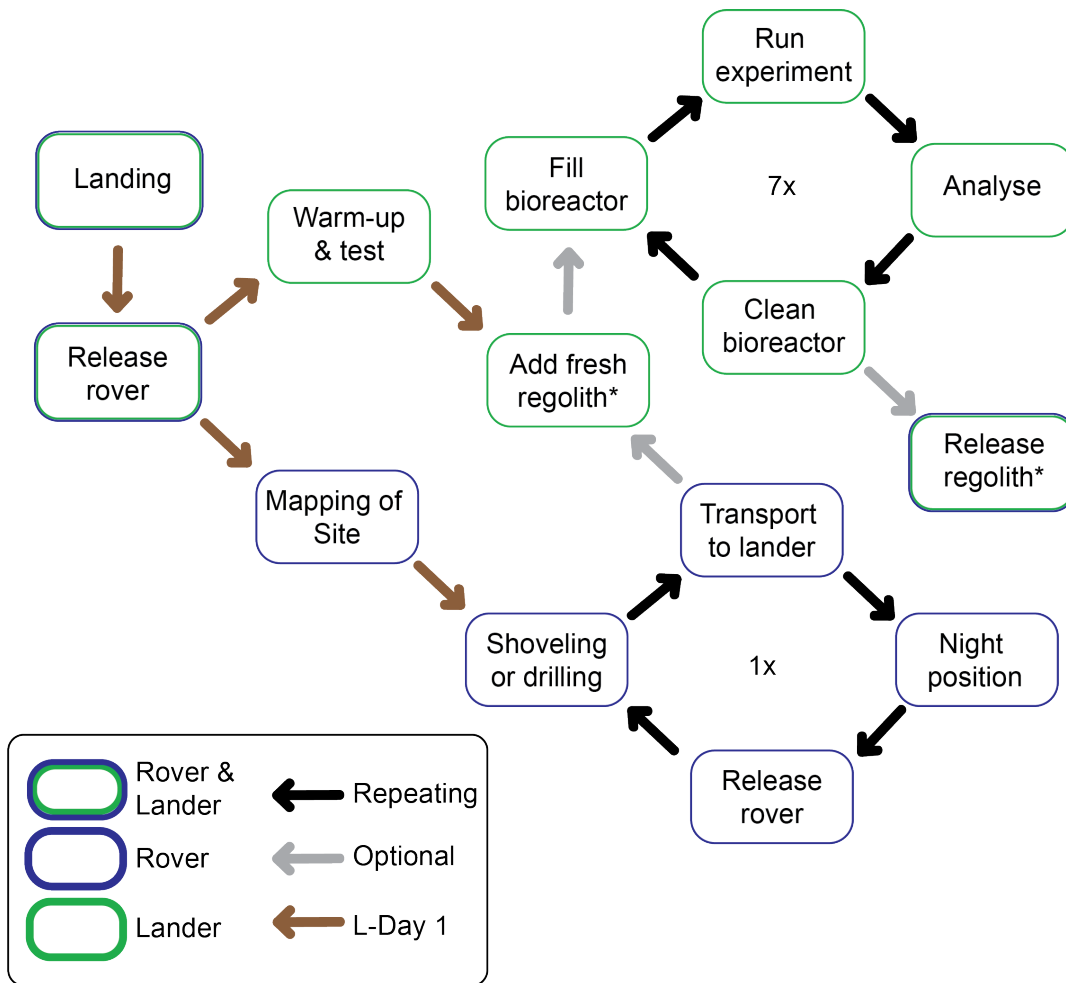
Fig. 5.4 Overview of the rover and lander operations. Arrows in light brown indicate operations only done on the start of a Lunar day. Grey arrows are optional operations depending on the exact experiment, and black ones show repeating processes. The rover has normally only one iteration per Lunar day/night cycle, while the bioreactor can have up to 7 iterations. (*) All regolith stored and used in the bioreactor can be released to allow testing of different locations and drilling depths.

5.3.4 Additional systems

The lander has four landing legs similar to the Apollo missions [31] and eight radiators (two each side) to get rid of excess heat during Lunar day and shield it during Lunar night. The rover storage area is used for initial transport of the rover, safeguarding the rover throughout Lunar night and transfer regolith from and to the rover. Antennas are used to enable

communication between the rover and the lander as well as to transfer data to the Earth.

5.3.5 Extraction process

The rover supplies the lander with regolith to be mixed with bacteria, water, and growth medium. The modified bacteria can extract or alter certain elements from the regolith (e.g., iron, silicon, gases). The extracted materials will be stored in an additional tank and can be accessed via an airlock. The produced gas will be stored in the empty fuel tanks. Growth medium can only be used once, but water can be evaporated and reused for multiple runs. Bacterial kinetics and total number are continuously observed by optical density. After the extraction process a small number of bacteria can be stored for an additional batch, while the rest of the reactor is decontaminated and the materials (iron, silicon, gases) are extracted.

5.3.6 Silicon extraction

Silicon is an important building block for all types of electronic devices and in particular energy devices (solar cells, fuel cells). Genetic modifications of *E. coli* (Top 10) allowed the bacterium to express the enzyme silicatein-alpha at the surface. This enzyme is used by marine demosponges to build layers of poly-silicate, a complex of SiO_4^{2-} salts bound to a protein [32, 33]. The TU Delft iGEM team 2016 visualized this formation of a poly-silicate using a sodium silicate solution and fluorescence microscopy [34]. We applied the same methodology to test the capability of this genetically modified *E. coli* to extract silicon from the Lunar regolith simulant EAC-1. The cells were grown with a Lunar simulant concentration of 4 g/L in Luria-Bertani (LB) medium under continuous shaking (250 rpm) and 37 °C. The optical density (O.D.$_{600}$) value was observed hourly in a photo spectrometer, and 0,1 mM IPTG solution was added after the O.D.$_{600}$ reached 0.4 (an indication that the bacteria are in exponential growth and are having a maximal metabolic activity). After 4 hours of incubation, the

cells were stained with 2 µg/mL rhodamine 123 for 10 minutes and kept in the dark to prevent bleaching. Six washing steps (exchanging the whole volume with phosphate buffer saline (PBS)) were performed and the cells were resuspended in PBS. An inverted fluorescent microscope (Nikon Eclipse Ti inverted microscope with A1R confocal module) was used to visualize the stained and unstained cells (Fig. 5.5). Quantification of the cells (n > 19) was automated using a macro implemented in the image analyzing software *Fiji.* The quantification of stained cells is selected based on intensity, size and shape. The findings indicate that the genetically modified bacteria can utilize the alkoxy silicates present in the Lunar regolith simulant to encapsulate themselves with a poly-silicate layer (Fig. 5.5). In the presence of 4 g/L regolith simulant (EAC-1), 13.4 ± 0.9% of the genetically modified bacteria and 1.3 ± 0.2% of the wild-type bacteria are covered with a poly-silicate layer. Without regolith simulant, 6.7 ± 1.3% of the genetically modified bacteria show silicate expression (errors are standard errors of the mean). The extraction of silicon covered bacteria from the rest of the regolith is still problematic because they share the mechanochemical properties of regolith particles. An agglomeration of the silicon rich surfaces based on a changing pH value could resolve this issue but has still to be optimized.

5
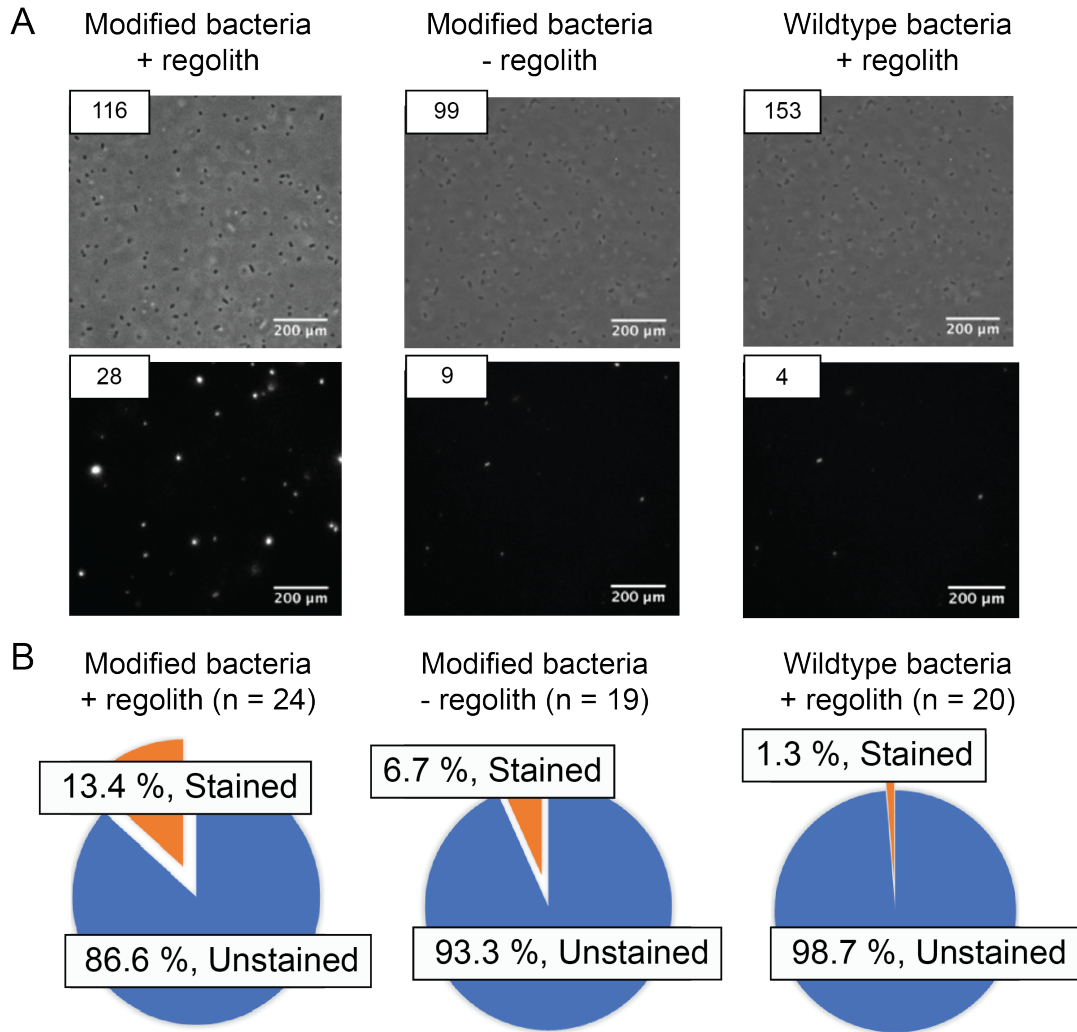
Fig. 5.5 Fluorescence microscopy showed the modified *E. coli* to be able to form a silicone layer from Lunar regolith simulant (EAC-1) around its cell membrane. (A) Exemplary light microscopy (top) and fluorescence pictures (bottom) of rhodamine 123 stained *E. coli* cells. The left two refer to the genetically modified, the right one to the wild-type *E. coli*. The numbers in the left top show the total number of visible cells. (B) Quantitative analysis of the modified and unmodified with rhodamine 123 stained bacteria.

5.3.7 Iron extraction

Stable structures on Earth rely strongly on iron and its derivatives. Construction material, as well as replacement parts on another planetary surface, can be built from iron as well. The main disadvantage of iron derivatives, the high mass, plays a minor role in in-space applications on low-gravity planets and Moons, where their weight is lower. Iron is also very abundant in Lunar and even more in Martian regolith; it is a very bioactive element.

Our collaborators at Newcastle university engineered an additional *E. coli* strain (DH5α) to incorporate a high amount of iron ions from a liquid solution. Magnetic forces (neodymium magnets) separate the iron stored within the bacteria from the rest of the material (Fig. 5.6A). The bacterial growth was performed aerobically in a 30 °C incubator under constant shaking with 250 rpm. Colony forming units and $O.D._{650}$ measurements were done every 3 hours. For the magnetic extraction, 3 mL were pipetted onto a cover glass slide and washed with 5 mL distilled water. The extracted amount of regolith increased significantly from 3.34 ± 0.58 mg to 7.25 ± 1.83 mg after a 48-hour treatment with bacteria but showed no significant difference in the no-bacteria control (3.34 ± 1.15 mg at 0h and 4.57 ± 1.13 mg after 40h) (ANOVA Turkey PostHoc test: p_{T0-T48}: 0.600, p_{E0-E48}: 0.004, p_{E0-T0}: 0.999, $p_{E48-T48}$: 0.010; errors are standard deviation).

A

B
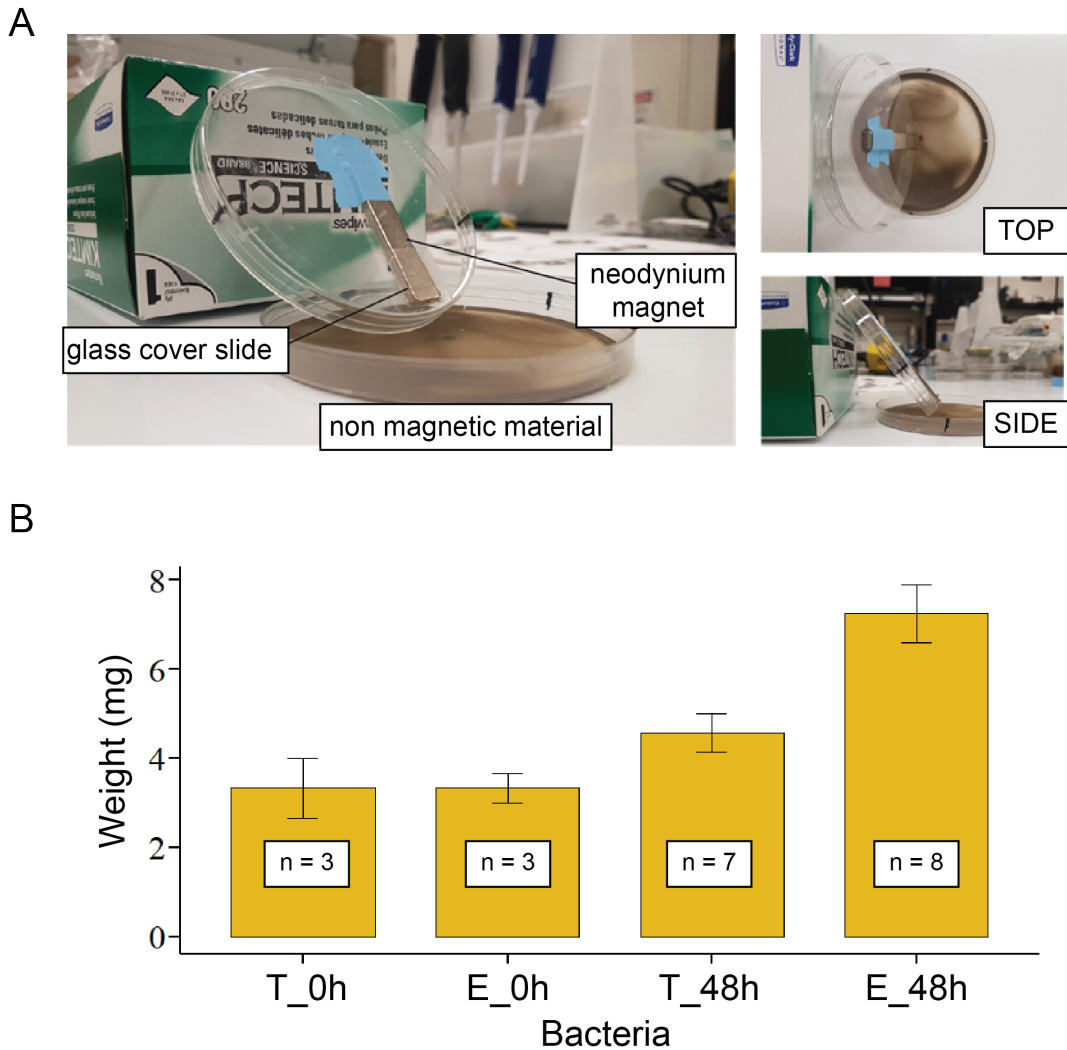
Fig 5.6 Bacterial modification of the regolith allows for an improved magnetic extraction rate than without treatment (A) Laboratory set-up for the magnetic extraction. The neodymium magnet was mounted in a 55° angle, which allows for extraction of only strongly-magnetically attracted material (the rest will be washed away). The material is deposited on cover glass slides to quantify and compare the total amount of extracted material. (B) Weight measurements of the magnetically extracted regolith. Bacterial samples: E...*E .coli* and non-bacterial controls: T...TSB were performed after 0h and 48 h (Errors are the standard deviation of the mean).

5.3.8 Gas and other extraction types

During any metabolically active process, bacteria produce technical useful gases (CH_4, CO_2, O_2 H_2), which are collected into the emptied fuel tanks. The amount of these gases is measured after each iteration (see section 5.3.3). Over time, this arrangement stores a significant amount of gas-by-products useful for rocket fuel, life-support system, and similar applications. Bacteria can also be used for other types of extraction. It was shown that they could help to recycle copper from electrical circuits [35], leach the ores for further mechanical methodologies [36] and even produce biofuel or medicine [37] on demand. One bioreactor can host several different operational modes and might be used for a variety of different purposes depending on the current need. Resupply missions of the bioreactor can supply not only fresh medium and water but also different organisms.

5.3.9 Scientific analysis

The understanding of the interaction between biological systems and the Lunar environment will be critical for any future Moon mission. It is possible (Vis-spectroscopy and flow-cytometry) for an autonomous system to observe the health of microorganisms or even cell cultures. The proposed Vis-spectroscopy uses a laser with a wavelength of 600 nm to measure the optical density (O.D.) of four 5 μL samples every two hours. The result shows the number of grown bacteria in the sample and can be used to understand the kinetics of the microorganisms grown. The flow-cytometer complements this measurement with the total number of life/dead stained cells in four additional 5 μL samples at the same time points [38].

Gas sensors (O_2, CH_4, CO_2, H_2) will observe the composition and production of gases with different organisms and environmental conditions. An electromagnet together with a scale will specifically help in understanding how much iron/magnetic material can be extracted from different Lunar

soil samples with and without treatment. The integrated ChemCam enables, meanwhile, the measurement and visualization of ore compositions and the comparison of ores before and after bacterial treatment as well as in different ground depths and areas (shovel & drill) [30, 39].

The same bioreactor will work simultaneously in LUNA [16] a Lunar training hall currently under construction at the European Astronaut Centre (EAC) on Earth. The terrestrial bioreactor allows for a better understanding of the biotoxicity caused by Lunar radiation and Lunar dust as well as an exact comparison of Lunar regolith with its simulant. This mission will acquire critical data to understand the effect of Lunar dust particles and the high radiation field on the Moon towards biological systems. Furthermore, it will measure the production yields of microorganisms under Lunar conditions in comparison to conditions on Earth.

5.3.10 Potential problems regarding bacterial growth in a closed containment on the Moon

Mutation rate: After the extraction, the same bacterial culture can be used to re-inoculate a new batch. This process is limited due to the, in comparison to Earth, increased mutation rate caused by higher cosmic radiation and the nanoparticles expected in Lunar regolith. If the yield or health of the bacterial culture declines or the extraction methodology is switched, fresh bacteria can be used from a frozen stock (-80°C). The frozen stock is due to the inactive metabolism of the bacteria barely affected by the radiation.

There is a low chance of having a strong disturbing mutation during a single batch if the process takes longer than a few days. However, the core extraction processes suggested here are done in 48 hours which makes this issue neglectable. **Biofilm formation:** Bacteria tend to form biofilms which can cloak tubing and cause other mechanochemical and biochemical issues leading to a decreased yield or even failure of our bioreactor.

Several studies showed the enhanced biofilm formation of different organisms under stress [40] and in the case of low gravitational fields [41]. Our reactor design induces a turbulent flow to counteract this effect, but a pretest performed with the exact reactor on Earth will be necessary to better understand the potential problems for the mission due to biofilm formation. **Slicing of cells:** Lunar regolith is composed of sharp-edged nanoparticles which can be a severe threat for the microorganisms [42]. A better understanding of the interaction of Moon dust with cellular systems will be of utmost importance for any human endeavor to the Moon. Our here proposed mission can be seen as a first scientific testbed for this interaction.

5.4 The gather rover

5.4.1 Rover design

The main task of the rover is to gather and transport Lunar regolith to the bioreactor. It consists of a front shovel and a vertical drill to gather the material from different positions as well as a chamber for internal storage. Next to the drill are transfer-ports to drop the material into the lander. The rover's navigation is partly telerobotic and partly autonomous, its navigation is mainly done via optical cameras including infrared sensors at the head camera and the back camera. The solar cells are mounted on a rotating frame to always face the sun (Fig. 5.7A). The rover dimension will be very similar to resource prospector (approximately 300 kg, 1.4 m x 1.4 m x 2 m) [9] and the rover will reuse originally for resource prospector designed instrumentation. The main difference is the design with six legs instead of four which allows for redundancy and driving in terrains with higher slopes.
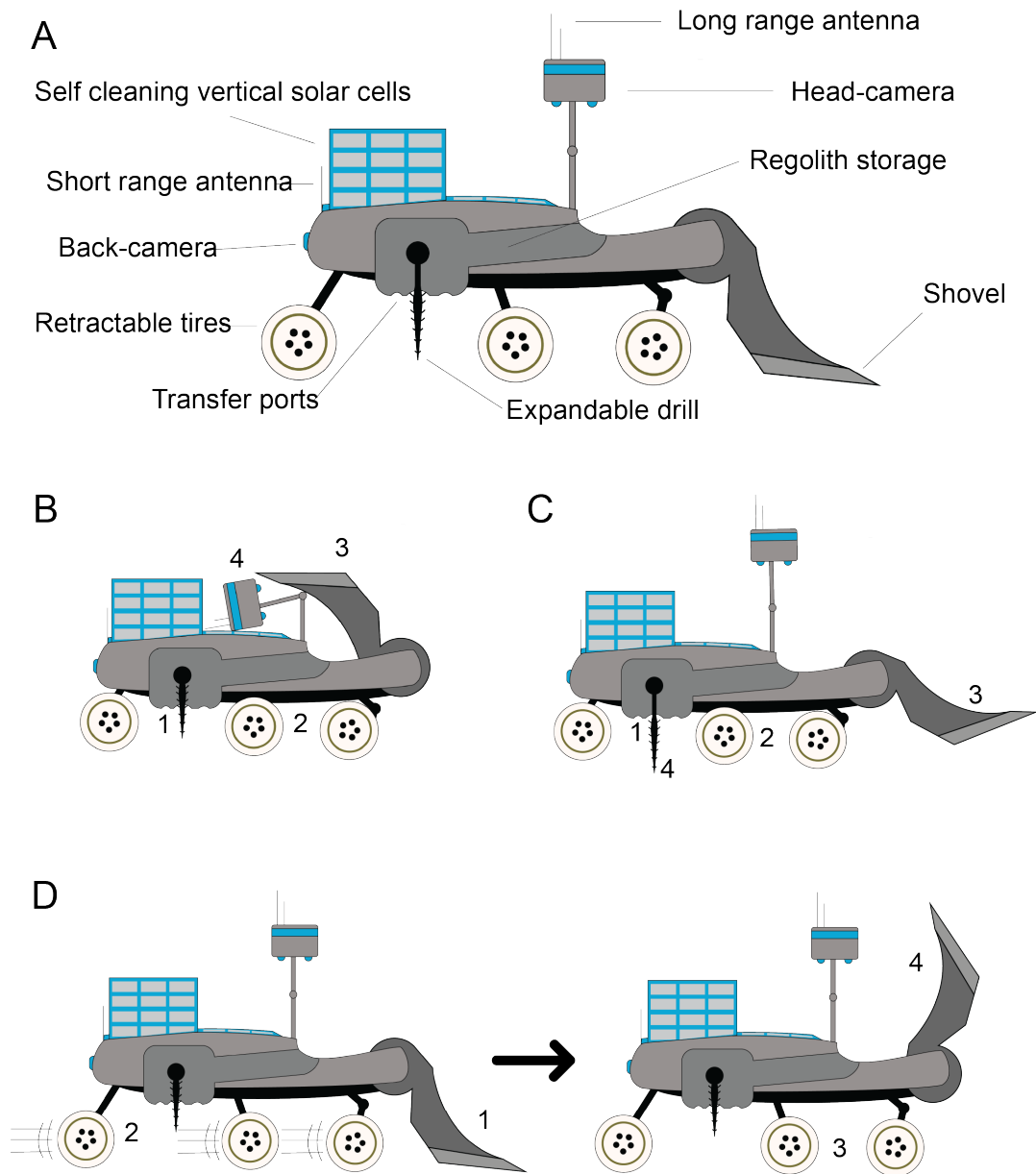
Fig. 5.7 Rover positions and tasks. (A) Overview of the instruments and parts of the rover. (B) Rover in transport-position with open transfer ports (1), retracted legs (2), folded shovel (3) and head camera (4). C: Rover in drilling position with closed transfer ports (1) retracted legs (2), half-folded shovel (3) and active drill (4). D: Rover in shovelling position starting with a grounded shovel (1) and a forward movement (2). Ending in a standing position (3) with a raised shovel (4)

5.4.2 Transport & night position

The rover is designed to be transported inside the lander and is, therefore, foldable (Fig 5.7B). In this position, the legs are retracted which leads to a blocking of the tires. The drill is retracted not to scratch the lander nor to get damaged throughout the journey. The head camera is inactive and folded together with the shovel. In this position, the rover is unlikely to slide around and can withstand the launch and landing (with additional support). After the landing, the legs are partly extended to enable the rover to move out of the lander. The back camera can be used for this maneuver.

To avoid damaged electronics and to add new Lunar regolith to the lander the rover approaches its indoor position during Lunar nights as well. The rover is moved backward towards the gateway to enter the lander, the head camera is deactivated and folded together with the shovel. The legs are retracted to the minimal moving position, and the rover is navigated autonomously into the lander. Its regolith transfer ports are opened, and the gathered material drops into the lander's storage.

5.4.3 Drilling & shovel position

The head camera is used to move the rover to a previously screened and for drilling suitable location. As soon as the drill is aligned the rover retracts its legs, blocks the tires and the shovel gets half-way folded. After the rover is in a stable position, the drill starts spinning and is extended to engage the ground. The material is moved throughout the drilling process into the storage area of the rover. The so-gathered material will be transported back to the lander (Fig. 5.7C). The drill concept is mainly to acquire regolith and, therefore, the drilling depth is limited to a few centimeters. The head camera is used to navigate the rover to a for shovelling suitable location. The shovel is moved downwards to touch the ground, and the rover is moved slowly forward to gather material in the shovel. The shovel is raised to lift the material into the storage chamber.

5

5.5 Power supply and thermal shielding

The design of the electrical power supply unit for the mission is crucially dependent on diverse mission drivers; the most important of which is the selection of the landing site. In fact, a selection of a permanently illuminated site would probably push the selection of the power source as mainly solar. However, given the assumptions made in 5.2.2, it is best to strive for a design which is as robust and flexible as possible, that is, which could be re-adapted for different environments. So, the main power source would be based on radioisotope thermoelectric generator (RTG) technology, with additional support coming from solar panels for the rover.

The main components of the system are:

a) The bioreactor: running at 30-40 °C with short peaks of 100 °C.

b) The water tank: high volume of water, which shall be reused. Heating the bioreactor to 100 degrees and refilling the tank after each cycle.

c) Pumps: Airflow pumps (< 5 L) to move the gas through the reactor into the inflatable module and waterflow pumps (< 5 L) to move the liquid to the reactor and mix it with the medium and regolith.

d) Extraction mechanism: magnetic or weight dependent extraction (i.e. electromagnet), and/or small centrifuge.

e) Freezer for the different cell types and scientific/analytical instruments

f) Communications system.

g) UV lamps for sterilization.

h) Controlling electronics: automatic controlling of the valves, pumps, heating system with potential human interference from Earth.

5.5.1 Lander/Bioreactor power supply

The power requirement for the bioreactor and attached systems is estimated at 2.4 kW (including all previously mentioned systems). The power will be mainly supplied via RTG technology. In fact, as per section 5.1.2, even on a semi-permanent illuminated area, it is too optimistic to rely on solar panels only, with a rover that would move and potentially cover the solar panels partially with Lunar dust. To survive the Lunar night, the need for a high-efficiency thermoelectric transformation technology appears to be still crucial. Currently, the most realistic method is to utilize the RTG, which is based on the Seebeck principle to transform the heat energy into the electric energy. When generating electric power, the RTG can also supply great heat energy to regulate temperature. Generally, Pu-238 is used as the RTG source [43].

However, to strive for a more sustainable form of energy supply in the framework of a Lunar habitat, the potential solar panels will be designed to satisfy most of the power requirements. Since the Earth-Moon system is in heliocentric orbit, they share a similar solar constant of about 1.36 kW/m^2 [44]. Given the current Solar panel technology and considering solar cells arrangement, an efficiency of about 30% can be considered, which gives roughly 330 W/m^2 on state-of-the-art spacecraft. So, producing 2.4 kW of power would require approximately 7.2 m^2 of solar panels with a weight of 40 kg. Considering the environmental conditions of a Lunar south sole landing site [see section 5.2.2], the focus shall be set on Sun illumination angles: while Azimuth varies 0-360 degrees in a Moon cycle (~27 days), elevation angles features much lower variations during the same period. The power system design features the selection of a "Power Generation Area", which shall be as flat as possible to allow for Sun tracking during the entire mission lifetime and avoid possible panel shadings due to orography. The solar panel will track the Sun only in Azimuth, neglecting the small variations in Elevation.

In order to support this sun tracking feature, the base of the panel will be equipped with a DC motor [45], the rotation speed needed is affordable for state of the art components (360 deg in 27 days is a very slow rotation). The solar panels will gather sun power and store it in rechargeable batteries; this power will be used for Lunar nights and in case of contingency (e.g. low/no power available due to malfunctions, dust on cells, etc.).

5.5.2 *Rover power supply*

The rover will be designed to be a smart machine, with the purpose in mind to achieve a mobility item that is agile, rapid, and simple. It is crucial to reduce at most its complexity and its weight: the rover will be powered by a combination of solar panel and rechargeable batteries, which are used to maintain system survivability during times without sun illumination (e.g. shadowed areas). In such cases, the rover will activate a series of heaters to allow it to resist to the low temperatures and possibly move back to an illuminated area.

5.6 Discussion & conclusion

Space agencies all over the globe are proposing return missions to the Moon and the Lunar vicinity with the ultimate goal of human exploration and habitation. Our understanding of how biological systems interact with the very hostile environmental factors on the Lunar surface is insufficient and only based on the short visits during the Apollo missions. This data, however, is essential to understand the behavior of life support systems, biomining or bioleaching approaches and of course the health risks posed to astronauts throughout a prolonged visit. The mission proposed here will act as a test-bed to gather such data and findings for a variety of biological systems and will also act as a technical demonstration in a closed environment on the Lunar surface.

The summit of the Malapert mountain, near the South Pole, was considered the best location for this mission. Being designed as precursor research, it makes sense for this mission to take place on a site that is already evaluated for a future settlement. With its exceptional environment in term of illumination, temperature, and topography, this site does not only provide excellent conditions for operations, but it is also close to numerous areas of scientific interest.

The rover and the lander are well-equipped to test critical ISRU processes such as the transport of Lunar regolith from the surface into a closed environment, shoveling as well as low-depth drilling operations to gather regolith, controlled liquid as well as gas-flow under low gravity and the mixture of telerobotic with autonomous operations of the rover.

Direct extraction and production experiments done via microbial processes will build on prior tests with regolith simulant here on Earth. There are several proposals to use microorganisms as nano-factories and to produce, for example, on-demand medication, extract materials from the regolith or produce gases for life-support systems and as rocket fuel.

Our successful tests to bind silicon from Lunar regolith simulant onto our genetically engineered bacteria showed that 13.4 ± 0.9% of the total cells are covered with silicon in comparison to 1.3 ± 0.2% in control with no modified bacteria. Currently, we are investigating methods to extract the silicon-covered bacteria from the rest of the regolith. Also, experiments with magnetic iron extraction were improved from 3.34 ± 0.58 mg to 7.25 ± 1.83 mg after a 48-hour treatment with bacteria using a differently modified *E. coli*.

The experimental set-up and scientific instrumentation allow for an analysis of the biotoxicity caused by Lunar dust and Lunar regolith particles in general. The simultaneous running experiment in LUNA at the EAC in Cologne will directly compare these results to bacteria grown with regolith simulant. We expect to have higher toxicity due to the sharp edges and small sizes occurring in Lunar regolith. Experiments with eukaryotic cells or

even cell cultures might enable even further insights into their toxicity on humans.

Different approaches for the power supply of the system and its communication with Earth are discussed. To our knowledge, this is the first mission architecture designing a bioreactor for the Lunar environment and enabling biological tests in the sectors life-support-systems, biotoxicity, biological ISRU and technological demonstrations. These are critical for a human presence on another planet or Moon.

5.7 References

[1] M. Anand, I.A. Crawford, M. Balat-Pichelin, M. Abanades, W. van Westrenen, R. Peraudeau, R. Jaumann, W. Seboldt, A brief review of chemical and mineralogical resources on the Moon and likely initial in situ resource utilization (ISRU) applications, Planetary and Space Science 74(1) (2012) 42-48.

[2] W.E. Larson, G.B. Sanders, K.R. Sacksteder, NASA's In-Situ Resource Utilization Project: Current Accomplishments and Exciting Future Plans American Institute of Aeronautics and Astronautics

[3] C. Schwandt, J. A. Hamilton, D. Fray, I. Crawford, The production of oxygen and metal from Lunar regolith, 2012.

[4] L.J. Rothschild, Synthetic biology meets bioprinting: enabling technologies for humans on Mars (and Earth), Biochem Soc Trans 44(4) (2016) 1158-64.

[5] M. Montague, G.H.t. McArthur, C.S. Cockell, J. Held, W. Marshall, L.A. Sherman, N. Wang, W.L. Nicholson, D.R. Tarjan, J. Cumbers, The role of synthetic biology for in situ resource utilization (ISRU), Astrobiology 12(12) (2012) 1135-42.

[6] ISECG, The Global Exploration Roadmap, https://www.nasa.gov/sites/default/files/atoms/files/ger_2018_small_mobile.pdf, 2018.

[7] F.E. Meyen, M.H. Hecht, J.A. Hoffmann, Thermodynamic model of Mars Oxygen ISRU Experiment (MOXIE), Acta Astronautica 129 (2016) 82-87.

[8] P. Bagla, India plans to land near Moon's south pole, Science 359(6375) (2018) 503-504.

[9] D. Andrews, Resource Prospector (RP): A Lunar volatiles prospecting and In-Situ Resource Utilization (ISRU) demonstration mission, Briefing to IEEE Robotics and Automation Society, 2016.

[10] P. Ye, Z. Sun, H. Zhang, F. Li, An overview of the mission and technical characteristics of Change'4 Lunar Probe, Science China Technological Sciences 60(5) (2017) 658-667.

[11] K. Huang, China plans to grow potatoes in space … like Matt Damon did in The Martian, South China Morning Post, 2017.

[12] C. Schwandt, J.A. Hamilton, J.D. Fray, I.A. Crawford, W. Marshall, The production of oxygen and metal from Lunar regolith, Planetary and Space Science 74(1) (2012) 49-56.

[13] D.J. Fray, T.W. Farthing, Z. Chen, Removal of Oxygen from Metal Oxides and Solid Solutions by Electrolysis in a Fused Salt., in: W. Application (Ed.) 1999.

[14] J.O. Burns, D.A. Kring, J.B. Hopkins, S. Norris, T.J.W. Lazio, J. Kasper, A Lunar L2-Farside exploration and science mission concept with the Orion Multi-Purpose Crew Vehicle and a teleoperated lander/rover, Advances in Space Research 52(2) (2013) 306-320.

[15] B.A. Lehner, D.T. Schmieden, A.S. Meyer, A Straightforward Approach for 3D Bacterial Printing, ACS Synth Biol (2017).

[16] A. Cowley, A. Diekmann, S. Coene, V. Nash, S. Cristoforetti, Human Lunar Exploration at EAC – the LUNA analogue facility and the Spaceship EAC project, 2017.

[17] A.G. Trudeau, Project Horizon, Volume I: Summary and Supporting Considerations, United States Army, 1959.

[18] L.L. MISSION, APOLLO 11 LUNAR LANDING MISSION, (1969).

[19] M. Flanegan, J. Gal-Edd, L. Anderson, J. Warner, T. Ely, C. Lee, B. Shah, A. Vaisnys, J. Schier, NASA Lunar Communication and Navigation Architecture, SpaceOps 2008 Conference, 2008, p. 3589.

[20] S.A. Striepe, C.D. Epp, E.A. Robertson, Autonomous precision landing and hazard avoidance technology (ALHAT) project status as of May 2010, (2010).

[21] D. Stanley, S. Cook, J. Connolly, J. Hamaker, M. Ivins, W. Peterson, J. Geffre, B. Cirillo, C. McClesky, J. Hanley, NASA's exploration systems architecture study, NASA Final Report, TM-2005-214062 (2005).

[22] B.L. Sharpe, D.G. Schrunk, Malapert mountain: Gateway to the Moon, Advances in Space Research 31(11) (2003) 2467-2472.

[23] D. Schrunk, B. Sharpe, B.L. Cooper, M. Thangavelu, The Moon: Resources, future development and settlement, Springer Science & Business Media2007.

[24] J.-L. Margot, D.B. Campbell, R.F. Jurgens, M. Slade, Topography of the Lunar poles from radar interferometry: A survey of cold trap locations, Science 284(5420) (1999) 1658-1660.

[25] SpaceX, Fairing, 2013.

[26] Arianespace, ARIANE 6: The next-generation launch vehicle, 2018. http://www.arianespace.com/ariane-6/. (Accessed 08/27/18.

[27] ULA, Delta IV, 2018. https://www.ulalaunch.com/rockets/delta-iv.

[28] NASA, space launch system, 2012.

[29] R. Volger, S.J. Brouns, A. Cowley, B.A. Lehner, Bioreactor design to perform microbial mining activities on another celestial body, International Astronautic Congress Bremen, 2018.

[30] R.C. Wiens, S. Maurice, B. Barraclough, M. Saccoccio, W.C. Barkley, J.F. Bell, S. Bender, J. Bernardin, D. Blaney, J. Blank, M. Bouyé, N. Bridges, N. Bultman, P. Caïs, R.C. Clanton, B. Clark, S. Clegg, A. Cousin, D. Cremers, A. Cros, L. DeFlores, D. Delapp, R. Dingler, C. D'Uston, M. Darby Dyar, T. Elliott, D. Enemark, C. Fabre, M. Flores, O. Forni, O. Gasnault, T. Hale, C. Hays, K. Herkenhoff, E. Kan, L. Kirkland, D. Kouach, D. Landis, Y. Langevin, N. Lanza, F. LaRocca, J. Lasue, J. Latino, D. Limonadi, C. Lindensmith, C. Little, N. Mangold, G. Manhes, P. Mauchien, C. McKay, E. Miller, J. Mooney, R.V. Morris, L. Morrison, T. Nelson, H. Newsom, A. Ollila, M. Ott, L. Pares, R. Perez, F. Poitrasson, C. Provost, J.W. Reiter, T. Roberts, F. Romero, V. Sautter, S. Salazar, J.J. Simmonds, R. Stiglich, S. Storms, N. Striebig, J.-J. Thocaven, T. Trujillo, M. Ulibarri, D. Vaniman, N. Warner, R. Waterbury, R. Whitaker, J. Witt, B. Wong-Swanson, The ChemCam Instrument Suite on the Mars Science Laboratory (MSL) Rover: Body Unit and Combined System Tests, Space Science Reviews 170(1) (2012) 167-227.

[31] K. Tate, The Apollo Moon Landings: How They Worked 2014.

[32] W.E.G. Müller, M. Rothenberger, A. Boreiko, W. Tremel, A. Reiber, H.C. Schröder, Formation of siliceous spicules in the marine demosponge Suberites domuncula, Cell and Tissue Research 321(2) (2005) 285-297.
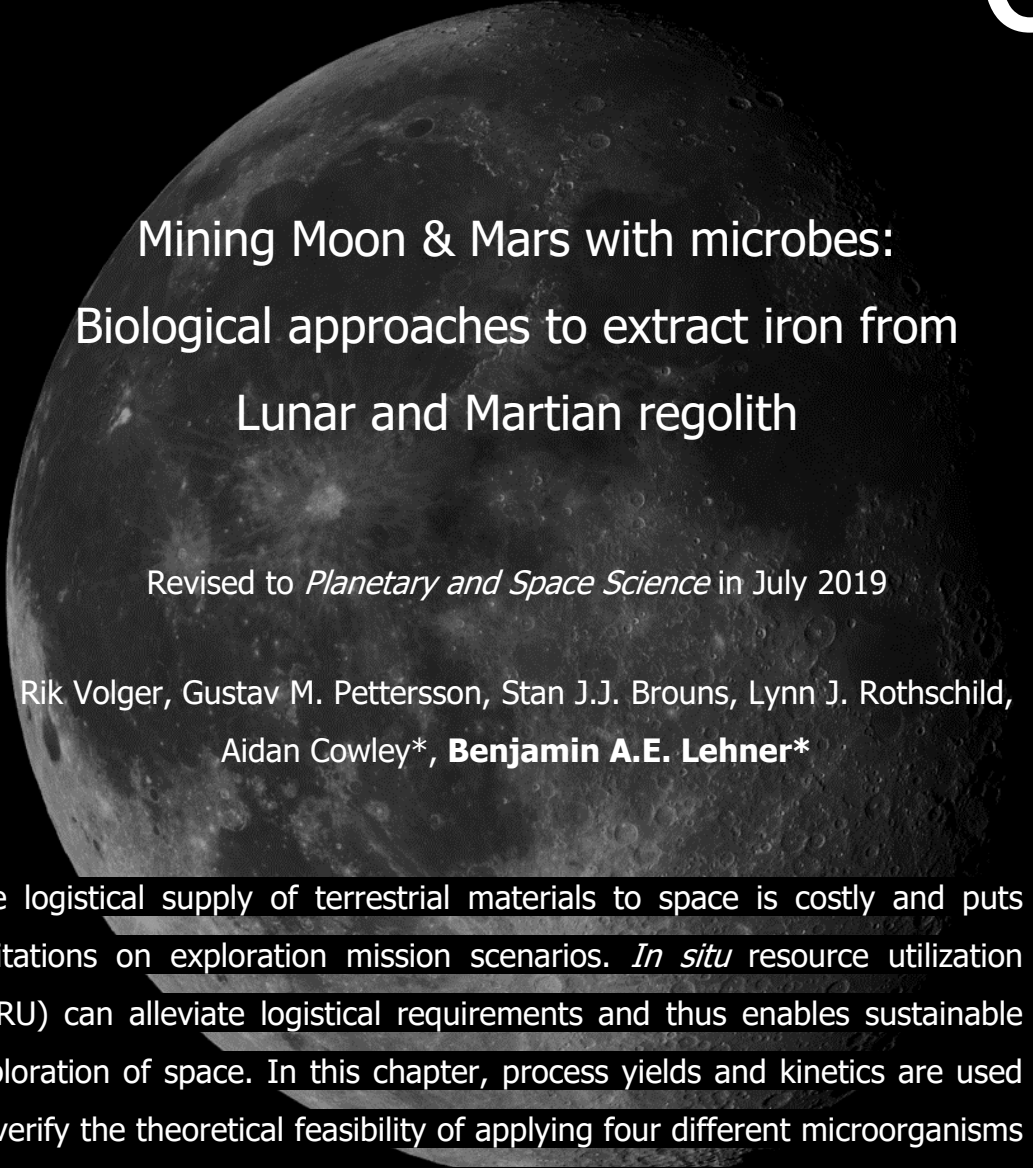
[33] W.E.G. Müller, S. Engel, X. Wang, S.E. Wolf, W. Tremel, N.L. Thakur, A. Krasko, M. Divekar, H.C. Schröder, Bioencapsulation of living bacteria (Escherichia coli) with poly(silicate) after transformation with silicatein-α gene, Biomaterials 29(7) (2008) 771-779.

[34] i.T. Delft, COATING THE CELL IN POLYSILICATE USING SILICATEIN, 2016.

[35] J. Urbina, Biomining: A Biological Approach to Recycling Elemental Components from End-Of-Life Electronics, Microbiology and Environmental Toxicology, University of California Santa Cruz, 2018.

[36] J.U. Navarrete, I.J. Cappelle, K. Schnittker, D.M. Borrok, Bioleaching of ilmenite and basalt in the presence of iron-oxidizing and iron-scavenging bacteria, International Journal of Astrobiology 12(2) (2013) 123-134.

[37] S. Herrera, Industrial biotechnology—a chance at redemption, Nature Biotechnology 22 (2004) 671.

[38] V.O. Karas, I. Westerlaken, A.S. Meyer, The DNA-Binding Protein from Starved Cells (Dps) Utilizes Dual Functions To Defend Cells against Multiple Stresses, J Bacteriol 197(19) (2015) 3206-15.

[39] R.C. Wiens, Chemistry & Camera (ChemCam), 2009. https://msl-scicorner.jpl.nasa.gov/Instruments/ChemCam/. (Accessed 08/27/18.

[40] P. Landini, Cross-talk mechanisms in biofilm formation and responses to environmental and physiological stress in Escherichia coli, Research in Microbiology 160(4) (2009) 259-266.

[41] W. Kim, F.K. Tengra, Z. Young, J. Shong, N. Marchand, H.K. Chan, R.C. Pangule, M. Parra, J.S. Dordick, J.L. Plawsky, C.H. Collins, Spaceflight Promotes Biofilm Formation by Pseudomonas aeruginosa, PLOS ONE 8(4) (2013) e62437.

[42] Y. Liu, J. Park, D. Schnare, E. Hill, A. Taylor Lawrence, Characterization of Lunar Dust for Toxicological Studies. II: Texture and Shape Characteristics, Journal of Aerospace Engineering 21(4) (2008) 272-279.

[43] N.R. Council, Radioisotope Power Systems: An Imperative for Maintaining U.S. Leadership in Space Exploration, The National Academies Press, Washington, DC, 2009.

[44] B. Khoshnevis, A. Carlson, M. Thangavelu, ISRU-BASED ROBOTIC CONSTRUCTION TECHNOLOGIES FOR LUNAR AND MARTIAN

INFRASTRUCTURES, University of Southern California, NIAC Phase II Final Report, 2017.

[45] R. Space, SEPTA® 24 Solar Array Drive Assembly Zurich, Switzerland, 2015.

5

6

Mining Moon & Mars with microbes:
Biological approaches to extract iron from
Lunar and Martian regolith

Rik Volger, Gustav M. Pettersson, Stan J.J. Brouns, Lynn J. Rothschild, Aidan Cowley*, **Benjamin A.E. Lehner***

The logistical supply of terrestrial materials to space is costly and puts limitations on exploration mission scenarios. *In situ* resource utilization (ISRU) can alleviate logistical requirements and thus enables sustainable exploration of space. In this chapter, process yields and kinetics are used to verify the theoretical feasibility of applying four different microorganisms to the extraction of iron. Based on yields alone, three of the four organisms were not investigated further for use in biological ISRU. For the remaining organism, *Shewanella oneidensis*, the survivability impact of Martian regolith simulant JSC-Mars1 and magnesium perchlorate were studied and found to be minimal. With a water recycling efficiency of 99.99% and initial regolith concentration of 300 g/L, leading to an iron concentration of approximately 44.7 g/L, a payback time of 3.3 years was found.

6.1 Introduction

The next step in human space exploration will revolve around the Moon, as a stepping stone for an eventual human presence on Mars [1]. In the context of longer stays on the Moon's surface, the supply and maintenance of a functional habitat requires the input of resources. Transport of these resources is a major cost for an extra-terrestrial base, and reducing this cost will bring us closer to realizing a sustained human presence on another celestial body [2]. In situ resource utilization (ISRU), the use of local resources for production and maintenance, can help us bring down long-term transport requirements and brings us closer to colonizing another celestial body [3]. In this chapter, to help address this challenge, we investigate the use of microorganisms for the extraction of iron from Lunar and Martian regolith.

Microorganisms as used in production processes can be described as self-reproducing modifiable nano-factories, catalysing a wide range of chemical conversions. Some branches of microbial life on earth have developed a metabolism around the use of metal oxides as electron donors or acceptors [4]. A subsection of these organisms can utilize solid metal oxides as substrate, converting them to more soluble forms, which makes them interesting for use in mining operations [5]. Such use of microorganisms on earth is widespread and is actively used in the biomining of copper, cobalt, gold, uranium and other metals [6, 7]. In the case of copper, biomining accounts for more than 20% of the yearly worldwide production [8]. These facts give a promising outlook on the application of biomining in space exploration [9]. Lab-scale experiments on the interaction between bacteria and Lunar regolith simulant confirm this expectation [10]. However, so far, no design for full-scale biomining operations in space has been presented.

Iron is one of the most utilized metals on Earth and a variety of building materials rely on it in some way. It can be hypothesized that the construction and maintenance of an extra-terrestrial base will also rely on

iron. Considering the abundance of iron in both Lunar and Martian regolith, at 5-22 wt% and 17.9 ±0.6 wt%, respectively [11, 12], this element is likely to be useful in construction-oriented ISRU. Within this chapter, we show a general setup for a biological iron extraction process, we investigate the feasibility of several candidate organisms and perform a sensitivity analysis for the payback time of the biological process. *Shewanella oneidensis* was evaluated as the most feasible organism with a payback time of about 3.3 years and its survivability in a Martian regolith simulant was studied Combined with a lander concept [13] , this provides a framework for future evaluations of biomining processes in space exploration and a basis for evaluation of other bioprocesses.

6.2 Results and Discussion

6.2.1 Biomining process

The general process of using bacteria for mining applications in space, is the dissolution and accumulation of specific resources from Lunar or Martian regolith (Fig 6.1A). The biological methodologies can be split up in two categories: (1) Accumulation of dissolved iron in concentrated form, allowing for magnetic extraction (Fig 6.1B). (2) Leaching of iron from mineral ores, bringing it in a dissolved state, allowing for precipitation of magnetic particles and ores (6.1C).

These categories could be combined to allow for the magnetic extraction of iron from a variety of ferrous mineral ores. The leaching process alone can also be connected to electrochemical manipulation of the solution to promote magnetite precipitation [31–33].
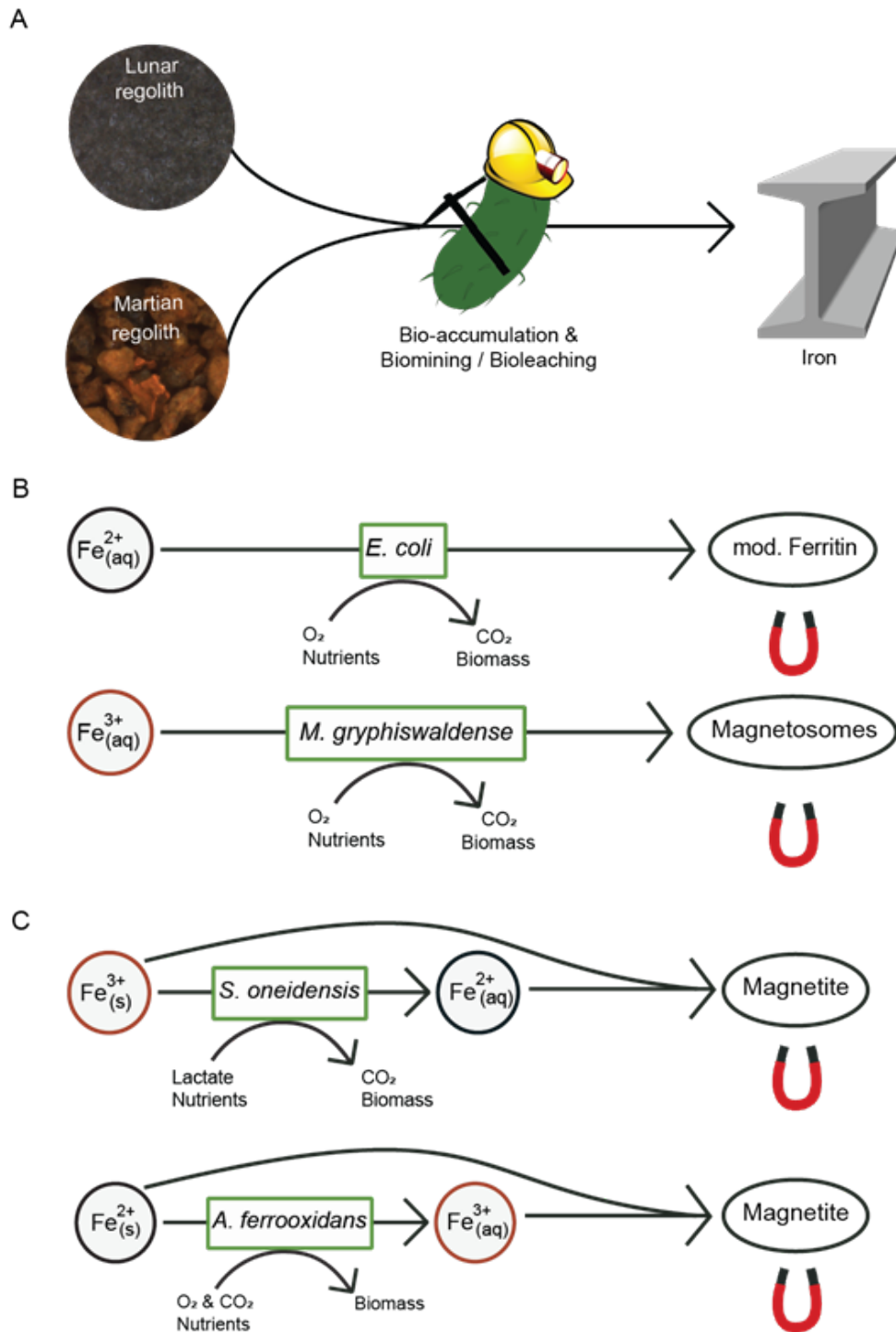
Fig. 6.1 (A) Conceptual workflow of the bacterial iron extraction. (B) Bio-accumulation processes using *E. coli* to bind aquatic Fe^{2+} in a modified Ferritin molecule, and *M. gryphiswaldense* to combine aquatic Fe^{3+} molecules in magnetosomes. (C) Biomining and Bioleaching approaches using *S.oneidensis*, to reduce in ore bound Fe^{3+} to Fe^{2+} and allow for magnetite precipitation, and *A. ferroxidans* to oxidize Fe^{2+} to Fe^{3+} and allow for magnetite precipitation.

The considered candidates for the accumulation are a genetically modified *Escherichia coli* strain and the magnetotactic wildtype bacterium *Magnetospirillum gryphiswaldense*. The constructed *E. coli* overexpresses a modified ferritin complex, has a dysfunctional iron export mechanism and an improved iron import mechanism [34]. The combination of those modifications leads to a high intracellular iron concentration.

M. gryphiswaldense accumulates iron to produce magnetosomes, intracellular vesicles filled with magnetite that form a backbone for the organism [35]. The resulting capability to swim along magnetic field lines is commonly known as magnetotactic behavior [36]. *M. gryphiswaldense* readily uses lactate as electron donor and carbon source.

For the bioleaching category, *Shewanella oneidensis* and *Acidithiobacillus ferrooxidans* were considered. *S. oneidensis* is well-known for its capability to use a wide range of electron acceptors [37], one of which is Fe^{3+}, both in aqueous and solid state [18, 22]. Fe^{3+} from mineral sources is converted into Fe^{2+}, which is both excreted in aqueous form and precipitated on the cell surface in magnetite [38, 39]. In the current work, the use of lactate as electron donor and carbon source is considered, which is then oxidized to acetate and CO_2 (Fig 6.1C). Other possible electron donors are pyruvate, formate, amino acids or N-acetylglucosamine [40, 41].

A. ferrooxidans is often used in biomining operations on earth [5]. It preferably grows in very acidic conditions (pH 1-2) and can fix both carbon and nitrogen from atmospheric sources. For the current work, nitrogen from ammonium is considered instead of atmospheric nitrogen. *A. ferrooxidans* requires oxygen as electron acceptor when it oxidizes Fe^{2+} to Fe^{3+}.

6.2.2 Nutrient consumption

The kinetics (Tab. 6.2) were used to set up mass balances, which were solved over time to the point where one of the nutrients was used up (Fig 6.2). For an ideal process, the growth is expected to resemble batch

growth, with an exponential increase in biomass concentration. In the accumulation processes by *E. coli* and *M. gryphiswaldense*, significant uptake of extracellular dissolved iron is expected. For the leaching processes by *S. oneidensis* and *A. ferrooxidans*, the iron conversion is a key part of the organism's metabolism, so growth should be accompanied by a rapid iron conversion.

The accumulation process in *E. coli* (Fig 6.2A), takes slightly over 50 hours to consume the initially provided lactate (7.2 g/L). The predicted growth profile is initially exponential, but changes into a linear profile after 15 hours. The decreasing dissolved oxygen concentration indicates that the growth is limited by the oxygen transfer rate. If the process would show otherwise favourable results, methods for an increased oxygen transfer rate could be explored to decrease process time. However, the extracellular iron concentration does not decrease notably over the course of the simulation and thus the process does not fulfil its main purpose of accumulating dissolved iron. The overexpression of the encapsulated ferritin leads to an estimated 20-50 encapsulated ferritin complexes per cell, which corresponds to an iron concentration in biomass of only 8-20 µg / g_X. This value is too low to have a significant effect on the extracellular concentration.

The model for *M. gryphiswaldense* (Fig 6.2B) predicts batch growth for the 39 hours to fully consume the initial lactate and ammonium. The decreasing level of dissolved oxygen indicates its consumption, but the oxygen transfer rate is not the limiting factor. Again, the concentration of extracellular iron does not decrease notably. *M. gryphiswaldense* reportedly accumulates iron to a concentration of 4.4 mg / g_X [17], three orders of magnitude more than the proposed *E. coli* strain. Still, this is not enough to have a substantial impact on the extracellular iron concentration.

For the bio-accumulation of iron to be a feasible approach to ISRU activities, the amount of iron accumulated in one gram of biomass should outweigh the amount of transported nutrients required to generate that

one gram of biomass. In the case of *M. gryphiswaldense* growing on lactate, it means that one gram of lean biomass should contain 2.8 grams of iron (Tab 6.1), i.e. 74% of total biomass should be iron. For *E. coli* growing on lactate, these values are 7.73 gram and 88.5%.

This strict requirement regarding how many percent of the total biomass will have to be iron is likely to become more lenient when the process is integrated with other biological systems. These systems can provide nutrients for the mining operation or make use of the by-products of the process.

The Fe^{3+} reduction by *S. oneidensis* (Fig 6.2C) takes 22 hours to reduce all the initial Fe^{3+} and doesn't follow a full exponential growth curve. The growth rate slowly decreases from 80 to 70% of the μ_{max} value in the first 20 hours, and rapidly drops further after that. The reduction of the growth rate occurs due to a decrease of both the lactate and iron concentration. The acetate concentration (not shown) will increase over the course of the process, mirroring the concentration profile of lactate. Acetate has an inhibitory effect on *S. oneidensis* [42], but the extent of that effect in anaerobic conditions has not been quantified.

The Fe^{2+} oxidation by *A. ferrooxidans* (Fig 6.2D) is by far the slowest process in the analysis and requires 500 hours to fully consume the initial iron. The slow process is mainly due to the inhibitory effect of Fe^{3+}. In the current model, no further reactions consuming dissolved Fe^{3+} or precipitation are considered, and the resulting continuous accumulation is detrimental for the growth rate of *A. ferrooxidans*. The dissolved gasses in the bottom panel show that no O_2 or CO_2 limitation is expected with the current growth rates.
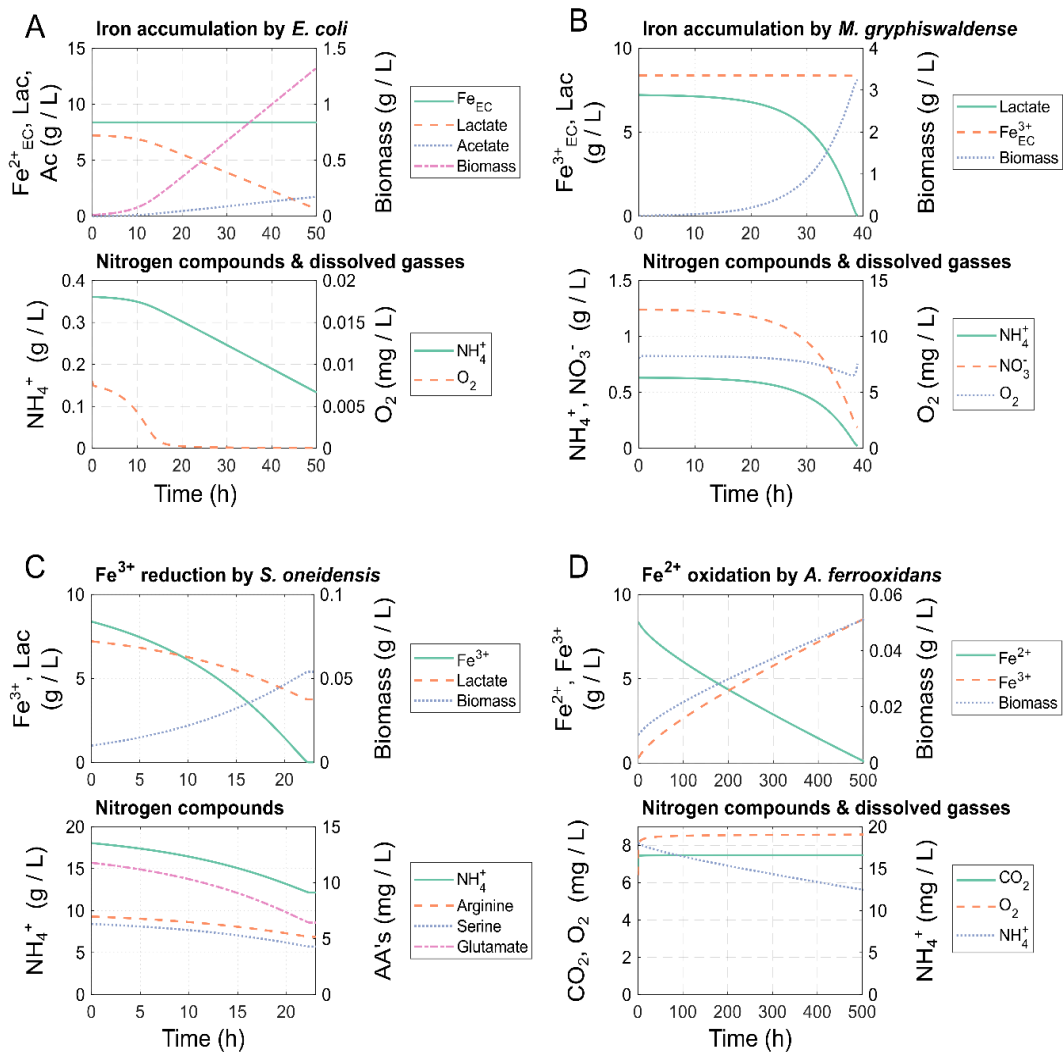
Fig. 6.2 Literature-based growth models for *E. coli*, *M. gryphiswaldense*, *S. oneidensis* and *A. ferrooxidans*, showing nutrient consumption, dissolved gasses and iron dynamics. (A) Predicted growth and iron accumulation by *E. coli* with an overexpressed ferritin complex. After 10 hours, the oxygen transfer rate is predicted to be the limiting factor. The uptake of extracellular iron is negligible. (B) Predicted growth and iron accumulation by *M. gryphiswaldense*. The exponential growth rate is maintained until lactate is depleted. The uptake of extracellular iron is negligible. (C) Predicted growth and iron conversion for S. oneidensis reducing Fe^{3+} to Fe^{2+} from solid mineral substrates. Exponential growth is maintained until iron is depleted. AA's: Amino Acids (D) The predicted growth and iron conversion for *A. ferrooxidans* oxidizing Fe^{2+} to Fe^{3+}. Product inhibition by Fe^{3+} results in a linear growth profile.

	E. coli	M. gryphiswaldense	S. oneidensis *	A. ferrooxidans *
Fe^{2+}	$-2.1*10^{-5}$			
Fe^{3+}		$-4.4*10^{-3}$		200.7
Fe_2O_3 (Fe)			-817.74 (566)**	
FeO				-258.22
Fe_3O_4 (Fe)			790.45 (566)**	
Lactate	-4.95	-2.22	-78.90	
Acetate	1.31		51.64	
NH_4^+	-0.24	-0.19	-0.13	-0.13
NO_3^-		-0.33		
CO_2	3.62	0.65	37.84	-1.65
O_2	-2.61	-0.05		-27.60
H_2O	1.83		15.85	96.64
Arginine			$-41.1*10^{-3}$	
Serine			$-45.9*10^{-3}$	
Glutamate			-0.12	
HCl			-0.006	-392.9

*The *S. oneidensis* process considers the biological conversion of Fe^{3+} and precipitation of magnetite (Fe_3O_4) simultaneously, since both these processes occur at a similar pH-level. The *A. ferrooxidans* process considers just the biological conversion due to the low pH required for *A. ferrooxidans* growth.

** Equivalent Fe mass.

Table 6.1 Mass-wise yields for the considered components in each process, normalized for the production of one gram biomass. All values in gram / gram biomass. Iron uptake in both *E. coli* and *M. gryphiswaldense* is multiple orders of magnitude smaller than the consumption of other nutrients.

The yields and nutrient requirements of the four organisms were analysed in further detail (Tab 6.3). The large difference between iron uptake and consumption of nutrients for both *E. coli* and *M. gryphiswaldense* is emphasized once more. In the case of *S. oneidensis*, its essential amino acids were added to the equation to evaluate their impact on the mass yield. Even though the amino acids are essential for growth, their impact in terms of mass is negligible. In the *S. oneidensis* process, performed at a pH level of 7, the reduction of iron is combined with the precipitation of magnetite. In this combination, the precipitation of magnetite is assumed to be non-limiting and to consume all bio-reduced iron. Since the biological process consumes protons, but the precipitation produces protons, the combination results in only a very small acid consumption.

In the *A. ferrooxidans* process, performed at a pH level of 2, this combination is not possible, and thus a large amount of acid is required to maintain the process pH-value. The resulting acid requirement, converted to a mass of HCl, is larger than the amount of leached iron, which makes this process unfeasible.

There are several key changes for bioprocesses carried out on the Moon or Mars as opposed to those carried out on Earth. The process has to work under lower gravity, which will impact fluid dynamics, but might also have an impact on bacterial performance [43, 44]. On top of that, the composition of the local regolith can have a negative effect on survival rates of some organisms, such as the case with perchlorates in the Martian soil [45].

6.2.3 Bacterial survivability on Martian regolith simulant

The bacterial survivability if they are mixed with Martian regolith is a key factor for the successful appliance of bacterial *in situ* resource utilization (ISRU). *S. oneidensis* was, therefore, added and grown in two different concentrations of JSC-Mars1 intermixed with magnesium perchlorate, which was reported of being toxic to a variety of organisms [45,46] and abundant on the Martian surface.

First, the bacteria were observed via 3D microscopy while growing in a high concentration setting with about 50 g/L JSC1-Mars1 (Fig 3AB). To quantify the so-obtained data and test the effect of the perchlorates, optical density (OD) measurements at a wavelength of 600 nm were performed. The concentration of the iron had to be lowered to 0.5 g/L and 5 g/L for the planktonic culture to limit the effect of light reflection by the ore-particles at this wavelength.

The growth curves of two different sub strains of *S. oneidensis* (MR1 and ANA 3) showed no differences between the tryptic soy broth (TSB) bacteria only, the 0.5 g/L JSC-Mars1 sample and the 0.5 g/L JSC-Mars1 one mixed with 0.05 M magnesium perchlorate (Fig. 3C). The no-bacteria control of the JSC-Mars1 medium together with the 0.05 M magnesium perchlorate showed a strong fluctuation. This might be due to the acidity of perchloric acid and its interaction and oxidation of the regolith ores in the aquatic solution [47].

The increased baseline and fluctuations of the $O.D._{650}$ curves was even more severe in the samples with 5 g/L JSC-Mars1 (Fig. 3D). The $\Delta O.D._{650}$ and, therefore, the growth of the bacteria seems to be lower in the JSC-Mars1 and JSC-Mars1+$Mg(ClO_4)_2$ samples, but these results are not significant because of the high fluctuations. With the lower concentration of regolith simulant and perchlorate S. oneidensis MR1 and ANA3 growth is not influenced for high concentrations of regolith a quantification is barely possible, but the visual check of 3D microscopy showed normal growth activity.
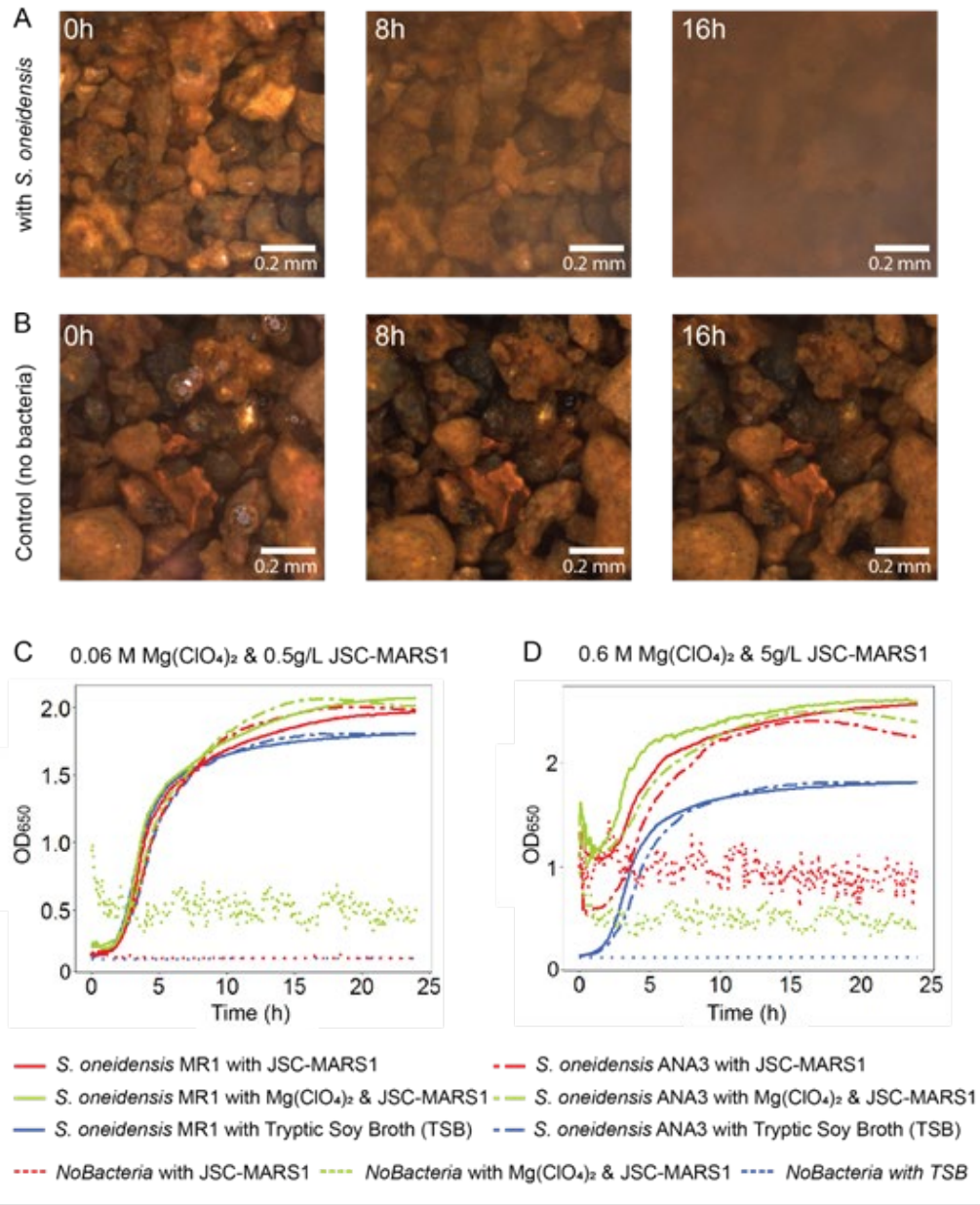
Fig. 6.3 Growth of *S. oneidensis* MR1 and ANA3 in JSC-Mars1. (A) Bacterial growth observed via a 3D microscope. After 8 and 16 hours clear increase in the bacterial sample is visible. (B) Control experiment without bacteria. No change in the 3D microscopy pictures was observed. (C) Bacterial growth of S. oneidensis ANA3 & MR1 under the influence of 0.5 g/L JSC-Mars1 and 0.06 mol/L magnesium perchlorate. No differences in the growth behavior was seen. (D) Bacterial growth of S. oneidensis ANA3 & MR1 under the influence of 5 g/L JSC-Mars1 and 0.6 mol/L magnesium perchlorate. The baseline of the control was shifted due to the higher number of particles in the solution. The absolute growth rate was not influenced.

6.2.4 Payback time analysis

The *S. oneidensis* process was used for a further analysis, where the process performance was combined with estimated bioreactor lander characteristics [13] to calculate the payback time of the entire process (Fig. 6.4). This process uses ferric iron (Fe^{3+}) as a starting material, and thus is focused on Martian applications. The process consists of three phases:

1) Intake phase: Fresh regolith is loaded in the reactor, water and nutrients are added and finally inoculated with *S. oneidensis* biomass.

2) Growth phase: *S. oneidensis* grows exponentially while reducing and leaching iron from the regolith.

3) Extraction phase. Magnetite and other magnetically active minerals are separated from the rest of the medium, the water is evaporated and recycled, and the rest of the regolith is sterilized and disposed.

The duration of the growth phase is determined with the kinetics from Tab. 1, while the other two phases combined are assumed to take 24 hours. The minimal payback time is defined as the moment where the mass of extracted iron exceeds the initial mass of the lander.

The impact of several parameters on the payback time was investigated (Fig 6.4). An increase in initial biomass concentration will lead to a faster process and increased mass gains per hour, but more inoculate from a frozen stock (assumed 10 g_X / L) is needed per run, increasing the required transported mass (Fig 6.4A). These effects counteract each other; when the initial biomass is increased up to 5 mg / L, the payback time decreases, but any further increase result in a decrease of the performance. The optimal initial biomass concentration was found to be 4.5 mg / L.

The efficiency of the water recycling step was varied, and it was found that a certain minimal efficiency was required (Fig 6.4B). At lower efficiencies, the process loses more water than it gains in iron. Higher efficiency always leads to a better payback time. For the base case, with an initial iron concentration of 0.27 mol / L, the minimum required recycling efficiency is

99.79%. For most further analyses, a water recycling efficiency of 99.9% is assumed [48], unless stated otherwise.

If the process starts with a higher iron concentration, a higher amount of iron is extracted at the end of the process, which weighs up against the water loss in the recycling steps. On top of that, a higher initial iron concentration increases the duration of the growth phase, so the productive time per run increases. With the water recycling efficiency of 99.79% (Fig. 6.4C left), the base case initial iron concentration of 0.27 mol / L was also found to be the minimum required for a positive payback time. If the water recycling efficiency was increased to 99.90% (Fig. 4C right), the minimum initial iron concentration decreased to 0.13 mol / L. Higher initial iron concentrations always lead to a reduced payback time. It should be noted that mixing issues due to the resulting slurry and abrasion from the increased regolith concentration have not been considered and so no maximum concentration will be found with the current models.

The relation between minimum water recycling efficiency and minimum initial iron concentration was further investigated, and a linear relation between the two was found (Fig. 6.4D). The higher the water recycling efficiency, the lower the initial iron concentration needs to be for a positive payback time. A combination of very efficient water recycling and high initial iron concentration leads to lower payback times.

The environment of another celestial body will have an impact on the performance of a bioprocess. The increased radiation and altered gravity can lead to increased stress for the organism, changing its performance. This effect was simulated by changing the maximal growth rate and analysing the effect on the payback time (Fig. 6.4E). The process was found to be sensitive to low growth rates, with high sensitivity between 0 and 0.3 h^{-1}. The chosen growth rate of 0.1 h^{-1} is in this regime, so a small change in the growth rate will have a large impact on the payback time.
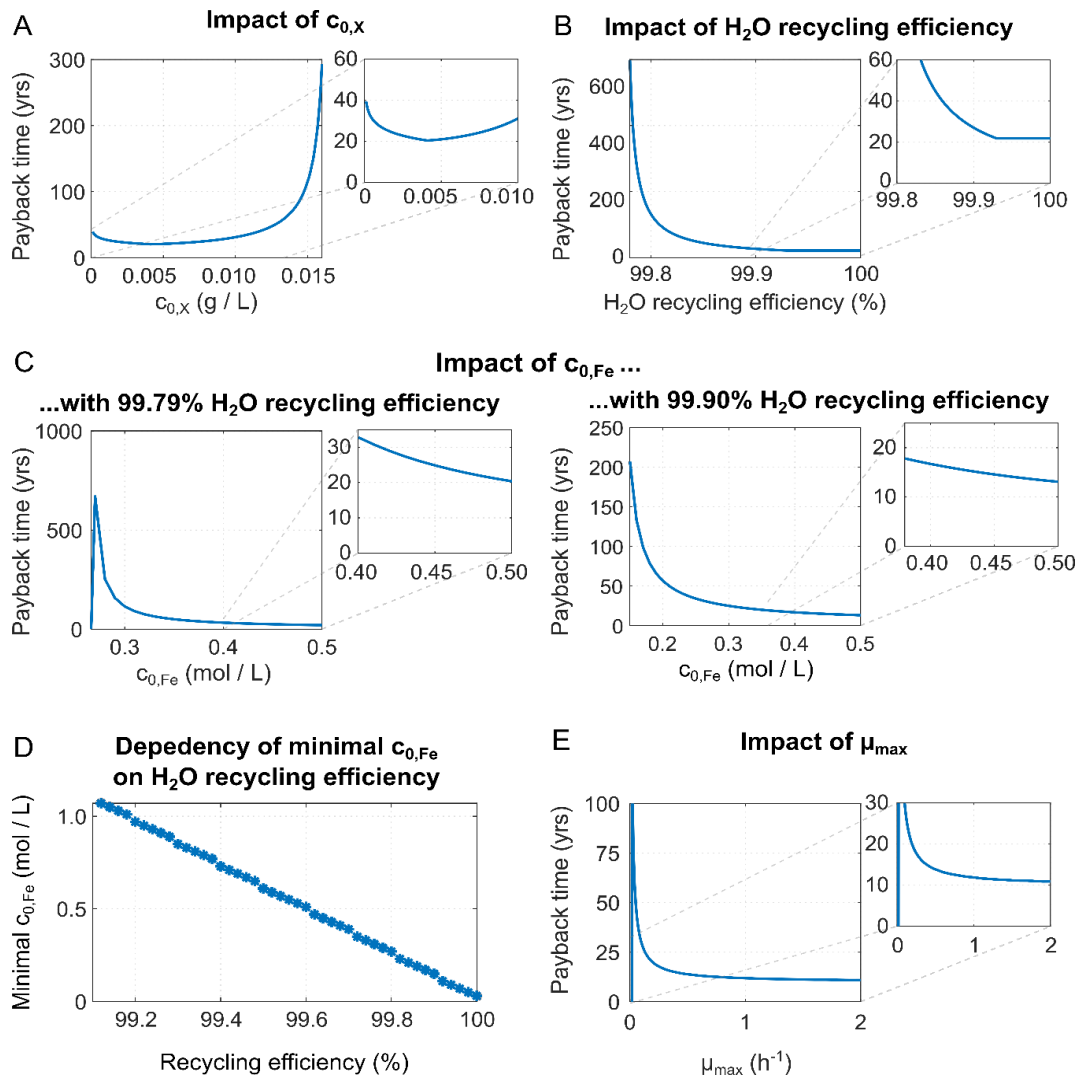
Fig. 6.3 Sensitivity analysis on the mass-dependent payback time. (A) Impact of initial biomass concentration on process payback time, assuming 99.9% water recycling efficiency. Asymptotic behaviour is observed when the initial biomass concentration exceeds 0.014 g / L. (B) Payback time shows high sensitivity to the water recycling efficiency. A higher water recycling efficiency leads to lower payback times. Asymptotic behaviour is observed when recycling efficiency drops below 99.8%. (C) Impact of initial iron concentration both with 99.79% water recycling efficiency and 99.90% recycling efficiency. The payback time decreases with increasing initial iron concentration. (D) The linear relation between water recycling efficiency and minimum required initial iron concentration for a positive payback time is displayed. (E) The impact of maximum growth rate (μ_{max}) on payback time is shown. A higher μ_{max} leads to shorter payback times and asymptotic behaviour is observed when μ_{max} drops below 0.02 h^{-1}.

The insights about the different parameters were combined, and a payback time of 3.3 years was found at a water recycling efficiency of 99.99%, an initial iron concentration of 0.8 mol / L (300 g regolith / L) and an initial biomass concentration of 0.088 g / L. Addition of Martian ice water can reduce the required water recycling efficiency to more achievable levels.

Independent of the exact biological properties, the fact that bioprocesses take place in watery solutions results in general process limitations. A key trade-off is that high concentrations of solids will lead to impaired mixing and reduced gas-liquid mass transfer, but at the same time these high solids concentrations result in more concentrated iron output. Assuming a maximum regolith concentration of 500 g / L with an iron content of ~15%, a maximum of 75 g iron will be extracted with one litre of biological culture. This puts a lower limit on the water recycling efficiency: a 92.5% recycling efficiency is required to extract more iron than the lost water. When ores with higher iron concentration are fed, lower water recycling efficiency is required; at 22% iron the minimum water recycling efficiency is 88.9%. Dependent on the characteristics of mixing in reduced gravity and iron content of the ores, a precise maximum solids concentration and minimum recycling efficiency can be determined.

6.3 Conclusion

In this chapter, a general process setup for biological extraction of iron from Lunar or Martian regolith is presented, consisting of a leaching step and an accumulation or precipitation step. These are combined with a magnetic extraction to obtain the iron-rich minerals. Four organisms were investigated for their use in either an iron leaching or iron accumulation step. Their yields and kinetics were derived from elemental balancing as well as literature, and kinetic models were set up. *M. gryphiswaldense*, modified *E. coli* and *A. ferrooxidans* were found to be incompatible with the envisioned process due to a disappointing level of accumulation and low

yield. Their nutrient requirements outweigh the extracted iron, which makes the process inherently infeasible with from Earth supplied nutrients. In the case of *A. ferrooxidans*, the most important factor was the acid consumption, something that needs close attention in the analysis of bioprocesses. If the acids could be provided *in situ A. ferrooxidans* would be an optimal organism for bioleaching on the Fe^{2+} rich Moon.

S. oneidensis was identified as a promising candidate, with an iron yield of 2.5 g / $g_{nutrients}$ for just the biological conversion, and a yield of 7.14 g / $g_{nutrients}$ after combination with magnetite precipitation. This combination with magnetite precipitation also minimizes the acid consumption of the process. The effect of JSC-Mars1 and $Mg(ClO_4)_2$ on the growth of *S. oneidensis* was found to be small, a promising feature to apply it for biomining on Mars.

The payback time of the process utilizing *S. oneidensis* was analysed, and the sensitivity to various parameters was investigated. Key factors for a feasible process are highly efficient water recycling and a high initial concentration of iron. With a water recycling efficiency of 99.99% and initial iron concentration of 0.8 mol / L, a payback time 3.3 years can be achieved.

The current conclusions are based on literature data and will rely on further experimental work with *S. oneidensis*. The process set-up assumes a watery or slurry-like solution. Other modes of operation, such as a trickle bed reactor, could provide higher or longer productivity in the same volume of water due to a higher amount of solids per volume of liquid and continuous waste removal. Lower water requirements can counteract the negative effects of water losses and thus increase the potential of biological ISRU processes.

6.4 Materials and Methods

6.4.1 Kinetic models

Growth kinetics for *Escherichia coli*, *Magnetospirillum gryphiswaldense*, *Shewanella oneidensis* MR-1 and *Acidithiobacillus ferrooxidans* were derived from literature (Tab. 6.1) and combined with mass balances for the relevant chemical compounds. The resulting system of differential equations was solved with the MATLAB ode15s or ode45 solver. Initial concentrations were chosen similar for all simulations (Table 2).

Growth on lactate was considered for all heterotroph organisms (*S. oneidensis, M. Gryphiswaldense, E. coli*). Only *A. ferrooxidans* uses CO_2 as a carbon source and grows autotrophically. Production of acetate by both *S. oneidensis* and *E. coli* is indicated in table 1, but inhibitory effects are not considered in their models. *A. ferrooxidans* grows aerobically and shows oxygen-limited behavior at concentrations below 1 mg / L ($3.1*10^{-2}$ mM) [14]. The current kinetics hold if the concentration remains above this level. Inhibition by Fe^{3+} is considered in the model.

Organism	By-product	Kinetics	Parameters
E. coli [15,16]	Acetate	$\mu = \mu_{max} * \dfrac{c_{Lac}}{c_{Lac} + K_{Lac}} * \dfrac{c_{O2}}{c_{O2} + K_{O2}}$	$\mu_{max} = 0.22\,h^{-1}$ $K_{Lac} = 10\,\mu M$ $K_{O2} = 0.01\,mM$
M. gryphiswaldense [17]		$\mu = \mu_{max} * \min(f_{NO_3}, f_{Lac})$ $f_{NO_3} = 0.5 + 0.5 * \dfrac{c_{NO_3}}{c_{NO_3} + K_{NO_3}}$ $f_{Lac} = \dfrac{c_{Lac}}{c_{Lac} + K_{Lac}}$	$\mu_{max} = 0.15\,h^{-1}$ $K_{Lac} = 1\,mM$ $K_{NO_3} = 0.2\,mM$
S. oneidensis [18–22]	Acetate	$\mu = \mu_{max} * \dfrac{c_{Lac}}{c_{Lac} + K_{Lac}} * \dfrac{c_{Fe^{3+}}}{c_{Fe^{3+}} + K_{Fe^{3+}}}$	$\mu_{max} = 0.1\,h^{-1}$ $K_{Lac} = 19.4\,mM$ $K_{Fe^{3+}} = 0.55\,mM$
A. ferrooxidans [10,14,23]		$\mu = \mu_{max} * \dfrac{c_{Fe^{2+}}}{c_{Fe^{2+}} + K_{Fe^{2+}}} * \dfrac{K_{Fe^{3+}}}{c_{Fe^{3+}} + K_{Fe^{3+}}}$	$\mu_{max} = 0.082\,h^{-1}$ $K_{Fe^{2+}} = 0.072\,mM$ $K_{Fe^{3+}} = 2.5\,mM$

Table 6.2 Kinetic characteristics and expected byproducts for each proposed organism. Both *E. coli* and *M. gryphiswaldense* are intended for accumulation of dissolved iron in magnetic forms, while *A. ferrooxidans* and *S. oneidensis* are utilized for the extraction of iron from minerals.

Organism	Lactate	Fe^{2+}	Fe^{3+}	NH_4^+	O_2	CO_2	Biomass
E. coli	0.08	0.15	0	0.02	$2.5*10^{-4}$	0	$4.0*10^{-4}$
M. gryphiswaldense	0.08	0.15	0	0.035	$2.5*10^{-4}$	0	$4.9*10^{-4}$
S. oneidensis	0.08	0	0.15	0.001	$2.5*10^{-4}$	0	$4.8*10^{-4}$
A. ferrooxidans	0	0.15	0.005	0.001	$2.0*10^{-4}$	$1.5*10^{-4}$	$3.7*10^{-4}$

Table 6.3. Initial conditions used for solving the kinetic models of the different organisms. Concentrations in mol / L, biomass concentration in Cmol / L.

The biomass mass balance was set up as follows:

$$\frac{dc_X}{dt} = \mu * c_X$$

And for the relevant chemical species in i:

$$\frac{dc_i}{dt} = Y_{i/X} * \mu * c_X$$

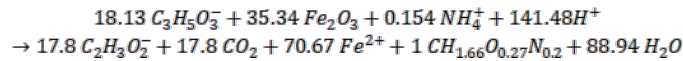In the case of gaseous components, a mass transfer term was included:

$$\frac{dc_i}{dt} = Y_{i/X} * \mu * c_X + (k_L a)_i * \left(c_{l,i}^* - c_{l,i}\right)$$

The internal pressure is assumed to be 1 bar and a gas composition with 21% O_2, 0.05% CO_2 and an inert gas such as N_2 for the remainder is assumed when the process requires oxygen. In the anaerobic processes, the medium will be continuously sparged with an inert gas to induce mixing. The composition could be further tuned if an otherwise feasible process is significantly slowed down due to the gas-liquid mass transfer [24].

The maximum concentration of dissolved gas ($c_{l,i}^*$) was determined by Henry's law. The values for $k_L a$, which combines interfacial area and diffusivity, were assumed to be 10.8 and 8.6 h^{-1} for O_2 and CO_2, respectively. The value for CO_2 is slightly lower because of the larger molecule size, which slows diffusion. These values are chosen on the low end of typical $k_L a$ values for slurry bioprocesses on earth [25–28] to

account for the decreased volumetric gas-liquid mass transfer in a reduced gravity setting [29].

The process stoichiometry for the *S. oneidensis* process, which was found to be the only feasible process under our current conditions.

$$18.13 \, C_3H_5O_3^- + 35.34 \, Fe_2O_3 + 0.154 \, NH_4^+ + 141.48H^+$$
$$\rightarrow 17.8 \, C_2H_3O_2^- + 17.8 \, CO_2 + 70.67 \, Fe^{2+} + 1 \, CH_{1.66}O_{0.27}N_{0.2} + 88.94 \, H_2O$$

In Table 6.4 this stoichiometry is combined with the precipitation of magnetite, counteracting the acid requirements of the S. oneidensis reaction.

6.4.2 Bacterial growth

Shewanella oneidensis MR-1 (ATCC® 700550™) and *Shewanella oneidensis* ANA-3 [30] were aerobically cultured in Tryptic Soy Broth (TSB) media overnight at 30°C under continuous shaking (250 rpm). Different concentrations and compositions of JSC-Mars1 (0.5 g/L or 5 g/L) and Mg(ClO$_4$)$_2$ (0.06 M or 6 M) were added. Thereafter, the growth behaviour was observed for 48 hours by optical density (O.D.) measurements at a wavelength of 650 nm using a 96-well plate in a plate reader.

6.4.3 Payback time analysis

For analysis of the payback time, the approach to the kinetics and mass balances was repeated. The mass of the lander was approximated by first estimating the mass of the basic components [13]. The mass of the 1 m^3 cylindrical reactor was assumed to be 250 kg, filled with 700 L of water. Measuring devices and peripherals were assumed to add 100 kg. The equipment for water recovery was estimated to weigh 100 kg. The rover collecting regolith was assumed to weigh 300 kg. Power supply is covered with an RTG of 500 kg, which covers peak power consumption of the bioprocess, and can be used to power other processes at a Martian colony when the bioprocess needs less power. The resulting mass of the basic components (1950 kg) was combined with the variable mass of water and

nutrients and multiplied by 3 to account for structural components and fuel. The mass of nutrients and water was minimized to obtain the minimal payback time. With this approach, the payback time is that of the case in which the supply of water and nutrients runs out when the mass of extracted iron equals the mass of the lander. A launching cost of $ 20.000 per kg would correspond to a total cost of $ 117 million.

The mass of nutrients and water was minimized to obtain the minimal payback time. With this approach, the nutrient supply runs out when the extracted iron mass equals the total initial lander mass (including nutrients). Increased nutrient and water supplies result in a slightly longer payback time, but a final iron production exceeding the initial lander mass. The system provides its own power through the addition of an RTG, which is sized for use during the evaporation phase of the process and thus has an overcapacity during the other process phases. In terms of maintenance, the system is intended to be an autonomous reactor system requiring no astronaut intervention.

6.5 References

[1] NASA, The Global Exploration Roadmap 2018, (2018). www.globalspaceexploration.org. (accessed November 13, 2018).

[2] J. Carpenter, R. Fisackerly, B. Houdou, Establishing lunar resource viability, Space Policy. 37 (2016) 52–57. doi:10.1016/J.SPACEPOL.2016.07.002.

[3] C. Culbert, D. Linne, F. Chandler, L. Alexander, S. Jefferies, K.J. Kennedy, M. Lupisella, P. Metzger, N. Moore, K. Taminger, NASA Technology Roadmaps - TA 7: Human Exploration Destination Systems, 2015. https://www.nasa.gov/sites/default/files/atoms/files/2015_nasa_technology_road maps_ta_7_human_exploration_destination.pdf (accessed October 29, 2018).

[4] K.A. Weber, L.A. Achenbach, J.D. Coates, Microorganisms pumping iron: Anaerobic microbial iron oxidation and reduction, Nat. Rev. Microbiol. 4 (2006) 752–764. doi:10.1038/nrmicro1490.

[5] J. Valdés, I. Pedroso, R. Quatrini, R.J. Dodson, H. Tettelin, R. Blake, J.A. Eisen, D.S. Holmes, Acidithiobacillus ferrooxidans metabolism: from genome

sequence to industrial applications, BMC Genomics. 9 (2008) 597. doi:10.1186/1471-2164-9-597.

[6] D.E. Rawlings, Heavy Metal Mining Using Microbes, Annu. Rev. Microbiol. 56 (2002) 65–91. doi:10.1146/annurev.micro.56.012302.161052.

[7] A. Schippers, S. Hedrich, J. Vasters, M. Drobe, W. Sand, S. Willscher, Biomining: Metal Recovery from Ores with Microorganisms, in: Springer, Berlin, Heidelberg, 2013: pp. 1–47. doi:10.1007/10_2013_216.

[8] S. Yin, L. Wang, E. Kabwe, X. Chen, R. Yan, K. An, L. Zhang, A. Wu, Copper Bioleaching in China: Review and Prospect, Minerals. 8 (2018) 32. doi:10.3390/min8020032.

[9] C.R. Cousins, C.S. Cockell, An ESA roadmap for geobiology in space exploration, Acta Astronaut. 118 (2016) 286–295. doi:10.1016/j.actaastro.2015.10.022.

[10] J.U. Navarrete, I.J. Cappelle, K. Schnittker, D.M. Borrok, Bioleaching of ilmenite and basalt in the presence of iron-oxidizing and iron-scavenging bacteria, Int. J. Astrobiol. 12 (2013) 123–134. doi:10.1017/S1473550412000493.

[11] D.J. Lawrence, W.C. Feldman, R.C. Elphic, R.C. Little, T.H. Prettyman, S. Maurice, P.G. Lucey, A.B. Binder, Iron abundances on the lunar surface as measured by the Lunar Prospector gamma-ray and neutron spectrometers, J. Geophys. Res. Planets. 107 (2002) 13-1-13–26. doi:10.1029/2001JE001530.

[12] A.N. Halliday, H. Wänke, J.-L. Birck, R.N. Clayton, The Accretion, Composition and Early Differentiation of Mars, Space Sci. Rev. 96 (2001) 197–230. doi:10.1023/A:1011997206080.

[13] R. Volger, S.J.J. Brouns, A. Cowley, C. Picioreanu, B.A.E. Lehner, Bioreactor design to perform microbial mining activities on another celestial body, in: 69th Int. Astronaut. Congr., Bremen, 2018.

[14] M.S. Liu, R.M.R. Branion, D.W. Duncan, The effects of ferrous iron, dissolved oxygen, and inert solids concentrations on the growth of thiobacillus ferrooxidans, Can. J. Chem. Eng. 66 (1988) 445–451. doi:10.1002/cjce.5450660315.

[15] Q. Hua, A.R. Joyce, B.O. Palsson, S.S. Fong, Metabolic Characterization of Escherichia coli Strains Adapted to Growth on Lactate, Appl. Environ. Microbiol. 73 (2007) 4639–4647. doi:10.1128/AEM.00527-07.

[16] M.F. Núñez, O. Kwon, T.H. Wilson, J. Aguilar, L. Baldoma, E.C.C. Lin, Transport of L-Lactate, D-Lactate, and Glycolate by the LldP and GlcA Membrane Carriers of Escherichia coli, (2002). doi:10.1006/bbrc.2001.6255.

[17] M. Naresh, S. Das, P. Mishra, A. Mittal, The chemical formula of a magnetotactic bacterium, Biotechnol. Bioeng. 109 (2012) 1205–1216. doi:10.1002/bit.24403.

[18] J.E. Kostka, J.W. Stucki, K.H. Nealson, J. Wu, Reduction of Structural Fe(III) in Smectite by a Pure Culture of Shewanella Putrefaciens Strain MR-1, Clays Clay Miner. 44 (1996) 522–529. doi:10.1346/CCMN.1996.0440411.

[19] G.E. Pinchuk, E.A. Hill, O. V. Geydebrekht, J. De Ingeniis, X. Zhang, A. Osterman, J.H. Scott, S.B. Reed, M.F. Romine, A.E. Konopka, A.S. Beliaev, J.K. Fredrickson, J.L. Reed, Constraint-Based Model of Shewanella oneidensis MR-1 Metabolism: A Tool for Data Analysis and Hypothesis Generation, PLoS Comput. Biol. 6 (2010) e1000822. doi:10.1371/journal.pcbi.1000822.

[20] C. Liu, Y.A. Gorby, J.M. Zachara, J.K. Fredrickson, C.F. Brown, Reduction kinetics of Fe(III), Co(III), U(VI), Cr(VI), and Tc(VII) in cultures of dissimilatory metal-reducing bacteria, Biotechnol. Bioeng. 80 (2002) 637–649. doi:10.1002/bit.10430.

[21] X. Feng, Y. Xu, Y. Chen, Y.J. Tang, Integrating Flux Balance Analysis into Kinetic Models to Decipher the Dynamic Metabolism of Shewanella oneidensis MR-1, PLoS Comput. Biol. 8 (2012) e1002376. doi:10.1371/journal.pcbi.1002376.

[22] J.E. Kostka, D.D. Dalton, H. Skelton, S. Dollhopf, J.W. Stucki, Growth of Iron(III)-Reducing Bacteria on Clay Minerals as the Sole Electron Acceptor and Comparison of Growth Yields on a Variety of Oxidized Iron Forms, Appl. Environ. Microbiol. 68 (2002) 6256–6262. doi:10.1128/AEM.68.12.6256-6262.2002.

[23] S. Molchanov, Y. Gendel, I. Ioslvich, O. Lahav, Improved experimental and computational methodology for determining the kinetic equation and the extant kinetic constants of Fe(II) oxidation by Acidithiobacillus ferrooxidans., Appl. Environ. Microbiol. 73 (2007) 1742–52. doi:10.1128/AEM.01521-06.

[24] P.M. Doran, Bioprocess engineering principles, 2nd ed., Elsevier/Academic Press, 2013. https://www.sciencedirect.com/book/9780122208515/bioprocess-engineering-principles#book-info (accessed February 8, 2019).

[25] J.W. Neale, A. Pinches, Determination of gas-liquid mass-transfer and solids-suspension parameters in mechanically-agitated three-phase slurry reactors, Miner. Eng. 7 (1994) 389–403. doi:10.1016/0892-6875(94)90078-7.

[26] G. Van Weert, D. Van Der Werff, J.J. Derksen, Transfer of O2 from air to mineral slurries in a rushton turbine agitated tank, Miner. Eng. 8 (1995) 1109–1124. doi:10.1016/0892-6875(95)00076-3.

[27] A. Schumpe, A.K. Saxena, L.K. Fang, Gas/liquid mass transfer in a slurry bubble column, Chem. Eng. Sci. 42 (1987) 1787–1796. doi:10.1016/0009-2509(87)80183-5.

[28] S. Zokaei-Kadijani, J. Safdari, M.A. Mousavian, A. Rashidi, Study of oxygen mass transfer coefficient and oxygen uptake rate in a stirred tank reactor for uranium ore bioleaching, Ann. Nucl. Energy. 53 (2013) 280–287. doi:10.1016/J.ANUCENE.2012.07.036.

[29] D.R. Pettit, D.T. Allen, Unit Operations for Gas-Liquid Mass Transfer in Reduced Gravity Environments, in: Second Conf. Lunar Bases Sp. Act. 21st Century, Vol. 2, NASA. Johnson Space Center, 1992: p. p 647-651. https://ntrs.nasa.gov/archive/nasa/casi.ntrs.nasa.gov/19930004823.pdf.

[30] G. Wang, F. Qian, C.W. Saltikov, Y. Jiao, Y. Li, Microbial reduction of graphene oxide by Shewanella, Nano Res. 4 (2011) 563–570. doi:10.1007/s12274-011-0112-2.

[31] C.W. Bale, E. Bélisle, P. Chartrand, S.A. Decterov, G. Eriksson, A.E. Gheribi, K. Hack, I.-H. Jung, Y.-B. Kang, J. Melançon, A.D. Pelton, S. Petersen, C. Robelin, J. Sangster, P. Spencer, M.-A. Van Ende, FactSage thermochemical software and databases, 2010–2016, (2016). doi:10.1016/j.calphad.2016.05.002.

[32] I. Lozano, N. Casillas, C.P. de León, F.C. Walsh, P. Herrasti, New Insights into the Electrochemical Formation of Magnetite Nanoparticles, J. Electrochem. Soc. 164 (2017) D184–D191. doi:10.1149/2.1091704jes.

[33] D. R. Dasgupta, A. L. Mackay, β-Ferric Oxyhydroxide and Green Rust, J. Phys. Soc. Japan. 14 (1959) 932–935. doi:10.1143/JPSJ.14.932.

[34] D. He, S. Hughes, S. Vanden-Hehir, A. Georgiev, K. Altenbach, E. Tarrant, C.L. Mackay, K.J. Waldron, D.J. Clarke, J. Marles-Wright, Structural characterization of encapsulated ferritin provides insight into iron storage in bacterial nanocompartments, Elife. 5 (2016). doi:10.7554/eLife.18972.

[35] C.T. Lefèvre, F. Abreu, U. Lins, D.A. Bazylinski, A Bacterial Backbone: Magnetosomes in Magnetotactic Bacteria, in: Met. Nanoparticles Microbiol., Springer Berlin Heidelberg, Berlin, Heidelberg, 2011: pp. 75–102. doi:10.1007/978-3-642-18312-6_4.

[36] D. Schüler, E. Baeuerlein, Dynamics of iron uptake and Fe3O4 biomineralization during aerobic and microaerobic growth of Magnetospirillum gryphiswaldense., J. Bacteriol. 180 (1998) 159–62. http://www.ncbi.nlm.nih.gov/pubmed/9422606 (accessed July 11, 2018).

[37] C.R. Myers, K.H. Nealson, Bacterial Manganese Reduction and Growth with Manganese Oxide as the Sole Electron Acceptor, Science (80-.). 240 (1988) 1319–1321. doi:10.1126/science.240.4857.1319.

[38] B.D. Bennett, E.D. Brutinel, J.A. Gralnick, A Ferrous Iron Exporter Mediates Iron Resistance in Shewanella oneidensis MR-1, Appl. Environ. Microbiol. 81 (2015) 7938–7944. doi:10.1128/AEM.02835-15.

[39] T. Perez-Gonzalez, C. Jimenez-Lopez, A.L. Neal, F. Rull-Perez, A. Rodriguez-Navarro, A. Fernandez-Vivas, E. Iañez-Pareja, Magnetite biomineralization induced by Shewanella oneidensis, Geochim. Cosmochim. Acta. 74 (2010) 967–979. doi:10.1016/j.gca.2009.10.035.

[40] A.L. Kane, E.D. Brutinel, H. Joo, R. Maysonet Sanchez, C.M. VanDrisse, N.J. Kotloski, J.A. Gralnick, Formate Metabolism in Shewanella oneidensis Generates Proton Motive Force and Prevents Growth Without an Electron Acceptor, J. Bacteriol. 198 (2016) JB.00927-15. doi:10.1128/JB.00927-15.

[41] D.R. Lovley, E.J.P. Phillips, D.J. Lonergan, Hydrogen and Formate Oxidation Coupled to Dissimilatory Reduction of Iron or Manganese by Alteromonas putrefaciens, Appl. Environ. Microbiol. 55 (1989) 700–706. http://aem.asm.org/content/55/3/700.

[42] Y.J. Tang, A.L. Meadows, J.D. Keasling, A kinetic model describing Shewanella oneidensis MR-1 growth, substrate consumption, and product secretion, Biotechnol. Bioeng. 96 (2007) 125–133. doi:10.1002/bit.21101.

[43] M.A. Kacena, G.A. Merrell, B. Manfredi, E.E. Smith, D.M. Klaus, P. Todd, Bacterial growth in space flight: logistic growth curve parameters for Escherichia coli and Bacillus subtilis, Appl. Microbiol. Biotechnol. 51 (1999) 229–234. doi:10.1007/s002530051386.

[44] D. Demey, V. Hermans, J.-F. Cornet, J.-J. Leclercq, C. Lasseur, A. Delahaye, BIORAT: Preliminary Evaluation of Biological Life Support in Space Environment, in: 2000. doi:10.4271/2000-01-2384.

[45] J. Wadsworth, C.S. Cockell, Perchlorates on Mars enhance the bacteriocidal effects of UV light, Sci. Rep. 7 (2017) 4662. doi:10.1038/s41598-017-04910-3.

[46] A.F. Al Soudi, O. Farhat, F. Chen, B.C. Clark, M.A. Schneegurt, Bacterial growth tolerance to concentrations of chlorate and perchlorate salts relevant to Mars, Int. J. Astrobiol. 16 (2017) 229–235. doi:10.1017/S1473550416000434.

[47] W.A. Jackson, T. Anderson, G. Harvey, G. Orris, S. Rajagopalan, N. Kang, Occurrence and Formation of Non-Anthropogenic Perchlorate, in: Perchlorate Environ. Occur. Interact. Treat., Kluwer Academic Publishers, Boston, 2006: pp. 49–69. doi:10.1007/0-387-31113-0_3.

[48] Y. Fu, L. Li, B. Xie, C. Dong, M. Wang, B. Jia, L. Shao, Y. Dong, S. Deng, H. Liu, G. Liu, B. Liu, D. Hu, H. Liu, How to Establish a Bioregenerative Life Support System for Long-Term Crewed Missions to the Moon or Mars, Astrobiology. 16 (2016) 925–936. doi:10.1089/ast.2016.1477.

6

7

Extraction of iron from Lunar and Martian regolith simulants using a microbial approach in conjunction with 3D printing

Manuscript in preparation

Benjamin A.E. Lehner*, Sofie Castelein[+], Tom Aarts[+], Juergen Schleppi, Ruud Hendrikx, Dominik Benz, Amarante J. Bottger, Advenit Makaya, Martin Schwentenwein, Florian Ertl, Jessica Snyder, Lynn J. Rothschild, Bertus Beamount, Stan J.J. Brouns, Anne S. Meyer

In situ resource utilization (ISRU) is increasingly acknowledged as an essential part of sustainable space exploration. Typical approaches towards ISRU are often constrained by the mass and energy requirements of transporting processing machineries, such as rovers and massive reactors, and the vast amount of consumables needed. Self-reproducing bacteria for the extraction of resources are an excellent way to avoid this issue. In this chapter, the bacterium *Shewanella oneidensis* was utilized to reduce three different types of Lunar and Martian regolith simulants allowing for the magnetic extraction of iron rich materials. The quantity of extracted material could be increased up to 5.5 times and the iron concentration up to 43.6% in comparison to untreated material. The materials were 3D printed to show a proof of concept for the on-demand production of construction and replacement parts in space exploration.

7.1 Introduction

A human outpost on another celestial body needs to fulfill several requirements. Transportation, shelter, supplies, waste removal, hazard protection, and power sources have to be provided to ensure its viability [1]. Every space exploration endeavor to date, however, has used resources originating from Earth, which necessitates high transportation costs and, ultimately, a high degree of dependence. The two most common solutions to tackle this issues are to reduce the payload weight and to minimize the launching cost [2], but sustainability and economic attractiveness can only be ensured via the direct usage of resources found in space, also called *in situ* resource utilization [3].

Traditionally, research in the sector of *in situ* resource utilization has focused on investigating technical processes already in use on Earth and how they may be implemented in the harsh environment of space [4]. Technological approaches that have survived in the free market over a longer period have proven themselves in this highly selective process. Current Earth technologies have been optimized and tested extensively and may also be suitable for adaptation to the environment on another celestial body [4]. The same microwaves which are used for heating food may, for instance, be a key technology to sinter building blocks for a possible extraterrestrial outpost [5].

The main disadvantage of direct adaptation of current mechanochemical approaches to space applications is the need for outsized factories and machinery. A novel approach to prevent this demand is the usage of microbes for in situ resource utilization. These organisms are self-reproducing and only require water and an easily transportable growth medium to become active [2]. In many cases, they can produce [6], extract [7], and pattern [8] material in a manner comparable to the equivalent technological process. Microbes do not require sophisticated factories, high energy investment, or strong chemicals. Therefore, bacterial

methodologies are increasingly being applied to terrestrial applications [9-12] and may be even more valuable for space exploration and colonialization, where resupply and a limiting initial amount of materials are major constraints [1, 13].

This work develops a new approach for microbial iron extraction from Lunar and Martian regolith simulants and its utilization via 3D printing applications (Fig. 7.1). The bacterium *Shewanella oneidensis,* which was shown to be useful for space-based biomining applications [chapter 6], can reduce a variety of metal oxides under both aerobic and anaerobic conditions [14, 15]. Martian regolith contains a high concentration of iron in its Fe(III) state [16], which can be reduced and even precipitated as magnetite by *Shewanella oneidensis* [17] and afterwards magnetically extracted.

Our results indicate that none of the three tested regolith simulants are toxic to *Shewanella* under either aerobic or anaerobic conditions. Further, we show that anaerobic extraction of JSC-Mars1 regolith simulant with minimal growth medium produces up to a 5.5-fold increase in the quantity of magnetically extracted material and an iron concentration that is 18.2% higher than in the starting material. Finally, we provide a proof-of-principle to 3D print the extracted magnetic material by plasma sintering and lithography-based ceramic manufacturing. Either technology, especially if coupled with our bacterial extraction methodology, would enable the rapid, on-demand production of infrastructure materials as well as replacement parts for a future space colony.
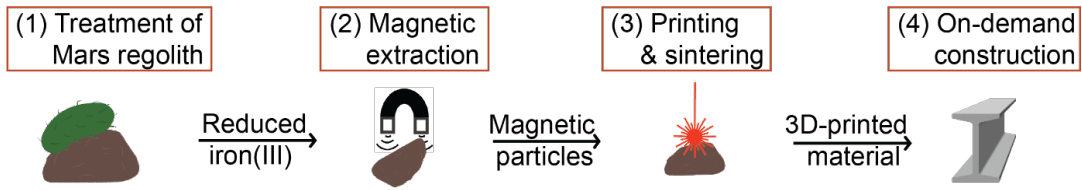
7

Fig. 7.1 Conceptual flow of the microbial biomining process. Bacterial treatment (1) makes the material more magnetic by reducing iron. A magnet is applied to extract the magnetic material (2), and those particles are 3D printed and sintered (3). The material is then ready for construction, maintenance, and repair applications (4).

7.2 Results & discussion

7.2.1 Regolith simulants

Our microbial methodology for the reduction of regolith combined with magnetic extracting and 3D-printing material *in situ* is highly applicable to Mars due to its high abundance of Fe(III). Despite the low abundance of Fe(III) on the Moon, we also applied our methodology to several Moon regolith simulants, which contain Fe(III), to test its robustness towards minor changes in the mineral composition.

X-ray fluorescence (XRF) measurements on two Lunar Mare and one Martian regolith simulant were performed to analyse their elemental compositions. Comparing the two Lunar Mare simulants EAC-1 and JSC-2A with the average Mars regolith values (Tab. 7.1) [18] revealed that both simulants contained metal oxides within the same concentration ranges as the average Mars soil. The Martian regolith simulant JSC-Mars1 exhibited several apparent differences to the average actual major elemental composition of Mars, especially for SiO_2, Al_2O_3, and MgO.

However, since the actual composition of Lunar and Martian soil varies between different locations on the surfaces of the celestial objects, it is not desirable to utilize exact matches of the actual average compositions. Rather, it is useful to use a number of different simulants with varying compositions to test for multiple different scenarios. Only measurements of

the soil at a potential landing site can ultimately determine the actual composition of the available soil. Since an exact landing site for a potential surface mission is still unknown, we chose to test a variety of different compositions until more details on a landing site become available.

When using regolith simulants due to the lack of actual soil available, it is important to know each simulant's differences or weak points. Since simulants are typically sourced and produced in different ways, and the quality-assurance processes of manufacturing companies and agencies tend to be different, the actual simulant quality will vary. The Moon regolith simulants JSC-1A and EAC-1 have both been mined from the surface of a volcanic basaltic deposit. However, JSC-1A was mined from a volcanic ash deposit in the San Francisco volcano field in Arizona (35°20' N, 111°17' W), which erupted only approximately 0.15 ± 0.03 million years ago [19], whereas EAC-1 was mined from a deposit in the Eifel region (50°41'N, 7°19'E), which is approximately 20 million years old.

Although both simulants could have been in contact with water, air, and vegetation, the older age of EAC-1 increases the chance of processes that could change its composition. For example, EAC-1 shows alterations such as the presence of chlorite, which is usually found in igneous rocks and results from water interacting with pyroxene minerals. JSC-2A in contrast is produced from synthetic minerals [20] as the successor of JSC-1A and shares, therefore, the composition of JSC-1A without its natural alterations due to air, water and vegetation interactions.

The Mars regolith simulant JSC-Mars1 was sourced on the island of Hawai'i from sieved palagonatized tephra ash from the 1843 Mauna Loa lava flow on Pu'u Nene (19°41'N, 155°29'W) [21]. Although all three regolith types were excavated close to the surface of the Earth, JSC-Mars1, at 175 years of age, is very young compared to the Lunar simulants EAC-1 and JSC-1A. Hence, little to no alterations are expected in this simulant. Nevertheless, a substantial amount of water and carbon was found in this simulant (combined approx. 8%, Table 1), which is relatively high compared to the

other simulants. These contaminations can be partially removed by heating the simulant prior to its use, which will remove most of the water and some of the carbon but not necessarily all. Notably, actual Martian regolith contains sulfur trioxide (avg. 6.16%) and chlorine (avg. 0.68%), neither of which have been measured by the supplier or for the work presented here. The iron and calcium content of the Viking and Pathfinder Mars samples are best approximated by JSC-Mars1, while the aluminum content is closer to that of EAC-1 and the magnesium content is the closest to JSC-2A (Tab. 7.1).

	Mars Viking 1 [22]	Mars Viking 2 [22]	Path-finder [23]	JSC-Mars1 [24] (sup)	JSC-Mars 1 (XRF)	JSC-2A (sup) [25]	JSC-2A (XRF)	EAC-1 (sup) [26]	EAC-1 (XRF)
SiO_2	43	43	44	43.5	42.2	47.5	44.9	43.7	43.6
Al_2O_3	7.3	7	7.5	23.3	23.5	15	19.6	12.6	11.5
Fe_2O_3	18.5	17.8	16.5	15.6	17.6	10.8	12.8	12	12.7
MgO	6	6	7	3.4	3.4	9	4.7	11.9	14.1
CaO	5.9	5.7	5.6	6.2	6.0	11	10.1	10.8	10.2
K_2O	<0.2	<0.3	0.3	0.6	0.5	0.8	0.7	1.3	1.2
TiO_2	0.7	0.6	1.1	3.8	3.8	2	2.2	2.4	2.2

Tab 7.1 Average major element composition at different Mars locations [22, 23, 27] and the composition of three different regolith simulant types obtained via X-ray fluorescence (XRF) (JSC-Mars1 [24], JSC-2 [25], EAC-1 [26]) as well as reported by the suppliers (= "sup").

The mineral composition of the different regolith simulants was inspected by X-ray diffraction spectrometry (XRD). The most abundant Martian minerals plagioclase, olivine, and pyroxene were detected in all three regolith simulants. EAC-1 showed the presence of Nepheline and manganese iron oxide, both of which were not yet detected on Mars, and JSC-2A contained a small fraction of magnetite, similar to the results from Mars Curiosity (Tab. 7.2).

Mineral	Chemistry	Mars Curiosity Rocknest soil [16]	JSC-Mars1 (XRD)	JSC-2A (XRD)	EAC-1 (XRD)
Plagioclase (Anorthite)	$(Ca_{0.57(13)}Na_{0.43})$ $(Al_{1.57}Si_{2.43})O_8$	40.8%	X	X	X
Olivine (Forsterite)	$(Mg_{0.62(3)}Fe_{0.38})_2 SiO_4$	22.4%	X	X	X
Pyroxene (Augite)	$(Mg_{0.88(10)}Fe_{0.37}$ $Ca_{0.75(4)}) Si_2O_6$	14.6%	X	(X)*	X
Pyroxene (Pigeonite)	$(Mg_{1.13}Fe_{0.68}Ca_{0.19})$ Si_2O_6	13.8%	-	-	-
Magnetite	Fe_3O_4	2.1%	-	(X)*	-
Anhydrite	$CaSO_4$	1.5%	-	-	-
Quartz	SiO_4	1.4%	-	-	-
Manganese Iron Oxide	$Mn_{0.43}Fe_{2.57}O_4$	-	-	-	X
Nepheline	$(K_{0.69}Na_{3.03}Ca_{0.03}Fe_{0.04}Al_{3.75}Si_{0.21})(SiO_4)_4$	-	-	-	X

Tab. 7.2 X-Ray diffraction spectroscopy analysis of the Mars Rocknest soil [16] and the three different regolith simulants. Minerals that were detected are denoted with "X"; minerals that were not detected are denoted with "-".

* These elements were only detected in the magnetically-extracted fraction.

7.2.2 Toxicity of regolith simulants

To acquire a working concentration of regolith for our bacterial treatment, the toxicity of the Lunar and Martian regolith simulants for *Shewanella oneidensis* was determined at a range of regolith concentrations. *Shewanella oneidensis* was grown for 48 hours in a rich medium under aerobic (Fig. 7.2A, C, E) or anaerobic (Fig. 7.2B, D, F) conditions. Colony forming units (CFU) and optical density (O.D.$_{600}$) were measured to observe the effect of increasing regolith simulant concentrations (0 g/L, 0.1 g/L, 1 g/L, 10 g/L and 100 g/L) on both bacterial viability and growth.

We tested the Martian regolith simulant JSC-Mars1 (Fig. 7.2A, B) and two lunar regolith simulants: EAC-1 (Fig. 7.2 C,D) and JSC-2A (Fig. 7.2E,F). The CFUs of the samples were evaluated at three different time points (0, 24, and 48 hours) and all control samples containing regolith, but no bacteria produced 0 CFU/μL. The O.D.$_{600}$ absorbance was measured every 5 minutes, and the optical density of control samples containing regolith but no *Shewanella* was subtracted from the data. *Shewanella oneidensis* did not show any reduced growth behavior upon exposure to increasing regolith concentrations.

The bacteria in JSC-2A and EAC-1 appear to prefer the aerobic growth environment since the CFUs result in higher total number compared to anaerobic conditions. In JSC-Mars1 the anaerobic growth revealed a higher CFU than the aerobic one. This might be due to the increased amount of Fe(III) as electron acceptor in this regolith type. The starting CFUs of all anaerobe samples was slightly higher due to the transfer time of the samples from the glove box to the agar plates. The growth curves and CFU results indicate similar growth behavior for all regolith types under the same environmental conditions, suggesting no toxicity or affinity for any particular type or concentration of regolith.
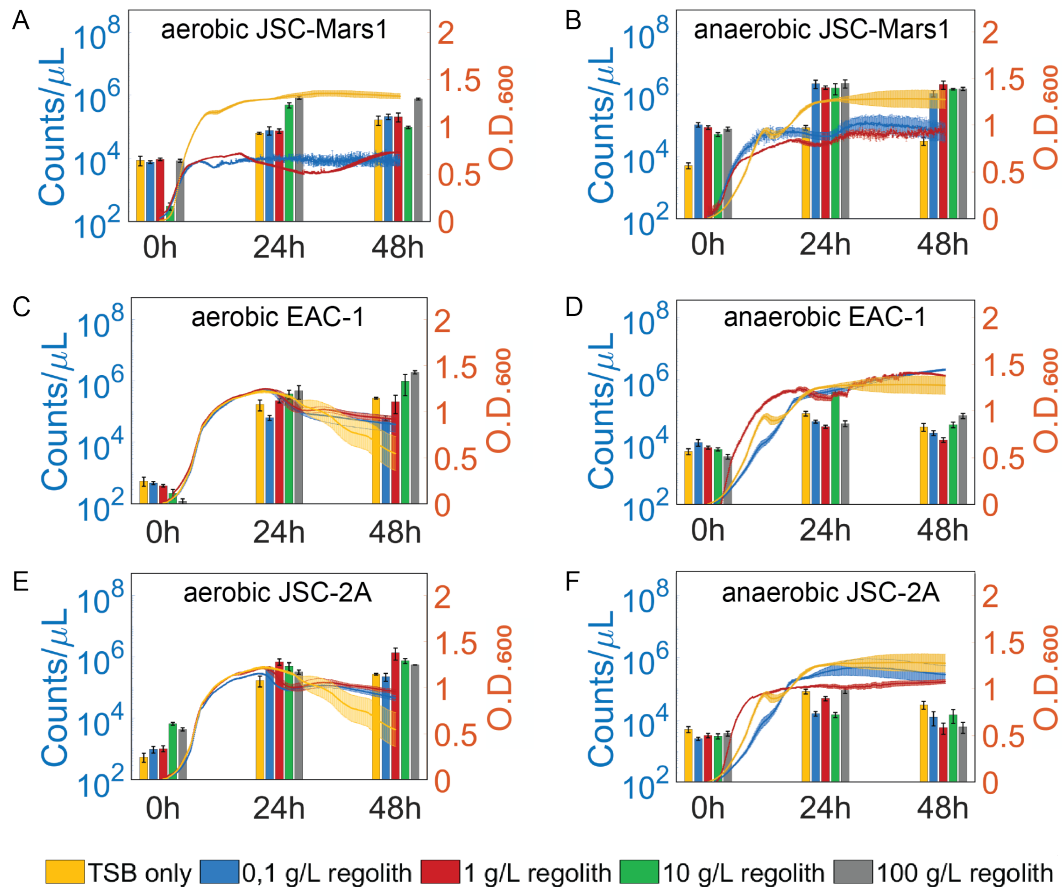
Fig 7.2 Evaluation of the toxicity of different Lunar and Martian regolith simulants to *Shewanella oneidensis* MR-1 under aerobic and anaerobic conditions. CFUs (counts/µL) are depicted on the left axis and the O.D.$_{600}$ measurements on the right axis. The yellow, blue, red, green, and grey bars represent regolith concentrations of 0, 0.1, 1, 10, and 100 g/L respectively. Optical density at 600 nm of control samples without *S. oneidensis* were subtracted from the O.D.$_{600}$ measurements. The error bars represent the standard error of the mean. Aerobic growth behaviour of *S. oneidensis* in the presence of JSC-Mars1 (A), EAC-1 (C) and JSC-2A (E). Anaerobic growth behaviour of *S. oneidensis* in the presence of JSC-Mars1 (B), EAC-1 (D) and JSC-2A (F).

7.2.3 *Magnetic extraction and Fe(II)$_{aq}$ content under aerobic conditions*

Construction material will be of utmost importance for any space colony and magnetism would be an easy way to separate different ores. In order to produce more magnetic minerals in the regolith and concentrate the iron content, *Shewanella oneidensis* was incubated over 168h with TSB medium and 10 g/L of EAC-1, JSC-2A or JSC-Mars1 regolith simulant. The reduction of Fe(III) to Fe(II) together with a local pH increase at *Shewanella's* cell membrane allows for the precipitation of magnetite. This methodology might increase the quality and quantity of the extractable magnetic material from regolith simulants.

An aerobic magnetic extraction experiment utilizing handhold neodymium magnets (Fig. 7.3A) and previously weighed cuvettes was used to assess the amount of magnetic material per mL at different timepoints with and without bacterial treatment. In short, 1 mL of sample was pipetted into a cuvette then a magnet was used to extract the magnetic fraction, washed and transferred in another previously weighed cuvette. The weight difference after drying of the material was measured.

A colorimetric assay with 1,1 O-phenanthroline as a complexing reagent and NaF to inactivate Fe(III) (Fig. 7.3B) was performed to determine the aqueous iron concentration (Fe(II)$_{(aq)}$) with and without bacterial treatment at different timepoints. An increase in Fe(II) bound to the complexing reagent can be checked via an O.D.$_{510}$ absorbance scan. The absorbance of samples with a known iron concentration and the complexing reagent was measured, to make a standard curve for Fe(II)$_{(aq)}$ and check for any potential interference by Fe(III)$_{(aq)}$ (Fig 7.3B).

A Fe(II) standard was prepared by mixing ammonium iron(II)sulfate hexahydrate to TSB in a concentration of 0, 50, 100, 150 and 200 ppm. A Fe(III) containing standard was mixed by using the same Fe(II) concentrations together with 100ppm iron(III)citrate. A linear fit showed no difference between the two curves.

$y_{Fe(II)+Fe(III)}$ = 4.3e-3*x + 8.0e-2; $y_{Fe(II)}$ = 4.4e-3*x + 8.4e-2;

The amount of magnetically extracted material from EAC-1, determined with the extraction set-up (Fig. 7.3A), increased significantly (Fig. 7.3C) from 1.4 ± 0.44 mg at the 0h sample to 2.0 ± 0.19 mg (1.4-fold) after 168h of incubation with *Shewanella* ($p_{S0h\text{-}S168h} = 0.044$), while there was no significant difference between the no-bacteria control at 0h and at 168h (one-way ANOVA with Tukey PostHoc test, n = 6, $p_{C0h\text{-}S0h} = 0.83$, $p_{C0h\text{-}C168h} = 0.35$). The for 168 h incubated bacterially treated sample was also significantly higher than the 168 no-bacteria control ($p_{S168h\text{-}C168h} = 0.0069$). However, there was no significant difference between the control at 0h and the sample at 168h ($p_{C0h\text{-}S168h} = 0.22$), which might suggest that the significant difference between the bacterial sample at 0h and 168h was a false positive. Therefore, no clear statement can be drawn regarding whether the amount of material magnetically extracted from EAC-1 can be increased.

For the $Fe(II)_{aq}$ concentration, the no-bacteria controls of EAC-1 do not display any significant differences between the timepoints (Fig. 7.3D) (one-way ANOVA with Tukey PostHoc test, n=9, p > 0.05). The absorbance of the bacterial sample increased significantly within the first 48 hours ($p_{S0h\text{-}S48h} = 0.0015$) from 0.33 ± 0.029 A.U. to 0.40 ± 0.023 A.U., but was not significantly different from the control at 48h ($p_{C48h\text{-}S48h} = 0.87$). The bacterially treated sample continued to increase throughout the remainder of the experimental time course to a final O.D. of 0.61 ± 0.15 A.U. (1.9-fold) ($p_{S0h\text{-}S168h} = 1e\text{-}8$), corresponding to an aqueous iron concentration ($Fe(II)_{(aq)}$) of 132.5 ± 17.5 ppm. The absorbance in the bacterial sample after 168h was also significantly greater than the control at 168h ($p_{C168h\text{-}S168h} = 0.004$). This indicates a successful and significant reduction after 72 and 168 hours of Fe(III) to Fe(II) in EAC-1.
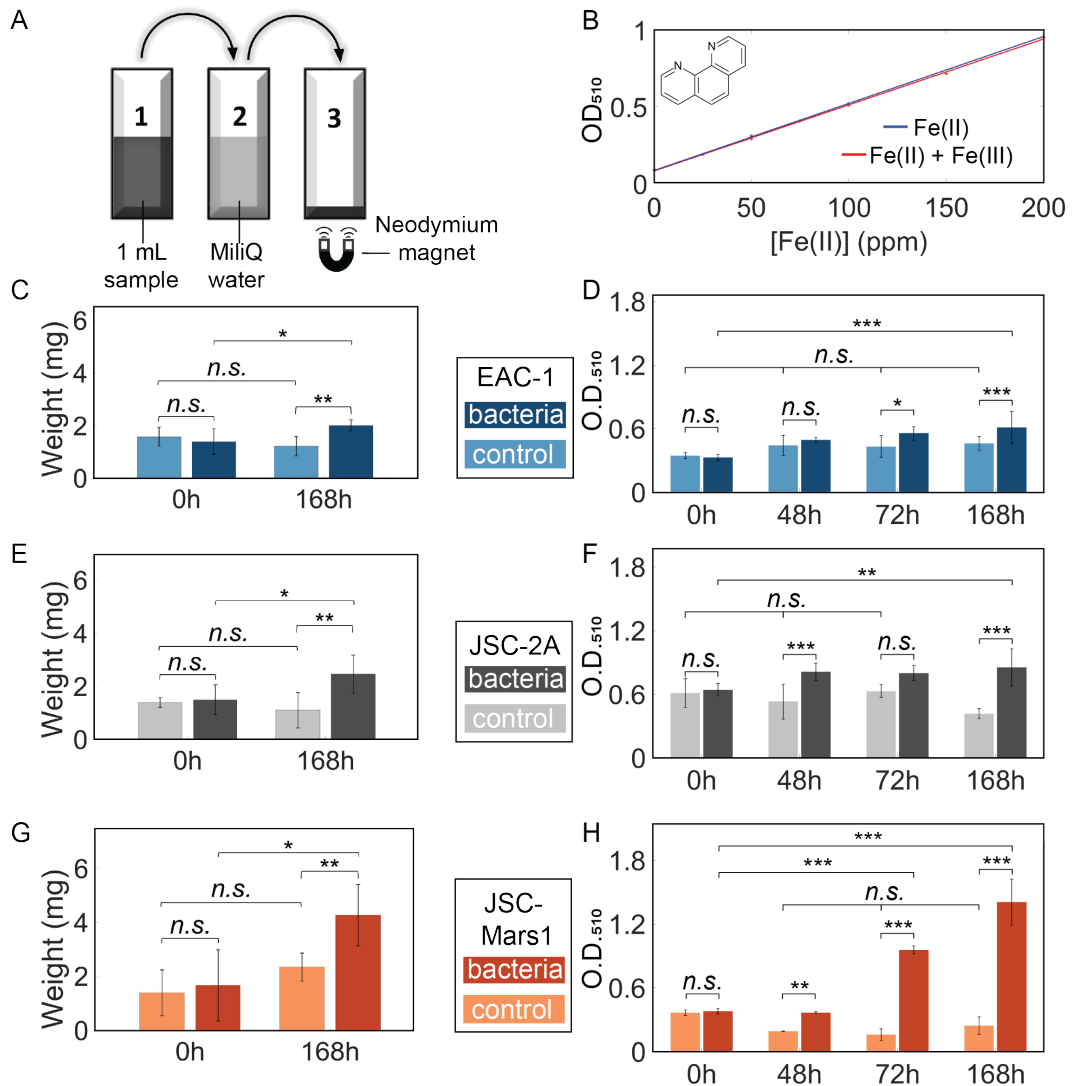
Fig. 7.3 Aerobic extraction of magnetic material from EAC-1 (blue), JSC-2A (grey), and JSC-Mars1 (orange) regolith simulants. The darker colour in each plot represents the bacterial sample, the lighter one the no-bacteria control. The set-up of the assay to quantify the magnetically extracted material (A) is displayed. Absorbance of iron standards bound to 1,1 O-phenanthroline (B) in the absence and presence of Fe(III). Weight of magnetically extracted material from samples containing a 10g/L EAC-1 (C), JSC-2A (E) and JSC-Mars1 (G) solution with and without *Shewanella* after 0h and 168h (n=6). Absorbance of the colorimetric iron determination of 10 g/L EAC-1 (D), JSC-2A (F) and JSC-Mars1 (H) treated with aerobic *Shewanella oneidensis* MR-1 over 168h (n=9). The standard deviation is given for the bar plots (one-way ANOVA with Tukey PostHoc test: n.s. > 0.05; * ≤ 0.05; ** ≤ 0.01; *** ≤ 0.001).

In comparison to EAC-1, the amount of magnetically extracted material from JSC-2A regolith (Fig. 7.3E) increased more strongly between the 0h (1.5 ± 0.21 mg) and 168h (2.5 ± 0.27 mg) bacterially treated sample ($p_{S0h\text{-}S168h}$ = 0.038). The 168h bacterially treated sample showed also significantly higher extraction weights than the 0h ($p_{C0h\text{-}S168h}$ = 0.019), and the 168h no bacteria control ($p_{S168h\text{-}C168h}$ = 0.0027). No significant differences were detected between the two no-bacteria controls ($p_{C0h\text{-}C168h}$ = 0.83), nor between the bacterial sample and the control at 0h (n = 6, one-way ANOVA with Tukey PostHoc test, $p_{S0h\text{-}C0h}$ = 0.98). *Shewanella oneidensis* is, therefore, capable to increase the amount of magnetically extracted material in JSC-2A significantly (1.7-fold).

The starting $Fe(II)_{(aq)}$ concentration in the JSC-2A bacterial samples (Fig. 7.3F) at 0h was almost double (0.64 ± 0.059 A.U.) that of EAC-1. The bacterially treated sample was significantly higher than the no bacteria control at 48 hours ($p_{C48h\text{-}S48h}$ = 3e-5), and 168 hours ($p_{S168h\text{-}C168h}$ = 1e-8), but not for 72h ($p_{C72h\text{-}S72h}$ = 0.087). There was a significant increase between the bacterial sample at 0h and 48h ($p_{S0h\text{-}S48h}$ = 0.035) as well as 168h ($p_{S0h\text{-}S168h}$ = 0.0051) to a maximum of 0.85 ± 0.18 A.U. (1.3-fold), corresponding to a $Fe(II)_{(aq)}$ concentration of 192.5 ± 25 ppm. However, the control at 168h was also significantly different from the control at 0h ($p_{C0h\text{-}C168h}$ = 0.0086). The rest of the controls did not have any significant differences between each other at any timepoint (n = 9, one-way ANOVA with Tukey PostHoc test, p > 0.05). This shows a significant, but smaller, reduction also happens in the Fe(III) poor bacterially treated JSC-2A regolith simulant.

The JSC-Mars1 sample (Fig. 7.3G) showed the highest increase (2.5-fold) between the 0h (1.7 ± 1.2 mg) and the 168h (4.3 ± 1.04 mg; $p_{S0h\text{-}S168h}$ = 5.5e-5) bacterial sample in all aerobically tested regolith simulants. The magnetically extracted weight of the 168h bacterial sample was also significantly higher than the 168h control ($p_{S168h\text{-}C168h}$ = 0.025) and 0h control ($p_{C0h\text{-}S168h}$ = 1.02e-5). There were no significant differences

between the controls ($p_{C0h-C168h}$ = 0.32), nor the control and bacterial sample at 0h (One-way ANOVA with Tukey PostHoc test, $p_{S0h-C0h}$ = 0.89). The ferrous iron (Fe(II)$_{(aq)}$) concentration of *Shewanella oneidensis* grown aerobically on 10 g/L JSC-Mars1 (Fig. 7.3H) was significantly elevated in the 0h no-bacteria control compared to the 48h and 72h controls ($p <$ 0.05), but not in the 168h control ($p_{C0h-C168h}$ = 0.071). However, significant changes in the Fe(II)$_{(aq)}$ concentration did occur in the bacterial JSC-Mars1 sample, which increased from an initial value of 0.38 ± 0.025 A.U. at 0h to 0.95 ± 0.036 A.U. after 72h ($p_{S0h-S72h}$ = 1e-8) and to 1.4 ± 0.22 A.U. after 168h equalling a 3.7-fold increase and a total Fe(II)$_{(aq)}$ concentration of 330 ± 35 ppm ($p_{S0h-S168h}$ = 1e-8). For all timepoints besides 0h, the bacterial sample was also significantly different from its respective controls (One-way ANOVA with Tukey PostHoc test, $p <$ 0.05). JSC-Mars1 was therefore the best candidate for bacterial treatment and magnetic extraction showing the highest increase in extractable material and dissolved Fe(II)$_{(aq)}$ concentration. All anaerobic measurements were performed on this regolith simulant.

7.2.4 Magnetic extraction and Fe(II)$_{(aq)}$ content under anaerobic conditions

Anaerobic growth experiments were performed to assess the reduction capability of *Shewanella oneidensis* without the availability of oxygen as additional electron acceptor. The first anaerobic set of experiments used rich TSB as the growth medium. Quantification of the magnetically extracted materials (Fig. 7.4A) displayed a significant increase after both 72h (4.0 ± 0.74 mg) and 168h (3.6 ± 1.4 mg) compared to the no-bacteria control samples and the 0h bacterial sample (1.5 ± 0.31 mg) ($p_{S72h-C72h}$ = 3.3e-5, $p_{S0h-S72h}$ = 0.00021, $p_{S168h-C168h}$ = 0.0059, $p_{S0h-S168h}$ = 0.00061). The amount of material extracted from the bacterial samples increased 2.7-fold between 0h and 72h and 2.4-fold between 0h and 168h. No significant increase in extracted material was seen in the no-bacteria sample over time, nor between the bacterially treated samples at 72h and

168h (One-way ANOVA with Tukey PostHoc test, $p > 0.05$). The anaerobic magnetically extracted and bacterially treated material of JSC-Mars1 gave, therefore, a similar result after 168h than the aerobic one, but unlike the aerobic one the maximal yield was already reached after 72hours.

The colorimetric assay, testing the ferrous iron concentration ($Fe(II)_{(aq)}$), displayed no significant differences between the absorbances of the control samples (Fig. 7.4B), nor between the bacterial sample and the control at 0h (One-way ANOVA with Tukey PostHoc test, $p > 0.05$). The bacterially treated sample showed a 3.6-fold, significant increase of $Fe(II)_{(aq)}$ after 48h and a 5.8-fold significant increase to a maximum of 270 ± 52.5 ppm after 72h compared to the 0h sample ($p_{S48h-C48h} = 1e-8$, $p_{S0h-S48h} = 1e-8$, $p_{S72h-C72h} = 1e-8$, $p_{S0h-S72h} = 1e-8$). Interestingly, the $Fe(II)_{(aq)}$ concentration of the bacterial sample decreased significantly after 168h (100 ± 12 ppm) compared to the 72h one (One-way ANOVA with Tukey PostHoc test, $p_{S168h-S72h} = 1e-8$). The higher and faster increase in $Fe(II)_{(aq)}$ than in the aerobic JSC-Mars1 samples indicates that the reduction of Fe(III) to Fe(II) was improved under anaerobic conditions.

JSC-Mars1 regolith simulant was also incubated anaerobically with *Shewanella* in a minimal, defined medium instead of the nutrient-rich TSB medium. A minimal medium holds the advantage that its nutrients can be fully utilized, which is essential to reduce the transportation weight for space applications. Quantification of the magnetically extracted material (Fig. 7.4C) showed no significant differences between any of the controls ($p > 0.5$). However, the bacterially treated, magnetically extracted samples increased significantly after 72h to 3.1 ± 0.70 mg (3.8-fold) and 168h to 4.4 ± 2.8 mg (5.5-fold) in comparison to the 0h bacterially treated sample (0.8 ± 0.34 mg) and the no-bacteria control at 168h ($p_{S0h-S72h} = 0.05$, $p_{S168h-C168h} = 0.0059$, $p_{S0h-S168h} = 0.00061$). Unlike the anaerobic sample with TSB, no significant difference between the bacterially treated sample and the control after 72h was measured (One-way ANOVA with Tukey PostHoc test, $p_{S72h-C72h} = 0.36$). The absolute weight of the magnetically

extracted material after 168h of anaerobic bacterial treatment of JSC-Mars1 in minimal defined medium (4.4 ± 2.8 mg) is comparable to the one of the anaerobic extractions from JSC-Mars1 in TSB (3.6 ± 1.4 mg) and the aerobic JSC-Mars1 one (4.3 ± 1.04 mg).

The $Fe(II)_{(aq)}$ concentration in the colorimetric assay didn't display significant differences between the no-bacteria controls at any timepoint (Fig. 7.4D), nor between the control and the bacterial sample at 0h (p > 0.05). A significant, 3.1-fold increase in Fe(II) to a maximum concentration of 97.5 ± 0.47 ppm was observed for the bacterial sample after 72h compared to 0h ($p_{S0h-S72h} = 0.0082$), followed by a significant decrease to 45 ± 1.75 ppm after 168 ($p_{S72h-S168h} = 0.013$). Only the 72h bacterially-treated sample showed a significant higher $Fe(II)_{(aq)}$ concentration compared to its respective 72h no bacteria control (One-way ANOVA with Tukey PostHoc test, $p_{S72h-C72h} = 0.00089$). However, the increase in ferrous iron was lower than observed in the experiments using TSB. This later and lower increase of $Fe(II)_{(aq)}$ corresponded with the non-significant increase in the extracted weight after 72h in the bacterial sample. The experiments in a minimal defined medium showed a significant increase in both, the $Fe(II)_{(aq)}$ concentration as well as the magnetically extracted material, after 72h and need the least resources, which makes them the optimal choice for space exploration.

We performed high-resolution X-ray photoelectron spectroscopy (XPS) measurement (Fig. 7.4E) to investigate the shift between the total Fe(II) and Fe(III) amount in the anaerobically bacterially treated JSC-Mars1 samples after 0h and 168h. The XPS spectrum indicated the successful partial reduction of Fe(III) to Fe(II). An increase in the signal was observed around 715 eV and 728 eV corresponding to Fe(II) satellite peaks. On the other hand, the signals at 720 eV and 734 eV, corresponding to Fe(III) satellite peaks, showed a lower intensity for the treated samples. The XPS measurement confirmed the results of the colorimetric assay that a successful anaerobic reduction of Fe(III) in JSC-Mars1 is visible.
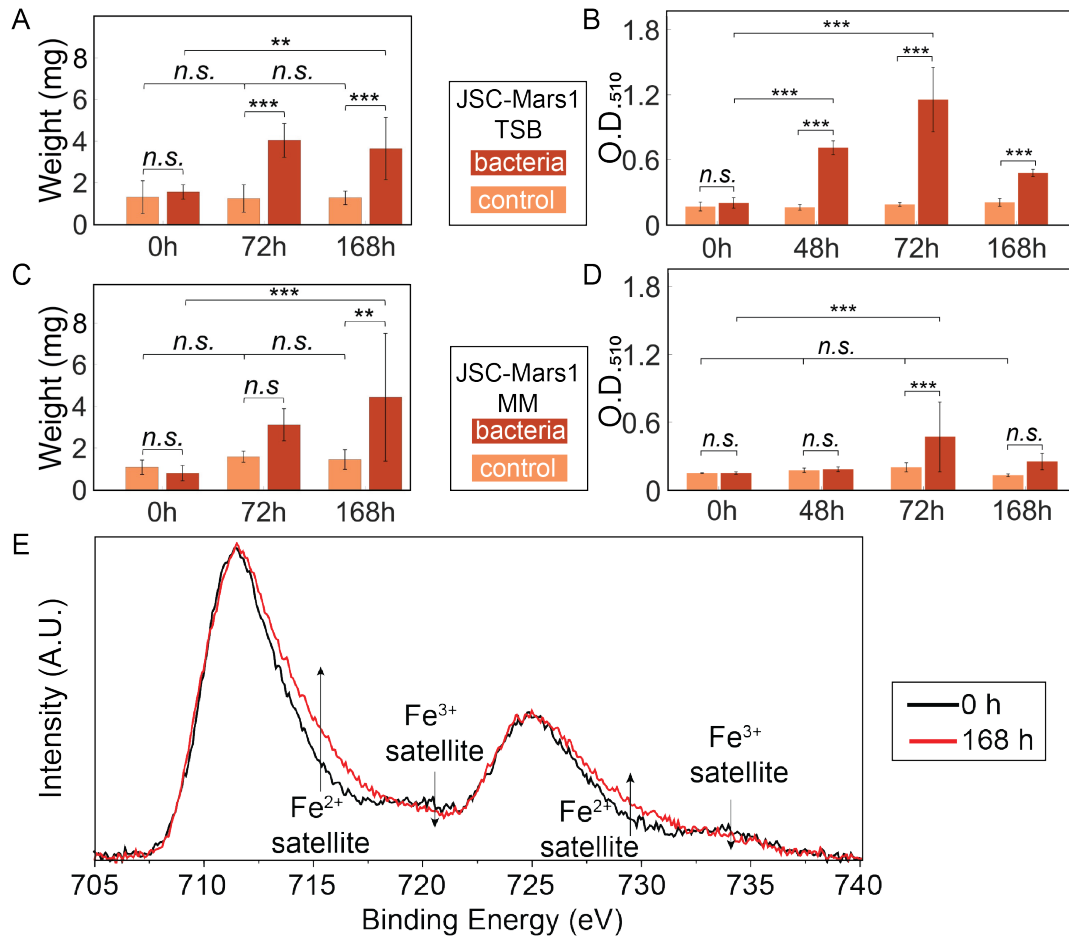
Fig. 7.4 Anaerobic extraction of magnetic material from bacterially-treated JSC-Mars1 regolith simulant. The amount of magnetically extracted material from a 10g/L JSC-Mars1 regolith simulant anaerobically incubated with (red) or without (orange) *Shewanella* bacteria in TSB (A) or defined minimal medium (C) after 0h, 72h and 168h is displayed. The O.D.$_{510}$ values of the colorimetric assay to determine the Fe(II)$_{(aq)}$ concentration of 10 g/L JSC-Mars1 regolith anaerobically incubated with (red) or without (orange) *Shewanella* bacteria in TSB (B) and defined minimal medium (D) is shown. The standard deviation is given for all bar plots (one-way ANOVA with Tukey PostHoc test: n.s. > 0.05; * ≤ 0.05; ** ≤ 0.01; *** ≤ 0.001). (E) X-ray photoelectron spectroscopy of the iron spectrum. A change in the Fe(II) and Fe(III) satellites between the 0h control (black line) and the 168h incubation with *Shewanella oneidensis* (red line) is visible.

7.2.5 Iron and silicon concentration in the magnetically extracted materials

An analysis of the weight percent of iron oxides (Fig. 7.5A) and silicon oxides (Fig. 7.5B) in the different regolith simulant samples was performed via X-ray fluorescence measurement (XRF). A high iron and low silicon concentration are critical to improve the electric as well as mechanical properties and decrease the melting point of the material. *Shewanella oneidensis* was used to reduce Fe(III) and provide more magnetic material which was extracted by a handheld neodymium magnet. The XRF measurements evaluate the compositional changes of this treatment.

No magnetic or bacterial methodology were applied to the "untreated" regolith samples, which are directly comparable to the values given by the supplier. The "treated" samples were regolith simulants incubated with an aerobic *Shewanella oneidensis* culture for 168h. Afterwards, a neodymium magnet was several times applied to the sample to extract as much magnetic material as possible.

In all three regolith types, an increase in the iron wt% (EAC-1 43.6%, JSC-2A 17.1%, JSC-Mars1 18.2%) and a decrease in the silicon wt% (EAC-1 -22.6%, JSC-2A -7.4%, JSC-Mars1 -25.0%) were observed upon bacterial treatment and magnetic extraction compared to the untreated material. The alteration of the composition upon treatment shows that not only the quantity but also quality of the material improves through the application of *Shewanella.* Mechanical tests of 3D printed samples are necessary to understand this alteration completely.
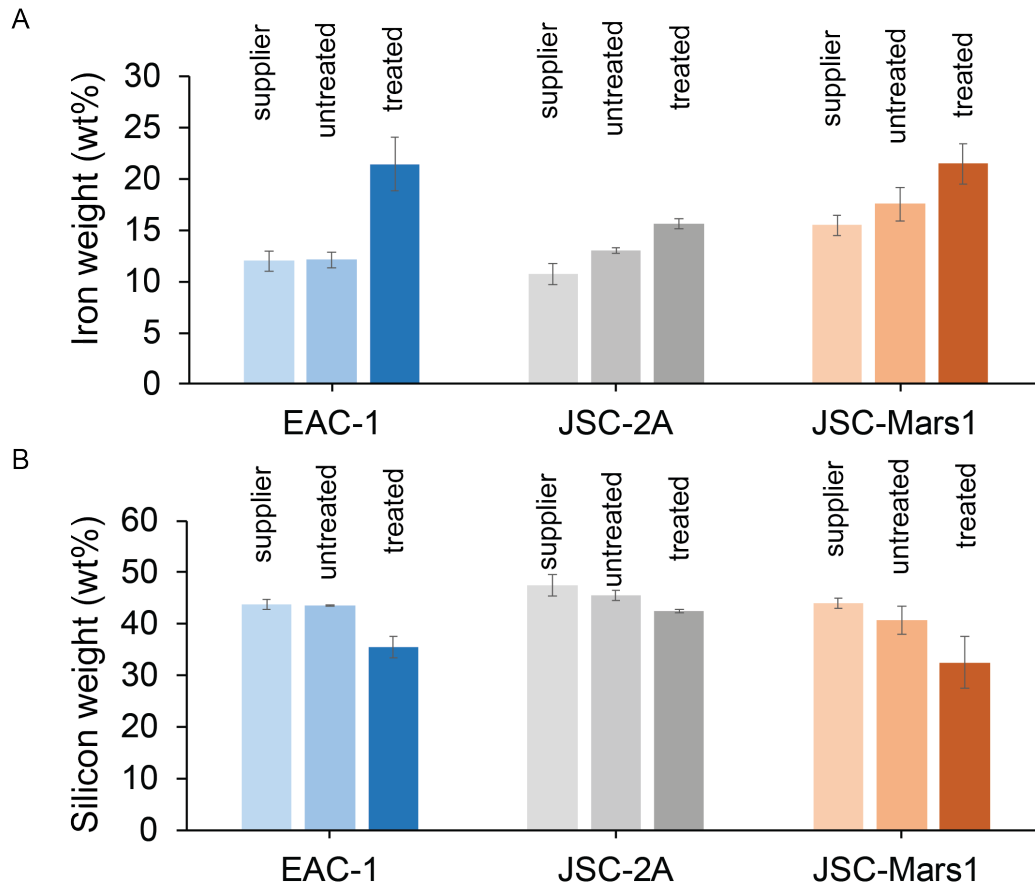
Fig. 7.5 X-Ray fluorescence spectroscopy analyzing the (A) iron concentration (wt%) and (B) silicon concentration (wt%) of the three different regolith simulants types as given by the supplier: "supplier", measured without treatment: "untreated", or bacterially and magnetically treated "treated". The color intensity displays the treatment of the sample (very bright = values from supplier, middle = XRF measurement of the untreated sample, dark = XRF of the 168h bacterially treated and magnetically extracted material) and the color shows the different regolith types (blue = EAC-1, grey = JSC-2A, red = JSC-Mars1). Error bars display the standard deviation.

7.2.6 Plasma printing and lithography based ceramic manufacturing

Two 3D-printing technologies were applied as proof-of-principle technologies for the additive manufacturing of regolith simulants.

Oxygen-plasma treatment of the surface (Fig. 7.6A) of unmodified JSC-1A and EAC-1 with a system from Space Foundry resulted in a solidification of the top layer of the material. However, the energy transferred to the surface was not enough to achieve the necessary melting of the regolith particles leading to incomplete solidification. In a second approach, direct ionization and printing through the plasma nozzle was attempted. We were able to deposit microscopic batches of material, but the system was not optimized for particles of this macroscopic size (up to 63 µm in diameter) leading to continuous clogging of the system.

In a second approach, lithography-based ceramic manufacturing was applied to our samples by Lithoz (Fig. 7.6B). In short, a photosensitive binding material was used to prepare a paste of regolith which was solidified by an LED and mirror system. The first few proof-of-principle prints were successfully performed on unmodified JSC-2A, however, the optimal sintering conditions of the 3D-printed material to prevent cracks are currently investigated. After this fine-tuning process we plan to compare the mechanical properties of bacterially- and magnetically-treated material versus untreated regolith simulants.
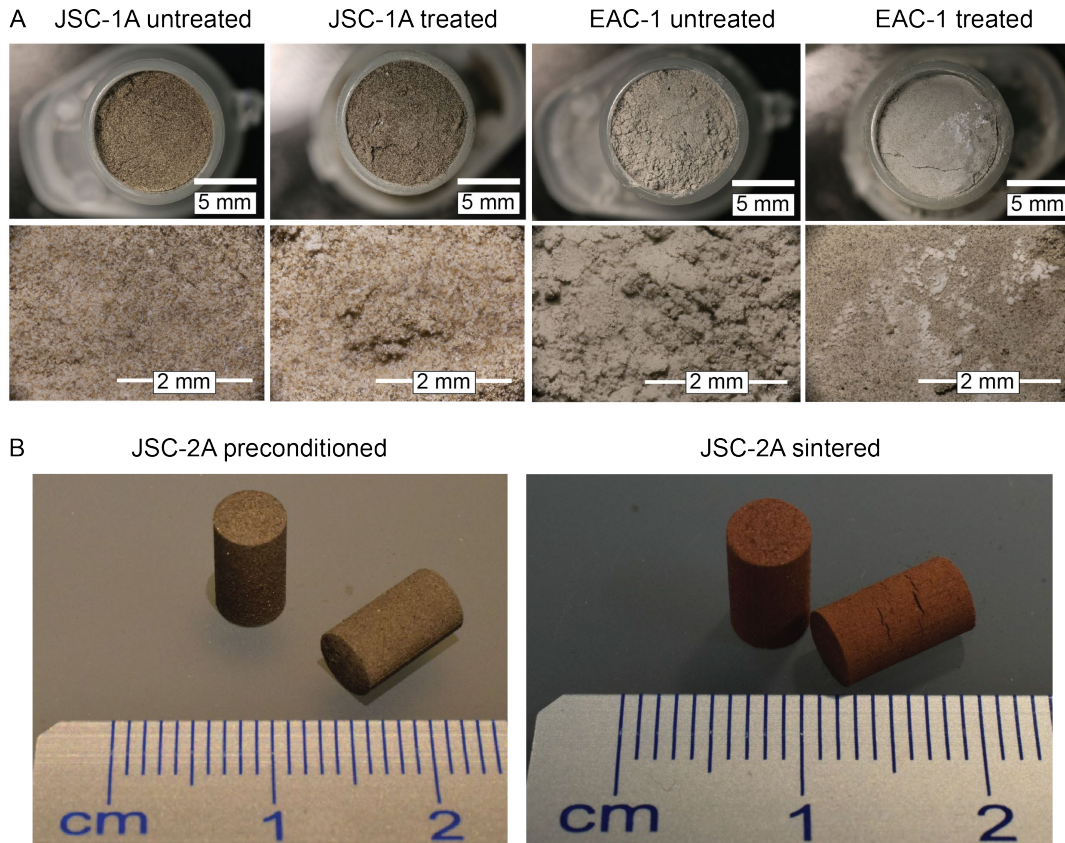
Fig. 7.6 Plasma and lithography based ceramic manufacturing (LCM) prints of three regolith simulants. (A) Light microscope images of plasma-treated and untreated regolith samples (JSC-1A and EAC-1) indicate that the regolith was only altered on the surface and the solidification was weak. (B) Lithography-based ceramic manufacturing of the regolith simulant JSC-2A in precondition state (left) and after sintering (right).

7.5 Conclusion

Altogether, we demonstrate an increase in the iron concentration and the quantity of magnetically extracted material with the bacterial treatment of three different regolith simulants. The iron concentration and quantity are both critical for applying our methodology to 3D printing applications demonstrating an on-demand production work-flow for a space colony.

Shewanella oneidensis growth kinetics were not influenced by the presence of differing regolith simulant types or concentrations, which makes it an excellent candidate for ISRU operations. Its main function in this study is the reduction of Fe(III) to Fe(II) in a range of different regolith simulants, but also other factors as the, with the reduction connected, bioleaching activity [28] and the generation of local pH values [17] at the cell membrane might be beneficial for our methodology. The two lunar regolith simulants JSC-2A and EAC-1 consist primarily of Fe(II)-containing minerals, making them a worse target than the mainly Fe(III)-containing Mars regolith simulant JSC-Mars1.

The ratio of Fe(II) to Fe(III) in JSC-2A [25] is 2.2 : 1 compared to a ratio of 1 : 3.5 in JSC-Mars1 [24]. Those ratios explain the high starting concentration of EAC-1 (62.5 $\pm$ 12.75 ppm Fe(II)$_{(aq)}$) and JSC-2A (140 $\pm$ 5.25 ppm Fe(II)$_{(aq)}$). JSC-Mars1 has a higher total amount of iron, which resulted in an increased starting concentration of 75 $\pm$ 13.75 ppm Fe(II)$_{(aq)}$ in aerobic conditions, however this value for the 0h sample is significantly elevated in comparison to the other controls and the anaerobic starting concentrations of Fe(II)$_{(aq)}$ in JSC-Mars1. Variations like that might appear due to difficulties in pipetting the same number of not dissolved particles every time.

The aerobic bacterially treated EAC-1 and JSC-2A samples only show a 1.9-fold and 1.3-fold increase in dissolved Fe(II)$_{(aq)}$ respectively, compared to the 3.7-fold upturn in bacterially treated JSC-Mars1. Remarkably, the quantity (weight in mg) of extracted material, nevertheless, increased

significantly by 1.7-fold in JSC-2A after 168 hours of bacterial treatment. The magnetic extraction in EAC-1 show some significant increases in the bacterially treated sample but are inconclusive. The comparison of the $Fe(II)_{(aq)}$ concentration (JSC-2A < EAC1) and the increase in the bacterially treated, magnetically extracted material (EAC-1 < JSC-2A) samples indicate that not only the reduction, but also other bacterial functions as bioleaching and the generation of local pH values, play an important role in this methodology.

Nevertheless, the highest increase in weight of magnetically extracted material (2.5-fold) and $Fe(II)_{(aq)}$ concentration (3.7-fold) under aerobic conditions was measured in bacterially treated JSC-Mars1 samples. Because of the high Fe(III) concentration in JSC-Mars1 this result was to be expected. The successful magnetic extraction in the mainly Fe(II) bearing regolith simulants JSC-2A and EAC-1 might also be due to surface oxidation during their storage leading to more Fe(III). None of the regolith simulants were stored in an oxygen-free environment and especially the surface is vulnerable to atmospheric oxidation.

The anaerobic bacterially induced reduction of Fe(III) in JSC-Mars1 with TSB as growth medium resulted in an even further, compared to the aerobic experiments, improved increase of $Fe(II)_{(aq)}$ after 72h (5.8-fold). Interestingly, the $Fe(II)_{(aq)}$ concentration of the bacterial sample decreased after 168h. The enhanced reduction and high concentration of reduced iron could potentially favour a faster precipitation of the produced magnetite, making the iron unavailable for the colorimetric assay. The same result was seen in the defined minimal medium, where the reduction had a maximum at 72 hours of 3.1-fold increase, compared to the 0 hour bacterially treated sample. The overall lower values might be caused by fewer Fe(III) ions in the defined medium compared to the rich TSB medium.

A less efficient reduction mechanism, due to starvation, in the minimal medium under anaerobic conditions is unlikely because of the 5.5-fold increase in magnetically extracted bacterially treated JSC-Mars1 regolith

simulant after 168h compared to the bacterial sample at 0h. This is the highest increase in extracted material, however, the standard deviation in the sample is more than 50% of the average and the sample at 0h resulted in a very low starting weight of 0.8 mg. The anaerobic magnetic extraction in TSB medium was already after 72h at its maximum which shows the improved reduction capability in a rich medium under anaerobic conditions. The improved reduction and extraction in anaerobic conditions was expected due to absence of oxygen as an alternative electron acceptor. In this environment, all electrons produced during the incubation with *Shewanella oneidensis* have to be donated to the metal oxides of the regolith simulants as end terminal acceptor. Nevertheless, the maxima of all three conditions in which JSC-Mars1 was bacterially treated are without significant differences, making the minimal medium under anaerobic conditions the optimal candidate for space exploration, where the transport of additional nutrients or oxygen is a high burden on its feasibility.

The increase in iron and decrease in silicon concentration after the bacterial and magnetic treatments are essential quality factors for 3D printing application. The stability of the 3D printed material might be positively influenced due to the good mechanical properties of iron. Also, the melting point of the material is further reduced, which allows for better sintering conditions [29]. Additional 3D printing experiments coupled to material tests are necessary to confirm this claim.

Our general hypothesis is that primarily the surface of the regolith simulant particles gets reduced by *Shewanella oneidensis* [30]. It is likely that bacterial reduction of Fe(III) to Fe(II) results in the appearance of more magnetic areas on the surface of regolith particles, so that an increased number of particles can be magnetically extracted. JSC-Mars1 has both a higher iron concentration as well as a higher Fe(III) : Fe(II) ratio, presumably leading to an increased extraction yield after applying our methodology. This JSC-Mars1 regolith simulant is expected to have a composition similar to many potential landing sites on Mars.

The methodology presented here shows the extraction of iron-rich material from different regolith materials for 3D-printing application to build habitat or replacement parts with, compared to raw regolith, improved mechanical properties (screws, airlock, antennas, etc.). This technology will enhance the *in situ* resource utilization possibilities of humans using microorganisms and will, therefore, pave the way for future space exploration and Mars colonialization.

7.4 Materials & methods

7.4.1 Growth conditions & regolith pretreatment

Shewanella oneidensis MR-1 (ATCC® 700550™) was inoculated into sterilized 32 g/L Tryptic Soy Broth (TSB) media and planktonically grown overnight under aerobic conditions at 30°C under continuous shaking (180-250 rpm) to an O.D.$_{600}$ of 0.5.

All regolith simulant samples were sieved down to a maximum diameter of 63 μm. Only the particles smaller than 63 μm were used for further experiments.

7.4.2 Preparation of anaerobic samples

Regolith was diluted to the desired concentration in TSB or defined minimal medium. The defined minimal medium was prepared by mixing 100 mM NaCl, 50 mM sodium 4-(2-hydroxyethyl)-1-piperazineethanesulphonic acid (HEPES), 7.5 mM NaOH, 16 mM NH_4Cl, 1.3 mM KCl, 4.3 mM $NaH_2PO_4 \cdot 2H_2O$ and 10 mL/L trace mineral supplement (ATCC® MD-TMS™) [31]. The defined minimal medium was autoclaved, after which it was supplemented with 10 mL/L vitamin solution (ATCC® MD-VS™) [32], 20 mg/L of L-arginine hydrochloride, 20 mg/L L-glutamate, 20 mg/L L-serine, and 20 mM lactate [33]. The samples were prepared in anaerobic culture tubes (Sigma Aldrich) and flushed 3x with 100% nitrogen gas to deplete the oxygen present in the solutions. After 24 hours, *Shewanella oneidensis* overnight cultures were added to the samples to a final O.D.$_{600}$ of 0.05. The samples

were sealed with sterilized nontoxic chlorobutyl stoppers and aluminium lids (Sigma Aldrich).

7.4.3 Toxicity study

Previously sterilized regolith simulant samples were sterilized via autoclaving and diluted to the desired concentration in TSB. Overnight cultures of *Shewanella oneidensis* were added to the samples to a final O.D.$_{600}$ of 0.05. The bacterial growth in the samples was observed in a 96-well plate via optical density (O.D.) measurements in a plate reader (Synergy HTX, Multimode reader) at a wavelength of 600 nm, during incubation at 30°C with continuous shaking (250 rpm) under aerobic or anaerobic conditions. Absorbance was measured every 5 minutes for 48 hours. The samples were measured in triplicate.

In parallel, the same samples were used to measure colony forming units (CFU). A logarithmic dilution curve to a 10^{-7} dilution of every sample was prepared and plated out in triplicate onto LB agar plates at the 0, 24, and 48-hour timepoints. Dilution was carried out using phosphate-buffered saline (PBS) solution. After a growth period of 24 hours at room temperature (20-22°C), individual colonies were counted.

7.4.4 Fe(II)$_{(aq)}$ concentration determination

Iron concentrations were determined based on a colorimetric method [34], which is a modification of the phenanthroline method [35]. By dissolving 0.6 grams sodium fluoride (Sigma-Aldrich, 99%) in 28 mL MilliQ water and 0.57 mL sulfuric acid (Sigma-Aldrich, 99.999%), a complexing reagent was formed. An 1,1O-phenanthroline solution was prepared mixing 30 µL of hydrochloric acid (37%) with 7 mL MiliQ water and dissolving 0.2 grams 1,1O-phenanthroline monohydrate (Sigma-Aldrich, 99%) in it. The complexing reagent was shaken and 10 mL of MilliQ water was added.

An acetate buffer was prepared by mixing 3 mL MilliQ water with 12 mL acetic acid (50 mM) and dissolving 5 grams ammonium acetate (Biosolve

B.V.) into it. The acetate buffer was shaken, and MilliQ water was added up to a total volume of 20 mL. The reaction reagent was prepared by mixing 5 mL of the 1,1O-phenanthroline solution with 5 mL of the acetate buffer. To determine the ferrous iron concentration of a specific sample, 0.1 mL of the sample was pipetted into a 5 mL microtube (Eppendorf). Next, 1 mL of the complexing fluoride reagent was added, the solution was shaken, and 0.4 mL of the reaction reagent was pipetted into it. Samples were agitated, then MilliQ water was added to the samples up to 2.5 mL. A volume of 200 µL of the sample was pipetted in triplicate into a 96-well plate (SARSTEDT). Samples were incubated for five minutes, then the absorbance of the 96-well plate was measured at 510 nm (Tecan infinite M200 pro microplate reader).

7.4.5 Magnetic extraction apparatus

The magnetic extraction set-up consisted of three 3 mL cuvettes (Sigma Aldrich) and a 60x10x3 mm neodymium magnet (Mikede) with a self-made Parafilm-wrapped aluminium cover. In short, the bottom half of the magnet was tightly wrapped with two layers of aluminium foil and two layers of parafilm. The design allowed for an easy removal and insertion of the magnet. The first cuvette was filled with 1 mL of the sample, and the second and third were filled with MilliQ water. The magnet with cover was inserted into the first cuvette twice. Magnetic material was attracted to the magnet's cover, and the covered magnet with associated magnetic material was transferred to the second cuvette for washing. The magnet with cover and magnetic material were finally placed into the third pre-weighed cuvette. The cover was left in the cuvette, the magnet was removed and an additional neodymium magnet was placed underneath the cuvette. The liquid, which was not attracted by the magnet was decanted, and the cuvettes were weighted after they had dried. The original weight of each individual cuvette was subtracted from the total weight after addition of extracted material.

7.4.6 Large-scale magnetic extraction

Magnetic extractions were performed by preparing a 10 g/L solution of previously sieved (<63 µm) EAC-1, JSC-2A, or JSC-Mars1 regolith simulants with TSB medium. An overnight culture of *Shewanella* was added to an O.D.$_{600}$ of 0.05 and grown for 168h at 30℃ with shaking at 120 rpm. Neodymium magnets were wrapped in two layers of aluminum foil covering the ends of the magnets, after which the foil-tipped magnets were wrapped completely in a layer of Parafilm. After the 168-hour incubation, the wrapped magnet was placed into the solution, the flask was swirled five times, the material was allowed to settle for 30 seconds, and the magnet was extracted again by using rubber tweezers and additional neodymium magnets. The extracted magnet was washed in a 50 mL Falcon tube containing MilliQ water. Scissors were used to cut open the middle region of the Parafilm magnet-cover, the magnet was removed from the cover, and the cover was rinsed into an empty petri dish. This process was repeated until the amount of extracted material per magnet was so little that continuation would not result in an effectively higher yield. The non-magnetic material was collected by rinsing it out of the flask into an additional Petri dish.

7.4.7 X-ray fluorescence measurements (XRF)

A pressed powder tablet was prepared by adding 0.25 g Boreox (FLUXANA) to 1 g of the tested regolith simulant (untreated and treated JSC-2A, JSC-Mars1, EAC-1). The mixture was milled using a malachite mortar until a uniform mixture was achieved. About 5 g of Boreox was added to a hollow metal cylinder and pressed on a hydraulic press up to 10 kPa/cm^2 (P/O/Weber Laborpresstechnik). The mixture of regolith and Boreox was added to the metal cylinder and pressed up to 250 kPa/cm^2. The pressed tablet was analyzed with an X-ray fluorescence spectrometer (Axios Max WD-XRF, Malvern Panalytical Ltd). Analysis of the XRF data was performed with SuperQ5.0i/Omnian software.

7.4.8 X-ray diffraction measurements (XRD)

Approximately 100 mg of regolith simulant was equally distributed over a silicon crystal sample holder (Si510 wafer). XRD measurements were taken using a diffractometer (D8 Advance, Bruker) with Bragg-Brentano geometry and a Lynxeye position-sensitive detector. Cu Kα radiation was used at under 45 kV and 40 mA, with a scatter screen height of 5 mm. The sample was scanned with an incident ray varying from 8° - 110°, with a step size of 0.021° * 2θ (in which θ is the angle between the incident ray and the surface of the sample) and a counting time of 1 second per step. Analysis of the XRD data was performed with Bruker software DiffracSuite.EVA v 5.0.

7.4.9 X-ray photoelectron spectrometry (XPS)

The samples were analysed with X-ray photoelectron spectroscopy (XPS) on a ThermoFisher K-Alpha system using Al Kα radiation with a photon energy of 1486.7 eV. The powders were immobilized onto a copper tape (Plano GmbH, G3397) and were loaded into the XPS chamber without further purification. Iron high-resolution XPS spectra were acquired using a spot size of 400 μm, 50 eV pass energy, and 0.1 step size, averaging 50 scans from 705 eV to 740 eV with charge neutralizing. The peaks were calibrated for the C 1s peak at 285 eV. The background was subtracted using the "smart" function of the ThermoFisher Advantaged software.

7.4.10 Plasma printing

The regolith simulants JSC-1AF (bacterially treated and untreated) as well as untreated EAC-1 were deposited in the top of a 1 mL Eppendorf vial. An aerosol plasma jet printer (Space Foundry, San Jose, CA, USA) produced the dielectric barrier discharge plasma jet used to treat the samples [36]. Unlike a global treatment across the entire surface, the system used a precision motion system to localize the energy deposition to a spot and then move that spot along a programmed trajectory to draw patterned

lines of energy deposition across the surface. The plasma is ignited through a potential between two electrodes with Argon at a flow rate of 1200 SCCM passing through a quartz nozzle. The nozzle moved with a speed of 0.05 mm/s. The surface was treated three times. After the plasma treatment, the experimental samples (and controls) were examined for grain structure and topographic changes using a camera (EOS T5i, Canon) outfitted with a manual-focus macro photo lens (MP-E 65mm, Canon). A programmable rail system (Stack Shot Macro Rail Package, Cognisys) incrementally raised the sample towards the camera as images were taken, thereby capturing a sequence of dozens of photographs across several millimetres of depth. The final images from each sample represent a composite automatically prepared using focus stacking software (Zerene Stacker, Zerena Systems LLC).

7.4.10 Lithography based ceramic printing

The regolith simulant JSC-2A was mixed with 46vol% of a photopolymer (Lithoz) to prepare a printing paste. The lithography based 3D prints were produced on a CeraFab 7500. In short, the light engine (based on LEDs) with a digital micromirror device was used to harden the previously prepared regolith simulant containing paste layer by layer into the appropriate shape [37]. The so-preconditioned 3D-print was dried at 120°C and sintered at 1000 °C.

7.5 References

[1] L.J. Rothschild, Synthetic biology meets bioprinting: enabling technologies for humans on Mars (and Earth), Biochem Soc Trans 44(4) (2016) 1158-64.

[2] M. Montague, G.H.t. McArthur, C.S. Cockell, J. Held, W. Marshall, L.A. Sherman, N. Wang, W.L. Nicholson, D.R. Tarjan, J. Cumbers, The role of synthetic biology for in situ resource utilization (ISRU), Astrobiology 12(12) (2012) 1135-42.

[3] C. Schwandt, J.A. Hamilton, J.D. Fray, I.A. Crawford, W. Marshall, The production of oxygen and metal from lunar regolith, Planetary and Space Science 74(1) (2012) 49-56.

[4] M. Anand, I.A. Crawford, M. Balat-Pichelin, M. Abanades, W. van Westrenen, R. Peraudeau, R. Jaumann, W. Seboldt, A brief review of chemical and mineralogical resources on the Moon and likely initial in situ resource utilization (ISRU) applications, Planetary and Space Science 74(1) (2012) 42-48.

[5] L.A. Taylor, T.T. Meek, Microwave Sintering of Lunar Soil: Properties, Theory, and Practice, Journal of Aerospace Engineering 18(3) (2005).

[6] D.T. Schmieden, Meyer, A.S., Aubin-Tam, M.-E., Using bacteria to make improved, nacre-inspired materials., MRS Advances 1(8) (2016) 559-564.

[7] T. Lytvynenko, I. Zaetz, T. Voznyuk, M. Kovalchuk, I. Rogutskyy, O. Mytrokhyn, D. Lukashov, V. Estrella-Liopis, T. Borodinova, S. Mashkovska, B. Foing, V. Kordyum, N. Kozyrovska, A rationally assembled microbial community for growing Tagetes patula L. in a lunar greenhouse, Res Microbiol 157(1) (2006) 87-92.

[8] B.A. Lehner, D.T. Schmieden, A.S. Meyer, A Straightforward Approach for 3D Bacterial Printing, ACS Synth Biol (2017).

[9] G.K. Dosier, Methods for Making Construction Material Using Enzyme Producing Bacteria, Google Patents, 2011.

[10] T. Hiraishi, Poly(aspartic acid) (PAA) hydrolases and PAA biodegradation: current knowledge and impact on applications, Appl Microbiol Biotechnol 100(4) (2016) 1623-30.

[11] G. Wang, F. Qian, C.W. Saltikov, Y. Jiao, Y. Li, Microbial reduction of graphene oxide by Shewanella, Nano Research 4(6) (2011) 563-570.

[12] B.A.E. Lehner, V.A.E.C. Janssen, E.M. Spiesz, D. Benz, S.J.J. Brouns, A.S. Meyer, H.S.J. van der Zant, Creation of Conductive Graphene Materials by Bacterial Reduction Using Shewanella Oneidensis, ChemistryOpen 8(7) (2019) 888-895.

[13] B.A.E. Lehner, J. Schlechten, A. Filosa, A. Canals Pou, D.G. Mazzotta, F. Spina, L. Teeney, J. Snyder, S.Y. Tjon, A.S. Meyer, S.J.J. Brouns, A. Cowley, L.J. Rothschild, End-to-end mission design for microbial ISRU activities as preparation for a moon village, Acta Astronautica 162 (2019) 216-226.

[14] C.R. Myers, K.H. Nealson, Bacterial Manganese Reduction and Growth with Manganese Oxide as the Sole Electron Acceptor, Science 240(4857) (1988) 1319.

[15] O. Bretschger, A. Obraztsova, C.A. Sturm, I.S. Chang, Y.A. Gorby, S.B. Reed, D.E. Culley, C.L. Reardon, S. Barua, M.F. Romine, J. Zhou, A.S. Beliaev, R. Bouhenni, D. Saffarini, F. Mansfeld, B.-H. Kim, J.K. Fredrickson, K.H. Nealson, Current Production and Metal Oxide Reduction by Shewanella oneidensis MR-1 Wild Type and Mutants, Applied and Environmental Microbiology 73(21) (2007) 7003.

7

[16] D.L. Bish, D.F. Blake, D.T. Vaniman, S.J. Chipera, R.V. Morris, D.W. Ming, A.H. Treiman, P. Sarrazin, S.M. Morrison, R.T. Downs, C.N. Achilles, A.S. Yen, T.F. Bristow, J.A. Crisp, J.M. Morookian, J.D. Farmer, E.B. Rampe, E.M. Stolper, N. Spanovich, X-ray Diffraction Results from Mars Science Laboratory: Mineralogy of Rocknest at Gale Crater, Science 341(6153) (2013) 1238932.

[17] T. Perez-Gonzalez, C. Jimenez-Lopez, A.L. Neal, F. Rull-Perez, A. Rodriguez-Navarro, A. Fernandez-Vivas, E. Iañez-Pareja, Magnetite biomineralization induced by Shewanella oneidensis, Geochimica et Cosmochimica Acta 74(3) (2010) 967-979.

[18] J. F Lindsay, Lunar stratigraphy and sedimentology / by John F. Lindsay, 2018.

[19] J.A. Bard, D.W. Ramsey, E.W. Wolfe, G.E. Ulrich, C.G. Newhall, R.B. Moore, N.G. Bailey, R.F. Holm, Database compilation for the geologic map of the San Francisco volcanic field, north-central Arizona, Data Series, Reston, VA, 2015.

[20] A. Meurisse, A. Makaya, C. Willsch, M. Sperl, Solar 3D printing of lunar regolith, Acta Astronautica 152 (2018) 800-810.

[21] JSC-1A Production and Distribution, 2007.

[22] B.C. Clark, Geochemical components in Martian soil, Geochimica et Cosmochimica Acta 57(19) (1993) 4575-4581.

[23] R. Rieder, T. Economou, H. Wänke, A. Turkevich, J. Crisp, J. Brückner, G. Dreibus, H.Y. McSween, The Chemical Composition of Martian Soil and Rocks Returned by the Mobile Alpha Proton X-ray Spectrometer: Preliminary Results from the X-ray Mode, Science 278(5344) (1997) 1771.

[24] F.B. Gross, JSC Mars-1 Martian Regolith Simulant particle-charging experiments in the presence of AC and DC corona fields, Journal of Electrostatics 58(1) (2003) 147-156.

[25] JSC-1AF, JSC-1A, JSC-1AC Lunar Mare Regolith Simulant, in: M.S.D.S.O.T. Corporation (Ed.) 2005.

[26] EAC-1 Lunar Mare Regolith Simulant, Chemical Analysis RPBL GmbH & Co. oHG, 2015.

[27] A.S. Yen, R. Gellert, C. Schröder, R.V. Morris, J.F. Bell Iii, A.T. Knudson, B.C. Clark, D.W. Ming, J.A. Crisp, R.E. Arvidson, D. Blaney, J. Brückner, P.R. Christensen, D.J. DesMarais, P.A. de Souza Jr, T.E. Economou, A. Ghosh, B.C. Hahn, K.E. Herkenhoff, L.A. Haskin, J.A. Hurowitz, B.L. Joliff, J.R. Johnson, G. Klingelhöfer, M.B. Madsen, S.M. McLennan, H.Y. McSween, L. Richter, R. Rieder, D. Rodionov, L. Soderblom, S.W. Squyres, N.J. Tosca, A. Wang, M. Wyatt, J. Zipfel, An integrated view of the chemistry and mineralogy of martian soils, Nature 436 (2005) 49.

[28] J.A. Baranska, Z. Sadowski, Bioleaching of uranium minerals and biosynthesis of UO2 nanoparticles, Physicochemical Problems of Mineral Processing 49(1) (2013) 71-79.

[29] J. Schleppi, J. Gibbons, A. Groetsch, J. Buckman, A. Cowley, N. Bennett, Manufacture of glass and mirrors from lunar regolith simulant, Journal of Materials Science 54(5) (2019) 3726-3747.

[30] S.K. Lower, M.F. Hochella, T.J. Beveridge, Bacterial Recognition of Mineral Surfaces: Nanoscale Interactions Between Shewanella and α-FeOOH, Science 292(5520) (2001) 1360-1363.

[31] D.-B. Li, Y.-Y. Cheng, C. Wu, W.-W. Li, N. Li, Z.-C. Yang, Z.-H. Tong, H.-Q. Yu, Selenite reduction by Shewanella oneidensis MR-1 is mediated by fumarate reductase in periplasm, Scientific Reports 4 (2014) 3735.

[32] F. Zhang, S.-J. Yuan, W.-W. Li, J.-J. Chen, C.-C. Ko, H.-Q. Yu, WO3 nanorods-modified carbon electrode for sustained electron uptake from Shewanella oneidensis MR-1 with suppressed biofilm formation, Electrochimica Acta 152 (2015) 1-5.

[33] C.R. Myers, K.H. Nealson, Respiration-linked proton translocation coupled to anaerobic reduction of manganese(IV) and iron(III) in Shewanella putrefaciens MR-1, Journal of Bacteriology 172(11) (1990) 6232.

[34] L. Herrera, P. Ruiz, J.C. Aguillon, A. Fehrmann, A new spectrophotometric method for the determination of ferrous iron in the presence of ferric iron, Journal of Chemical Technology & Biotechnology 44(3) (1989) 171-181.

[35] M.K. Muir, T.N. Andersen, Determination of ferrous iron in copper-process metallurgical solutions by the o-phenanthroline colorimetric method, Metallurgical Transactions B 8(2) (1977) 517-518.

[36] R.P. Gandhiraman, V. Jayan, J.-W. Han, B. Chen, J.E. Koehne, M. Meyyappan, Plasma Jet Printing of Electronic Materials on Flexible and Nonconformal Objects, ACS Applied Materials & Interfaces 6(23) (2014) 20860-20867.

[37] M. Schwentenwein, J. Homa, Additive Manufacturing of Dense Alumina Ceramics, International Journal of Applied Ceramic Technology 12(1) (2015) 1-7.

7

8

Theoretical bioreactor design to perform microbial mining activities on Mars

Rik Volger[+], Marijn J. Timmer[+], Juergen. Schleppi, Corinne N. Haenggi, Anne S. Meyer, Cristian Picioreanu, Aidan Cowley, **Benjamin A.E. Lehner***

Transporting materials from Earth to Mars is a significant logistical constraint on mission design. Thus, a sustained settlement will be enhanced if it can perform elemental extraction and utilization *in situ*. In this study, all requirements to test a novel, biological approach for *in situ* resource utilization (ISRU) are conceptualized. We present designs for two bioreactor systems to be incorporated in a Mars habitat. The first system is a standard algae bioreactor which produces oxygen and biomass. The second is capable of taking in Martian regolith and extracting iron ores from it via biological processes. Additionally, we propose the use of the leftover iron-poor but biomass rich material in a plant compartment. The multiple, different compartments feed into each other, creating an interconnected process enhancing self-sufficiency.

8.1 Introduction

It is a long-standing ambition of humanity to explore space and to establish a habitat on another celestial body. A functional habitat requires the presence of a certain amount of building blocks and technology, and transport of those is the major cost in space exploration. *In situ* resource utilization (ISRU), the use of materials already present on another celestial body, has the potential to strongly reduce the required transport overheads and bring us closer to realizing a sustainable outpost on another celestial body [1].

8.1.1 Potential for biological ISRU

Biological ISRU focuses on the use of microorganisms for extracting materials from *in situ* resources. Life on earth is versatile, and multiple organisms have evolved to use unconventional substrates (e.g. metal oxides) in their metabolism either as electron donors or electron acceptors. These organisms can be potentially applied to help us extract specific metals from Martian regolith. To illustrate, here on earth, this approach is used in copper production where 20% of all produced copper is extracted through bioleaching with microorganisms [2]. In a similar fashion, organisms such as *Shewanella oneidensis* [3], *Acidithiobacillus ferrooxidans* [4] and several members of the genus *Geobacter* [5,6] can be applied to extract iron and other metals from solid minerals. Furthermore, secondary metabolites of the fungi *Cladosporum resinae* have been shown to corrode aluminium alloys [7], a property that could help extract aluminium from extra-terrestrial regolith. In this chapter a design for a bioreactor to facilitate these processes, considering the specific challenges that arise from the Martian environment, is presented.

8.1.2 Benefits of a biological approach

In a production process, microorganisms can be described as self-reproducing, modifiable nano-factories capable of catalysing a wide variety

of chemical conversions [8]. A whole group of bacteria called extremophiles, have evolved to survive in extreme conditions such as sustained temperatures of up to 121 °C [9, 10]. The resilience of these organisms could be harnessed to set up a long-term process on another celestial body [11]. Unicellular lifeforms can remain unchanged for decades at a temperature of -80 °C. Due to the self-replicating nature of microorganisms, a single drop is enough to start a new production cycle in supportive conditions. One heavy-duty freezer can provide a long-term supply of microorganisms and sustain a bioprocess. Furthermore, evolutionary engineering or synthetic biology can be used to increase microbial resistance to strongly inhibiting environments [12, 13].

Integration of the biomining process with algae cultivation in a photobioreactor (PBR) and a plant growth compartment helps recycle waste streams and can provide essential nutrients for the biomining process from *in situ* resources (Fig 8.1). While producing nutrients for the biomining process, the algae convert CO_2 into O_2, which can be used as part of a life support system for humans [14–16].

The plants can potentially use left-over material from the metal extraction, with lower heavy metal concentrations, as support material and will produce edible biomass and oxygen. Using regolith as plant support negates the need to bring growing structures from earth, but fresh regolith impairs plant growth due to the presence of toxic amounts of several heavy metals [17]. The output regolith from the biological ISRU process is expected to contain less iron and should, therefore, have a smaller inhibitory effect on plant growth, which makes it a more suitable plant support material [18]. On top of that, the biomining process will result in the presence of bacterial biomass in the spent regolith. The amino acids contained within this biomass can be taken up by the plants, providing them with a supplementary source of essential building blocks [19, 20].

The system of bioreactors is intended to be installed inside of a human habitat. By doing so, it will benefit from the radiation shielding while

providing oxygen and edible biomass for the astronauts [21]. The current proposed system supports the realization of a permanent habitat on another planet.
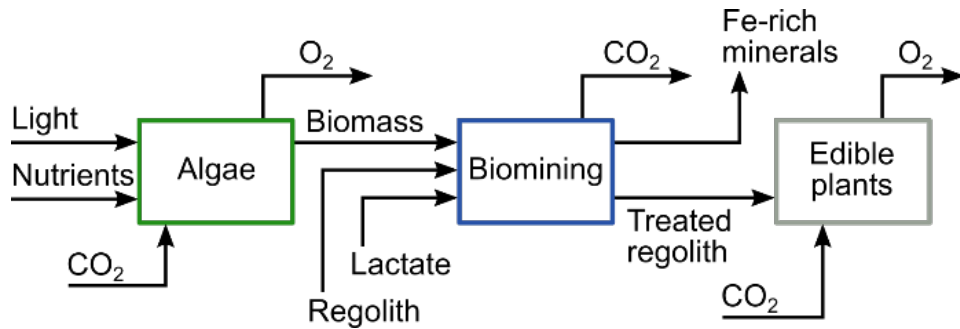

Fig. 8.1 General overview of the three process compartments including the main in- and outputs.

8.1.3 Mining target element and organism

Our focus for biological ISRU is on the extraction of iron, which fulfills an essential role in building and production processes on earth, and as such can readily be beneficial when establishing and maintaining a Martian habitat. Iron is the most-processed metal on Earth and most of our building materials incorporate this material in some capacity. Given the terrestrial heritage, construction and repairs on another planet will also rely heavily on iron, especially when we consider the abundance of iron in Martian regolith (17.9 ±0.6 wt.% [22]). The groundwater bacterium *S. oneidensis* will be considered for the biomining operation. *S. oneidensis* is an organism that uses a wide variety of unusual electron acceptors [23], and its interaction with Fe^{3+} is of interest for the current case study. *S. oneidensis* can utilize Fe^{3+} ingrained in mineral structures, reducing it to aqueous Fe^{2+} while consuming lactate [24].

8.1.4 Assumptions and requirements

The algae reactor is a thin-layer PBR, with a plate thickness of 1 cm and surface area of 1x1 m. It has a total working volume of 60 L which results in a total weight of 246.3 kg (*8.6.1 C. vulgaris model details*). A laminar

flow profile was assumed based on an estimation of the Reynolds number [25]. An average liquid velocity of 0.15 m/s was chosen for the laminar flow profile. Light is supplied from both sides of the plates (Fig. 8.2).

The mining reactor is a 1400 L cylindrical reactor, with an internal wall construction guiding the flow pattern and a gas/liquid separator on top [26]. The total mass of the carbon composite reactor is estimated to be 300 kg (*8.5.2 S. oneidensis model details*). The regolith should be collected in small grain size (diameter < 50 µm) through selective beneficiation by a rover with a tire or power shovel and shake-sieved to remove big rock particles.

The microbial performance and interaction between bacteria and the solid substrates are assumed to be similar to that on Earth. We expect minimal impact of reduced gravity on the micro-organisms in a well-mixed reactor, and thus we assume negligible impact on the growth behaviour for modelling purposes.

8.2 Results & discussion

8.2.1 Expected Martian regolith composition and bacterial interaction

Based on data obtained by the Mars science laboratory at the Rocknest soil the main ores at this area of Mars are:

Mars Science Laboratory (Curiosity) Rocknest soil [27]	
Mineral	**Chemistry**
Plagioclase	$(Ca_{0.57(13)}Na_{0.43})(Al_{1.57}Si_{2.43})O_8$
Olivine (Forsterite)	$(Mg_{0.62(3)}Fe_{0.38})_2SiO_4$
Pyroxene (Augite)	$(Mg_{0.88(10)}Fe_{0.37}\ Ca_{0.75(4)})Si_2O_6$
Pyroxene (Pigeonite)	$(Mg_{1.13}Fe_{0.68}Ca_{0.19})Si_2O_6$

Tab. 8.1 Minerals previously identified via X-Ray diffraction measurements (XRD) on the Mars Rocknest soil.

All ores are expected to have a variety of different mineral deposits on their surfaces. *Shewanella sp.* was shown to be able to interact with a variety of Fe^{3+} bearing mineral types (e.g. Jarosite (Fe^{3+}) [28], Al-goethite

(Fe^{3+}) [29], Smectite (Fe^{3+}) [3]. Smectites (clay minerals) were also identified by the NASA Science laboratory in an ancient steam bed in Gale crater on Mars [30] and via the Viking biology experiments [31]. Based on this interactions with similar (the same) minerals on Earth, it is likely that *Shewanella sp.* will interact with iron(III) and manganese(IV) bearing elements in Martian soil, which results in their reduction.

Additional reports of ferric sulfate [32], nanophase of chlorine-rich ferric oxides [33] and the high abundance of Fe^{3+} in its nanophase ferric oxide state [34] increase our confidence in the potential reduction capabilities of *Shewanella* in a Martian environment. Coupled with *Shewanella sp.* capability of precipitating magnetite during the reduction of Fe^{3+} [35, 36] give a good evidence that a magnetic extraction of iron rich ores on Mars with this organism will be possible.

8.2.2 Storage and inoculation of microbial stocks and growth medium

The algae and bacterium stocks need to be stored in glycerol stocks at -80 degrees Celsius, to have a back-up for inoculation whenever needed. For the general operations a small volume of the previous batch can be stored in a chamber inside the reactor. If a decrease in productivity (O$_2$ production for the *C. vulgaris*, CO$_2$ production for *S. oneidensis*) is observed, a new batch must be started from the freezer. In the latter case, the bacteria will first be activated in a small batch to ensure optimal growth behaviour.

The cultivability of some microorganisms was shown to be significantly decreased during space flight experiments [37], further investigations are needed to understand the implications for the proposed organisms. Results of tests with *S. oneidensis*, which was sent to the ISS on the 15th SpaceX cargo missions are pending [38]. Growth medium will be stored in autoclaved pulverous form and the hydration of it occurs only for production.

8.2.3 Algae reactor design

For the algae cultivation, the algae species *Chlorella vulgaris* was chosen for its high growth rate in thin layer PBRs (Fig. 8.2A, B) [39]. A production rate per hour of biomass, O_2 and CO_2 was obtained by integration of the in- and outgoing streams and subtraction of the difference (Tab 8.2). The highest oxygen production rate is not directly at the wall, due to a low CO_2 concentration and photoinhibition (Fig. 8.2C, D, E).

Location	Biomass (kg/h)	O_2 (kg/h)	CO_2 (kg/h)
Inlet	54	0	$1.71*10^{-3}$
Outlet	54.0003	$6.39*10^{-4}$	$1.11*10^{-3}$
Production	$3.23*10^{-4}$	$6.39*10^{-4}$	$-5.98*10^{-4}$

Tab. 8.2 Biomass, oxygen and carbon dioxide production (kg per hour per 10 L PBR plate). Data obtained by integration of the concentrations at the exit and entrance.

S. oneidensis requires addition of serine, glutamate and arginine to its medium to ensure growth [23, 40]. We propose to supply these as *C. vulgaris* biomass. It is assumed that these amino acids are also used to produce secondary amino acids: cysteine and tryptophan from serine, and glutamine and proline from glutamate [41]. The concentration of these amino acids in *S. oneidensis* biomass was combined with amino acid concentrations in *C. vulgaris* (Tab. 8.3) to calculate the amount of *C. vulgaris* biomass required to fulfil the nutritional requirements of *S. oneidensis*.

Amino acid	Concentration (mg AA / g CDW)
Shewanella oneidensis	
Serine	33.08
Cysteine	6.82
Tryptophan	13.44
Glutamate (inc. glutamine)	88.03
Proline	26.42
Arginine	41.15
Chlorella vulgaris	
Serine	9.55

Cysteine	0.67
Tryptophan	5.91
Glutamate (inc. glutamine)	31.62
Proline	22.84
Arginine	18.96

Tab. 8.3 Selected amino acid concentrations in S. oneidensis [42] and C. vulgaris [43] biomass.

Cysteine is likely to be the limiting amino acid, assumed that the uptake yield for each amino acid is the same. Without reactions interconverting the amino acids, over 10 g *C. vulgaris* biomass is needed for the production of 1 g of *S. oneidensis* biomass. When metabolic reactions converting serine and tryptophan into cysteine are considered [41], this requirement drops to about 4 g *C. vulgaris* per 1 g *S. oneidensis.*

This covers only the requirement for essential amino acids, the main electron donor for *S. oneidensis*, lactate, still needs to be provided from other sources. The mining reactor produces 21 g *S. oneidensis* per batch (50 h), which requires 84 g *C. vulgaris* biomass. Over the duration of one batch, one 10 L *C. vulgaris* plate produces 16.13 g biomass (Tab. 8.2). A total of 6 plates (60 L) is needed to produce the required amount of *C. vulgaris* biomass for the biomining reactor. Those 6 plates correspond to 92.03 g Oxygen per 24 h [44]. Further upscaling and optimization for the oxygen production of the algae bioreactor can increase its potential as bioregenerative life-support system.
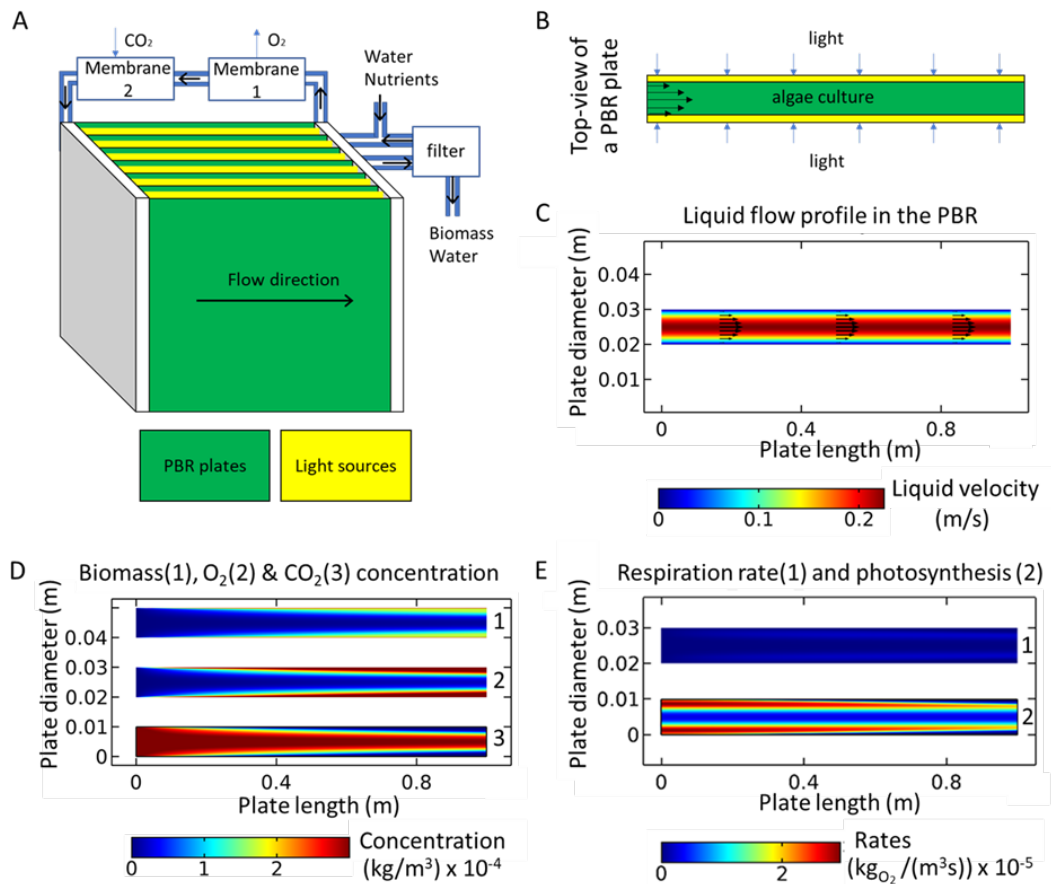
8

Fig. 8.1 PBR geometry, flow profile, concentration profile and reaction rate. (A) Reactor geometry. Culture plates are displayed in green. LEDs are displayed in yellow. A system filtering out the biomass to keep the steady state concentration of 10 g X l^{-1} is displayed as well as the hollow fiber membrane system used to remove the O_2 and supply the broth with CO_2. (B) Top-view of a photobioreactor plate imbedded between two LED plates. (C) Steady state flow profile (m s^{-1}) in a flat plate of the reactor. Arrows display the direction of the flow. D) Concentration profile of (top to bottom) produced biomass (1), oxygen (2) and carbon dioxide (3) concentration (g l^{-1}) in the reactor. (E) Rates of respiration (1) and photosynthesis (2) in kg O_2 m^{-3} s^{-1}.

8.2.4 Biomining reactor design

The bioreactor will be equipped with intake ports for water, an inoculation chamber (in which bacteria will be grown or stored at a certain OD before used for the new batch), nutrients, gas and fresh regolith (Fig 8.3A). Additionally, there will be ports for the outflow of gas, evaporated water, purified product and spent regolith. The process will be monitored by an array of probes, continuously measuring pH, temperature, optical density (measure for biomass concentration) and osmolality. Measurement of the osmolality will provide insight into the accumulation of salts from the regolith in the reactor. Furthermore, the concentration of various gasses in the offgas (CO_2, N_2) will be measured and the CO_2 will be bound by a CO_2 scrubber. The CO_2 production rate is stoichiometrically linked to substrate consumption and biomass formation. After correction for pH and dissolved CO_2 concentration, the pCO_2 profile gives insight in bioprocess performance.

A flow cytometer is introduced to provide more detailed information on cellular health, which is strongly correlated with the bioprocess performance. It is not yet known how bacteria and Martian regolith will interact, and Martian regolith simulants have been reported to have different effects on microbial growth [18]. These effects should be elucidated before a full-scale biomining process is greenlighted, and during operation longer-term effects should be monitored.

8.2.5 Operational sequence

The bioreactor process is separated in three phases: the intake phase, the growth phase and the extraction phase (Fig 8.3B). In the intake phase, regolith (previously harvested by a rover) is loaded into the reactor, then water is added, and nutrients follow. The amount of nutrients is chosen in stoichiometric ratio to the added regolith, to avoid excess after extraction. Finally, the bacteria are added from the last batch or a freshly prepared one. In the second phase bacteria are utilizing the provided nutrients for

growth and for the extraction of the desired elements from the regolith. In this phase the process is monitored with the introduced probes, and gas is continuously circulated for mixing. The concentration of CO_2 in the offgas is an indicator of process performance and substrate consumption.

When CO_2 production ceases, the extraction phase is started. First, magnets at the reactor walls are activated to capture the magnetic iron precipitates. The nonmagnetic regolith is settled, removed from the reactor and used as plant growth support material. Then, the magnets are turned off, and the magnetic, iron-rich precipitates are settled and evacuated. Finally, part of the planktonic biomass is stored, after which the water is evaporated and recovered. This process combined with the preparation of the next batch, is estimated to take approximately 24 hours.

8.2.6 Nutrient requirements and magnetite precipitation

For the biological iron extraction process to be feasible, the amount of extracted iron should outweigh the amount of nutrients consumed by the process. The amount of iron extracted is dependent on the precise iron oxides formed from the dissolved Fe^{2+}, Fe^{3+} and other ions introduced with the regolith and bacterial media. Ideally, each released Fe^{2+} ion would recombine with two Fe^{3+} and oxygen to form magnetite (Fe_3O_4), a ferrimagnetic material [35]. In this best-case scenario, each reduced Fe^{3+} leads to three extracted Fe atoms, tripling the mass efficiency. With about 0.41 g nutrients required per gram Fe^{3+} reduced (Tab. 8.4), this would lead to approximately 0.14 g of nutrients consumed per extracted g of Fe.

In a more realistic situation, the iron will also precipitate in multiple other, less magnetic forms of iron oxide (siderite, green rust) sometimes incorporating other cations [45]. This will increase the consumption of nutrients per magnetically extracted gram of iron. Experiments are required to assess the extent of these effects and to find conditions that best promote precipitation of magnetic iron oxides. Some iron-reducing bacteria reportedly form a product that consists of > 60% magnetite under

the right conditions [46]. Assuming that the 50% of the converted iron is magnetically extracted following the magnetite formation stoichiometry, an hourly production of 21.6 g is expected.

Compound	Consumption / Conversion (g/L)	Yield (g / g Fe^{3+})
Fe^{3+}	0.761	1
Lactate	0.315	0.41
NH_4^+	$5.35*10^{-4}$	0.00070

Tab 8.4 Nutrient consumption/conversion and iron extraction after 50 hours as predicted by the kinetic model.

8.2.7 Method of mixing

Operation of an internal airlift bioreactor [47] under Martian gravity (3.72 m s^{-2}) was investigated using computational fluid dynamics (CFD). *S. oneidensis* requires a continuous availability of nutrients and Fe^{3+} for growth. The Fe^{3+} is extracted from regolith particles with a density of 1.91 $* 10^3$ kg m^{-3} [48]. To ensure availability of both iron and nutrients for the bacteria, settling of these particles should be prevented. Adequate mixing can be achieved with an impeller (mechanical agitation) or by introducing a gas phase in the bottom of the reactor. To minimize moving parts inside of the reactor, a gas-mixed system was chosen. An internal airlift reactor was chosen over a bubble column reactor because of its higher liquid velocity [49]. The 1400-litre reactor geometry and process parameters were set up to obtain turbulent flow and sufficient circulation (*8.6.2 S. oneidensis model details*).
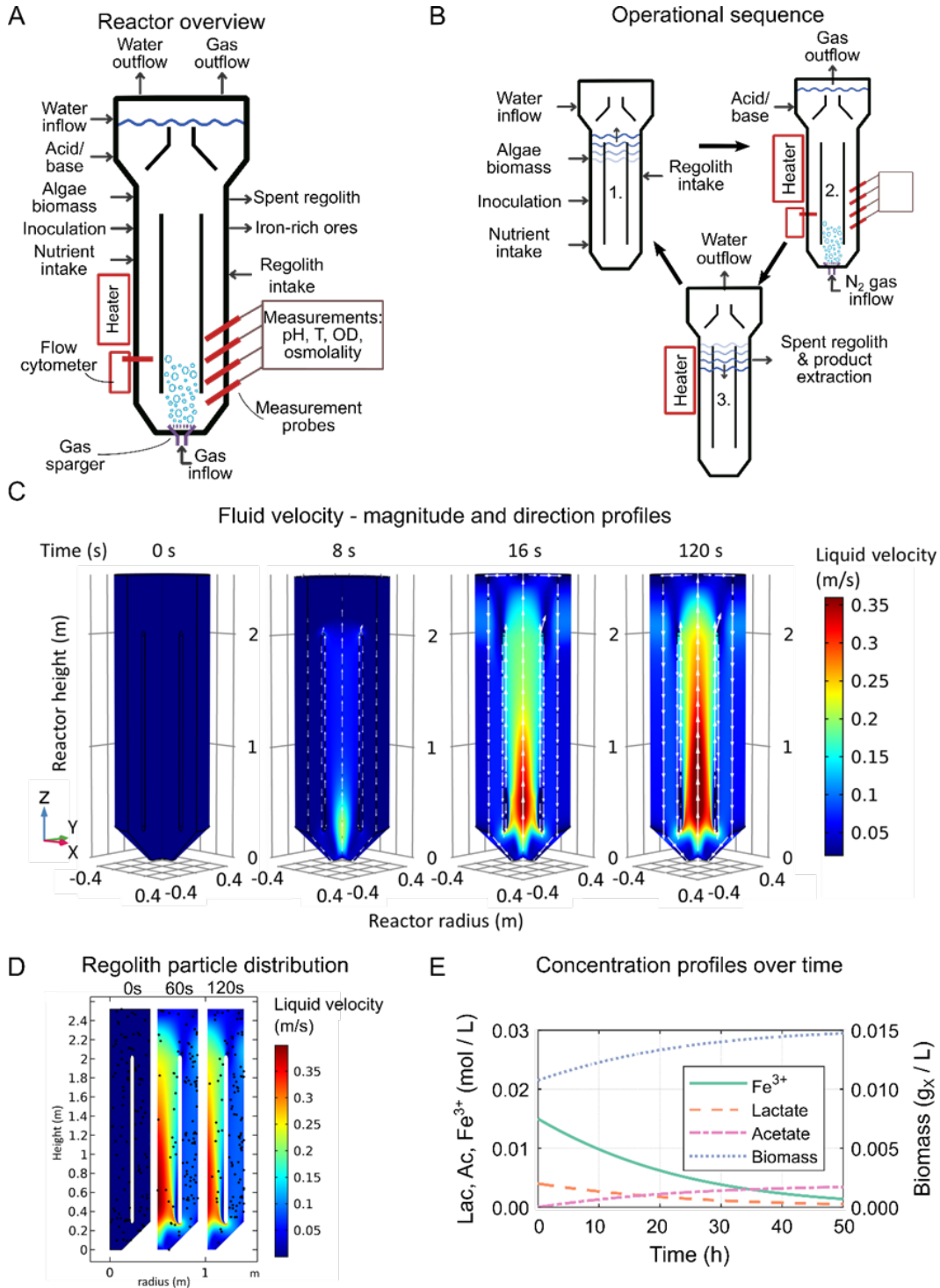
Fig 8.3 (A) General layout of the reactor with all required in- and output connections. The top construction facilitates G/L separation. (B) Operational sequence: (1.) Intake phase: Regolith, water, nutrients and bacteria are loaded into the reactor. (2.) Growth phase: The reactor is operated as an airlift reactor, bacteria consume the nutrients and extract the required elements. (3.) Extraction

phase: The desired products are extracted, water is evaporated and recovered and waste regolith is discarded. (C) Establishment of the turbulent flow profile over time. Flow magnitude in m/s indicated with colour, flow direction indicated with cyan arrows. A 270° 2D-revolution displays the 3D reactor geometry. (D) Regolith distribution at 0, 60 and 120s after initiation of gas flow, simulated for particles with d = 50 * 10^{-6} m. (E) Concentration profiles (mol/L) of lactate, Fe^{3+}, biomass and acetate over the batch duration of 50h.

The turbulent flow profile of the reactor was solved for 120 seconds after initiation of aeration, to determine the steady state flow profile that would be achieved (Fig. 8.3C). The resulting mixing ensures a homogeneous concentration profile over the reactor. Furthermore, the particle tracing proves that the particles will stay in suspension with the provided flow. This leads to the conclusion that a uniform reaction and concentration is achieved in the reactor (Fig 8.3E).

8.2.8 Impact of high radiation

Due to its weak magnetic field and low-pressure atmosphere, Mars has only minimal natural radiation mitigation mechanisms. Radiation on Mars can be divided in two types: Galactic Cosmic Rays (GCR) and solar UV radiation (200 nm). UV-C radiation (100-280 nm) contains wavelengths easily absorbed by DNA [50], which makes it biologically dangerous. However, UV radiation is relatively easy to shield against [51]. By positioning our system inside a human habitat, the danger of UV radiation is expected to be negligible.

GCR are harder to shield against, and a portion of this radiation will always penetrate the base [52]. In a worst-case scenario, the yearly Martian surface dose of 0.242 Sv [53] will penetrate the reactor. According to literature, an acute radiation dose of 12 Sv extends the lag phase of S. oneidensis by approximately 1.5 hours and has no effect on the growth yield [54]. After comparing these numbers, it was assumed that radiation will not have a significant effect on productivity.

The increased radiation could impact the shelf-life of the nutrients, in particular vitamins, as organic compounds can be significantly degraded by solar energetic particles [55]. The degradation of amino acids within the range of a few years is expected to be minimal [56].

8.2.9 Iron availability

The microbial reduction process was assumed to only have access to iron at the surface of the particles, i.e. the iron deeper inside the regolith particles is not available for reduction. To account for this limited penetration depth, a contact layer model was introduced. Only the outer layer of thickness δ_{CL} is assumed to be accessible to the bacteria (Fig. 8.4A). The particles were assumed to have a spherical shape, which corresponds to the lowest surface area to volume ratio possible. Particles with more irregular shapes have a larger surface area to volume ratio and increased available iron.
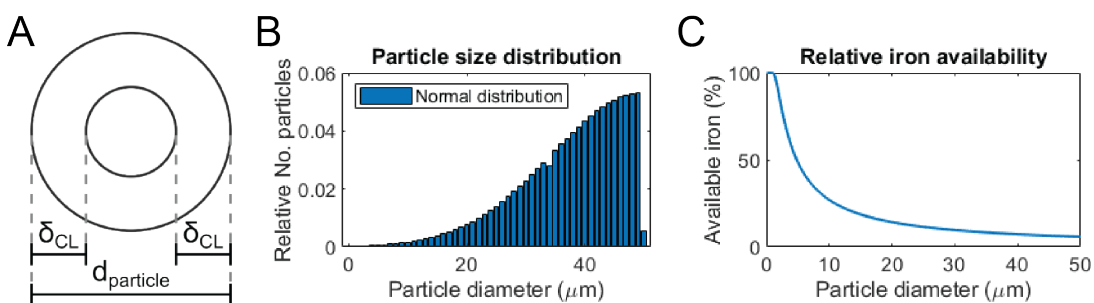

Fig. 8.4 (A) Visualization of the contact layer model. (B) Expected particle size distribution grouped in bars of 1 μm. (C) Iron availability for each particle diameter, decreasing with particle size.

It is assumed that the outer 0.5 μm is available for reduction [57]. The effect of such a system on the iron availability was assessed. The particle size was assumed to follow a normal distribution with μ = 50 μm and σ = 15 μm, cut off at 50 μm (Fig. 8.4B, C). When the expected particle size distribution and calculated relative iron availability are combined, it follows that 8.4% of the total iron is available for the bacteria.

8.2.10 Plant compartment

The main challenge for growing plants directly on Martian regolith (in an enclosed environment) is the toxicity of certain elements it contains and its capability to store water. Martian regolith simulants (JSC-Mars1) tend to act similarly to Loess soil, which can hold substantial quantities of water [58].

Toxic metals within Martian simulants include:

• Aluminium may be a toxic and growth-limiting reagent, especially in acidic soils. This problem is exacerbated with the addition of nitrogen-containing fertilizers. Aluminium toxicity reduces plant root growth and subsequently increases plant susceptibility to drought and decreases the uptake of nutrients [59, 60].

• Although manganese is a vital micronutrient, it can also be toxic [61, 62] in alkaline (pH above 8) or acidic (below pH 5.5) soils under reducing circumstances. These conditions occur for example during flooding events, due to the accumulation of organic matter, or in the case of compression of the soil and the subsequent lack of oxygen [59, 63].

• Iron, also an essential nutrient to plants [64], can lead to brown spots (and therefore insufficient chlorophyll) on the plant surface if present excessively. This problem is more prevalent under reducing circumstances such as flooding [59].

Alteration of regolith before using it as a structure-giving surface for plant growth is important to reduce the high concentration of heavy metals and to increase the number of biomolecules. These modifications should enable plants to grow better on the provided substrate and in the long run, make space-exploration more sustainable (Fig. 8.5).
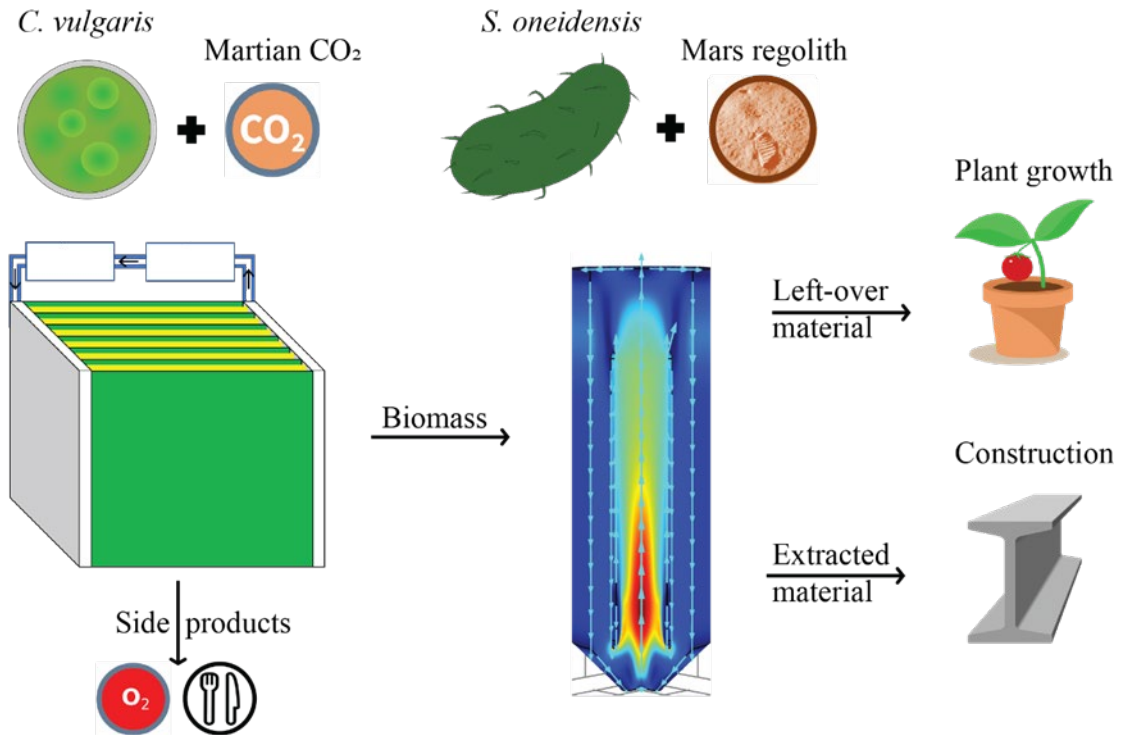
8

Fig. 8.5 Schematic overview of the proposed bioprocesses. An algae reactor with *C. vulgaris* is operated using compressed Martian CO_2 rich atmosphere as carbon source to produce biomass for a biomining reactor. Oxygen and additional biomass, which are produced during this process can be used for the astronauts. The biomining reactor hosts *S. oneidensis* and Martian regolith. Latter gets reduced by the bacterium. Leading to the generation of more magnetic iron species which can be extracted as a construction material. The left-over material can be used as a structure giving, biomass rich material for plants.

8.2.11 Planetary protection

A key objective of Mars exploration is the careful investigation for microbial traces of current or extinct life. However, every human operation increases the chance for false-positives because of the diverse bacterial community every human being carries. The here proposed algae and biomining reactor will be part of a closed human habitat and will follow the same planetary protection procedures as for the rest of the habitat. No further increase in false-positives due to these reactors is expected.
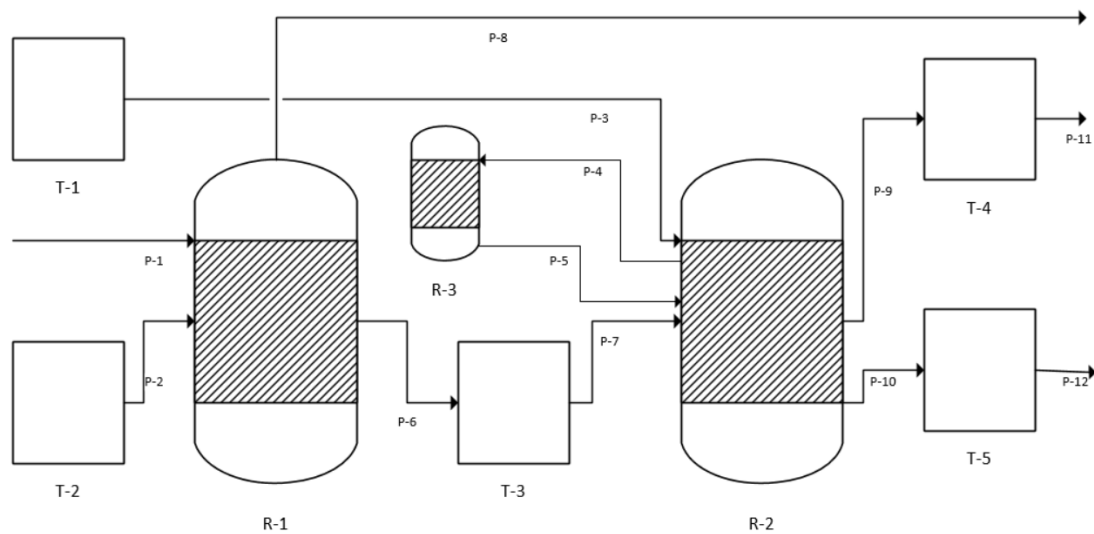
Fig. 8.6 Unit operation flowsheet for biomining reactor system. R=reactor (R-1 algae reactor, R-2 Biomining reactor, R-3 Inoculum reactor), T=tank (T-1 *S. oneidensis* medium tank; T-2 *C. vulgaris* medium tank; T-3 Biomass storage tank; T-4 Magnetite storage tank; T-5 Left-over regolith storage tank); P=pipe (P-1 Algae reactor, $CO_{2,in}$; P-2 Algae reactor, $medium_{in}$; P-3 Biomining reactor, $medium_{in}$; P-4 Inoculum reactor, $medium_{in}$; P-5 Biomining reactor, $inoculum_{in}$; P-6 Algae reactor, $biomass_{out}$; P-7 Biomining reactor, $biomass_{in}$; P-8 Algae reactor, $oxygen_{out}$; P-9 Biomining reactor, $CO2_{out}$; P-10 Biomining reactor, $Magnetite_{out}$; P-11 Biomining reactor, $Regolith_{out}$; P-12 Storage, $Magnetite_{out}$; P-13 Storage, $Regolith_{out}$

8.3 Conclusion

In this chapter, a concept for ISRU and explorative modelling studies for a biological production cycle aimed at obtaining high-grade iron ores from Martian regolith was described (Fig 8.5, 8.6).

The system consists of an algae reactor, biomining reactor and plant growth compartment. With the current design, it follows that a 60 L flat plate PBR can sustain part of the main nutrient requirements for a 1400 L biomining reactor. The total hardware is estimated to weigh approximately 550 kg. In return, the PBR system produces 0.28 kg O_2 per day and a production of 350 kg iron per Mars year is expected. Biofilm formation in

the PBR could drastically decrease the light path through the reactor [65], and a scrubber should be introduced to prevent biofilms from forming. Systems using automatic magnetic scrapers are proposed as a low-maintenance solution [66, 67].

The currently proposed PBR setup generates laminar flow, which results in inactive zones in the reactor due to depleted CO_2 and dark zones. A turbulent flow pattern could provide better axial mixing, resulting in a higher total productivity. However, the PBR makes the biomining-reactor system more sustainable by providing essential nutrients via a photoautotrophic pathway, while at the same time enabling tests on bioregenerative life-support systems on Mars.

This work describes an operational sequence for the biomining reactor. The general framework presented here can be used to design other specific extraction processes as further feasible conversion approaches are discovered. The effects of reduced gravity on the behaviour of biomining organisms are not yet clear, further experiments will be required to assess these. Current and future experiments on the ISS [68] or Moon [69] could help investigate the effects of partial- or microgravity on the herewith proposed organisms. Further experimental research into the precipitation of magnetite from the final solution and the magnetic extractability thereof will provide data to complete the picture of biological iron extraction. Experiments regarding the agitation and mineral precipitation in a well-mixed bioreactor in comparison to a packed-bed bioreactor will give further insights in the operational procedure.

8

8.4 Material and methods

8.4.1 Modelling of algae growth performance

A detailed description of the modelling process can be found in the supplemental information (*8.5.1 C. vulgaris model details*). In short, the stoichiometry of the photosynthetic reaction of *C. sorokiniana* was applied [70], only considering the compounds of interest (CO_2, O_2 and biomass) (Eq. 8.1). The respiratory reaction was assumed to be the inverse of the photosynthetic reaction. The photosynthetic rate (R_{photo}) was assumed to be limited by the carbon dioxide concentration, the light intensity (I) and photoinhibition (set by $K_{i,I}$) at high light intensities (Eq. 8.2) [39]. The light intensity half velocity constant is difficult to estimate at high cell densities [39], but was estimated based on several modelling studies [71, 72]. The rate of respiration ($R_{respiration}$) was assumed to be limited by the O_2 concentration and inhibited by the light intensity (Eq. 8.3). A Lambert-Beer relation was used to describe the light intensity over the diameter of the culture (Eq. 8.6).

A concentration balance was set up including a diffusive, a convective and a reactive term for compounds oxygen, carbon dioxide and biomass (Eq. 8.6). A computational fluid dynamics (CFD) analysis was executed in COMSOL Multiphysics 5.4 to simulate the performance of the reactor.

$$CO_2 + 0.93\,H_2O \rightarrow$$
$$CH_{1.71}O_{0.4}N_{0.15} + 1.42\,O_2 + 0.15\,OH^- \tag{8.1}$$
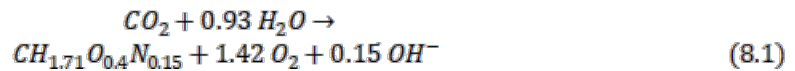
$$R_{photo} = \mu_{max} * \frac{c_x c_{co2}}{K_{co2} + c_{co2}} * \frac{I}{K_I + I} * \frac{K_{i,I}}{K_{i,I} + I} \tag{8.2}$$

$$R_{respiration} = m_s * \frac{c_x c_{o2}}{K_{o2} + c_{o2}} * \frac{K_I}{K_I + I} \tag{8.3}$$

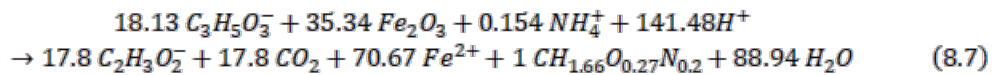$$I_z = I_0 * e^{-\varepsilon c_x z} \tag{8.4}$$

$$\varepsilon = \varepsilon_0 (1 - a_1 h)(1 - a_2 X) \tag{8.5}$$

$$\frac{\partial C_i}{\partial t} = D_i \nabla^2 C_i - v \nabla C_i + r_i \tag{8.6}$$

8.4.2 Modelling of biomining performance

The elemental composition of *Shewanella oneidensis* biomass, standardized for 1 mol of carbon, was assumed to be $CH_{1.66}O_{0.27}N_{0.2}$ [73]. To derive the process reaction, the methodology from Kleerebezem et al (2010) was adapted to work with a known yield (Tab 8.5) [74]. This resulted in the following process reaction:

$$18.13\ C_3H_5O_3^- + 35.34\ Fe_2O_3 + 0.154\ NH_4^+ + 141.48H^+$$
$$\rightarrow 17.8\ C_2H_3O_2^- + 17.8\ CO_2 + 70.67\ Fe^{2+} + 1\ CH_{1.66}O_{0.27}N_{0.2} + 88.94\ H_2O \qquad (8.7)$$

S. oneidensis requires addition of glutamate, arginine and serine to the medium to ensure proper growth [23, 75]. Consumption of these was calculated to be 17, 20 and 9 mmol / Cmol X, respectively [42]. Taking into consideration the biomass composition of *C. vulgaris* [43], the required amino acids may all be supplied in excess by using 4 gram of *C. vulgaris* biomass per gram of *S. oneidensis* biomass. Nitrogen for the remaining amino acids was assumed to come fully from NH_4^+, leading to a requirement of 0.154 mol NH_4^+ / Cmol X.

It was assumed that the outer 0.5 µm layer of the regolith particles was available to the bacteria [57]. Combined with the expected particle size distribution [76] this yielded an iron availability of about 8.4 %. A turbulent flow profile was simulated with a bubbly flow model in COMSOL Multiphysics 5.4. A particle tracing study was done to assess the distribution of regolith particles within the gaslift-reactor. A continuous random walk model was used to account for the fluctuating local turbulent velocity (*8.5.2 S.oneidensis model details*). The growth kinetics were assumed to rely on both the concentration of Fe^{3+} and lactate following Monod kinetics, and growth was assumed to be inhibited by acetate (Eq. 8.8).

$$\mu = \mu_{max} * \frac{c_{Fe^{3+}}}{K_{Fe^{3+}} + c_{Fe^{3+}}} * \frac{c_{Lac}}{K_{Lac} + c_{Lac}} * \frac{K_{I,Ac}}{K_{I,Ac} + c_{Ac}} \qquad (8.8)$$

The parameters in Tab. 8.5 were combined with equation 8.8 and mass balances for biomass, iron, lactate and ammonium based on the reaction in equation 8.7. This system was solved for 50 h of growth with Matlab's ODE45 solver (Tab. 8.5).

Parameter	Value	Units	Description
Algae			
(*Chlorella vulgaris*)			
Reactor			
T	310	K	Temperature
u_{in}	0.15	m * s^{-1}	Inlet liquid velocity
$c_{in,X}$	10	g * L^{-1}	Biomass inlet concentration
c_{in,CO_2}	7.2 * 10^{-3}	mol * m^{-3}	CO$_2$ inlet concentration
c_{in,O_2}	0	mol * m^{-3}	O$_2$ inlet concentration
P_a	1	atm	Absolute pressure
I_0	2000	μmol * m^{-2} * s^{-1}	Light intensity (PPFD)
ε_0	0.175	m^2 *g^{-1}	Extinction coefficient
$a1$	46.165	m^{-1}	Light attenuation coefficient 1
$a2$	9.664 * 10^{-6}	m^3 g^{-1}	Light attenuation coefficient 2
$\mu_{realized}$	0.008	h^{-1}	Realized growth rate
μ_{max}	0.018	h^{-1}	Maximum growth rate
Y_{X/O_2}	0.68	Cmol X * mol O$_2^{-1}$	Yield of biomass per mol oxygen
Y_{X/CO_2}	1.00	Cmol X * mol CO$_2^{-1}$	Yield of biomass per mol carbon dioxide
m_S	$0.28 * \mu_{max}$	h^{-1}	Maintenance coefficient
K_I	175	μmol m^{-2} s^{-1}	Half-velocity constant of light absorption
$K_{I,inhibitory}$	500	μmol m^{-2} s^{-1}	Half-velocity constant of light inhibition
Biomining			
(*Shewanella oneidensis*)			
Reactor			
T	303	K	Temperature
$u_{g,in}$	0.15	m * s^{-1}	Superficial inlet velocity
g_{mars}	3.72	m * s^{-2}	Martian gravity acceleration
d_{bubble}	3	cm	Bubble diameter
$P_{gas,in}$	0.97	kg * m^{-3}	Inlet gas density
$\varepsilon_{regolith}$	0.025	-	Regolith holdup in liquid
a_1	2.5	-	Viscosity coefficient 1
a_2	14.1	-	Viscosity coefficient 2

μ_{liquid}	$2.0 * 10^{-3}$	Pa * s^{-1}	Liquid viscosity
Biological			
μ_{max}	0.1	h^{-1}	Maximum growth rate [3,42,77,78]
$Y_{X/Fe^{3+}}$	0.01415	Cmol X * mol Fe^{3+} $^{-1}$	Biomass produced per mol Fe^{3+} reduced [24,77]
$K_{Fe^{3+}}$	$5.47 * 10^{-4}$	mol * L^{-1}	Half-velocity constant for Fe^{3+} [78]
K_{Lac}	$1.94 * 10^{-2}$	mol * L^{-1}	Half-velocity constant for lactate [79]
$K_{I,Ac}$	$12.6 * 10^{-3}$	mol * L^{-1}	Half-velocity constant for acetate inhibition [80]
$c_{X,init}$	$5.94 * 10^{-4}$	mol * L^{-1}	Initial biomass concentration
$c_{Lac,init}$	$4.0 * 10^{-3}$	mol * L^{-1}	Initial lactate concentration
$c_{Fe^{3+},init}$	$1.5 * 10^{-2}$	mol * L^{-1}	Available Fe^{3+} concentration
$c_{Ac,init}$	0	mol * L^{-1}	Initial acetate concentration
$c_{NH_4^+,init}$	$1 * 10^{-3}$	mol * L^{-1}	Initial ammonium concentration
$c_{arginine,init}$	$5.5 * 10^{-5}$	mol * L^{-1}	Initial arginine concentration
$c_{serine,init}$	$7.58 * 10^{-5}$	mol * L^{-1}	Initial serine concentration
$c_{glutamate,init}$	$6.5 * 10^{-5}$	mol * L^{-1}	Initial glutamate concentration

Tab. 8.5 Reactor and biological parameter choices for the algae and biomining models.

8.5 Supplementary information

8.5.1 C. vulgaris model details

Reactor design: The reaction will be performed in a continuous flat plate photobioreactor (PBR). Continuous cultures are more beneficial as they can grow at maximum oxygen productivity rate in the most constant environment. Especially, in life support systems an uninterrupted O$_2$ supply is mandatory [14, 81, 82].

A flat plate PBR was chosen because of the high surface-to-volume ratio, and straight forward biofilm cleaning procedures. The plates will have a width (z) of 1 cm and an area-size of 1 x 1 m^2. The culture is aerated with hydrophobic polypropylene micropore membranes hollow fibre membranes to obtain efficient aeration of the broth [83].

8

The type of flow we use was calculated with the Reynolds number (Eq. 8.9). For the viscosity and density, we assume the values for water (η = 0.002 Pa s^{-1}, ρ = 1000 kg m^{-3}) will approximate the broth values close enough to not influence the flow. With a flow through the tube of 15 cm/s a Reynolds number of 750 was calculated. As this is below the cut-off for turbulent flow (Re > 1000) a laminar flow was be considered [25].

$$Re = \frac{\bar{v}L\rho}{\eta} = \frac{15.0 * 10^{-2}\, m\, s^{-1} * 1.0 * 10^{-2}\, m * 1.0 * 10^3\, kg\, m^{-3}}{2.0 * 10^{-3}\, Pa\, s^{-1}} = 750 \tag{8.9}$$

A mass balance was set up for each compound including respectively diffusive, convective and reactive contributions. Since a single-phase domain is studied, an incompressible flow can be assumed to describe the system. This results in the mass balance for compound i over time being expressed in Eq. 8.10, with the concentration gradient expressed (Eq. 8.11).

$$\frac{\partial C_i}{\partial t} = D_i \nabla^2 C_i - v\nabla C_i + r_i \tag{8.10}$$

$$\nabla C_i = \frac{\partial C_i}{\partial x} + \frac{\partial C_i}{\partial y} \tag{8.11}$$

The assumption of a stationary system for the reaction (continuous, steady state) lead to no change of concentration over time ($\frac{\partial C_i}{\partial t} = 0$). This partial differential equation (PDE) can be solved to obtain the concentration profile of compound i in the reactor. Inlet concentration of carbon dioxide was set at the maximum solubility determined with the temperature dependent henry coefficient (Eq. 8.12) to prevent bubble formation in the liquid. Henry coefficients were retrieved from [84].

$$H = H^0 * \exp\left(-\frac{\Delta solH}{R}\left(\frac{1}{T} - \frac{1}{T_0}\right)\right) \tag{8.12}$$

parameter	value	Description
T	310 [K]	Temperature
u_{in}	15 [cm s^{-1}]	Inlet velocity
$C_{in,x}$	10 [g L^{-1}]	Biomass inlet concentration
$C_{in,co2}$	7.2*10^{-3} [mol m^{-3}]	CO$_2$ inlet concentration
$C_{in,o2}$	0 [mol m^{-3}]	O$_2$ inlet concentration
P_a	1 [atm]	Absolute pressure
$d_{culture}$	0.01 [m]	Diameter of culture

Tab. 8.6 Reactor and flow parameters with a short description of their meaning.

Reaction stoichiometry: *Chlorella vulgaris* was chosen for its high photoautotrophic growth capacity [39]. An optimum oxygen production capacity of 45 g X L^{-1} was reported. Since a laminar flow without bubbles decreases mixing, a lower biomass concentration of 10 g X L^{-1} was chosen. A growth rate μ of 0.008 h^{-1} and a C_x of 45 g L^{-1} was reported. It was derived that $μ_{max}$ of this culture would be 0.018 h^{-1}, following from the daily maximum growth rate of 2.15 with a 12-12 h light-dark cycle.

Monod-kinetics were assumed for growth and inhibitory relations. A photosynthesis and a respiration reaction were considered in our system: The light reaction was assumed to be limited by [CO$_2$], light, and photo inhibitory effects while the dark reaction is limited by [O$_2$] and inhibited by light. The sensitivity to light intensity is set by the half-saturation constant K_i. We assumed an inverse relation for the maintenance reaction, with the same inhibition constant. The maintenance reaction is considered to be the catabolic consumption of biomass.

A difference between gross and net oxygen production of 35-40% was derived for *C. sorokiniana* (no data for *C. vulgaris* available), with the uptake of oxygen maximizing at 0.3 mmol O$_2$ g X^{-1} h^{-1}. Therefore, a maintenance coefficient of 0.28 should be taken into account with a Monod-term for maximization at 0.3 mmol O$_2$ gx^{-1} h^{-1} [70]. This resulted in the following block of equations (Eq. 8.13 - 8.17) to solve the stoichiometry for the micro-organisms in the system.

8

$$R_{photosynthesis} = \mu_{max} * \frac{c_x c_{co2}}{K_{co2} + c_{co2}} * \frac{I}{K_I + I} * \frac{Ki, I}{Ki, I + I} \tag{8.13}$$

$$R_{respiration} = m_s * c_x * \frac{c_{o2}}{K_{o2} + c_{o2}} * \frac{K_I}{K_I + I} * \tag{8.14}$$

$$r_x = R_{photosynthesis} - R_{respiration} \tag{8.15}$$

$$r_{O_2} = \frac{R_{pho}}{Y_{xo2}} - \frac{R_{res}}{Y_{xo2}} \tag{8.16}$$

$$r_{co_2} = -\frac{R_{pho}}{Y_{xco2}} + \frac{R_{res}}{Y_{xco2}} \tag{8.17}$$

Parameter	Expression	Description
$\mu_{realized}$	0.008 [h^{-1}]	Realized growth rate
μ_{max}	0.018 [h^{-1}]	Maximum growth rate
$M_{biomass}$	23.6 [g mol^{-1}]	Biomass weight
$Y_{X/O2}$	0.68[mol X mol O$_2$$^{-1}$]	Yield of biomass per mol O_2
$Y_{X/CO2}$	1.00 [mol X mol CO$_2$$^{-1}$]	Yield of biomass per mol CO_2
m_s	0.28*μ	Maintenance coefficient
K_I	175 [μmol m^{-2} s^{-1}]	Half-velocity constant of light absorption
$K_{I,inhibitory}$	500 [μmol m^{-2} s^{-1}]	Half-velocity constant of light inhibition

Tab 8.7 Parameters assumed related to the micro-organism.

A stoichiometry was derived for *C. sorokiniana* [70] and the same stoichiometry for *C. vulgaris* was assumed (Eq. 8.18). The reverse reaction was assumed to be the maintenance reaction (Eq. 8.19). Since we do not yet take the NO_3^- balance into account this assumption can be made: When nitrogen, phosphorus and sulphur balances are implemented, we cannot assume regeneration of those compounds by maintenance as other compounds (e.g. inhibitory compounds) are more likely to be formed.

$$\mu * (CO_2 + 0.93\, H_2O \rightarrow CH_{1.71}O_{0.4}N_{0.15} + 1.42\, O_2 + 0.15\, OH^-) \tag{8.18}$$

$$Ms * (CH_{1.71}O_{0.4}N_{0.15} + 1.42\, O_2 + 0.15\, OH^- \rightarrow CO_2 + 0.93\, H_2O) \tag{8.19}$$
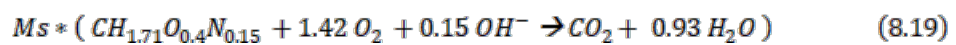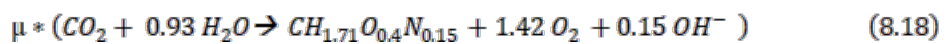
Light profile: Light intensity over the reactor width is decreasing due to attenuation by the chlorophyll of the algae. Most functions are based on Lambert-Beer's law including an empirically determined extinction coefficient (Eq. 8.20). Doucha & Lívanský, (2009) gives a relation based on empirically derived attenuation coefficients a_1 and a_2 (Eq. 8.21).

$$I_z = I_0 * e^{-\varepsilon c_x z} \tag{8.20}$$

$$\varepsilon = \varepsilon_0(1 - a_1 h)(1 - a_2 X) \tag{8.21}$$

They experimentally determined these coefficients to be 46.165 m^{-1} and 9.664 10^{-6} m^3 g^{-1}. We choose to use this attenuation relation for the *Chlorella* model as these coefficients are specially derived for the culture of interest. The lighting takes place from both sides with an intensity of 2000 µmol m^{-2} s^{-1} to obtain a symmetrical profile (Fig 8.7).

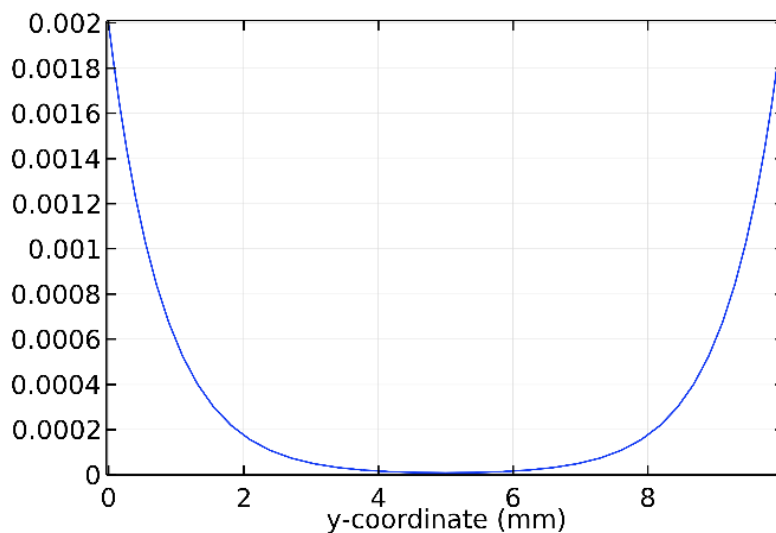| Parameter	Value	Description
I_0	2000 [µmol m^{-2} s^{-1}]	Light intensity at walls
a1	46.165 [m^{-1}]	Light attenuation coefficient 1
a2	9.664e-6 [m^3 g^{-1}]	Light attenuation coefficient 2

Tab. 8.8 Parameters related to light profile in the reactor

Fig. 8.7. Light intensity profile over width of reactor. Intensity is displayed in mol photons m^{-2} s^{-1} (PPFD).

Boundary conditions: For the inlet, a concentration of compounds was set by the maximum solubility for CO_2, 0 g l^{-1} for O_2 and 10 g X l^{-1} for biomass. In the outlet a flux continuity of the concentration in the reactor domain was set. Neither reactions nor diffusion take place at the boundaries. At the light penetrable plates (length of reactor), we set a zero-flux boundary.

Computational model in COMSOL Multiphysics: Finite element analysis was used to create an *in-silico* model of the reactor. One plate of the reactor was modelled in COMSOL Multiphysics 5.4. The system was simplified to a 2-D geometry since the reaction is expected to take place homogenously over the height of the plate. A steady state laminar flow profile was calculated first, then the concentration profile was calculated using a transport of diluted species study. A mapped mesh was used with a symmetric element ratio of 6 towards the walls.

Measuring devices: The process will be monitored by an array of probes, continuously measuring pH, temperature, optical density (measure for biomass concentration) and osmolality. The pH should be kept constant as OH^- is produced in the reactor and CO_2 is consumed. The oxygen concentration in the membrane off gas is measured to track the productivity of the reactor. The optical density is measured and kept constant to maintain the steady state in the reactor.

Reactor weight: A flat plat reactor usually contains glass plates of 6 mm thickness [85]. The glass required per culture plate is 2 * 6 * 10^{-4} m * 1 m * 1 m = 0.012 m^3. For 6 plates this would be 0.072 m^3 of glass. With an average density of $2.6*10^3$ kg m^{-3} [86] the weight requirement results in 187 kg. Alternatively, it can be made from clear plastics [87]. With the same dimensions and a density of $1.2*10^3$ kg m^{-3} [86], this would result in a weight requirement of 86.3 kg.

Another 60 kg would be required for the culture liquid. Hydrophobic polypropylene micropore membranes are used as these membranes facilitate high mass transfer per area, requiring less volume [83]. It is

assumed that the membrane systems and the pumps can be covered with 100kg. This leads to the final required weight of 246.3 kg for the reactor.

8.5.2 S. oneidensis model details

Reactor geometry and fluid dynamics: Continuous supply of nutrients to *S. oneidensis* is required for iron reduction and bacterial growth. Since the Fe^{3+} is extracted from regolith particles with a higher density than water ($1.91*10^3$ kg m^{-3}), [48] the regolith particles should be prevented from settling. Mixing can be performed through mechanical agitation with an impeller, or through the introduction of a gas phase in the bottom of the reactor. Due to the abrasive nature of regolith particles, mechanical agitation is expected to soon lead to deterioration of the equipment. The problem of deterioration is less prevalent in gas-mixed systems; thus, these systems are preferred.

A gaslift Pachuca tank will perform the necessary mixing. An internal airlift-reactor [47] was chosen because it provides a higher liquid velocity than a bubble column reactor, preventing the regolith particles from settling [49]. The cylindrical geometry was chosen to prevent regolith accumulation in corners, where no flow persists (dead zones). Normally, the gas inlet is positioned slightly above the bottom of the Pachuca gaslift reactor to better guide the gas to the riser-region of the reactor [26]. In this case, the bottom was sloped with the gas inlet at the lowest point to prevent settling of the regolith by guiding it to the rising gas flow.

With a required volume of 1400 L and a height taken of 2.5 m. The mixing time of the airlift increases significantly if the liquid height above the baffle is smaller than 0.4 - 0.5 m in a geometry closely resembling ours [47]. Therefore, the baffle height was set at 1.7 m and a starting height of 0.3 m. Assuming a wall diameter of 4 mm and a hollow structure inside the internal wall leading to an effective inner wall thickness of 1 cm, we expect the weight of the carbon composite reactor to be about 100 kg [88], with about 100 kg of process metrology devices attached. The water recovery

equipment is assumed to have a mass of about 100 kg and it is necessary to harvest additional water from local resources [89].

$$\pi * W_f^2 * H_f = V_f \qquad (8.22)$$

Parameter	Value	Description
V_f	0.7 [m^3]	Fermenter volume
H_f	2.5 [m]	Fermenter height
W_f	0.42 [m]	Fermenter width
W_{baffle}	0.04 [m]	Baffle width
H_{baffle}	1.7 [m]	Baffle height

Tab. 8.9 Geometry parameters of the gaslift tank.

An estimation of the flow regime in the reactor was done based on the Reynolds number, using the viscosity and density of water (Eq. 8.23). With an average liquid velocity of $25*10^{-2}$ m s^{-1} and a diameter 0.5 m of the riser part in the reactor, the threshold for turbulence is easily reached [47]. A fully-turbulent flow regime is expected to be reached.

$$Re = \frac{\bar{v}L\rho}{\eta} = \frac{25*10^{-2}\,m\,s^{-1}*0.5m*1.0*10^3\,kg\,m^{-3}}{2.0*10^{-3}\,Pa\,s^{-1}} = 62500 \qquad (8.23)$$

If the gas holdup ε_g is lower than 10%, coalescence should play a minor role and bubbles can be treated as dissolved species in the liquid using a continuity equation [90, 91]. A turbulent flow regime allows for decent mixing, reaching a flow speed of 0.8 m s^{-1} in a reactor domain similar to ours with ε_g of 6% [49]. Since the gas flow is only used for mixing and removal of CO_2, a low ε_g with small bubbles should sufficiently mix the reactor for these purposes.

Nitrogen is used for sparging. Recycling can be done from the off-gas as it is not consumed by *S. oneidensis.* We propose to remove the produced CO_2 with a CO_2-selective removal system (CRDA) as used in the International Space Station (ISS) [92].

Since the particles take up a part of the liquid phase, this was accounted for in the density (Eq. 8.24) and viscosity (Eq. 8.25). The particle hold-up was calculated to be only 0.025. An expansion for viscosity with coefficients a_1 = 2.5 and a_2 = 14.1 was used to adjust for the regolith particles, assuming they are spherical (Eq. 8.25) [93, 94].

$$\rho_{broth} = \varepsilon_{l,fluid} * \rho_{fluid} + \varepsilon_{l,regolith} * \rho_{regolith} \tag{8.24}$$

$$\mu_{broth} = \mu_{liquid} * \left(1 + a_1 * \varepsilon_{regolith} + a_2 * \varepsilon_{regolith}^2\right) \tag{8.25}$$

Reaction stoichiometry: Monod kinetics were used to describe the growth of *S. oneidensis*. The assumption was made that lactate and iron were the limiting compounds for growth. The acetate concentration was assumed to be growth inhibiting (Eq. 8.26) [80].

$$\mu = \mu_{max} * \frac{C_{lactate}}{K_{lactate} + C_{lactate}} \frac{C_{Fe}}{K_{Fe} + C_{Fe}} \frac{K_{I,actetate}}{K_{I,acetate} + C_{acetate}} \tag{8.26}$$

Concentration differences resulting from the growth reaction were calculated with the yield in the iron reduction stoichiometry of *S. oneidensis* (8.7). For simplicity, it was assumed that no other reactions take place in the reactor.

8

Parameter	Value	Description
μ_{max}	0.1 [h^{-1}]	Growth rate of *S. oneidensis*
$M_{biomass}$	20.7 [g mol^{-1}]	Biomass weight
K_{Fe}	$5.47*10^{-4}$ [M]	Half velocity constant of iron consumption
$K_{lactate}$	$1.94*10^{-2}$ [M]	Half velocity constant of lactate cons.
$K_{i, acetate}$	$12.6*10^{-3}$ [M]	Half velocity constant of acetate inhibition
$C_{x, init}$	$5.94*10^{-4}$[M]	Biomass initial concentration
$C_{lactate, init}$	$4.0*10^{-3}$[M]	Lactate initial concentration
$C_{Fe^{3+}, init}$	$1.5*10^{-2}$[M]	Iron initial concentration
$C_{NH4, init}$	$1*10^{-3}$[M]	NH$_4^+$ initial concentration
$C_{acetate, init}$	0 [M]	Acetate initial concentration

Tab. 8.10 Parameters used for the growth kinetics of S. oneidensis on lactate.

Boundary conditions: A zero-flow condition was applied to the walls. The gas-inlet disperses bubbles with a diameter of 3 mm and a superficial velocity u_{in} of $1.5*10^{-3}$ m s^{-1}. A pressure-drag balance slip model was used to compensate for the difference in liquid and gas velocity, which is suggested to be more accurate that a homogenous flow model [93]. At the top of the reactor, for the gas, the outlet boundary condition was set, and a slip boundary condition was used for the liquid. The centre of the reactor (r=0) was given the boundary condition of axial symmetry. A reference pressure was set with a pressure constraint to the upper right corner, in which the relative pressure was set at p = 0 atm.

Flow model in COMSOL Multiphysics A detailed turbulent flow CFD-simulation in COMSOL Multiphysics was designed to predict the distribution of regolith particles in the reactor in reduced gravity. With a small gas holdup (>10%) the Navier-Stokes equation for the gas-phase can be neglected. This enables us to solve the flow profile with the computationally less-intense bubbly flow model, while treating the gas as transported species [49].

The bubbly flow interface of COMSOL Multiphysics was used to solve for the flow profile. We expect the reactor to be symmetrical over the angle φ. Therefore, the model geometry could be simplified to an axial 2-D geometry over radius r and height z. The RANS-equation set is solved for each point in the mesh we created. Forces for (Martian) gravity, pressure and viscosity were taken into account. Since we assume the standard bubble size (d = 3 * 10^{-3} m), the large bubble model was used. The turbulent viscosity ($μ'_T$) is adjusted for with the Eddy Viscosity Model (EVM). The (k-Ɛ) turbulence model [25] was used to describe the turbulence kinetic energy and the rate of dissipation of turbulence energy (using standard turbulence parameters).

As a turbulent flow regime is hard to solve for steady state, a time dependent study was set over 120 seconds to calculate the steady state flow pattern in the reactor. The flow was calculated separately from the particle tracing.

Parameter	value	description
$u_{g,in}$	0.015 [m s^{-1}]	Superficial inlet velocity
g_{mars}	3.72 [m s^{-2}]	Martian gravity acceleration
d_{bubble}	3*10^{-3} [m]	Bubble diameter
$ρ_{gas, in}$	0.97 [kg m^{-3}]	Inlet gas density
$Ɛ_{regolith}$	0.025 [-]	Regolith holdup in liquid
a_1	2.5 [-]	Viscosity coefficient 1
a_2	14.1 [-]	Viscosity coefficient 2
$μ_{liquid}$	2*10^{-3} [Pa s^{-1}]	Liquid viscosity

Tab. 8.11 Parameters used for the flow computation.

Particle tracing model in COMSOL Multiphysics: According to the national coal board [95] particles distribution of coal with diameter <50µm should be uniformly distributed among a reactor even with low liquid velocity. The validity of this result in Martian operation circumstances with regolith (higher density then coal) was verified using particle tracing. The regolith particles contain the iron, so it should be verified that they are

mixed abundantly through the reactor to obtain a high enough iron concentration throughout the reactor.

A simulation of the movement and location of the regolith particles was done using the COMSOL particle-tracing module. Flow was assumed to not be influenced by the particles, other than the density and viscosity corrections already made in the flow profile calculations (Eq. 8.24, 8.25), since the regolith holdup ($\varepsilon_{regolith}$) is low (0.025). The previously calculated flow was used. Hundred 50 μm-sized particles with $\rho_{regolith}$ of $1.91*10^3$ kg m^{-3} were simulated for 120 s. The drag force based on Stokes-law was used with a continuous random walk model taking into account the turbulent dispersion (standard k-ε parameters). Since we predict, based on the particle tracing, that the iron will be homogenously available throughout the reactor, the reaction rate and the production should also be homogenously spread. This reduces the concentration profile to a 0-D problem. An ODE-45 solver in Matlab with initial conditions as presented in table 8.10 was used to solve the system for 50h.

8.6 References

[1] J. Carpenter, R. Fisackerly, B. Houdou, Establishing lunar resource viability, Space Policy. 37 (2016) 52–57. doi:10.1016/J.SPACEPOL.2016.07.002.

[2] S. Yin, L. Wang, E. Kabwe, X. Chen, R. Yan, K. An, L. Zhang, A. Wu, Copper Bioleaching in China: Review and Prospect, Minerals. 8 (2018) 32. doi:10.3390/min8020032.

[3] J.E. Kostka, J.W. Stucki, K.H. Nealson, J. Wu, Reduction of Structural Fe(III) in Smectite by a Pure Culture of Shewanella Putrefaciens Strain MR-1, Clays Clay Miner. 44 (1996) 522–529. doi:10.1346/CCMN.1996.0440411.

[4] J.U. Navarrete, I.J. Cappelle, K. Schnittker, D.M. Borrok, Bioleaching of ilmenite and basalt in the presence of iron-oxidizing and iron-scavenging bacteria, Int. J. Astrobiol. 12 (2013) 123–134. doi:10.1017/S1473550412000493.

[5] A.L. Neal, L.K. Clough, T.D. Perkins, B.J. Little, T.S. Magnuson, In situ measurement of Fe(III) reduction activity of Geobacter pelophilus by simultaneous in situ RT-PCR and XPS analysis, FEMS Microbiol. Ecol. 49 (2004)

163–169. doi:10.1016/j.femsec.2004.03.014.

[6] L.A. Zacharoff, D.J. Morrone, D.R. Bond, Geobacter sulfurreducens Extracellular Multiheme Cytochrome PgcA Facilitates Respiration to Fe(III) Oxides But Not Electrodes, Front. Microbiol. 8 (2017) 2481. doi:10.3389/fmicb.2017.02481.

[7] W.P. Iverson, Microbial Corrosion of Metals, in: A.I. Laskin (Ed.), Adv. Appl. Microbiol. Vol. 32, Academic Press, Inc., Orlando, Florida, 1987: pp. 1–36.

[8] B.A.E. Lehner, R. Volger, S. Brouns, A. Meyer, A. Cowley, L.J. Rothschild, A biological nutrient cycle for a partially self-sufficient colony, in: 69th Int. Astronaut. Congr., Bremen, 2018.

[9] M.T. Madigan, A. Orent, Thermophilic and halophilic extremophiles, Curr. Opin. Microbiol. 2 (1999) 265–269. doi:10.1016/S1369-5274(99)80046-0.

[10] M. Podar, A.-L. Reysenbach, New opportunities revealed by biotechnological explorations of extremophiles, Curr. Opin. Biotechnol. 17 (2006) 250–255. doi:10.1016/j.copbio.2006.05.002.

[11] L.J. Rothschild, Synthetic biology meets bioprinting: enabling technologies for humans on Mars (and Earth)., Biochem. Soc. Trans. 44 (2016) 1158–64. doi:10.1042/BST20160067.

[12] R. Koppram, E. Albers, L. Olsson, Evolutionary engineering strategies to enhance tolerance of xylose utilizing recombinant yeast to inhibitors derived from spruce biomass, Biotechnol. Biofuels. 5 (2012) 32. doi:10.1186/1754-6834-5-32.

[13] E. Fletcher, A. Feizi, M.M.M. Bisschops, B.M. Hallström, S. Khoomrung, V. Siewers, J. Nielsen, Evolutionary engineering reveals divergent paths when yeast is adapted to different acidic environments, Metab. Eng. 39 (2017) 19–28. doi:10.1016/J.YMBEN.2016.10.010.

[14] T. Niederwieser, P. Kociolek, D. Klaus, A review of algal research in space, Acta Astronaut. 146 (2018) 359–367.

[15] G. Olivieri, P. Salatino, A. Marzocchella, Advances in photobioreactors for intensive microalgal production: configurations, operating strategies and applications, J. Chem. Technol. Biotechnol. 89 (2014) 178–195.

[16] C. Verseux, M. Baqué, K. Lehto, J.-P.P. de Vera, L.J. Rothschild, D. Billi, Sustainable life support on Mars–the potential roles of cyanobacteria, Int. J. Astrobiol. 15 (2016) 65–92.

[17] F. Ashfaque, A. Inam, S. Sahay, S. Iqbal, Influence of Heavy Metal Toxicity on Plant Growth, Metabolism and Its Alleviation by Phytoremediation - A Promising Technology, J. Agric. Ecol. Res. Int. 6 (2016) 1–19. doi:10.9734/JAERI/2016/23543.

[18] B.A.E. Lehner, C.N. Haenggi, J. Schleppi, S.J.J. Brouns, A.S. Meyer, A. Cowley, Bacterial modification of lunar and Martian regolith for plant growth in life support systems, in: Int. Astronaut. Congr., Bremen, 2018.

[19] L. Sauheitl, B. Glaser, A. Weigelt, Uptake of intact amino acids by plants depends on soil amino acid concentrations, Environ. Exp. Bot. 66 (2009) 145–152. doi:10.1016/J.ENVEXPBOT.2009.03.009.

[20] B. Adamczyk, A. Smolander, V. Kitunen, M. Godlewski, Proteins as nitrogen source for plants: a short story about exudation of proteases by plant roots, Plant Signal. Behav. 5 (2010) 817–819. doi:10.4161/psb.5.7.11699.

[21] P. Janczyk, H. Franke, W.B. Souffrant, Nutritional value of Chlorella vulgaris: Effects of ultrasonication and electroporation on digestibility in rats, Anim. Feed Sci. Technol. 132 (2007) 163–169. doi:10.1016/J.ANIFEEDSCI.2006.03.007.

[22] A.N. Halliday, H. Wänke, J.-L. Birck, R.N. Clayton, The Accretion, Composition and Early Differentiation of Mars, Space Sci. Rev. 96 (2001) 197–230. doi:10.1023/A:1011997206080.

[23] C.R. Myers, K.H. Nealson, Bacterial Manganese Reduction and Growth with Manganese Oxide as the Sole Electron Acceptor, Science (80-.). 240 (1988) 1319–1321. doi:10.1126/science.240.4857.1319.

[24] J.E. Kostka, D.D. Dalton, H. Skelton, S. Dollhopf, J.W. Stucki, Growth of Iron(III)-Reducing Bacteria on Clay Minerals as the Sole Electron Acceptor and Comparison of Growth Yields on a Variety of Oxidized Iron Forms, Appl. Environ. Microbiol. 68 (2002) 6256–6262. doi:10.1128/AEM.68.12.6256-6262.2002.

[25] B.E. Launder, D.B. Spalding, The numerical computation of turbulent flows, in: Numer. Predict. Flow, Heat Transf. Turbul. Combust., Elsevier, 1983: pp. 96–116.

[26] J.C. Merchuk, M. Gluz, Bioreactors, Air-lift Reactors, in: Encycl. Bioprocess Technol., John Wiley & Sons, Inc., Hoboken, NJ, USA, 2002. doi:10.1002/0471250589.ebt029.

[27] D.L. Bish, D.F. Blake, D.T. Vaniman, S.J. Chipera, R. V Morris, D.W. Ming,

8

A.H. Treiman, P. Sarrazin, S.M. Morrison, R.T. Downs, C.N. Achilles, A.S. Yen, T.F. Bristow, J.A. Crisp, J.M. Morookian, J.D. Farmer, E.B. Rampe, E.M. Stolper, N. Spanovich, M.S. MSL Science Team, X-ray diffraction results from Mars Science Laboratory: mineralogy of Rocknest at Gale crater., Science. 341 (2013) 1238932. doi:10.1126/science.1238932.

[28] O. Bingjie, L. Xiancai, L. Huan, L. Juan, Z. Tingting, Z. Xiangyu, L. Jianjun, W. Rucheng, Reduction of jarosite by Shewanella oneidensis MR-1 and secondary mineralization, Geochim. Cosmochim. Acta. 124 (2014) 54–71. doi:10.1016/J.GCA.2013.09.020.

[29] R.K. Kukkadapu, J.M. Zachara, S.C. Smith, J.K. Fredrickson, C. Liu, Dissimilatory bacterial reduction of Al-substituted goethite in subsurface sediments, Geochim. Cosmochim. Acta. 65 (2001) 2913–2924. doi:10.1016/S0016-7037(01)00656-1.

[30] P.I. Craig, A. Rudolph, R. V Morris, C.N. Achilles, E.B. Rampe, A.H. Treiman, T.F. Bristow, D.W. Ming, D.F. Blake, D.T. Vaniman, R.T. Downs, S.M. Morrison, A.S. Yen, J. Farmer, COLLAPSED SMECTITE IN GALE CRATER: MARTIAN CLAY MINERALS MAY HAVE BEEN ON ACID, in: 49th Lunar Planet. Sci. Conf. 2018, 2018. https://ntrs.nasa.gov/search.jsp?R=20180004268 (accessed June 18, 2019).

[31] A. Banin, J. Rishpon, Smectite clays in Mars soil: Evidence for their presence and role in Viking biology experimental results, J. Mol. Evol. 14 (1979) 133–152. doi:10.1007/BF01732373.

[32] R.G. Burns, Ferric sulfates on Mars, J. Geophys. Res. Solid Earth. 92 (1987) E570–E574. doi:10.1029/JB092iB04p0E570.

[33] P.-Y. Meslin, O. Gasnault, O. Forni, S. Schröder, A. Cousin, G. Berger, S.M. Clegg, J. Lasue, S. Maurice, V. Sautter, S. Le Mouélic, R.C. Wiens, C. Fabre, W. Goetz, D. Bish, N. Mangold, B. Ehlmann, N. Lanza, A.-M. Harri, R. Anderson, E. Rampe, T.H. McConnochie, P. Pinet, D. Blaney, R. Léveillé, D. Archer, B. Barraclough, S. Bender, D. Blake, J.G. Blank, N. Bridges, B.C. Clark, L. DeFlores, D. Delapp, G. Dromart, M.D. Dyar, M. Fisk, B. Gondet, J. Grotzinger, K. Herkenhoff, J. Johnson, J.-L. Lacour, Y. Langevin, L. Leshin, E. Lewin, M.B. Madsen, N. Melikechi, A. Mezzacappa, M.A. Mischna, J.E. Moores, H. Newsom, A. Ollila, R. Perez, N. Renno, J.-B. Sirven, R. Tokar, M. de la Torre, L. d'Uston, D.

Vaniman, A. Yingst, M.S. MSL Science Team, Soil diversity and hydration as observed by ChemCam at Gale crater, Mars., Science. 341 (2013) 1238670. doi:10.1126/science.1238670.

[34] R. V. Morris, G. Klingelhöfer, C. Schröder, D.S. Rodionov, A. Yen, D.W. Ming, P.A. de Souza, I. Fleischer, T. Wdowiak, R. Gellert, B. Bernhardt, E.N. Evlanov, B. Zubkov, J. Foh, U. Bonnes, E. Kankeleit, P. Gütlich, F. Renz, S.W. Squyres, R.E. Arvidson, Mössbauer mineralogy of rock, soil, and dust at Gusev crater, Mars: Spirit's journey through weakly altered olivine basalt on the plains and pervasively altered basalt in the Columbia Hills, J. Geophys. Res. Planets. 111 (2006). doi:10.1029/2005JE002584@10.1002/(ISSN)2169-9100.SPIRIT1.

[35] T. Perez-Gonzalez, C. Jimenez-Lopez, A.L. Neal, F. Rull-Perez, A. Rodriguez-Navarro, A. Fernandez-Vivas, E. Iañez-Pareja, Magnetite biomineralization induced by Shewanella oneidensis, Geochim. Cosmochim. Acta. 74 (2010) 967–979. doi:10.1016/j.gca.2009.10.035.

[36] D. Craig Cooper, Flynn Picardal, and Jason Rivera, C. Talbot, Zinc Immobilization and Magnetite Formation via Ferric Oxide Reduction by Shewanella putrefaciens 200, (1999). doi:10.1021/ES990510X.

[37] B. Byloos, I. Coninx, O. Van Hoey, C. Cockell, N. Nicholson, V. Ilyin, R. Van Houdt, N. Boon, N. Leys, The Impact of Space Flight on Survival and Interaction of Cupriavidus metallidurans CH34 with Basalt, a Volcanic Moon Analog Rock, Front. Microbiol. 8 (2017) 1–14. doi:10.3389/fmicb.2017.00671.

[38] C.L. Cheung, A. Tabor, Could Electricity-Producing Bacteria Help Power Future Space Missions?, (2018). https://www.nasa.gov/feature/ames/could-electricity-producing-bacteria-help-power-future-space-missions (accessed June 20, 2019).

[39] J. Doucha, K. Lívanský, Outdoor open thin-layer microalgal photobioreactor: potential productivity, J. Appl. Phycol. 21 (2009) 111–117.

[40] Lovley, D. R., Phillips, E. J. P., & Lonergan, D. J. (1989). Hydrogen and Formate Oxidation Coupled to Dissimilatory Reduction of Iron or Manganese by Alteromonas putrefaciens. Applied and Environmental Microbiology, 55(3), 700–706. Retrieved from http://aem.asm.org/content/55/3/700

[41] Karp, P. D., Billington, R., Caspi, R., Fulcher, C. A., Latendresse, M., Kothari, A., Subhraveti, P. (2017). The BioCyc collection of microbial genomes and

metabolic pathways. *Briefings in Bioinformatics*. https://doi.org/10.1093/bib/bbx085

[42] G.E. Pinchuk, E.A. Hill, O. V. Geydebrekht, J. De Ingeniis, X. Zhang, A. Osterman, J.H. Scott, S.B. Reed, M.F. Romine, A.E. Konopka, A.S. Beliaev, J.K. Fredrickson, J.L. Reed, Constraint-Based Model of Shewanella oneidensis MR-1 Metabolism: A Tool for Data Analysis and Hypothesis Generation, PLoS Comput. Biol. 6 (2010) e1000822. doi:10.1371/journal.pcbi.1000822.

[43] L. Fowden, The composition of the bulk proteins of Chlorella, Biochem. J. 50 (1952) 355–358. doi:10.1042/bj0500355.

[44] Wieland, P. O., Designing For Human Presence in Space: An Introduction to Environmental Control and Life Support Systems (ECLSS), 2005. https://ntrs.nasa.gov/search.jsp?R=20060005209 (accessed June 18, 2019).

[45] S. Staniland, W. Williams, N. Telling, G. Van Der Laan, A. Harrison, B. Ward, Controlled cobalt doping of magnetosomes in vivo, Nat. Nanotechnol. 3 (2008) 158–162. doi:10.1038/nnano.2008.35.

[46] C. Zhang, S. Liu, T.J. Phelps, D.R. Cole, J. Horita, S.M. Fortier, M. Elless, J.W. Valley, Physiochemical, mineralogical, and isotopic characterization of magnetite-rich iron oxides formed by thermophilic iron-reducing bacteria, Geochim. Cosmochim. Acta. 61 (1997) 4621–4632. doi:10.1016/S0016-7037(97)00257-3.

[47] M.Y. Chisti, M. Moo-Young, Airlift reactors: characteristics, applications and design considerations, Chem. Eng. Commun. 60 (1987) 195–242.

[48] C.C. Allen, R. V Morris, D.J. Lindstrom, M.M. Lindstrom, J.P. Lockwood, JSC MARS-1: Martian Regolith Simulant, in: Lunar Planet. Sci. XXVIII, Houston, TX, 1997.

[49] S. Becker, A. Sokolichin, G. Eigenberger, Gas—liquid flow in bubble columns and loop reactors: Part II. Comparison of detailed experiments and flow simulations, Chem. Eng. Sci. 49 (1994) 5747–5762.

[50] D. Markovitsi, T. Gustavsson, A. Banyasz, Absorption of UV radiation by DNA: Spatial and temporal features, Mutat. Res. Mutat. Res. 704 (2010) 21–28. doi:10.1016/j.mrrev.2009.11.003.

[51] G. Horneck, R. Facius, G. Reitz, P. Rettberg, C. Baumstark-Khan, R. Gerzer, Critical issues in connection with human missions to Mars: Protection of and from the martian environment, Adv. Sp. Res. 31 (2003) 87–95. doi:10.1016/S0273-

1177(02)00662-2.

[52] P.B. Saganti, F.A. Cucinotta, J.W. Wilson, L.C. Simonsen, C. Zeitlin, Radiation climate map for analyzing risks to astronauts on the mars surface from galactic cosmic rays, Space Sci. Rev. 110 (2004) 143–156. doi:10.1023/B:SPAC.0000021010.20082.1a.

[53] L.C. Simonsen, J.E. Nealy, L.W. Townsend, J.W. Wilson, Space Radiation Shielding for a Martian Habitat, SAE Trans. 99 (1990) 972--979. doi:10.2307/44472557.

[54] A.R. Brown, E. Correa, Y. Xu, N. AlMasoud, S.M. Pimblott, R. Goodacre, J.R. Lloyd, Phenotypic Characterisation of Shewanella oneidensis MR-1 Exposed to X-Radiation., PLoS One. 10 (2015) e0131249. doi:10.1371/journal.pone.0131249.

[55] R. Matthewman, I.A. Crawford, A.P. Jones, K.H. Joy, M.A. Sephton, Organic Matter Responses to Radiation under Lunar Conditions, Astrobiology. 16 (2016) 900–912. doi:10.1089/ast.2015.1442.

[56] G. KMINEK, J. BADA, The effect of ionizing radiation on the preservation of amino acids on Mars, Earth Planet. Sci. Lett. 245 (2006) 1–5. doi:10.1016/j.epsl.2006.03.008.

[57] D.P. Lies, M.E. Hernandez, A. Kappler, R.E. Mielke, J.A. Gralnick, K. Dianne, D.K. Newman, Shewanella oneidensis MR-1 Uses Overlapping Pathways for Iron Reduction at a Distance and by Direct Contact under Conditions Relevant for Biofilms, Appl. Environ. Microbiol. 71 (2005) 4414–4426. doi:10.1128/AEM.71.8.4414.

[58] G.W.W. Wamelink, J.Y. Frissel, W.H.J. Krijnen, M.R. Verwoert, P.W. Goedhart, Can Plants Grow on Mars and the Moon: A Growth Experiment on Mars and Moon Soil Simulants, PLoS One. 9 (2014) e103138. doi:10.1371/journal.pone.0103138.

[59] C.D. Foy, R.L. Chaney, M.C. White, The Physiology of Metal Toxicity in Plants, Annu. Rev. Plant Physiol. 29 (1978) 511–566. doi:10.1146/annurev.pp.29.060178.002455.

[60] G.R. Rout, S. Samantaray, P. Das, M. Trevisan, Aluminium toxicity in plants: a review G Aluminium toxicity in plants: a review, Agronomie. 21 (2001) 3–21. doi:10.1051/agro:2001105ï.

[61] R.-X. Li, F. Cai, G. Pang, Q.-R. Shen, R. Li, W. Chen, Solubilisation of

Phosphate and Micronutrients by Trichoderma harzianum and Its Relationship with the Promotion of Tomato Plant Growth, PLoS One. 10 (2015) e0130081. doi:10.1371/journal.pone.0130081.

[62] U.C. Gupta, E.W. Chipman, Influence of iron and pH on the yield and iron, manganese, zinc, and sulfur concentrations of carrots grown on sphagnum peat soil, Plant Soil. 44 (1976) 559–566. doi:10.1007/BF00011375.

[63] T. El-Jaoual, D.A. Cox, Manganese toxicity in plants, J. Plant Nutr. 21 (1998) 353–386. doi:10.1080/01904169809365409.

[64] E.L. Connolly, M. Guerinot, Iron stress in plants, Genome Biol. 3 (2002) reviews1024.1. doi:10.1186/gb-2002-3-8-reviews1024.

[65] B. Wang, C.Q. Lan, M. Horsman, Closed photobioreactors for production of microalgal biomasses, Biotechnol. Adv. 30 (2012) 904–912. doi:10.1016/J.BIOTECHADV.2012.01.019.

[66] M.A. Gross, Z. Wen, Photobioreactor systems and methods, (2018).

[67] B. Santek, M. Ivancic, P. Horvat, S. Novak, V. Maric, Horizontal tubular bioreactors in biotechnology, Chem. Biochem. Eng. Q. 20 (2006) 389–399.

[68] C.-M. Loudon, N. Nicholson, K. Finster, N. Leys, B. Byloos, R. Van Houdt, P. Rettberg, R. Moeller, F.M. Fuchs, R. Demets, J. Krause, M. Vukich, A. Mariani, C. Cockell, BioRock: new experiments and hardware to investigate microbe–mineral interactions in space, Int. J. Astrobiol. 17 (2018) 303–313. doi:10.1017/S1473550417000234.

[69] B.A.E. Lehner, J. Schlechten, A. Filosa, A. Canals Pou, D.G. Mazzotta, F. Spina, L. Teeney, J. Snyder, S.Y. Tjon, A.S. Meyer, S.J.J. Brouns, A. Cowley, L.J. Rothschild, End-to-end mission design for microbial ISRU activities as preparation for a moon village, Acta Astronaut. 162 (2019) 216–226. doi:10.1016/J.ACTAASTRO.2019.06.001.

[70] A.M.J. Kliphuis, M. Janssen, E.J. van den End, D.E. Martens, R.H. Wijffels, Light respiration in Chlorella sorokiniana, J. Appl. Phycol. 23 (2011) 935–947.

[71] H.-X. Chang, Y. Huang, Q. Fu, Q. Liao, X. Zhu, Kinetic characteristics and modeling of microalgae Chlorella vulgaris growth and CO2 biofixation considering the coupled effects of light intensity and dissolved inorganic carbon, Bioresour. Technol. 206 (2016) 231–238. doi:10.1016/J.BIORTECH.2016.01.087.

[72] J. Kim, J.-Y. Lee, T. Lu, A model for autotrophic growth of Chlorella vulgaris

8

under photolimitation and photoinhibition in cylindrical photobioreactor, Biochem. Eng. J. 99 (2015) 55–60. doi:10.1016/J.BEJ.2015.03.010.

[73] Y.J. Tang, J.S. Hwang, D.E. Wemmer, J.D. Keasling, Shewanella oneidensis MR-1 fluxome under various oxygen conditions, Appl. Environ. Microbiol. 73 (2007) 718–729. doi:10.1128/AEM.01532-06.

[74] R. Kleerebezem, M.C.M. Van Loosdrecht, A generalized method for thermodynamic state analysis of environmental systems, Crit. Rev. Environ. Sci. Technol. 40 (2010) 1–54. doi:10.1080/10643380802000974.

[75] D.R. Lovley, E.J.P. Phillips, D.J. Lonergan, Hydrogen and Formate Oxidation Coupled to Dissimilatory Reduction of Iron or Manganese by Alteromonas putrefaciens, Appl. Environ. Microbiol. 55 (1989) 700–706. http://aem.asm.org/content/55/3/700.

[76] A. Dollfus, M. Deschamps, Grain-size determination at the surface of Mars, Icarus. 67 (1986) 37–50. doi:10.1016/0019-1035(86)90172-7.

[77] C. Liu, J.M. Zachara, Y.A. Gorby, J.E. Szecsody, C.F. Brown, Microbial Reduction of Fe(III) and Sorption/Precipitation of Fe(II) on Shewanella putrefaciens Strain CN32, Environ. Sci. Technol. 35 (2001) 1385–1393. doi:10.1021/es0015139.

[78] C. Liu, Y.A. Gorby, J.M. Zachara, J.K. Fredrickson, C.F. Brown, Reduction kinetics of Fe(III), Co(III), U(VI), Cr(VI), and Tc(VII) in cultures of dissimilatory metal-reducing bacteria, Biotechnol. Bioeng. 80 (2002) 637–649. doi:10.1002/bit.10430.

[79] X. Feng, Y. Xu, Y. Chen, Y.J. Tang, Integrating Flux Balance Analysis into Kinetic Models to Decipher the Dynamic Metabolism of Shewanella oneidensis MR-1, PLoS Comput. Biol. 8 (2012) e1002376. doi:10.1371/journal.pcbi.1002376.

[80] Y.J. Tang, A.L. Meadows, J.D. Keasling, A kinetic model describing Shewanella oneidensis MR-1 growth, substrate consumption, and product secretion, Biotechnol. Bioeng. 96 (2007) 125–133. doi:10.1002/bit.21101.

[81] Cogne, G., Cornet, J.-F., & Gros, J.-B. (2008). Design, Operation, and Modeling of a Membrane Photobioreactor to Study the Growth of the Cyanobacterium Arthrospira platensis in Space Conditions. Biotechnology Progress, 21(3), 741–750. https://doi.org/10.1021/bp0495926

[82] Wagner, I., Braun, M., Slenzka, K., & Posten, C. (2015). Photobioreactors in

8

Life Support Systems. In Advances in biochemical engineering/biotechnology (Vol. 153, pp. 143–184). https://doi.org/10.1007/10_2015_327

[83] Duan, C.-H., Luo, M.-F., Yang, C., Jiang, H., & Xing, X.-H. (2010). Effects of different hollow fiber membrane modules on bubbleless aeration of methane and oxygen. In Guocheng Gongcheng Xuebao/The Chinese Journal of Process Engineering (Vol. 10).

[84] Sander, R. (2015). Compilation of Henry's law constants (version 4.0) for water as solvent. Atmospheric Chemistry and Physics, 15(8), 4399–4981. https://doi.org/10.5194/acp-15-4399-2015

[85] Hu, Q., Guterman, H., & Richmond, A. (1996). A flat inclined modular photobioreactor for outdoor mass cultivation of photoautotrophs. Biotechnology and Bioengineering, 51(1), 51–60.

[86] The engineering toolbox. (2019). Densities of Solids.

[87] de Vree, J. H. (2016). Outdoor production of microalgae. Wageningen University.

[88] Goodfellow. (2019). Carbon/Epoxy Composite - online catalogue source - supplier of research materials in small quantities - Goodfellow. Retrieved June 27, 2019, from http://www.goodfellow.com/E/Carbon-Epoxy-Composite.html

[89] Muscatello, A., & Santiago-Maldonado, E. (2012). Mars In Situ Resource Utilization Technology Evaluation. 50th AIAA Aerospace Sciences Meeting Including the New Horizons Forum and Aerospace Exposition. https://doi.org/10.2514/6.2012-360

[90] Schegel, F. (2015). Which Multiphase Flow Interface Should I Use? COMSOL BLOGS. Retrieved from https://www.comsol.com/blogs/which-multiphase-flow-interface-should-i-use/

[91] Young, A. (2019). Introduction to Simulating Multiphase Flow with COMSOL Multiphysics. COMSOL Webinars. Retrieved from https://www.comsol.com/video/introduction-to-simulating-multiphase-flow-with-comsol-multiphysics

[92] El Sherif, D., & Knox, J. C. (2005). International space station carbon dioxide removal assembly (iss cdra) concepts and advancements. SAE Technical Paper.

[93] Singh, V. (1992). Mathematical Modelling Of Particle Suspension In Pachuca Tanks. Digital Library of India. Retrieved from

https://archive.org/details/in.ernet.dli.2015.194538

[94] Simha, R. (1942). Relation Between Viscosity of Solutions and Physical Properties of High Polymers. Journal of Applied Physics, 13(3), 147–153. https://doi.org/10.1063/1.1714848

[95] National Coal Board; Scientific Control Great Britain. (1953). Proceedings of a Colloquium on the Hydraulic Transport of Coal. Retrieved from https://books.google.nl/books?id=LABrwgEACAAJ

8

9

Final remarks and future direction of this work

Benjamin A. E. Lehner

9.1 Improvements in the bacterial reduction mechanism

The work described in this thesis identifies various applications of microbiological processes, mainly involving *Shewanella oneidensis,* for nanotechnology and space exploration. The central theme is the reduction mechanism of the bacterium, and thus, the proposed methodology would benefit greatly if this mechanism could be further optimized. Recent work showed that genetic and environmental modifications can indeed improve the electron transport chain of *Shewanella oneidensis* [1-3] and further breakthroughs in this field are expected because of the various applications of the organism (fuel cells, waste-water treatment, material science, biomining, bioleaching, etc.) [4-7]. Also, the cultivation of new dissimilatory metal-reducing microorganisms (DIRM) will enhance the understanding of the biological limits of the reduction process, enabling new applications.

9.2 Limits for the microbial reduction mechanism

The bacterial reduction process, as shown in this thesis, is a great tool for a variety of applications. However, many challenges remain to adopt microbial approaches to reduce ketone, hydroxyl, epoxyl or carboxyl containing nanomaterials like graphene oxide (chapter 3). Firstly, biological systems have a variety of by-products, which stick to the oxygen groups of graphene oxide and tremendously increase the need for purification steps (downstream processes), which, if not carefully applied, also alter the properties of the nanomaterial. Secondly, the microbial reduction is with a 1-2 days process-time fairly slow compared to chemical reduction methodologies, which typically take a few hours. Thirdly, the improved sustainability and environmental friendliness of microbial methodologies have still to be shown in an upscaled process, which includes (1) the medium intake and (2) the gas outtake of the reactor as well as (3) all down-streaming and (4) reactor cleaning processes involved to achieve microbially reduced graphene oxide.

Instead, it might be useful to harvest a reduction agent, for example an organic acid, from bacteria and apply it to graphene oxide [8]. This reduction agent can remove the oxygen groups in a similar sustainable way as bacteria, but without the generation of sticky side products.

A further increase in sustainability can be achieved by applying an oxidizing strain, like *Acidithiobacillus ferrooxidans*, which could replace the strong chemistry involved to produce graphene oxide from graphite [9]. The latter would be in particular beneficial, considering the high number of applications for graphene oxide, mentioned in chapter 4, including biosensor, nanocomposites and drug delivery matrixes [10, 11].

9

9.3 Experiments to advance microbial impact on nanotechnology

The cost-efficient bacterial printing methodology (chapter 2) in conjunction with nanomaterial precursor molecules could be an excellent way to achieve biological patterning of those precursors and allow for a patterning of the graphene oxide surface. Our initial trials on the printing of *Shewanella oneidensis* inside an alginate matrix onto graphene oxide failed to show changes in conductivity between treated and non-treated areas. There were two main issues identified. Firstly, the contact between the graphene oxide surface and the bacteria, which were trapped in the alginate gel, was very weak. Secondly, the multiple, tightly stacked flakes of graphene oxide didn't allow for a penetration into even 1/10 of the materials thickness.

The first problem could be resolved by applying those bacteria for a longer timeframe in a less viscose bioink (to allow for sinking) and continiously adding fresh nutrients to them (to prevent starving). For the second, more severe issue, a new way to produce and deposit the graphene oxide precursor material is needed. Only a very thin and uniform deposition of graphene oxide flakes will allow for sufficient reduction of its surface.

This along with the previously described experiments to oxidize graphite with bacteria might enable cost-efficient, new and sustainable applications of patterned graphene oxide.

9

9.4 Outlook on biomining for space exploration

The kinetic and yield model in chapter 6 highlighted *S. oneidensis* out of four potential candidates as the only organism feasible to extract iron with a positive yield. For all others, the amount of nutrients needed outweighed the product. However, *A. ferroxidans, M. gryphisiwaldense,* and *E.coli*, the three other tested organisms, can be feasible if more resources, like sugars, ions or aminoacids, are available at the destination or if they are coupled to additional procceses like life-support systems. For example, the production of acids from the Lunar regolith would make *A. ferroxidans* an excellent choice to bioleach the iron(II) rich Lunar material.

The reduction of metal oxides as well as the connected capability to bioleach metal oxide containing minerals as done by *Shewanella oneidensis* might help to purify single elements like iron or aluminum and utilize them afterwards via on-demand 3D-printing (Fig. 9.1 5a, 6). Those 3D-printed objects will be essential for rocket-replacement parts and habitat building blocks. The advancement of new metal printing methodologies, which are also suitable for partial gravity, will further advance the possibilities in this sector. Companies like Lithoz, Space Foundry or Sisma are working in conjunction with ESA and NASA on those advancements.

Chapter 8 modelled how this entire process of a *Shewanella oneidensis* bioreactor could be added to a Mars colony. We assumed that a shaking bioreactor would perform the best, because all results in chapter 7 were obtained in a shaking environment and first trials of non-shaking batches showed insufficient reduction. Nevertheless, it would be interesting to test biofilm based sink-bed reactors for the exact same purpose of producing magnetite with *S. oneidensis* and compare their efficiency in an additional bioreactor model [12]. The main advantage of this type of system is the undisturbed formation of biofilms. A wide range of dissimilatory metal-reducing microorganisms are known to perform best if they are in direct contact with the electron acceptor [13]. The cell-to-rock contact can enable

an improved direct reduction via the cell membrane as well as the formation of nanowires [14]. Independent of the type of reactor, the extraction of iron initiated by *Shewanella oneidensis* (Fig. 9.1 3,4) or another similar biomining process, could be the core of a biological infrastructure on Mars. It fulfils the immediate need of on-demand construction parts for the newly established colony, while at the same time enhancing the available biomass for biology-based processes. Further experiments will be necessary to test the biomass recycling and transfer into life support systems (Fig, 9.1 5b). The CROP system at the DLR and the European Astronaut Centre (EAC-ESA) in Cologne might serve as a testbed for those trials.

The introduction of algae as nutrient source for the biomining process, as well as an oxygen source for human, into the biological infrastructure might increase its feasibility tremendously (Fig 9.1 2). Algae or cyanobacteria can fixate the atmospheric carbon dioxide on Mars. The Martian surface has a pressure of 700-1000 Pa [15], which consists to 95 % of carbon dioxide and 0.07 % of carbon monoxide with the latter being toxic for many photoautotrophic organisms [16, 17]. If the air is compressed to physiological levels the carbon monoxide has to be reduced or a very resistant algae strain must be used. Additional studies to proof the successful implementation of the algae as an amino acid or sugar source for *Shewanella oneidensis* will be essential. Lynn Rothschild's lab at NASA Ames already investigated the usage of algae as a nutrient source for *Bacillus subtilis* and different yeast strains, which is a positive indication that it will also work for *Shewanella oneidensis*. Another way to improve the feasibility of any biological process is the addition of *in-situ* water to the system. A majority of the ISRU efforts of space agencies around the world is currently focusing on this water mining process [18].
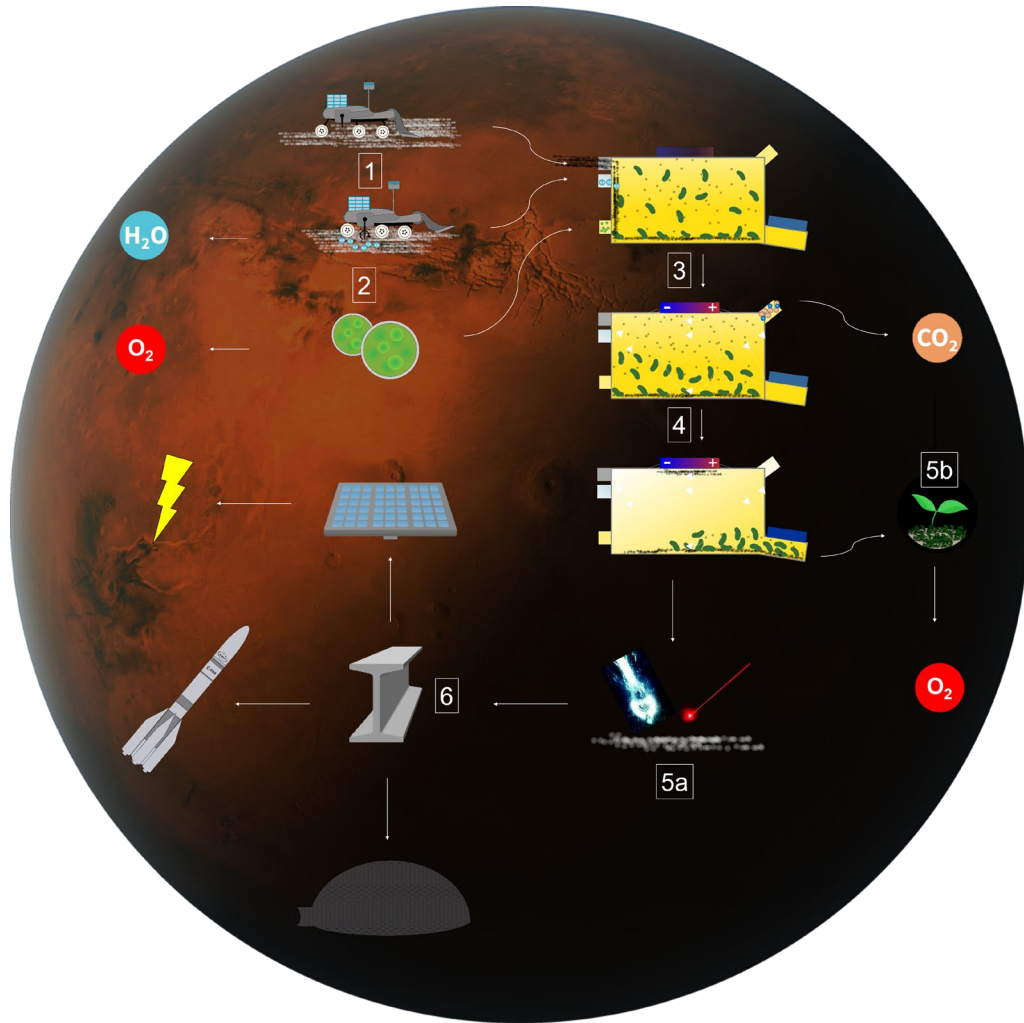
Fig. 9.1 Overview of the microbial infrastructure with a focus on biomining applications. A rover is mining regolith particles and water (1) from the Martian soil and transferring those to a bioreactor. Algaes are grown in a photoautotroph reactor (2) to supply nutrients for the biomining reactor as well as oxygen for the astronauts. A batch of bacteria leaches and changes the properties of the regolith particles (3) and an extraction methodology, in this case magnetic extraction, is applied (4). The magnetically extracted material can be 3D printed (5a) or stored and used if demand arises (6). The leftover material (5b) can be recycled for plant growth.

9

9.5 Experiments to advance biomining for space applications

After the previously mentioned model of a sink-bed reactor and some further experiments under non-shaking conditions a proof-of-concept bioreactor should be designed. The bioreactor has to combine the microbial reduction process with an optimized magnetic extraction mechanism. It could host multiple electromagnets on the top or even a central handmagnet, which is insulated from the liquid. Both solutions would only work in a shaking environment.

Besides the engineering challenges for the reactor design, there are also further biological tests considering the space environment to be conducted. The bacterial extraction should be exposed to partial gravitation and a increased radiation background. The first test could be done in a centrifuge at the ISS, a satellite or any launching vehicle which stays in orbit for more than a few days. The partial gravity of Mars (0.38 g) is not expected to influence the methodology negatively [19], but only a test under those conditions could bring clarity. *Shewanella oneidensis* was already once tested on the ISS between March and October, 2018, regarding its ability to survive and strive under microgravity. The three objectives of this study were to "(1) Measure *Shewanella oneidensis* MR-1 extracellular electron transport (EET) rates, and determine the EET mechanism(s) impacted by microgravity using biochemical and genetic approaches; (2) Characterize and quantify *S. oneidensis* MR-1 biofilm development under microgravity conditions; (3) Identify other key molecular and genetic components for biofilm formation, and extracellular electron transport, that are affected by microgravity by utilizing genome-wide gene expression and mutant fitness profiling". The results of this experiment are still pending and will help to understand better if we should use this organism or introduce the reduction mechanism into another bacterium instead.

9

9.6 Final thoughts

The electron transport mechanism of *Shewanella oneidensis* makes it a fascinating organism, and we will see even more real-world applications of it and others dissimilatory metal-reducing microorganisms in the future, especially due to improvements in its reduction capabilities. The convincing work showing that microorganism can be feasible in space-biomining applications in this thesis, is certain to have a lasting impact on the way we approach biology for space exploration. The combination of chapter 7, which shows an experimental proof-of-principle of the iron extraction mechanism together with chapter 6, which analyses the theoretical feasibility should be the standard procedure to convince decision makers of its value. Chapter 5 and 8 give examples of how to potentially implement those biological processes in the programs of space agencies around the world. I hope that this line of work will be further supported with manpower as well as funding to drive investigation of biomining approaches via dissimilatory metal-reducing microorganisms to the next level and finally apply it one day on Mars.

It was an insightful experience to study *Shewanella oneidensis* and work on potential applications in the field of nanotechnology as well as space exploration. My journey introduced me to a variety of new fields including geology, biotechnology, cleanroom-fabrication, aerospace engineering, and synthetic chemistry. I am looking forward to applying those as well as the management, planning, and presentation skills acquired to my start-up company, which will be my next personal endeavour. The start-up called IntuAir will use nanotechnology and biotechnology to build a high-tech urban forest for the fixation of carbon dioxide and the improvement of indoor air quality.

9

9.7 References

[1] D. Min, L. Cheng, F. Zhang, X.-N. Huang, D.-B. Li, D.-F. Liu, T.-C. Lau, Y. Mu, H.-Q. Yu, Enhancing Extracellular Electron Transfer of Shewanella oneidensis MR-1 through Coupling Improved Flavin Synthesis and Metal-Reducing Conduit for Pollutant Degradation, Environmental Science & Technology 51(9) (2017) 5082-5089.

[2] I.S. Ng, Y. Guo, Y. Zhou, J.-W. Wu, S.-I. Tan, Y.-C. Yi, Turn on the Mtr pathway genes under pLacI promoter in Shewanella oneidensis MR-1, Bioresources and Bioprocessing 5(1) (2018) 35.

[3] F. Li, Y.-X. Li, Y.-X. Cao, L. Wang, C.-G. Liu, L. Shi, H. Song, Modular engineering to increase intracellular NAD(H/+) promotes rate of extracellular electron transfer of Shewanella oneidensis, Nature Communications 9(1) (2018) 3637.

[4] F. Zhang, S.-J. Yuan, W.-W. Li, J.-J. Chen, C.-C. Ko, H.-Q. Yu, WO3 nanorods-modified carbon electrode for sustained electron uptake from Shewanella oneidensis MR-1 with suppressed biofilm formation, Electrochimica Acta 152 (2015) 1-5.

[5] T. Perez-Gonzalez, C. Jimenez-Lopez, A.L. Neal, F. Rull-Perez, A. Rodriguez-Navarro, A. Fernandez-Vivas, E. Iañez-Pareja, Magnetite biomineralization induced by Shewanella oneidensis, Geochimica et Cosmochimica Acta 74(3) (2010) 967-979.

[6] C.R. Myers, K.H. Nealson, Respiration-linked proton translocation coupled to anaerobic reduction of manganese(IV) and iron(III) in Shewanella putrefaciens MR-1, Journal of Bacteriology 172(11) (1990) 6232.

[7] G. Liu, X. Zhang, J. Zhou, A. Wang, J. Wang, R. Jin, H. Lv, Quinone-mediated microbial synthesis of reduced graphene oxide with peroxidase-like activity, Bioresour Technol 149 (2013) 503-8.

[8] K.K.H. De Silva, H.H. Huang, R.K. Joshi, M. Yoshimura, Chemical reduction of graphene oxide using green reductants, Carbon 119 (2017) 190-199.

[9] C. Zhu, L. Liu, M. Fan, L. Liu, B. Dai, J. Yang, D. Sun, Microbial oxidation of graphite by Acidithiobacillus ferrooxidans CFMI-1, RSC Advances 4(98) (2014) 55044-55047.

9

[10] N. Luo, J.K. Weber, S. Wang, B. Luan, H. Yue, X. Xi, J. Du, Z. Yang, W. Wei, R. Zhou, G. Ma, PEGylated graphene oxide elicits strong immunological responses despite surface passivation, Nat Commun 8 (2017) 14537.

[11] C. Zhang, L. Wang, T. Zhai, X. Wang, Y. Dan, L.S. Turng, The surface grafting of graphene oxide with poly(ethylene glycol) as a reinforcement for poly(lactic acid) nanocomposite scaffolds for potential tissue engineering applications, J Mech Behav Biomed Mater 53 (2016) 403-413.

[12] D. Ercan, A. Demirci, Current and future trends for biofilm reactors for fermentation processes, Critical Reviews in Biotechnology 35(1) (2015) 1-14.

[13] K.A. Weber, L.A. Achenbach, J.D. Coates, Microorganisms pumping iron: anaerobic microbial iron oxidation and reduction, Nature Reviews Microbiology 4(10) (2006) 752-764.

[14] Y.A. Gorby, S. Yanina, J.S. McLean, K.M. Rosso, D. Moyles, A. Dohnalkova, T.J. Beveridge, I.S. Chang, B.H. Kim, K.S. Kim, D.E. Culley, S.B. Reed, M.F. Romine, D.A. Saffarini, E.A. Hill, L. Shi, D.A. Elias, D.W. Kennedy, G. Pinchuk, K. Watanabe, S.i. Ishii, B. Logan, K.H. Nealson, J.K. Fredrickson, Electrically conductive bacterial nanowires produced by Shewanella oneidensis strain MR-1 and other microorganisms, Proceedings of the National Academy of Sciences 103(30) (2006) 11358-11363.

[15] G.M. Martínez, C.N. Newman, A. De Vicente-Retortillo, E. Fischer, N.O. Renno, M.I. Richardson, A.G. Fairén, M. Genzer, S.D. Guzewich, R.M. Haberle, A.M. Harri, O. Kemppinen, M.T. Lemmon, M.D. Smith, M. de la Torre-Juárez, A.R. Vasavada, The Modern Near-Surface Martian Climate: A Review of In-situ Meteorological Data from Viking to Curiosity, Space Science Reviews 212(1) (2017) 295-338.

[16] V.I. Moroz, Chemical composition of the atmosphere of Mars, Advances in Space Research 22(3) (1998) 449-457.

[17] Q. Zheng, Q. Meng, Y.Y. Wei, Z.M. Yang, Alleviation of Copper-Induced Oxidative Damage in Chlamydomonas reinhardtii by Carbon Monoxide, Archives of Environmental Contamination and Toxicology 61(2) (2011) 220-227.

[18] K. Zacny, P. Chu, G. Paulsen, A. Avanesyan, J. Craft, L. Osborne, Mobile In-Situ Water Extractor (MISWE) for Mars, Moon,

and Asteroids In Situ Resource Utilization, AIAA SPACE 2012 Conference & Exposition, American Institute of Aeronautics and Astronautics, Pasadena, California, 2012.

[19] A. Manzano, R. Herranz, L.A. den Toom, S. te Slaa, G. Borst, M. Visser, F.J. Medina, J.J.W.A. van Loon, Novel, Moon and Mars, partial gravity simulation paradigms and their effects on the balance between cell growth and cell proliferation during early plant development, npj Microgravity 4(1) (2018) 9.

9

Summary

Bacteria and other microorganisms are known and studied as an essential part of daily life and they are utilized in a variety of fields. This work identifies applications in nanotechnology and space research, using the same bacterium for both: *Shewanella oneidensis*. The extracellular electron transfer (EET) mechanism situated mainly in the cell membrane of *Shewanella oneidensis* transports electrons, which are produced during its regular metabolic activity, to the outside of the cells. In the presence of certain metal oxides, the bacteria can reduce them while releasing carbon dioxide.

In the field of nanotechnology, we applied this bacterial metabolism to graphene oxide. Graphene oxide (GO) is a 2-dimensional material consisting of a one atom layer thick carbon lattice with oxygen groups (epoxyl, hydroxyl, carboxyl) bound on the top and bottom of the lattice. In this oxidized state the material is stable in water and modifiable, but not conductive and less mechanically strong than if it is reduced. Therefore, we investigated the reduction mechanism of *Shewanella oneidensis* to reduce the oxygen groups and improve the conductance while keeping the material stable in water and its 2-dimensional structure. The microbially reduced graphene oxide (mrGO) was less conductive (2.5 magnitudes increase in conductance in comparison to GO) than the chemically reduced (crGO) one (3.1 magnitudes increase in conductance in comparison to GO), but it sustained its 2-dimensional structure better (average thickness – mrGO: 10.4 ± 0.4 nm, crGO: 31.3 ± 7.0 nm).

To adopt this microbial reduction process in a macroscopic application we build a set-up to 3D-print the bacteria together with the graphene oxide and enable reduction in the so-printed structure (conductive ink / conductive gel). The reduction of graphene oxide was not possible because of missing nutrients, limited penetration depth and the reduction of the alginate matrix by the

bacteria. Nevertheless, we could apply this methodology to show the general possibility of 3D printing bacteria for material production in multiple layers and with a resolution of 1.00 ± 0.15 mm.

The 2-dimensional structure of graphene oxide and therefore, its maximal surface-to-volume ratio also makes it an optimal material for biosensors because of the connection between sensitivity and surface area. Further chemical modifications are needed to passivate the surface of the material and with that, improve its specificity for targeted biomolecules as well as make it more biocompatible. We used a combination of colamine (CA) and polyethylene glycol (PEG) dissolved in either dimethylformamide (DMF) or dimethyl sulfoxide (DMSO) for the passivation and tested the material with X-Ray photoelectron spectroscopy (XPS) and fluorescence microscopy.

In space research, we focused on the application of bacteria for *in situ* resource utilization (ISRU) on Moon and Mars. ISRU describes the process of utilizing the natural resources found at the destination to construct, repair and refuel. This process should improve the sustainability of space missions while at the same time reducing the costs. For this purpose, experiments with *Shewanella oneidensis* and *Escherichia coli* were performed to show the extraction of iron and silicon from several different Lunar and Martian regolith simulants (JSC-1A, JSC-2, EAC-1, LHT3M and JSC-Mars1). The most successful extraction was performed with *S. oneidensis* on JSC-Mars1 and increased the extractable amount of iron by 5.5-fold after bacterial treatment.

Additionally, we modelled the general process, payback time and yields of the most promising bacteria for iron extraction in a feasibility study. To do so we calculated the amount of nutrients and infrastructure which needs to be transported from earth to enable the material extraction and combined it with experimental data regarding the bacterial growth. The only organism who had feasible yields was *Shewanella oneidensis* (payback time of 3.3 years), who reduces Fe(III) ions which can lead to a precipitation of magnetite. The magnetite can be extracted magnetically, and the iron therein can be utilized for maintenance materials, repairs and constructions. The left-over, non-

magnetic material is due to an increased amount of nutrients and less toxic iron molecules an improved growth medium for plants in biological life support systems. The whole process was ultimately combined in a potential mission architecture with the bioreactor as lander and a rover to gather the material as well as an integration in a Mars habitat connected to its life-support system. This work shows for the first time all aspects needed for a feasible biological *in situ* resource utilization including a mission architecture and study of the potential yields.

Samenvatting

Bacteriën en andere micro-organismen zijn onderdeel van ons dagelijks leven en worden intensief onderzocht. Dit werk identificeert toepassingen van bacteriën in nanotechnologie en ruimteonderzoek. Wij hebben voor beide velden dezelfde bacterie gebruikt: *Shewanella oneidensis*. Het elektron transfer mechanisme (MtrA, MtrB, MtrC, OmcA) in het celmembraan van *Shewanella oneidensis* vervoert elektronen, welke tijdens stofwisselingsprocessen geproduceerd worden, van binnen naar buiten. In de aanwezigheid van metaaloxiden kunnen de bacteriën deze reduceren.

In ons nanotechnologisch onderzoek hebben wij dit reductieproces op grafeenoxide toegepast. Grafeenoxide is een tweedimensionaal materiaal dat slechts één atoomlaag dik is, het is een koolstofraster met zuurstofgroepen (epoxyl, hydroxyl, carboxyl). In deze geoxideerde toestand is het materiaal stabiel in water en aanpasbaar, maar minder mechanisch sterk en niet geleidend. Daarom hebben we het reductiemechanisme van *Shewanella oneidensis* onderzocht om de zuurstofgroepen te reduceren en de geleiding te verbeteren terwijl het materiaal stabiel blijft in water en de tweedimensionale structuur behoud. Het door dit proces microbacterieel gereduceerde grafeenoxide (mrGO) (2,5 orde van groottes toename in geleiding) was minder geleidend dan het chemisch gereduceerde grafeenoxide (crGO) (3.1 orde van groottes toename in geleiding), maar het behield zijn 2-dimensionale structuur beter (gemiddelde dikte - mrGO: 10,4 ± 0,4 nm, crGO: 31,3 ± 7,0 nm)

Om dit microbacteriële reductieproces in een macroscopische toepassing over te nemen, bouwden we een set-up om de bacteriën samen met het grafeenoxide te 3D-printen en reductie van de aldus gedrukte grafeenoxide (geleidende inkt / geleidende gel) mogelijk te maken. De reductie van grafeenoxide was niet mogelijk vanwege ontbrekende voedingsstoffen en de

reductie van de alginaatmatrix door de bacteriën. Niettemin konden we deze methodiek toepassen om de algemene mogelijkheid van het 3D-printen van bacteriën voor materiaalproductie in meerdere lagen en een resolutie van 1,00 ± 0,15 mm laten zien.

De tweedimensionale structuur van grafeenoxide met een maximale verhouding van oppervlak tot volume maakt het ook een optimaal materiaal voor biosensoren door een enorme toename van de materiaalgevoeligheid. Verdere chemische modificaties zijn nodig om het oppervlak van het materiaal te passiveren en daar mee zijn specificiteit voor gerichte biomoleculen te verbeteren en het meer biocompatibel te maken. We gebruikten een combinatie van colamine (CA) en polyethyleenglycol (PEG) opgelost in dimethylformamide (DMF) of dimethylsulfoxide (DMSO) voor de passivering en testten het materiaal met X-Ray photoelectron spectroscopy (XPS).

In ruimteonderzoek concentreerden we ons op de toepassing van bacteriën voor in-situ resource-gebruik (ISRU) op Maan en Mars. ISRU beschrijft het proces van het gebruiken van natuurlijke hulpbronnen die op de bestemming zijn gevonden om te bouwen, te repareren en bij te tanken. Dit proces moet de duurzaamheid van ruimtemissies verbeteren en tegelijkertijd hun kosten verminderen. Voor dit doel werden experimenten met *Shewanella oneidensis* en *Escherichia coli* uitgevoerd om de extractie van ijzer en silicium van verschillende Maan- en Marsregoliet simulanten (JSC1A, JSC2, EAC1, JSC-1 Mars en LHT3M) te laten zien. Daarnaast modelleerden we het algemene proces, de terugverdientijd en de opbrengsten van de meest veelbelovende bacteriën voor ijzerwinning in een haalbaarheidsstudie. Om dit te doen hebben we de hoeveelheid voedingsstoffen en infrastructuur die van de aarde moet worden getransporteerd om de materiaalextractie mogelijk te maken berekend en deze gecombineerd met experimentele gegevens met betrekking tot de bacteriegroei. Het enige organisme dat haalbare opbrengsten had, was *Shewanella oneidensis*, die Fe(III) moleculen reduceert die kunnen leiden tot neerslag van magnetiet. Het magnetiet kan magnetisch worden geëxtraheerd en gebruikt worden voor onderhoudsmaterialen, reparaties en constructies. Het

resterend, niet-magnetisch materiaal is een optimaal groeimedium voor planten in biologische levensondersteunende systemen. Het hele proces werd uiteindelijk gecombineerd in een potentiële missiearchitectuur met de bioreactor als lander en een rover om het materiaal te verzamelen.

Acknowledgements

Hereby, I would like to thank everyone of you who accompanied me on this journey. Anne and Herre without the two of you I would have never ended up here. I am so grateful that you accompanied me and helped me to develop my english writing, inter-personal and especially my scientifical skill set in microbiology and nanomaterials. The guidance provided, and combined with the freedom given, made the experience tremendously worthwile and enjoyable. In this sense, also thanks to Stan whose lab "adopted" me in a time of high uncertainty. You and the entire lab always had an open door for me and significantly contributed to my scientific development. Aidan, when I left Spaceship EAC in 2016, I didn't dare to think of a collaboration during my PhD, but it worked out. It was great to see your whole group evolving and work with you throughout the years. Your scientific input and guidance was of utmost importance and I am happy to call you a dear friend. Lynn you fulfilled one of my biggest dreams – working at NASA. The 6 months in California were a life-changing experience and I learned a lot during that time. Thanks to you, Jess, Trevor!, Nils, Ivan, Jessica, Frauke, Conor and all the other members of your lab, and their significant others, I felt welcome from day one, eventhough USRA and NASA made it a bit difficult because of bureaucrazy and my nationality - I am after all an "Austrian spy".

Thanks to my students, Sabina for the contribution to the graphene oxide work, Saffira for the silicon extraction experiments, Rik for the great theoretic modelling – the feasibility model wouldn't have been possible without you. Your work helped significantly to understand the potential contribution of biological ISRU to space exploration and I am grateful to continue working with you in our young start-up; Marijn for his work on algae as a nutrient source for biological ISRU and great contributions to the bioreactor paper, Sophie and

Tom for your extremely valueable experiments on iron extraction and all the iGEMers throughout the years. All of you thaught me a lot and it was an honour to supervise you and see you grow. In this sense, I would also like to thank Bertus for numerous great discussions and the access to his lab and glove box, the Marles-Wright Laboratory at Newcastle University, Ferhat, Becca and the iGEM team of 2016 for a variety of genetic constructs as well Juergen Schleppi from Heriot-Watts university for all his help in the preparation of the regolith simulants and for just being a great friend in general.

Dominik, you thought me a lot about synthetic biology and microbiology. Your calmness always impressed me and it was an amazing experience to be an active part in your wedding. I will miss the time spent together – luckily we can still play via steam! Mathia, you are a great conversation, party and dance partner – I will miss our conversations and your always positive attitude. Lisa, your impressive sportsmanship is a real motivation and you were the best neighbor, in-private as well as in work, I could have imagened. I am happy to have you as one of my paranymphs Carsten, your scientific knowledge and smart explanations helped me in my first years as much as the shared calisthenics training and magic playing helped me in the last ones. You will indeed become a great teacher!

Talking about calisthenics: Filip, I will keep working on the muscle-up – next visit I'll challenge you! Thanks for accompanying me as a paranymph (and giving me shelter). Boris, you are not just an amazing musician but also a great sportsman and scientist – damet you got it all. Jose, your entrepeneurial spirit and occasinal sent songs are a real source of inspiration. Luuk you are an awesome dude. Our hike in Yosemite was one of the most amazing hikes ever. Thijs, thanks for all the laughs and great time – didn't know that electronics for physicists could be that much fun, but you and Wayne (Thanks!) proofed me wrong. Christian, you are a real energy bundle keep it going guy! Anouk, thanks for bringing some female power into the training – you are a real fighter. Lara, Mo, Sam, Ben, Iasonas and all the others who joined in for the training: Stay Tuned!

Tracey, Amanda, Sam, Kui, Xin Shi, Biswajit, Oscar, George, Aurora, Diego, Martin, Stanley and so many more. I will miss this environment – keep up the great work.

I would also like to thank the many great people I met at EAC before and during my PhD. Stephane and Dmitry, you thought me so much about myself and how to (not) make an Astronaut training. It was a pleasure to work with you. Matthias, you are one of the kindest and most inspiring persons I ever met. Yannick, you are an amazing engineer and I am very happy to work with you in the upcomming years! Tobi and Patrick, you guys are awesome – hope to train with you soon. Laura, Antoine, Corinne thanks for giving me shelter and spending many enjoyable hours together. Tom, Svetlana, Lionel, Alex, Jamel, Yannis, Francesco, Leo, Alberto, Daniele, Pablo, Stefan, Andrea, Shona, Jonathan, Matthew, Martin, Clara, Johanna, Thomas, Ingrid and all the others.

Thanks to the TEDxDelft team for some great training (Jolien and Wim), great organization (Anouk, Alexandra and Evi) and many new friends (Nima, Rushab).

Thanks to the EIT Health and Yes!Delft team. Through the bootcamp we had some great weeks together (and those were definitely the best graduate school credits of my PhD). Justin and Annemie the inspiration coming from you guys is like an eternal spring. We will make the world a world a little bit better with our new start-up and I am blessed to call you my friends. Tope and Mirte, you guys will help so many people! I will curiously follow your path. Ruben and Noor: frienship, passion and a variety of skills what more could we expect from our start-up trainers. Felix, thanks for the insightfull and honest discussions. Claudiu, Rory, Marteen, Joris, Ben, Tjarda, Iris, Georgia, Rachel and all the others thanks for this 9 weeks and the time after it. You all are a wonderful source of inspiration as well as motivation and I learned so much from each of you. Now it will be time to translate the knowledge into results.

In diesem Sinne moechte ich mich ebenso bei meiner Familie und Freunden zuhause in Österreich und Deutschland bedanken.

Mama du hast mich auf jedem Schritt dieser Reise begleitet und ich konnte mich immer auf deinen Rat verlassen. Wann immer ich nach Hause komme bekomme ich ein leckeres Schnitzel und deine ungeteilte Aufmerksamkeit. Jeder Besuch zu Hause ist der schönste vorstellbare Urlaub. Dazu trägst natürlich auch du maßgeblich bei Konni. Unser kleines Reich in den Bergen (Ja in Holland würde man unsere Anhöhe als Berg bezeichnen) von Attnang-Puchheim ist ein perfekter Zufluchtsort. Neben eurer elterlichen Fürsorge möchte ich mich ebenso für die finanzielle Unterstützung bedanken. Ohne diese wären wesentliche Teile meines beruflichen Werdegangs nicht möglich gewesen. Danke lieber Onkel Rudi, Tante Andrea und Chrisi für all die schönen Momente die wir bereits geteilt haben und auch noch in Zukunft teilen. Schade, dass Oma und Opa nicht mehr unter uns weilen, aber im Geiste sind sie bestimmt auch hier. Danke an Peter, Tante Silvia, Michi, Andi und Onkel Christian. Vielen Dank auch an meinen Papa der mir zahlreiche Lektionen in einem unkonventionellen Weg gelehrt hat und auch immer mehr ein Freund als eine Autoritätsperson war. Ihr alle habt meine grundlegenden Wertevorstellungen zu tiefst geprägt, mir den bestmöglichen Start ins Leben ermöglicht und begleitet mich auf Schritt und Tritt – vielleich sogar mehr als euch selbst klar ist. Ich habe euch sehr lieb!

Liebe Tina, ich danke dir für all die schönen Momente die wir Teilen durften. Du hast mich auf diesem Weg des Doktorats auf Schritt und Tritt begleitet und es war eine unglaubliche Zeit voll mit schönen Erfahrungen und Erlebnissen. Inge, Robert, Nici und Raphi ich möchte auch euch für all die schönen gemeinsamen Momente danken. Ihr habt mich so liebevoll in eure Mitte aufgenommen und ich habe die Zeit mit euch sehr genossen.

Auch einen großen Dank an meine Freunde. Alex BirnA für die vielen Gespräche, Tennisrunden, Zocknächte, Partys, Start-up Events und Urlaube die letzten 20 Jahre mit dir waren einfach der Hammer und ich bin sicher die nächsten 20 können das sogar noch toppen. Hitti für die Mathe-nachhilfe sowie auch unzählige philosophische, ethische, politische, wissenschaftliche Diskussionen und, of course, WoW. Conny & Markus, Margot, Johanna und

Curriculum Vitae

Benjamin Anton Egon Lehner

2016-2019	Ph.D research about Microbial application in nanotechnology and space research Department of Bionanoscience, Technical University Delft PI: Dr. Anne S. Meyer (Rochester University, NY) & Dr. Stan J.J. Brouns Department of Quantum Nanoscience, Technical University Delft PI: Prof. dr. Herre S.J. van der Zant Knowledge Exchange with NASA Ames, USA (6 months) PI: Prof. dr. Lynn J. Rothschild
2015-2016	Research Internship – Life Support Systems, Astronaut Training (Life science and survival training) European Astronaut Centre (EAC), ESA in Cologne, Germany PI: Dr. Aidan Cowley & Dr. Stephane Ghist
2013-2015	Research Assistant – EU Project CATO & BRIDGE (Counter-Terrorism) Paris Lodron University Salzburg, Austria PI: Prof. dr. Friedrich Steinhaeusler
2013-2015	M.Sc in Biology – Major: Radioactivity, Molecular Biology Paris Lodron University Salzburg, Austria
2012-2016	Engineering (B.eng) at Paris Lodron University Salzburg, Austria and Technical University Munich, Germany (unfinished)
2010-2013	B.Sc in Biology – Major: Physiology Paris Lodron University Salzburg, Austria
2009-2010	Civil Service in a retirement home – working with dementia patients Attnang-Puchheim, Austria
2005-2009	High school diploma – Major: Natural Science Schloss Wagrain, Voecklabruck, Austria
19-04-1991	Born in Vöcklabruck, Austria

List of Publications

10.   M.J. Timmer, **B.A.E. Lehner*** and C. Piciorean*, Theoretical algae-reactor design for zero-g conditions, Manuscript in prepararion.

9.   S. Castelein⁺, T. Aarts⁺, J. Schleppi, R. Hendrikx, D. Benz, A.J. Bottger, A. Makaya, M. Schwentenwein, B. Beamount, S.J.J. Brouns, A.S. Meyer and **B.A.E. Lehner***, Extraction of iron from Lunar and Martian regolith simulants using a microbial approach in conjunction with 3D printing, Manuscript in preparation.

8.   R. Volger, G. Pettersson, S.J.J. Brouns, L.J. Rothschild, A. Cowley* and **B.A.E. Lehner*,**   Mining Moon & Mars with microbes: Biological approaches to extract iron from Lunar and Martian regolith. Submitted to Planetary and Space Science 2019

7.   **B.A.E. Lehner,** D. Benz, Stanlislav, A. Moshkalev, A.S. Meyer, M.A. Cotta* and R. Janissen*, Homogenous and Biocompatible Covalent coating of Graphene Oxide for Biomedical Applications. Submitted to ACS Applied Nano Materials 2019

6.   R. Volger⁺, M.J. Timmer⁺, J. Schleppi, C.N. Haenggi, A.S. Meyer, C. Piciorean, A. Cowley* and **B.A.E. Lehner***, Bioreactor design to perform microbial mining activities on another celestial body. Submitted to Acta Astronautica 2019

5.   **B.A.E. Lehner,** V. A.E.C. Janssen, E.M. Spiesz, D. Benz, S.J.J. Brouns, A.S. Meyer*, and H. S. J. van der Zant*, Creation of conductive

graphene materials by bacterial reduction using Shewanella oneidensis"
Chemistry Open 2019, 8, 888, doi: 10.1002/open.201900186

4.   **B.A.E. Lehner,** J. Schlechten, A. Filosa, A. Canals Pou, D.G. Mazzotta, F. Spina, L. Teeney, J. Snyder, S. Tjorn, A.S. Meyer, S.J.J. Brouns, A. Cowley and L.J. Rothschild, End-to-end mission design for microbial in-situ resource utilization activities as preparation for a moon village. Acta Astronautica 2019, 162, doi: 10.1016/j.actaastro.2019.06.001

3.   E. Spiesz[+], K. Yu[+], **B.A.E. Lehner**, D. T. Schmieden, M.E. Aubin-Tam*, A.S. Meyer*, 3D patterning of engineered biofilms with a DIY bioprinter. Journal of Visualized Experiments 2019, 147, e59477, doi: 10.3791/59477

2.   **B.A.E. Lehner**, D.G. Mazzotta, L. Teeney, F. Spina, A. Filosa, A. Canals Pou, J. Schlechten, S. Campbell, P. López Soriano, Human Assisted Robotic Vehicle Studies - A conceptual end-to-end mission architecture. Acta Astronautica 2017, 140, doi: 10.1016/j.actaastro.2017.08.032

1.   **B.A.E. Lehner**, D. T. Schmieden, and A.S. Meyer*, A Straightforward Approach for 3D Bacterial Printing. ACS Synthetic Biology 2017, 6 (7), pp 1124–1130, doi: 10.1021/acssynbio.6b00395

Every failure you endure, every criticism you receive and every day you persevere has solely one goal: Bringing out the best in you. So, stay tuned and become the best version of yourself!